frontiers | Research Topics

Spinal cord development and neural regeneration

Edited by
Lingyan Xing, Qi Han, Biqin Lai and Feng Rao

Published in
Frontiers in Molecular Neuroscience

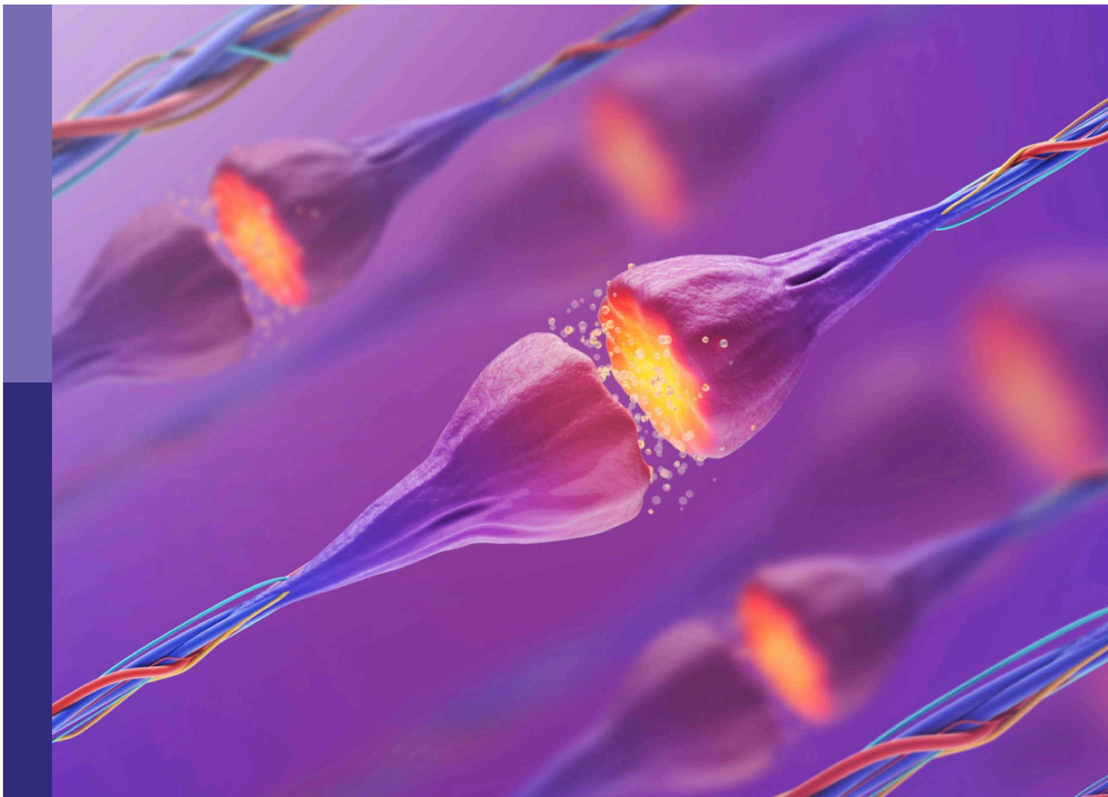

ISSN 1664-8714
ISBN 978-2-83251-578-5
DOI 10.3389/978-2-83251-578-5

About Frontiers

Frontiers is more than just an open access publisher of scholarly articles: it is a pioneering approach to the world of academia, radically improving the way scholarly research is managed. The grand vision of Frontiers is a world where all people have an equal opportunity to seek, share and generate knowledge. Frontiers provides immediate and permanent online open access to all its publications, but this alone is not enough to realize our grand goals.

Frontiers journal series

The Frontiers journal series is a multi-tier and interdisciplinary set of open-access, online journals, promising a paradigm shift from the current review, selection and dissemination processes in academic publishing. All Frontiers journals are driven by researchers for researchers; therefore, they constitute a service to the scholarly community. At the same time, the *Frontiers journal series* operates on a revolutionary invention, the tiered publishing system, initially addressing specific communities of scholars, and gradually climbing up to broader public understanding, thus serving the interests of the lay society, too.

Dedication to quality

Each Frontiers article is a landmark of the highest quality, thanks to genuinely collaborative interactions between authors and review editors, who include some of the world's best academicians. Research must be certified by peers before entering a stream of knowledge that may eventually reach the public - and shape society; therefore, Frontiers only applies the most rigorous and unbiased reviews. Frontiers revolutionizes research publishing by freely delivering the most outstanding research, evaluated with no bias from both the academic and social point of view. By applying the most advanced information technologies, Frontiers is catapulting scholarly publishing into a new generation.

What are Frontiers Research Topics?

Frontiers Research Topics are very popular trademarks of the *Frontiers journals series*: they are collections of at least ten articles, all centered on a particular subject. With their unique mix of varied contributions from Original Research to Review Articles, Frontiers Research Topics unify the most influential researchers, the latest key findings and historical advances in a hot research area.

Find out more on how to host your own Frontiers Research Topic or contribute to one as an author by contacting the Frontiers editorial office: frontiersin.org/about/contact

Spinal cord development and neural regeneration

Topic editors
Lingyan Xing — Nantong University, China
Qi Han — Shanghai Jiao Tong University, China
Biqin Lai — Sun Yat-sen University, China
Feng Rao — Peking University People's Hospital, China

Citation
Xing, L., Han, Q., Lai, B., Rao, F., eds. (2023). *Spinal cord development and neural regeneration*. Lausanne: Frontiers Media SA. doi: 10.3389/978-2-83251-578-5

Table of contents

Frontiers in Molecular Neuroscience

TYPE Editorial
PUBLISHED 23 January 2023
DOI 10.3389/fnmol.2023.1117887

Check for updates

OPEN ACCESS

EDITED AND REVIEWED BY
Clive R. Bramham,
University of Bergen, Norway

*CORRESPONDENCE
Lingyan Xing
✉ xlyan011@163.com

SPECIALTY SECTION
This article was submitted to Neuroplasticity and Development, a section of the journal Frontiers in Molecular Neuroscience

RECEIVED 07 December 2022
ACCEPTED 10 January 2023
PUBLISHED 23 January 2023

CITATION
Xing L, Han Q, Lai B and Rao F (2023) Editorial: Spinal cord development and neural regeneration. *Front. Mol. Neurosci.* 16:1117887. doi: 10.3389/fnmol.2023.1117887

Editorial: Spinal cord development and neural regeneration

Lingyan Xing[1]*, Qi Han[2], Biqin Lai[3] and Feng Rao[4]

[1]Nantong University, Nantong, China, [2]Shanghai Jiao Tong University, Shanghai, China, [3]Sun Yat-sen University, Guangzhou, Guangdong, China, [4]Peking University People's Hospital, Beijing, China

KEYWORDS

spinal cord injury, spinal cord development, neurocircuit, axon regeneration, zebrafish, nerve repair

Editorial on the Research Topic
Spinal cord development and neural regeneration

The spinal cord is essential for processing sensory information and motor function. Following spinal cord injury (SCI), neuronal networks in animals are damaged and difficult to repair. Limited endogenous neurogenesis and axon regeneration are observed, indicating a failure of recapitulating the developmental processes. There have been several significant developments in spinal cord development and regeneration studies in recent years. The cellular and molecular mechanisms of circuit creation in the growing spinal cord, circuit repair after SCI, and possible tactics for fostering neural plasticity after SCI are the focus of this Research Topic.

We were delighted to receive several papers from writers presenting their most recent research findings on spinal cord growth and regeneration. A summary of the 10 accepted articles is provided below.

Spinal cord regeneration

Boosting axonal growth potential is a challenge for spinal cord regeneration. Noristani et al. demonstrated that targeting B-RAF and PTEN simultaneously efficiently promoted DC axon growth in both the pre- and post-lesion states. Luo et al. showed that PDIA6 and spastin might collaborate as critical mediators of nerve healing. Larval zebrafish have been used in spinal cord injury because of their optical transparency, straightforward anatomy, and complex behavior. Alper and Dorsky discussed the benefits of using larval zebrafish in research on spinal cord regeneration, which could hasten the identification of new functions for genes and cell types involved in spinal cord regeneration.

Spinal cord development

Understanding the mechanism of spinal cord development will provide important knowledge for creating therapies and care plans for patients with spinal cord injuries and other neurological conditions. Zheng et al. demonstrated that NEXMIF is crucial for spinal motorneuron morphogenesis and that zebrafish swimming motility could be severely impaired by NEXMIF loss. Using an effective zebrafish model, Sheng et al. revealed that sema6D regulates spinal cord vascular patterning and motor neurons axon development. Oria et al.

reported that premature astrogliosis and astrocytic activation were seen in a spina bifida model, which seemed to involve upregulation of the Notch-BMP signaling pathway.

Spinal cord-related disease models

We also received a few papers highly relevant to spinal cord injury, e.g., pain. By inhibiting the expression of caspase-1 and IL-1, Probenecid reduces inflammation. This, in turn, restores the balance of immune cell subsets and has neuroprotective effects in rats with spinal cord injury, according to research by Qi et al. and Sun et al. showed that the STING-IFN-I pathway may play a role in the development of neuropathic pain by increasing PTPRD levels in the DRG after CCI. An exciting therapeutic approach for the clinical management of neuropathic pain without the danger of addiction may be represented by 7-BIA, an inhibitor of PTPRD with anti-addiction properties. Liang et al. discovered that several sagittal parameters were used to alter the saggital balance for patients with degenerative kyphosis, positioning the body. Wu et al. showed that Regenerative peripheral nerve interfaces (RPNI) effectively prevented the formation of neuromas.

We anticipate that the research on spinal cord development and regeneration will gain greater attention as a result of this Research Topic. We appreciate the reviewers' work in ensuring the collection's high caliber. The authors who have contributed are also thanked.

Author contributions

All authors listed have made a substantial, direct, and intellectual contribution to the work and approved it for publication.

Acknowledgments

We thank the reviewers for their efforts to guarantee the high quality of this Research Topic. We also thank all of the authors who have contributed.

Conflict of interest

The authors declare that the research was conducted in the absence of any commercial or financial relationships that could be construed as a potential conflict of interest.

Publisher's note

frontiers
in Molecular Neuroscience

ORIGINAL RESEARCH
published: 22 March 2022
doi: 10.3389/fnmol.2022.847857

Correlation Between Different Sagittal Parameters in Patients With Degenerative Kyphosis

Yan Liang[1]†, Shuai Xu[1]†, Chen Guo[1], Keya Mao[2]* and Haiying Liu[1]*

[1] Spinal Surgery, Peking University People's Hospital, Beijing, China, [2] The Chinese PLA General Hospital (301 Hospital), Beijing, China

Edited by:
Lingyan Xing,
Nantong University, China

Reviewed by:
Zhonghai Li,
First Affiliated Hospital of Dalian Medical University, China
Xuejian Wang,
Nantong First People's Hospital, China

***Correspondence:**
Haiying Liu
18511857285@163.com
Keya Mao
maokeya301spine@163.com

† These authors share first authorship

Specialty section:
This article was submitted to Neuroplasticity and Development, a section of the journal Frontiers in Molecular Neuroscience

Received: 03 January 2022
Accepted: 24 January 2022
Published: 22 March 2022

Citation:
Liang Y, Xu S, Guo C, Mao K and Liu H (2022) Correlation Between Different Sagittal Parameters in Patients With Degenerative Kyphosis.
Front. Mol. Neurosci. 15:847857.
doi: 10.3389/fnmol.2022.847857

Objective: To explore the relationship between different sagittal parameters and identify the fitting formula of spino-pelvic parameters in patients with degenerative kyphosis (DK).

Summary of Background: Sagittal balance is increasingly recognized as a predictor of clinical outcomes in patients with DK, while the relationship between different sagittal parameters in patients with DK remains unidentified.

Methods: A retrospective study with 279 participants was conducted. There were 168 DK patients which were divided into a sagittal balance group (SB:52 cases) and sagittal imbalance (SIB:116 cases). Radiographic measurements included thoracolumbar kyphosis (TLK), lumbar lordosis (LL), thoracic kyphosis (TK), pelvic incidence (PI), and pelvic tilt (PT). The correlations were analyzed between different sagittal parameters.

Results: There were significant differences between the SB and SIB groups in terms of TLK, LL, PI-LL, PT, SVA, sacral slope (SS), and TK. For patients with DK, the LL was correlated with PT and TK. The linear regression was $LL = 22.76 - 0.28 \times PT + 0.62 \times TK$. In the SB group, TK was the influencing factor for LL and the linear regression analysis showed that $LL = 33.57 + 0.33 \times TK$. While in the SIB group, PT and TK were in synergistic effect with PI-LL, the linear regression analysis showed that $LL = 22.76 - 0.28 \times PT + 0.62 \times TK$.

Conclusion: From the present study, we can see that LL has a significant correlation with PT and TK in patients with DK, while in SB, the LL was only correlated with TK. Therefore, the correction of LL in a different group should be calculated to avoid the incidence of proximal junction kyphosis (PJK).

Keywords: degenerative kyphosis, lumbar lordosis, thoracolumbar kyphosis, pelvic incidence, pelvic tilt, sagittal balance

---

Abbreviations: DK, degenerative kyphosis; DTLK, degenerative thoracolumbar kyphosis; DLLL, loss of lumbar lordosis; PI, pelvic incidence; PT, pelvic tilt; SB; sagittal balance; SIB, sagittal imbalance; SVA, sagittal vertical axis.

INTRODUCTION

The typical sagittal sequence of the spine and the balance status of the lumbar-pelvis are the main factors for spinal kinematics and energy expenditure. In a normal population, the structure of the spine is closely related to biomechanics and forms a unique "S-shaped" bend through bone adjustment (Roussouly and Pinheiro-Franco, 2011; Diebo et al., 2015). Lumbar kyphosis maintains a stable center of gravity in the area between the feet, maximizing energy efficiency while minimizing the impact of gravity on the joints, muscles, and ligaments with the "energy cone" (Le Huec et al., 2019). The ideal spino-pelvic sagittal sequence describes the ideal dynamic matching of bones in the sagittal position due to the interaction among various segments, while the focal disorders or breaking of the balance will cause sagittal deformity and a compensatory mechanism by other parts in order to minimize the energy cost (Liu et al., 2020).

With the aging of the population, the number of patients with degenerative kyphosis (DK) is gradually increasing by the spinal degeneration of vertebral deformation, facet disorders, disc aging, as well as osteophyte formation (Lee et al., 2011). DK is mainly characterized by the decrease of lumbar lordosis (LL) and/or the increase of thoracolumbar kyphosis (TLK) with enlarged prevalence in the elderly accompanied with or without neurological deficit. In cases of DK with either condition, the proximal and distal levels of the spine and pelvis are compensated accordingly to maintain a healthy state of balance. Once the compensatory capacity is overloaded, it leads to an unbalanced state (Schwab et al., 2012, 2013; Wu et al., 2014).

The spino-pelvic alignment has been quantified by a series of parameters with uniformed theory. Dubousset et al. (2005) proposed that the pelvis is the cornerstone of the sagittal sequence of the spine, and the pelvic tilt (PT) established a possible compensatory mechanism for spinal imbalance. Ginette Duval-Beaupere defined the geometric meanings of pelvic incidence (PI), PT, and sacral slope (SS): PI = PT + SS (Duval-Beaupere et al., 1992), and the pelvic incidence–lumbar lordosis (PI–LL) $<10°$ threshold was determined as the standard for spinal-pelvic sagittal fitting (Schwab et al., 2010), which linked the relationship between lumbo-pelvic matching.

Many studies have specifically discussed the correlation among sagittal spinal parameters. Kim pointed out that the loss of LL is the initial of spino-pelvic malalignment and the key factor of compensation (Kim et al., 2014). Lafage et al. (2016) proved that the compensatory mechanism of the spine usually starts from the flexible segments with a broad range of motion and gradually extends distally. The body compensates by moving the center of gravity back and forth, beginning with the traction of thoracic vertebrae, then regulated by pelvic rotation and hip-knee flexion. Schwab et al. (2013) put forward the correction formula LL = (PI + TK)/2 + 10 in adult spinal deformity, which skillfully correlates more parameters to fit the real sagittal sequence. However, the relationship among sagittal spino-pelvic parameters and the influence of spino-pelvis matching is seldom featured in patients with DK. Therefore, by enrolling the patients with DK, the purpose of this study was to explore the relationship among sagittal spino-pelvic parameters and identify the fitting formula of spino-pelvic parameters by the lumbo-pelvic balance status.

MATERIALS AND METHODS

Participants

A single-center retrospective study was performed in our institution from June 2016 to June 2020. The patients with DK of the whole spine were included, composed of the degenerative thoracolumbar kyphosis (DTLK) or loss of LL. According to the viewpoints of Schwab et al. (2007), PI-LL was a key parameter for quantifying sagittal balance, where a matched condition was PI-LL $\leq \pm 10°$. Hence, the series was divided into 2 groups, sagittal balance (SB) group: $|\text{PI-LL}| \leq 10°$ (**Figure 1**) and sagittal imbalance (SIB) group: $|\text{PI-LL}| > 10°$ (**Figure 2**; Lafage et al., 2017). The participants from the two groups were selected with a matching of 1:2 by propensity score matching. The protocol was approved by the ethics committee and all participants have signed the consent forms.

The inclusion criteria were (1) patients with TLK, loss of LL, or both caused by degeneration; (2) whole-spine X-ray and lumbar spine X-ray were completely obtained; and (3) an age of more than 50 years for all participants. The exclusion criteria were (1) patients sustaining coronary imbalance; (2) blurred images of radiographs for measurement; (3) patients with idiopathic scoliosis or other types of deformities; (4) patients with spine tumors, infections, or spondylolisthesis; and (5) patients who had undergone lumbar spine surgery before.

Radiological Parameters

Thoracolumbar kyphosis was the angle between the upper endplate of T10 and the lower endplate of L2 and DTLK was TLK $\geq 15°$ with degenerative factors; LL was the angle between the upper endplate of L1 and the upper endplate of S1 and the loss of LL was LL $\leq 25°$. TK was the angle between the upper endplate of T5 and the upper endplate of T12. The spino-pelvic parameters contained PI-LL and PT in this study. PT was the angle between the plumb line and the center of the femoral head to the midpoint of the upper endplate of S1. PI was defined as the vertical line passing through the midpoint of the upper endplate on S1, then the second line connecting the midpoint of the upper endplate on S1 and the femoral head and the angle between the second line and vertical line. Sagittal vertical axis (SVA) was the axis. All parameters were independently measured by two reviewers, and the mean value was adopted.

Statistical Analysis

The dichotomy between SB and SIB groups were analyzed by χ^2 test. An independent sample *t*-test was used for inter-group measurement data. Pearson correlation analysis was used to determine the relationship between LL, PI-LL, PT, and TK. Multiple linear regression analysis was for determining the influencing factors of PI-LL and LL. SPSS 22.0 (IBMC, Armonk, NY, United States) the software for statistical analysis, and $P < 0.05$ was statistically significant.

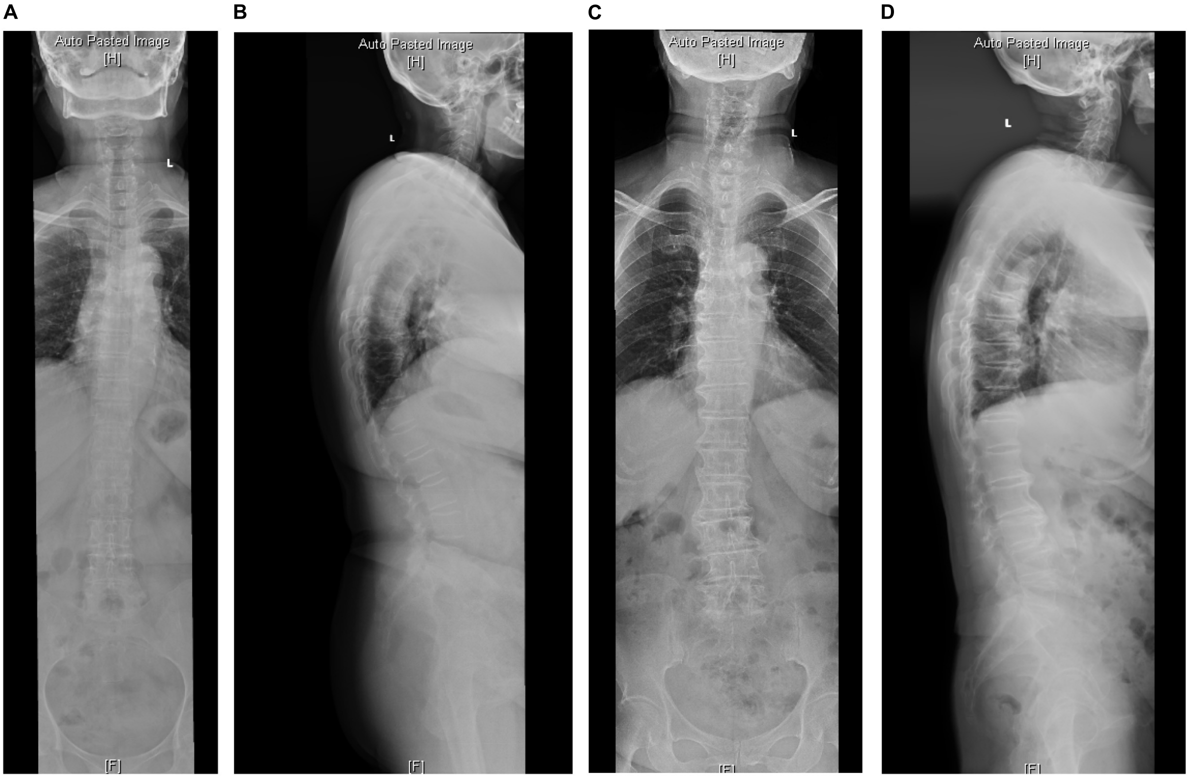

FIGURE 1 | The radiological parameters measured on standard anterior-posterior and lateral whole spine X-ray of cases from the SB group. **(A,B)** In a 70-year-old man, TK = 58, TLK = 26.1, LL = 56.1, PI = 51, PT = 20.4. **(C,D)** In a 68-year-old woman, TK = 29.4, TLK = 15.2, LL = 35.3, PI = 44.7, PT = 21.

RESULTS

Patient Clinical Characteristics

A total of 168 patients was included with 52 cases in the SB group and 116 cases in the SIB group. There were no differences between the subgroups in terms of gender ($P = 0.555$), age ($P = 0.686$), and BMI ($P = 0.278$). Thirty-seven cases both had TLK and loss of LL, and TLK was the majority (94.3%) in the SB group in contrast with the group with unmatched PI-LL ($P < 0.001$). There was a significant difference between the SB and SIB groups in terms of TLK, LL, PI-LL, PT, SVA, SS, and TK ($P < 0.05$) (**Tables 1**, **2**).

Pearson Correlation Analysis

In the SB group, PI-LL was negatively related to LL ($r = -0.492$, $P < 0.001$), and TK was positively related to PT ($r = 0.440$, $P = 0.02$) and LL ($r = 0.370$, $P = 0.008$). In the SIB group, PI-LL was positively correlated to PT while negatively related to TK and LL ($P < 0.01$). LL was correlated to PT ($P = 0.037$) and TK ($P < 0.001$) (**Table 3** and **Figures 1**, **2**).

Multiple Linear Regression Analysis

In the SB group, the linear regression analysis showed that TK was the influencing factor for PI-LL and LL ($\text{PI-LL} = 0.47 \times \text{PT} - 0.46 \times \text{TK}$ and $\text{LL} = 33.57 + 0.33 \times \text{TK}$). While in the SIB group, PI-LL, PT, and TK were in synergistic effect with $\text{PI-LL} = 6.81 + 0.66 \times \text{PT} - 0.47 \times \text{TK}$ and $\text{LL} = 18.2 – 0.26 \times \text{PT} + 0.62 \times \text{TK}$. When integrating the SB and SIB groups, PI-LL, PT, and TK were shown to be synergistic parameters regardless of being in a matched and unmatched group: $\text{PI-LL} = 4.92 + 0.64 \times \text{PT} - 0.50 \times \text{TK}$ and $\text{LL} = 22.76 - 0.28 \times \text{PT} + 0.62 \times \text{TK}$ (**Table 4**).

DISCUSSION

The sagittal spino-pelvic alignment has an important role in maintaining the normal function of the spine and provides explicit guidance for surgical reconstruction. The degenerative progression of sagittal deformity of the spine consumes a lot of energy for patients and may accelerate the progress of other spinal degenerative diseases (Kim et al., 2014; Lee et al., 2017). Therefore, many studies have attempted to explore and quantify the correlation between spino-pelvic parameters to provide clinical evidence. Schwab et al. (2010) quantified the relationship between the pelvis and LL by PI minus LL, and determined the PI-LL <10° as the standard threshold of spino-pelvic match (Barrey et al., 2007). Then, the team proposed that LL exceeding PI is relatively appropriate in patients with low PI according to the clinical practice, conversely, LL is less than PI; and high TK also need a larger LL than the theoretical value to compensate for thoracic kyphosis (TK),

FIGURE 2 | The radiological parameters measured on standard anterior-posterior and lateral whole spine X-ray of cases from the SIB group. **(A,B)** In a 68-year-old woman, TK = 16.4, TLK = 1.1, LL = 19.5, PI = 63.4, PT = 39.9. **(C,D)** In a 72-year-old man, TK = 40.9, TLK = 40, LL = 72.2, PI = 51.7, PT = 3.7.

that is, $LL = (PI + TK)/2$ (Le Huec et al., 2015a). A later study found that there is a correlation between parameters and age. In the middle-aged population, the normal range of parameters is different from that of young people. Lafage et al. (2017) believe that elderly patients have more compensation, more serious loss of LL and more anteversion, so they put forward an age-related correction formula. Zhou et al. (2019) studied the sagittal shape and sequence matching relationship of spino-pelvis in normal middle-aged population, and pointed out that there were great differences in pelvic parameters between China and foreign countries: $LL = 0.6PI + 0.4TK + 10$.

The normal sequence of lumbar vertebrae is the basis for the study of lumbar development and degenerative diseases and the premise of reconstruction surgery. Mangione et al. (1997) believe that to maintain a balanced posture with minimum energy consumption, the best sequence of the lumbar spine depends on the PI, while the definition of PT establishes a possible compensatory mechanism for spinal imbalance and quantifies the pelvic rotation around the femoral head. The sagittal alignment was a morphology parameter that correlated with anatomy, and the balance was a dynamic characteristic (Moal et al., 2015). Spinal degeneration can involve any segment, and the loss of LL is the main cause of sagittal sequence loss. PT, as a sensitive parameter of spino-pelvic mismatch, is the main compensatory mechanism. The continuous loss of lumbar kyphosis is usually accompanied by an increase in pelvic rotation and TLK, resulting in DK. For such patients, the compensation mechanism usually starts from the flexible segments with a large range of movement (Kim et al., 2014). With the pelvis as the cornerstone of spine, the body always tried to maintain the whole spino-pelvic balance through the interaction of various parts of the mechanical chain of the spine and pelvis. In the past, many studies focused on the regulation of the distal pelvis of the lumbar spine, and the compensation mechanism of the proximal end has been gradually quantified in recent years. In this study, the sagittal plane parameters of these kinds of patients were statistically analyzed, and it was concluded that the sagittal plane balance was regulated and maintained by LL, PT, and TK.

Regarding the sagittal compensatory mechanism of DK, Barrey et al. (2013) think that the severity of the imbalance corresponds to three stages: the state of equilibrium, the

TABLE 1 | Basic information in matched and unmatched groups.

	SB	SIB	P
Gender, M:F	19:33	37:79	0.555
Age, y	67.3 ± 8.8	66.6 ± 9.9	0.686
BMI, kg/m^2	25.3 ± 3.4	26.0 ± 4.0	0.278
No. of increased TLK	50	78	<0.001
No. of decreased LL	3	74	

BMI, body mass index; TLK, thoracolumbar kyphosis; LL, lumbar lordosis.

TABLE 2 | Spino-pelvic parameters in matched and unmatched groups.

	SB	SIB	P
TLK,°	25.4 ± 12.3	18.4 ± 15.2	0.004
LL,°	45.8 ± 11.9	23.4 ± 20.8	<0.001
PI,°	46.5 ± 10.4	44.6 ± 12.1	0.325
PI-LL,°	0.7 ± 5.2	21.2 ± 18.1	<0.001
PT,°	16.1 ± 6.6	23.5 ± 10.7	<0.001
SVA, mm	25.7 ± 27.2	56.4 ± 50.6	<0.001
TK,°	34.9 ± 13.8	21.2 ± 15.9	<0.001
SS,°	30.5 ± 10.0	21.1 ± 11.0	<0.001

TLK, thoracolumbar kyphosis; LL, lumbar lordosis; PI, pelvic incidence; PT, pelvic tilt; SVA, sagittal vertical axis; TK, thoracic kyphosis; SS, sacral slope.

TABLE 3 | Correlation analysis among PI-LL, PT, and TK in matched and unmatched groups.

		PI-LL		PT		TK	
		r	P	r	P	r	P
SB	PT	0.244	0.085				
	TK	−0.258	0.071	0.440	0.002		
	LL	−0.492	<0.001	0.222	0.117	0.370	0.008
SIB	PT	0.699	<0.001				
	TK	−0.522	<0.001	−0.073	0.471		
	LL	−0.801	<0.001	−0.303	0.001	0.634	<0.001
Total	PT	0.700	<0.001				
	TK	−0.564	<0.001	−0.094	0.255		
	LL	−0.827	<0.001	−0.357	0.000	0.650	<0.001

PI, pelvic incidence; LL, lumbar lordosis; PT, pelvic tilt; TK, thoracic kyphosis.

TABLE 4 | Multiple linear regression analysis on LL in matched and unmatched groups.

	Coefficient	Unstandardized		Standardized	T	P
		B	SE	Beta		
SB	(constant)	33.565	5.091		6.593	<0.001
	PT	0.133	0.279	0.073	0.478	0.635
	TK	0.291	0.133	0.333	2.186	0.034
SIB	(constant)	18.200	4.147		4.389	<0.001
	PT	−0.476	0.136	−0.261	−3.508	0.001
	TK	0.801	0.097	0.615	8.262	<0.001
Total	(constant)	22.756	3.444		6.607	<0.001
	PT	−0.563	0.117	−0.284	−4.817	<0.001
	TK	0.789	0.075	0.623	10.588	<0.001

LL, lumbar lordosis; PT, pelvic tilt; TK, thoracic kyphosis; SE, standard error.

balance under the compensatory mechanism, and the state of imbalance. The influence of the loss of thoracolumbar and lumbar curvature overall sagittal sequence is compensated and helps to maintain sagittal balance. Once the deformity aggravates and the compensation mechanism cannot maintain balance, the state of decompensation will occur. According to the sagittal parameters of the patient, Schwab et al. (2014) proposed that the patient's PT is greater than 20° and the patient's pelvic rotation is in the limit state, which cannot be compensated effectively, and the patient is in a state of decompensation. Clinically, the characteristic of the DK was the loss of LL and/or the increase of TLK (Roussouly and Pinheiro-Franco, 2011). Knowing the relationship between sagittal plane parameters in patients with DK was of great importance, which could better evaluate the patient and guide surgical treatment (Le Huec et al., 2015b). Therefore, in this paper, we divided the DK patients into two groups according to different PT: balance group and imbalance group, and explored the relationship between different sagittal parameters in different groups.

In our study, in the balance group, the LL was correlated with TK. The formula was LL = 33.57 + 0.33 × TK. For the DK patients with balance, the sagittal alignment was in a compensatory state. Due to the degeneration of the spine, the LL decreased. To keep the balance, the back-muscle system and skeleton system cooperated with each other as a whole, which makes the body stay in a balanced state (Liu et al., 2020). With the decrease of the LL, the pelvic retroversion and the TK decreased, which make the spine balanced. Through this study, we can see that the LL was correlated with TK but not PT. Because for such patients, the pelvis was in an adjustable state, the spine starts the self-adjustment mechanism. The reduction of the TK was to accommodate the decrease of LL, which can make the patient stay balanced enough (Lamartina et al., 2012; Bassani et al., 2019). Besides, the formula could provide a guideline of the surgical treatment. The main purpose of the operation was to restore the LL to alleviate the back pain in the treatment of the balanced DK patients. Over restoration of the LL may result in the enlargement of TK, which contributes to the high incidence of proximal junction kyphosis (PJK), so the LL should be properly restored to avoid the complication.

For the imbalance group, the LL was correlated with TK and PT, the formula was LL = 18.2−0.26 × PT + 0.62 × TK. For such patients, the body was out of control for various reasons. The reduction of the TK was not enough to make the patient stay in balance and the pelvic adjustment mechanism activated. Both try their best to put the whole body in an upright position. The patient's pelvic rotation is in a limited state, which cannot be compensated effectively (Le Huec et al., 2011; Lee et al., 2011). Therefore, for such patients, restoring the LL was not enough, and correcting the pelvic rotation was also necessary. The methods of the correction of pelvic rotation should be used in the treatment of such patients.

The current research has several limitations. Firstly, it is a retrospective study, which raises a concern about selection bias and loss of follow-up. Secondly, we only concentrated on the sagittal alignment of the patients, and coronal balance should be further studied in the next framework. Eventually, the number of cases in our study was relatively small. Larger case studies should be conducted in the future.

CONCLUSION

For the patients with DK, the sagittal balance was adjusted by different sagittal parameters, which positions the body. From the present study, we can see that the LL has a significant correlation with PT and TK in patients with DK, especially in the SIB group. So, the LL and pelvic rotation should both be of concern during the correction. While in SB, the LL was only correlated with TK. Over restoration of the LL may contribute to a high incidence of PJK. Therefore, the correction of LL in different groups should be calculated to avoid complication.

DATA AVAILABILITY STATEMENT

The original contributions presented in the study are included in the article/supplementary material, further inquiries can be directed to the corresponding authors.

ETHICS STATEMENT

The protocol was reviewed and approved by the Ethics committee of Peking University of people's hospital. Written informed consent was obtained from all participants for their participation in this study.

AUTHOR CONTRIBUTIONS

HL and YL: conceptualization. HL, SX, and CG: data curation. YL and SX: formal analysis and software. YL and CG: investigation. SX, YL, and KM: methodology. HL: project administration. SX and KM: resources. YL: validation. HL: visualization. HL, SX, and YL: writing and editing. All authors contributed to the article and approved the submitted version.

FUNDING

Procurement of Government of National Health Commission of China (grant number 2127000218).

ACKNOWLEDGMENTS

We acknowledge Yonggang Zhang who contributed to the study by making substantial contributions to the design and the acquisition of data.

REFERENCES

Barrey, C., Jund, J., Noseda, O., and Roussouly, P. (2007). Sagittal balance of the pelvis-spine complex and lumbar degenerative diseases. A comparative study about 85 cases. *Eur. Spine J.* 16, 1459–1467. doi: 10.1007/s00586-006-0294-6

Barrey, C., Roussouly, P., and Le, H. J. C. (2013). Compensatory mechanisms contributing to keep the sagittal balance of the spine. *Eur. Spine J.* 22(Suppl. 6), 834–841. doi: 10.1007/s00586-013-3030-z

Bassani, T., Galbusera, F., Luca, A., Lovi, A., Gallazzi, E., and Brayda-Bruno, M. (2019). Physiological variations in the sagittal spine alignment in an asymptomatic elderly population. *Spine J.* 19, 1840–1849. doi: 10.1016/j.spinee.2019.07.016

Diebo, B. G., Varghese, J. J., Lafage, R., Schwab, F. J., and Lafage, V. (2015). Sagittal alignment of the spine: what do you need to know? *Clin. Neurol. Neurosurg.* 139, 295–301. doi: 10.1016/j.clineuro.2015.10.024

Dubousset, J., Charpak, G., Dorion, I., Skalli, W., Lavaste, F., Deguise, J., et al. (2005). A new 2D and 3D imaging approach to musculoskeletal physiology and pathology with low-dose radiation and the standing position: the EOS system. *Bull. Acad. Natl. Med.* 189, 287–297; discussion 297–300.

Duval-Beaupere, G., Schmidt, C., and Cosson, P. (1992). A barycentremetric study of the sagittal shape of spine and pelvis: the conditions required for an economic standing position. *Ann. Biomed. Eng.* 20, 451–462. doi: 10.1007/BF02368136

Kim, Y. B., Kim, Y. J., Ahn, Y. J., Kang, G. B., Yang, J. H., Lim, H., et al. (2014). A comparative analysis of sagittal spinopelvic alignment between young and old men without localized disc degeneration. *Eur. Spine J.* 23, 1400–1406. doi: 10.1007/s00586-014-3236-8

Lafage, R., Schwab, F., Challier, V., Henry, J. K., Gum, J., Smith, J., et al. (2016). Defining spino-pelvic alignment thresholds: should operative goals in adult spinal deformity surgery account for age? *Spine* 41, 62–68. doi: 10.1097/BRS.0000000000001171

Lafage, R., Schwab, F., Glassman, S., Bess, S., Harris, B., Sheer, J., et al. (2017). Age-adjusted alignment goals have the potential to reduce PJK. *Spine* 42, 1275–1282. doi: 10.1097/BRS.0000000000002146

Lamartina, C., Berjano, P., Petruzzi, M., Sinigaglia, A., Casero, G., Cecchinato, R., et al. (2012). Criteria to restore the sagittal balance in deformity and degenerative spondylolisthesis. *Eur. Spine J.* 21(Suppl. 1), S27–S31. doi: 10.1007/s00586-012-2236-9

Le Huec, J. C., Aunoble, S., Philippe, L., and Nicolas, P. (2011). Pelvic parameters: origin and significance. *Eur. Spine J.* 20(Suppl. 5), 564–571. doi: 10.1007/s00586-011-1940-1

Le Huec, J. C., Faundez, A., Dominguez, D., Hoffmeyer, P., and Aunoble, S. (2015a). Evidence showing the relationship between sagittal balance and clinical outcomes in surgical treatment of degenerative spinal diseases: a literature review. *Int. Orthop.* 39, 87–95. doi: 10.1007/s00264-014-2516-6

Le Huec, J. C., Faundez, A., Dominguez, D., Hoffmeyer, P., and Aunoble, S. (2015b). Evidence showing the relationship between sagittal balance and clinical outcomes in surgical treatment of degenerative spinal diseases: a literature review. *Int. Orthop.* 39, 87–95.

Le Huec, J. C., Thompson, W., Mohsinaly, Y., Barrey, C., and Faundez, A. (2019). Sagittal balance of the spine. *Eur. Spine J.* 28, 1889–1905. doi: 10.5114/reum.2021.112352

Lee, C. H., Chung, C. K., Jang, J. S., Kim, S. M., Chin, D. K., and Lee, J. K. (2017). 'Lumbar degenerative kyphosis' is not byword for degenerative sagittal imbalance: time to replace a misconception. *J. Korean Neurosurg. Soc.* 60, 125–129. doi: 10.3340/jkns.2016.0607.001

Lee, S. H., Kim, K. T., Suk, K. S., Lee, J. H., Seo, E. M., and Huh, D. S. (2011). Sagittal decompensation after corrective osteotomy for lumbar degenerative kyphosis: classification and risk factors. *Spine* 36, E538–E544. doi: 10.1097/BRS.0b013e3181f45a17

Liu, C., Hu, F. Q., Hu, W. H., Song, K., Jiao, G. L., Zheng, G. Q., et al. (2020). Compensatory mechanism of maintaining the sagittal balance in degenerative lumbar scoliosis patients with different pelvic incidence. *Orthop. Surg.* 12, 1685–1692. doi: 10.1111/os.12805

Mangione, P., Gomez, D., and Senegas, J. (1997). Study of the course of the incidence angle during growth. *Eur. Spine J.* 6, 163–167. doi: 10.1007/BF01301430

Moal, B., Bronsard, N., Raya, J. G., Vital, J. M., Schwab, F., Skalli, W., et al. (2015). Volume and fat infiltration of spino-pelvic musculature in adults with spinal deformity. *World J. Orthop.* 6, 727–737. doi: 10.5312/wjo.v6.i9.727

Roussouly, P., and Pinheiro-Franco, J. L. (2011). Biomechanical analysis of the spino-pelvic organization and adaptation in pathology. *Eur. Spine J.* 20(Suppl. 5), 609–618. doi: 10.1007/s00586-011-1928-x

Schwab, F., Lafage, V., Farcy, J. P., Bridwell, K., Glassman, S., Ondra, S., et al. (2007). Surgical rates and operative outcome analysis in thoracolumbar and lumbar major adult scoliosis: application of the new adult deformity classification. *Spine* 32, 2723–2730. doi: 10.1097/BRS.0b013e31815a58f2

Schwab, F., Patel, A., Ungar, B., Farcy, J. P., and Lafage, V. (2010). Adult spinal deformity-postoperative standing imbalance: how much can you tolerate? An overview of key parameters in assessing alignment and planning corrective surgery. *Spine* 35, 2224–2231. doi: 10.1097/BRS.0b013e3181ee6bd4

Schwab, F., Ungar, B., Blondel, B., Buchowski, J., Coe, J., Deinlein, D., et al. (2012). Scoliosis research society-Schwab adult spinal deformity classification: a validation study. *Spine* 37, 1077–1082.

Schwab, F. J., Blondel, B., Bess, S., Hostin, R., Shaffrey, C. I., Smith, J. S., et al. (2013). Radiographical spinopelvic parameters and disability in the setting of adult spinal deformity: a prospective multicenter analysis. *Spine* 38, E803–E812. doi: 10.1097/BRS.0b013e318292b7b9

Schwab, F. J., Lafage, R., Liabaud, B., Diebo, B. G., Smith, J. S., Hostin, R. A., et al. (2014). Does one size fit all? Defining spinopelvic alignment thresholds based on age. *Spine J.* 14, S120–S121.

Wu, I. C., Lin, C. C., Hsiung, C. A., Wang, C. Y., Wu, C. H., Chan, D. C., et al. (2014). Epidemiology of sarcopenia among community-dwelling older adults in Taiwan: a pooled analysis for a broader adoption of sarcopenia assessments. *Geriatr. Gerontol. Int.* 14(Suppl. 1), 52–60. doi: 10.1111/ggi.12193

Zhou, S., Li, W., Su, T., Du, C., Wang, W., Xu, F., et al. (2019). Does lumbar lordosis minus thoracic kyphosis predict the clinical outcome of patients with adult degenerative scoliosis? *J. Orthop. Surg. Res.* 14:290. doi: 10.1186/s13018-019-1339-y

Conflict of Interest: The authors declare that the research was conducted in the absence of any commercial or financial relationships that could be construed as a potential conflict of interest.

frontiers
in Molecular Neuroscience

ORIGINAL RESEARCH
published: 31 March 2022
doi: 10.3389/fnmol.2022.848257

Nexmifa Regulates Axon Morphogenesis in Motor Neurons in Zebrafish

Yu-qin Zheng[1,2†]*, Gui-hai Suo*[2†]*, Dong Liu*[3]*, Hai-ying Li*[2]*, You-jia Wu*[2*] *and Hong Ni*[1*]

[1] *Division of Brain Science, Institute of Pediatric Research, Children's Hospital of Soochow University, Suzhou, China,* [2] *Department of Pediatrics, Affiliated Hospital of Nantong University, Nantong, China,* [3] *School of Life Sciences, Nantong University, Nantong, China*

Edited by:
Qi Han,
Shanghai Jiao Tong University, China

Reviewed by:
Thomas Becker,
University of Edinburgh,
United Kingdom
Dario Bonanomi,
San Raffaele Scientific Institute
(IRCCS), Italy

Correspondence:
Hong Ni
nihongdoctor@163.com
You-jia Wu
francis_nt@163.com

† These authors have contributed equally to this work

Specialty section:
This article was submitted to
Neuroplasticity and Development,
a section of the journal
Frontiers in Molecular Neuroscience

Received: *04 January 2022*
Accepted: *21 February 2022*
Published: *31 March 2022*

Citation:
Zheng Y-q, Suo G-h, Liu D, Li H-y, Wu Y-j and Ni H (2022) Nexmifa Regulates Axon Morphogenesis in Motor Neurons in Zebrafish. Front. Mol. Neurosci. 15:848257. doi: 10.3389/fnmol.2022.848257

Nexmif is mainly expressed in the central nervous system (CNS) and plays important roles in cell migration, cell to cell and cell-matrix adhesion, and maintains normal synaptic formation and function. Nevertheless, it is unclear how nexmif is linked to motor neuron morphogenesis. Here, we provided *in situ* hybridization evidence that nexmifa (zebrafish paralog) was localized to the brain and spinal cord and acted as a vital regulator of motor neuron morphogenesis. Nexmifa deficiency in zebrafish larvae generated abnormal primary motor neuron (PMN) development, including truncated Cap axons and decreased branches in Cap axons. Importantly, RNA-sequencing showed that nexmifa-depleted zebrafish embryos caused considerable CNS related gene expression alterations. Differentially expressed genes (DEGs) were mainly involved in axon guidance and several synaptic pathways, including glutamatergic, GABAergic, dopaminergic, cholinergic, and serotonergic synapse pathways, according to Kyoto Encyclopedia of Genes and Genomes (KEGG) pathway annotation. In particular, when compared with other pathways, DEGs were highest (84) in the axon guidance pathway, according to Organismal Systems. Efna5b, bmpr2b, and sema6ba were decreased markedly in nexmifa-depleted zebrafish embryos. Moreover, both overexpression of efna5b mRNA and sema6ba mRNA could partially rescued motor neurons morphogenesis. These observations supported nexmifa as regulating axon morphogenesis of motor neurons in zebrafish. Taken together, nexmifa elicited crucial roles during motor neuron development by regulating the morphology of neuronal axons.

Keywords: nexmifa, motor neuron, axon morphogenesis, efna5b, sema6ba, zebrafish

INTRODUCTION

Motor neuron diseases (MNDs) are characterized by muscle weakness and/or spastic paralysis and are an etiologically heterogeneous group of disorders resulting from motor neuron degeneration (Babin et al., 2014). Thus, exploring mechanisms underpinning motor neuron development may support and advance therapeutic strategies for MND.

The zebrafish model is a highly practical *in vivo* research tool for studying developmental mechanisms, as their transparent embryos, at all developmental stages, are easy to image and manipulate (Nozawa et al., 2017). In particular, the motor neurons of the spinal cord are excellent *in vivo* systems for studying mechanisms controlling axon extension and synaptic formation

(Babin et al., 2014). Growth cones at axon tips navigate using environmental cues, therefore, axons constantly follow stereotypical pathways to their targets and rarely deviate (Hilario et al., 2010). Zebrafish contain two different type of spinal motor neuron, i.e., primary motor neurons (PMNs) and secondary motor neurons (SMNs), which are based on several morphological features: soma shape, size, position, and axon diameter (Myers, 1985; Myers et al., 1986). PMNs are further divided into three groups: caudal primary motor neurons (Cap), middle primary motor neurons (Mip), and rostral primary motor neurons (Rop) in accordance with specific axonal pathways and soma positions within the spinal cord (Myers et al., 1986; Westerfield et al., 1986). Although the somata of the three identifiable PMNs are localized at different positions in the spinal cord, their axons travel to the myoseptum via a common exit point; after leaving the spinal cord, PMNs extend their axons via a common pathway to the horizontal myoseptum (Eisen et al., 1986). Finally, Cap, Mip, and Rop neurons extend their axons according to specific pathways to innervate dorsal, middle, and ventral trunk musculature, respectively (Myers, 1985; Moreno and Ribera, 2009). When compared with PMNs, SMNs are localized more ventrally in the motor column, with typically smaller somatas and thinner axons, which are born 5–6 h later than PMNs (Myers et al., 1986). Because of this unique stratification, PMNs are excellent cell systems for elucidating motor axon guidance mechanisms (Beattie, 2000; Beattie et al., 2002).

In vertebrates, motor neuron development is regulated by many genes. For example, mecp2 knockdown in zebrafish increases abnormal axonal branching of aps and decreases motor activity (Nozawa et al., 2017). lncrps25 is co-expressed with mnx1 at the spinal cord and is essential for motor neuron development, but neurons lacking lncrps25 result in Cap axon truncation and abnormal branching, however, these defects are rescued by olig2 overexpression (Gao et al., 2020). Similarly, HuD mutants exhibit decreased motor axon branches, dramatically fewer dendrites, and movement defects (Hao le et al., 2017). Deleted or overexpressed colXIX causes stumpy-like Cap axon defects (Hilario et al., 2010), whereas colXVIII knockdown causes Cap axon stalling soon after exiting the spinal cord (Schneider and Granato, 2006). Ccdc80-l1 is implicated in motor neuron axonal path-finding, however, loss-of-function does not prevent PMN formation and axon projection, but leads to PMN disorganization (Brusegan et al., 2012).

In our previous studies, we reported that insm1a, kinesin-12, and sox2 had key roles in motor neuron development (Xu et al., 2014; Gong et al., 2017, 2020). For example, the zebrafish insm1a mutant showed motor neuron loss and defects in PMN axons, including truncated length, excessive Cap branches, and disorganized distances between adjacent Caps, which were caused by the ectopic departure of motor axons from the spinal cord. In sox2 mutant zebrafish, besides truncated length and excessive Cap branches, defective PMNs also included changes in axon morphology and reductions in Mips and Rops.

Nexmif (also called KIDLIA, KIAA2022, or Xpn) is a novel gene localized to Xq13.2 (Gilbert et al., 2020). Cantagrel et al. (2004) first reported the gene in two males with intellectual disability. However, very little is known about nexmif. Previous studies reported that nexmif mRNA was strongly expressed in the cortex, hippocampus, cerebellum, and olfactory bulb (Allen Institute for Brain Science, 2004; Cantagrel et al., 2009). At the protein level, nexmif is specifically distributed in post-mitotic neuron nuclei but not in glia. Strong protein expression is also detected from the E17 developmental stage through adulthood in mice (Gilbert and Man, 2016). Thus, nexmif may have key roles in brain development.

In zebrafish, nexmif has two paralogs, nexmifa and nexmifb. Protein homology indicates 34 and 42% identity to the human protein, respectively. In humans, patients with nexmif mutations present with moderate to severe intellectual impairment, autism spectrum disorder (ASD), dystonia, intellectual disability, epilepsy, microcephaly, and facial deformities (Van Maldergem et al., 2013; de Lange et al., 2016). In animal models, nexmif was shown to participate in neurite morphological development, regulate cell migration, cell to cell and cell to matrix adhesion, and maintain normal synaptic formation and function (Ishikawa et al., 2012; Magome et al., 2013; Gilbert et al., 2020). For example, in the nexmif knockdown mouse, synapse density, spine density, and the expression of synaptic related proteins, such as AMPAR, PSD-95, and gephyrin were decreased. Also, immature spines were increased, synaptic transmission functions were defective, and mice exhibited ASD behaviors (Gilbert et al., 2020). In other work, KIAA2022 (nexmif alias) knockdown markedly suppressed neurite growth, including both dendrites and axons in cultured rat hippocampal neurons (Van Maldergem et al., 2013). Moreover, KIDLIA (nexmif alias) knockdown altered *in vivo* neuron migration, reduced dendritic growth, and disorganized apical dendrite projections in mouse layer II/III cortical neurons (Gilbert and Man, 2016). Magome et al. (2013) found that nexmif knockout inhibited cell migration by enhancing cell to cell and cell to matrix adhesion mediated by *N*-cadherin and β1- integrin in PC12 cells. However, no study has yet focused on the effects of nexmif on spinal motor neurons. Evidentially, nexmif deficiency leads to ASD behaviors, and 50–80% of patients with ASD show motor dysfunction (Kaur et al., 2018), therefore, we hypothesized nexmif exerted effects on the development of spinal motor neurons.

To verify our hypothesis, we assessed nexmifa expression using whole *in situ* hybridization (WISH) and reverse transcription-polymerase chain reaction (RT-PCR) in zebrafish. We then investigated nexmifa function during PMN morphogenesis via knockdown and knockout strategies in the Tg(mnx1:GFP)ml2 transgenic zebrafish line and investigated possible molecular mechanisms.

MATERIALS AND METHODS

Zebrafish Lines and Breeding

Zebrafish embryos and adults were maintained in at the Zebrafish Center of Nantong University in accordance with guidelines outlined in previous studies (Xu et al., 2014; Gong et al., 2017, 2020). The transgenic zebrafish line, Tg(mnx1:GFP)ml2 and

Tg(kdrl:EGFP) line have been described in the previous work (Flanagan-Steet et al., 2005; Jin et al., 2005).

Cell Separation, RNA Isolation, Reverse Transcription, Quantitative RT-PCR and RT-PCR

At 72 h post-fertilization (hpf), we collected 300–400 Tg(mnx1:GFP) zebrafish embryos and washed them three times in phosphate-buffered saline with Tween 20 and the same again in calcium-free Ringer's solution. Embryos were digested in 0.25% trypsin, then 10% fetal bovine serum was added to terminate the reaction. The volume was filtered through 100 and 40 μm filter membranes. Samples were then analyzed by flow cytometry (BD, Franklin Lakes, NJ, United States). Cells expressing GFP were identified as positive cells. Total RNA was extracted from zebrafish embryos and cells separated via flow cytometry by TRIzol reagent according to manufacturer's instructions (Invitrogen, Waltham, MA, United States). Contamination was removed by DNaseI (Roche, Basel, Switzerland) and then 2 μg total RNA was reversibly transcribed using a reverse first-strand cDNA synthesis kit (Fermentas, Waltham, MA, United States) and stored at −20°C. Quantitative RT-PCR was performed using corresponding primers (**Supplementary Table S1**) in a 20 μL final reaction volume with 10 μL SYBR premix (Takara, Kyoto, Japan). Elongation factor 1a was used as the internal control. All samples were analyzed in triplicate. RT-PCR was performed using corresponding primers (**Supplementary Table S1**) in a 50 μL final reaction volume, with 25 μL 2 × Taq enzyme mix (Vazyme, Nanjing, China). After amplification, 20 μL was taken for gel electrophoresis and sequencing.

Whole *in situ* Hybridization

A 424-base pair (bp) cDNA fragment from a wild-type embryo was amplified using nexmifa F1 and R1 primers (**Supplementary Table S1**). Digoxigenin (DIG)-labeled sense and antisense probes were synthesized using a linearized pGEM-Teasy vector and sub-cloned with the nexmifa fragment by *in vitro* transcription with a DIG-RNA labeling kit (Roche, Basel, Switzerland). We collected zebrafish embryos at different developmental stages (20, 48, 72, and 96 hpf), then fixed them in 4% paraformaldehyde for 2 h at room temperature or overnight at 4°C. They were then dehydrated through a series of increasing methanol concentrations, and finally stored in 100% methanol at −20°C. WISH was performed as previously described (Gong et al., 2020).

The sgRNA/Cas9 mRNA Synthesis and Injection

Cas9 mRNA was generated by *in vitro* transcription with the linearized pXT7-Cas9 plasmid as previously described (Gong et al., 2017). sgRNAs were transcribed from the DNA templates that amplified by PCR with a pT7 plasmid as the template, a specific forward primer and a universal reverse primer (**Supplementary Table S1**; Gong et al., 2017, 2020). The transgenic zebrafish line Tg(mnx1:GFP)ml2 was naturally mated to obtain embryos for microinjection. Then, 1–2 cell stage zebrafish embryos were injected in a 2–3 μL solution containing 250 ng/μL Cas9 mRNA and 15 ng/μL sgRNA. At 24 hpf, embryos were randomly sampled for genomic DNA extraction according to previous methods to identify a founder. Mutant sites were verified by comparison to the wild-type unaffected sequences (chimerism). Chimeric zebrafish were mated with wild-type fish to obtain F1 fish. After examine its genotype by sequence, heterozygotic mutants were mated with *Tg(mnx1:GFP)* transgenic fish to breed the F2 generation. At last, nexmifa+/+ and nexmifa−/− littermates were obtained by F2 in-cross followed by fluorescence selection and PCR genotyping for the following experiments (Gong et al., 2017).

Morpholino, mRNA Synthesis, and Microinjection

The nexmifa splice-blocking Morpholino (MO) and the standard control MO (Std MO) were synthesized by Gene Tools. The sequences are: 5′-AAAATGGTAGGAGTTATAAATGAGT-3′ and 5′-CCTCTTACCTCAGTTACAATTTATA-3, respectively. MOs were diluted to 0.3 mM in RNase-free water, injected into one-cell stage embryos, and then raised in E3 medium at 28.5°C to generate nexmifa knockdown embryos (morphants). To perform rescue experiments, we generated nexmifa mRNA, efna5b mRNA, and sema6ba mRNA *in vitro*. Briefly, we cloned zebrafish nexmifa, efna5b, and sema6ba separately into $PCS2^+$ vectors. Next, we linearized plasmids, then *in vitro* synthesized mRNA using the mMESSAGE mMACHIN Kit (Ambion, Austin, Texas, United States) according to manufacturer's instructions. Finally, we purified Capped mRNAs using the RNeasy Mini Kit (Qiagen, Hilden, Germany). MOs or mRNAs were injected into the yolk of one cell stage embryos using borosilicate glass capillaries (Sarasota, Florida, United States) and a PV830 pneumatic picopump (Sarasota, Florida, United States).

The cDNA Library Preparation and RNA Sequencing

We extracted total RNA from nexmifa morphants and wild-type zebrafish at 72 hpf using TRIzol reagent (Invitrogen) and calculated RNA integrity and purity by NanoDRop 2000 (Thermo Fisher Scientific Inc., Waltham, MA, United States). Only high-quality RNA samples ($OD_{260/280}$ = 1.8–2.2, RNA Integrity Number ≥ 8.0) were used to construct the sequencing library. We next quantified and sequenced the final cDNA libraries using the Illumina NovaSeq 6000 platform, with 2 × 150-bp pair-end reads (Illumina, San Diego, CA, United States).

Locomotion Analysis of Zebrafish Larvae

To determine whether nexmifa deficiency impaired motility and whether this impaired motility could be rescued by overexpress the possible downstream gene, larva zebrafish at 7 days post-fertilization (dpf) in different groups were placed into 24-well-culture plates (one larva/well) and transferred to the Zebralab Video-Track system (Zebrabox, Lyon, France). The unit was equipped with a sealed opaque plastic box insulated from the environment, and an infrared filter and monochrome camera. After 30 min adaptation, larval distances and average speeds were recorded for 30 min.

Microscopy

After anesthetizing zebrafish embryos by tricaine (Sigma, Saint Louis, Missouri, United States), they were embedded in 0.8% low melting agarose and examined using a Leica TCS-SP5 LSM confocal imaging system. Criteria for zebrafish embryos with abnormal PMNs were as follows: firstly, Caps length or the number of Caps branches per 1mm was less than 70% of the average of normal wild-type zebrafish. Secondly, PMNs abnormal in more than two hemisegment in the spinal cord in one fish. Otherwise, the embryo was normal. *In situ* hybridization images were Captured on an Olympus stereomicroscope MVX10.

Statistical Analysis

Statistical data comparisons were performed using Student's *t*-test or one-way analysis of variance if the data follow a normal distribution and variance between groups was uniform,

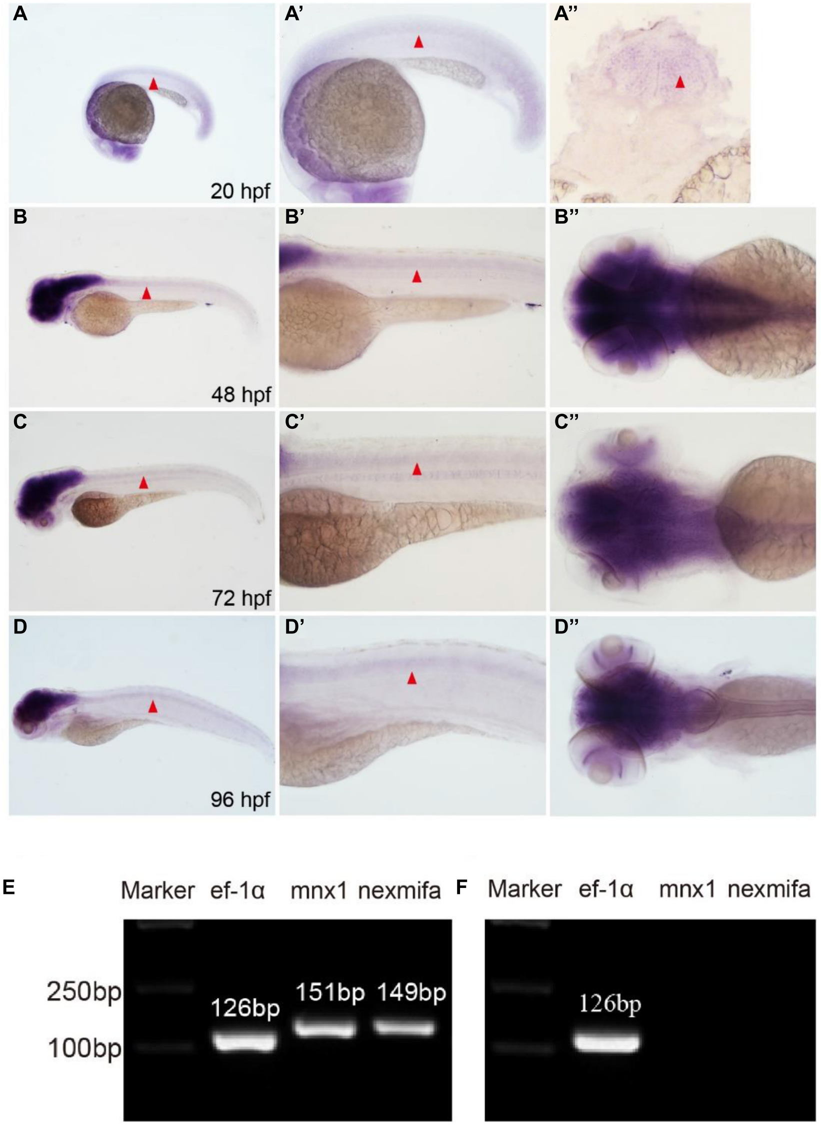

FIGURE 1 | Nexmifa expression analysis in spinal cord and motor neurons. **(A)** At 20 hpf, *in situ* hybridization nexmifa signals are localized in brain and spinal cord (lateral view). **(A')** Partially magnified image of **(A)**. **(A")** The trunk transverse section of the embryo. **(B)** At 48 hpf, *in situ* hybridization nexmifa signals are localized in the brain and spinal cord (lateral view). **(B')** Partially magnified image of **(B)**. **(B")** Dorsal view of the brain. **(C)** At 72 hpf, *in situ* hybridization nexmifa signals are localized in the brain and spinal cord (lateral view). **(C')** Partially magnified image of **(C)**. **(C")** Dorsal view of the brain. **(D)** At 96 hpf, *in situ* hybridization nexmifa signals are localized in the brain and spinal cord (lateral view). **(D')** Partially magnified image of **(D)**. **(D")** Dorsal view of the brain. **(E)** RT-PCR results on mnx1-GFP sorted cells. Nexmifa is expressed in selected neuron cells from the Tg (mnx1: EGFP) line. **(F)** The result of the RT-PCR on Kdrl-EGFP sorted cells. No signals of nexmifa and mnx1 are detected in the GFP-positive cells sorted from the Tg(kdrl:EGFP) line.

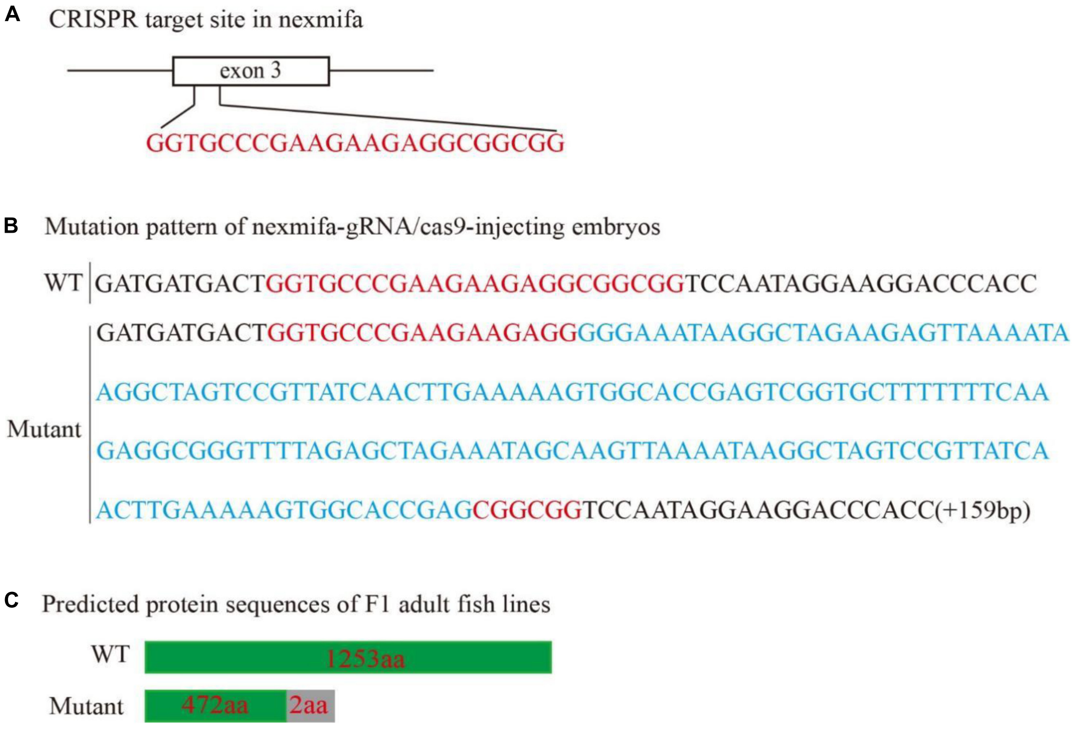

FIGURE 2 | Generation of the zebrafish nexmifa mutant using the CRISPR/Cas9 system. **(A)** Schematic showing the targeting site of the sgRNA in the third exon of nexmifa. **(B)** Mutation pattern of nexmifa-gRNA/cas9-injected embryos. Red letters represent the sgRNA sequence. Blue letters represent the additional 159 bp nucleotide sequence. **(C)** Schematic showing the predicted protein encoded by the mutated allele. Frameshift mutations resulted in truncated proteins. The gray rectangle indicates the wrong coded amino acid sequences.

otherwise, Kruskal–Wallis *H* or Mann–Whitney *U* was used. A $p < 0.05$ value was considered statistically significant. Statistical analyses were performed in SPSS 21.0 software (SPSS, Armonk, NY, United States).

RESULTS

Nexmifa Is Expressed in the Spinal Cord and PMNs of Zebrafish

To analyze nexmifa temporal and spatial expression patterns, we performed WISH using a DIG-labeled nexmifa probe at different times. Nexmifa was strongly expressed in the central nervous system (CNS), including the brain and spinal cord at 20, 48, 72, and 96 hpf. At 48 h, expression in the brain and spinal cord was the highest, but then decreased gradually (**Figures 1A–D, A′–D′, A″–D″**). To further assess if nexmifa was expressed in motor neurons in the spinal cord, we separated motor neurons from Tg(mnx1:GFP)ml2 cells and extracted RNA, as Tg(mnx1:GFP)ml2 motor neurons were GFP labeled. RT-PCR demonstrated that both mnx1 and nexmifa were present in selected neuron cells (**Figure 1E**) suggesting nexmifa was expressed in zebrafish motor neurons. Moreover, we performed RT-PCRs on nexmifa-negative tissue. The results showed that no nexmifa and mnx1 signal were detected in the GFP-positive cells sorted from the Tg(kdrl:EGFP) line (**Figure 1F**), in which endothelial cells were labeled with GFP.

Nexmifa Loss Causes Motor Neurons Defects

To explore if nexmifa regulated motor neuron morphogenesis in the spinal cord, we established a nexmifa knockout in Tg(mnx1:GFP)ml2 transgenic zebrafish (nexmifa mutant) to characterize PMN morphology. The selected sgRNA-Cas9 system effectively inserted a 159 bp frameshift mutation that prematurely altered protein translation and produced a truncated protein (**Figure 2**). There was no obvious difference in appearance between the two groups of zebrafish in the bright field (**Supplementary Figure S1**). In order to better understand the morphological changes of motor neurons, firstly, we drew a schematic for three different PMNs in one hemisegment in the spinal cord (**Figure 3A**). Secondly, we observed abnormal PMNs at 48 and 72 hpf under fluorescence microscope. We found the abnormalities in nexmifa mutant included the loss of Cap and/or Mip, motor neuron loss, reduced Cap length, and abnormal Cap branches (**Figure 3B**). Statistical analyses revealed the percentage of embryos with normal PMNs was lower than controls (55.5% ± 3.7% vs. 97% ± 1.4%) at 48 hpf and 57.5% ± 5.1% vs. 96% ± 1.9% at 72 hpf (**Figure 3C**). Cap development was also restricted, e.g., the Cap length in axons in nexmifa mutants was shorter than controls (103.8 μm ± 29.3 μm

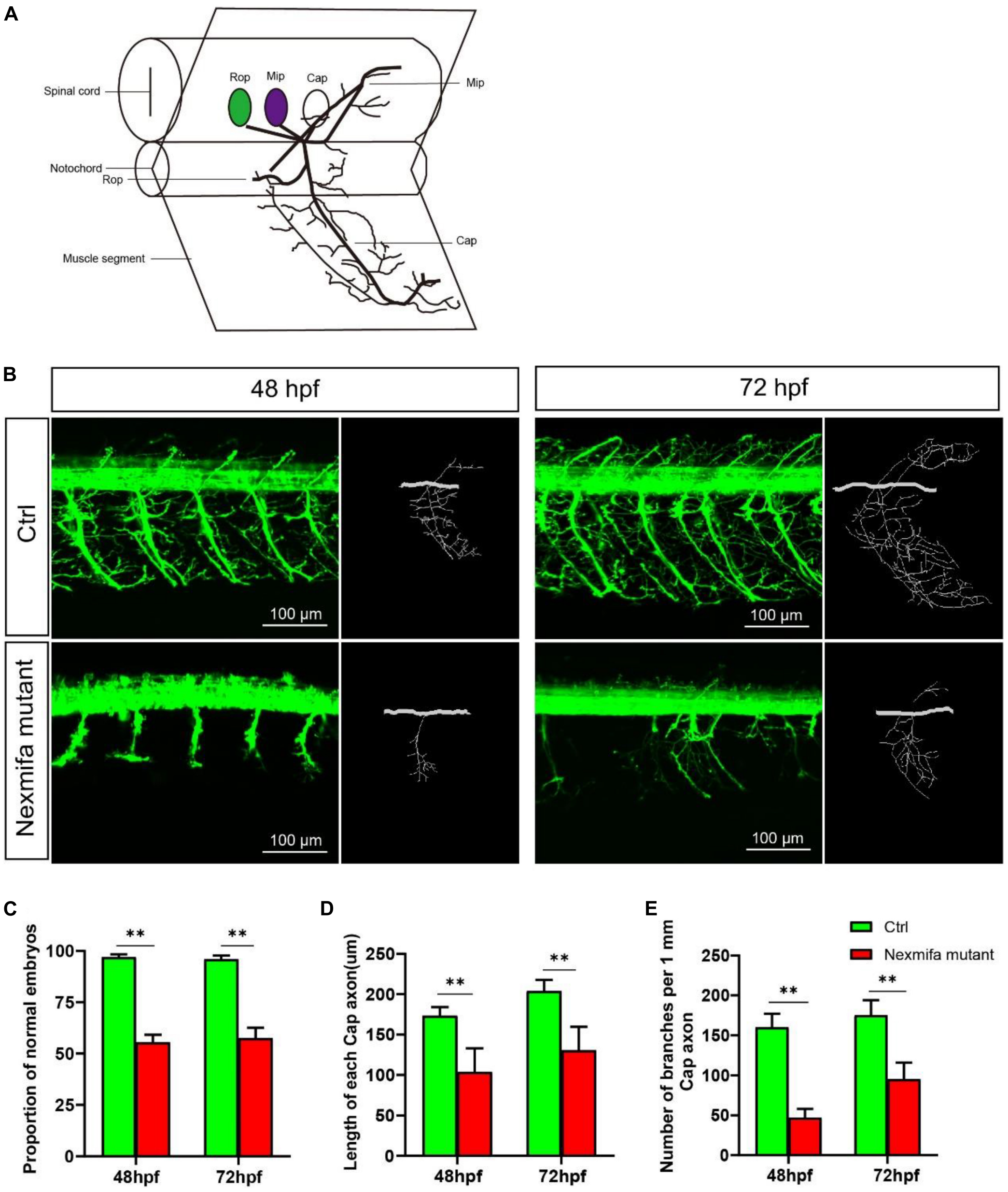

FIGURE 3 | Nexmifa affects motor neuron morphogenesis in nexmifa mutant zebrafish embryos. **(A)** The schematic for three different primary motoneurons (CaP, MiP, and RoP) in fish. **(B)** Confocal imaging of primary motor neurons in control and nexmifa mutant groups at 48 and 72 hpf. Scale bar = 100 μm **(C)** The percentage of embryos with normal PMNs in control and nexmifa mutants at 48 hpf (*n* = 125 and 240, respectively) and 72 hpf (*n* = 132 and 235, respectively). **(D)** Cap length in control and nexmifa mutants at 48 hpf (*n* = 20 and 31, respectively) and 72 hpf (*n* = 15 and 28, respectively). **(E)** Number of branches per 1 mm Cap axon in control and nexmifa mutants at 48 hpf (*n* = 8 and 10, respectively) and 72 hpf (*n* = 9 and 12, respectively). Bar represent the mean ± standard deviation (SD). $^{**}p < 0.01$.

vs. 173.5 μm ± 10.6 μm) at 48 hpf. When embryos developed to 72 hpf, mutant Cap lengths had grown, however, they remained shorter than controls (130.8 μm ± 28.8 μm vs. 203.8 μm ± 13.7 μm) (**Figure 3D**). These observations indicated that truncated axons had not completely recovered. In addition, Cap branches were also abnormal between controls and mutants; branch numbers were significantly lower in mutants than controls (47 ± 11 vs. 160 ± 17) at 48 hpf, and at 72 hpf, branches were less than controls (95 ± 21 vs. 175 ± 19) and were more disordered (**Figure 3E**).

To specifically confirm that motor neuron defects were caused by nexmifa loss, we established a knockdown nexmifa fish model by injecting a splice-blocking MO into one-cell stage zebrafish embryos. At 72 hpf, post-nexmifa-MO injection, splice-blocking MO effects were checked and quantitated by RT-PCR, then confirmed by sequencing. MO-nexmifa generated a

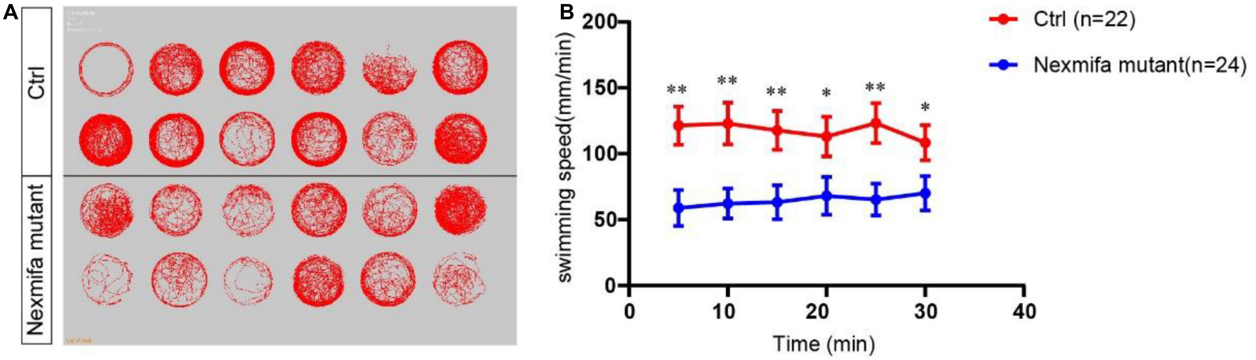

FIGURE 4 | Motor defects in nexmifa mutant zebrafish embryos at 7 dpf. **(A)** Thirty minutes of free movement trajectories of control and nexmifa mutants. **(B)** Quantification of swimming distances of control and nexmifa mutants at 7 dpf per 5 min (n = 22 and 24, respectively). Each point represents the mean ± standard error of the mean (SEM). *$p < 0.05$ and **$p < 0.01$.

larger alternatively spliced RT-PCR product [452 bp vs. 271 bp (Control MO)] (**Supplementary Figure S2B**). After sequencing, we confirmed that nexmifa-MO injection had caused intron 2 (181 bp) to be retained in nexmifa mRNA (**Supplementary Figure S2C**), resulting in a reading frame shift to generate successful nexmifa knockdown. We also investigated PMN morphology in nexmifa-MO fish at 48 and 72 hpf; the results were similar to those in nexmifa mutants. We also performed rescue experiments by co-injecting nexmifa mRNA with nexmifa-MO to confirm phenotypic changes induced by nexmifa-MO injection. We observed that this strategy partly rescued abnormal motor neuron (**Supplementary Figure S3A**). For example, the percentage of normal embryos was recovered from 62.3% ± 3.5% to 75.5% ± 4.0% at 48 hpf and 60.5% ± 6.0% to 73.4% ± 5.8% at 72 hpf (**Supplementary Figure S3B**). Also Cap length was recovered from 101.5 μm ± 16.2 μm to 133.2 μm ± 21.5 μm at 48 hpf and from 126.1 μm ± 34.4 μm to 175.6 μm ± 25.6 μm at 72 hpf (**Supplementary Figure S3C**). The number of Cap branches was also recovered from 57 ± 12 vs. to 126 ± 29 at 48 hpf and from 88 ± 21 to 119 ± 34 at 72 hpf, and were less disordered than the nexmifa morphant group (**Supplementary Figure S3D**).

Nexmifa Knockout Mutants Display Impaired Motility

To investigate if motor neuron defects affected motor ability, video-tracked swimming activities were performed for 30 min at 7 dpf. As shown (**Figure 4**), movement trajectories in nexmifa mutants were significantly decreased when compared with controls (**Figure 4A**). The swimming distance per 5 min decreased in nexmifa mutants when compared with controls (**Figure 4B**), consistent with movement trajectories.

Transcriptomic Profiling of Nexmifa Morphants and Control Zebrafish

To identify mechanisms where nexmifa may have affected motor neuron morphogenesis, we performed RNA sequencing using RNA samples from control and nexmifa morphant zebrafish at 72 hpf. We identified 6,556 differentially expressed genes (DEGs), with 3,770 up-regulated and 2,786 down-regulated DEGs between the two groups (fold change > 2 or < 0.5, $p < 0.05$) (**Figure 5A** and **Supplementary Table S2**). According to Kyoto Encyclopedia of Genes and Genomes (KEGG) annotations, many DEGs were involved in axon guidance pathways and various synaptic pathways. In particular, and according to Organismal Systems, DEG numbers involved in axon guidance (84) were the highest when compared with other groups (**Figure 5B**). We also observed 45 down-regulated DEGs in the axon guidance pathway (**Figure 5C**). Among these 45 DEGs, the top 3 genes with the largest fold changes are efna5b, bmpr2b and sema6ba. To verify the reliability of RNA-seq, we not only further test the expression of efna5b, bmpr2b and sema6ba but also test other 17 down-regulated DEGs randomly by qRT-PCR at 72 hpf. Then we found the expression of the most genes including efna5b and sema6ba were consistent with the RNA-seq results (**Figure 6A**). Moreover, we test the expression of the above 20 genes between Ctrl and nexmifa mutant by RT-PCR and gained the similar trend change (**Figure 6B**).

Efna5b and Sema6ba Overexpression Rescues the Motor Neuron Defects and Impaired Motility in Nexmifa Mutant Embryos

As the downregulation of efna5b and sema6ba in nexmifa loss of function embryos, we hypothesized if nexmifa regulated motor neurons in zebrafish by down-regulating efna5b and sema6ba expression. To confirm this, we synthesized efna5b and sema6ba mRNA *in vitro*, and injected molecules into the yolk of a one-cell stage nexmifa mutant embryos. Then, we found the relative mRNA expression of efna5b and sema6ba were significantly up-regulated compared with nexmifa mutants by qRT-PCR, which indicate the successful of overexpression (**Figures 7A–B**). We observed nexmifa mutant embryos had significantly reduced motor neuronal defects caused by nexmifa loss (**Figure 7C**). Only 54.5% ± 4.6% of embryos presented normal PMNs in nexmifa mutants at 48 hpf, whereas this

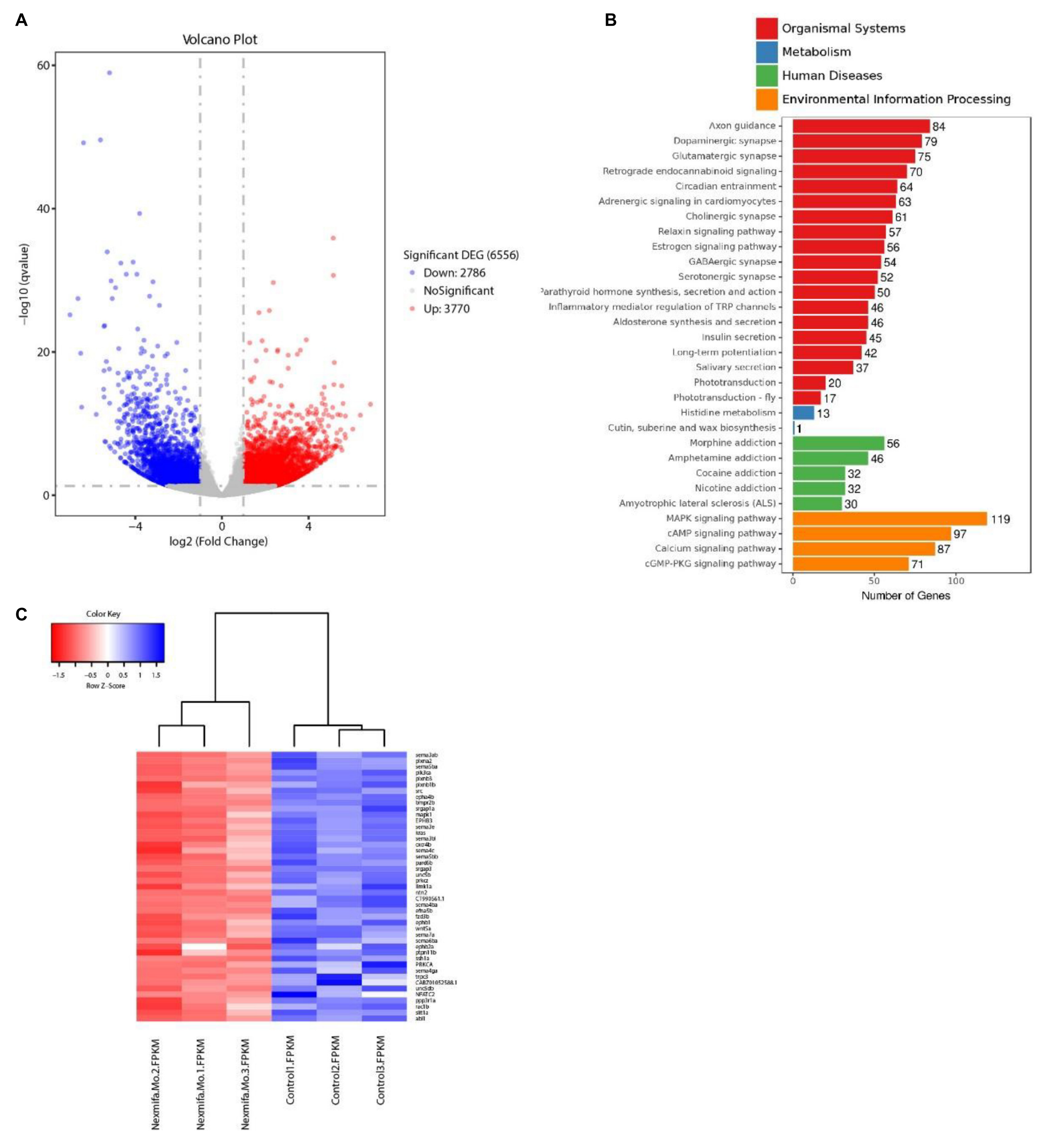

FIGURE 5 | Transcriptomics profiling in nexmifa morphant and wild-type zebrafish. **(A)** Volcano map showing DEGs in control and nexmifa morphants. Red and blue spots represent up-regulated and down-regulated genes, respectively. **(B)** KEGG pathway annotation of DEGs in control and nexmifa morphants. **(C)** Heatmap pathway differences between control and nexmifa morphants showing down-regulated genes in axon guidance.

percentage increased to 73.3% ± 7.9% after efna5b mRNA injection and 76.7% ± 7.9% after sema6ba mRNA injection (**Figure 7D**). As shown (**Figure 8A**), the movement trajectory was dramatically increased when the mutants were injected with efna5b RNA or sema6ba RNA compared with that in the nexmifa mutant at 7 dpf. Consistent with movement trajectory, the swimming distances per 5 min was also dramatically increased when the mutants were injected with efna5b RNA or sema6ba RNA compared with that in the nexmifa mutant (**Figure 8B**). The results demonstrated that efna5b and sema6ba overexpression could rescue the motor neuron defects and impaired motility which caused by loss of nexmifa.

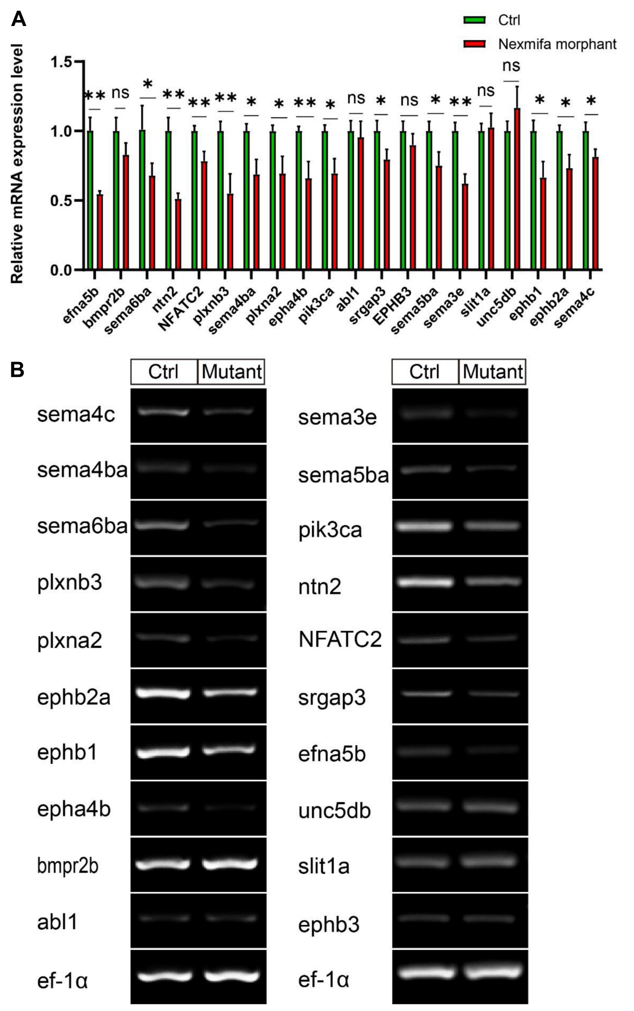

FIGURE 6 | The expression of 20 down-regulated DEGs. **(A)** Expression of 20 down-regulated DEGs between Ctrl and nexmifa morphant by qRT-PCR. Bars represent the mean ± standard deviation (SD). $^{*}p < 0.05$ and $^{**}p < 0.01$. ns: non-significant. **(B)** Expression of 20 down-regulated DEGs between Ctrl and nexmifa mutant by RT-PCR.

DISCUSSION

Previous studies demonstrated that nexmif was involved in neurite morphological development, cell to cell and cell to matrix adhesion, cell migration, and maintained normal synaptic formation in neurons (Ishikawa et al., 2012; Magome et al., 2013; Gilbert et al., 2020), however, little was known about nexmif function in spinal motor neuron development. Additionally, most studies have explored the *in vitro* effects of nexmif on neurite morphology (Van Maldergem et al., 2013), but none have done this *in vivo*. Here, our *in vivo* nexmifa expression and deficiency phenotype data provided new insights on nexmifa functions in regulating the morphogenesis of spinal motor neuron in zebrafish.

In mouse brains, nexmif mRNA expression commences as early as E10.5, increases throughout development and peaking at P3, but continues at lower levels into adulthood (Cantagrel et al., 2009; Ishikawa et al., 2012). Our WISH data showed that almost all nexmifa was expressed in the brain and spinal cord; expression was observed from 20 hpf, whereas at 48 hpf, expression peaked and then gradually decreased. These spatiotemporal expression patterns in zebrafish were similar to mice. Furthermore, using flow cytometry, we sorted motor neurons from the Tg(mnx1:GFP)ml2 transgenic zebrafish line as these motor neurons were labeled by GFP. RT-PCR data showed that nexmifa was highly expressed in GFP-positive cells, indicating that nexmifa may directly regulate motor neuron development in the spinal cord.

Embryo and larva motor neurons are similar in morphology and projection patterns with respect to adult motor neurons. All primary motoneurons are born between 9 and 16 hpf. During PMN development, these cells extend their axons along stereotyped pathways and develop branches to invade into the myotome to form distributed neuromuscular synapses to nerve musculature. At 48 hpf, the Cap somata are located within a short distance of the ventral root, with axons following a stereotyped pathway down the middle of the segment, making a collateral or varicosity at the horizontal septum. At the ventral edge of the musculature, each axon turns dorsally and laterally grows along the rostral myoseptum (Myers et al., 1986). At 72 hpf, exuberant branches are formed and further invade into the myotome to form distributed neuromuscular synapses (Liu and Westerfield, 1990; Downes and Granato, 2004). To explore if nexmifa was involved in the morphogenesis of motor neurons in the spinal cord, we established knockout and knockdown fish models. Our data showed that both models exhibited obvious motor neuron loss and defects in PMN axons. Moreover, after coinjecting nexmifa mRNA with nexmifa-MO, truncated Cap and disordered branches were partly rescued. Thus, nexmifa helped regulate axon morphology.

Motoneurons establish important connections between the CNS and muscle. If they develop incorrectly, they cannot form the required connections, resulting in movement defects or paralysis (Hao le et al., 2017). Previous studies showed several motor defects were related to abnormal PMN development in zebrafish (Brusegan et al., 2012; Gong et al., 2017). In our study, impaired motility was consistent with the motor neuron defects seen in nexmifa knockout zebrafish.

Previous studies also showed that when motor neuron dendrites are reduced, motoneurons receive less innervation, leading to decreased activity (Gao et al., 2020; Zhu et al., 2021). As swimming involves alternating side-muscle contractions caused by alternating motor neuron activation, less active motor neurons could lead to a reduction in alternating muscle contractions and less distance moved (Hao le et al., 2017). Thus, we hypothesized this impaired motility was due to a decreased number of branches induced by nexmifa loss. Both musculature and motor neuron are responsible for embryonic motility (Menelaou et al., 2008), however, whether nexmifa affects muscle development warrants further study.

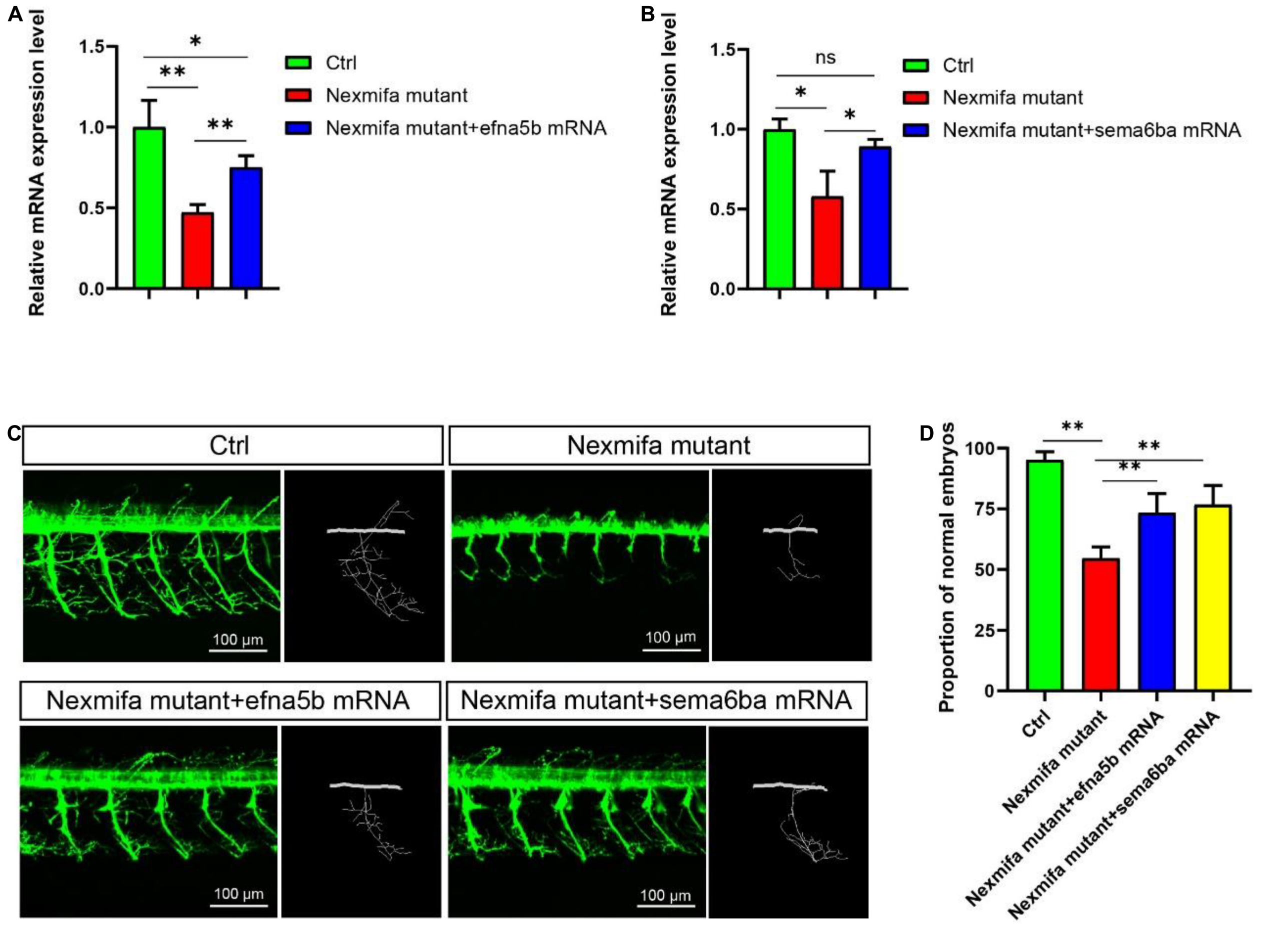

FIGURE 7 | Efna5b and sema6ba overexpression rescues motor neuron defects in nexmifa morphant embryos. **(A)** Expression of efna5b after injection of efna5b mRNA in nexmifa mutant embryos at 72 hpf. **(B)** Expression of sema6ba after injection of sema6ba mRNA in nexmifa mutant embryos at 72 hpf**. (C)** Abnormal PMNs in nexmifa morphant zebrafish were rescued by injecting efna5b or sema6ba mRNA. **(D)** Percentage of zebrafish embryos with normal Cap primary motor neurons (*n* = 150, 242, 250, and 257, respectively). **p* < 0.05 and ***p* < 0.01. ns: non-significant.

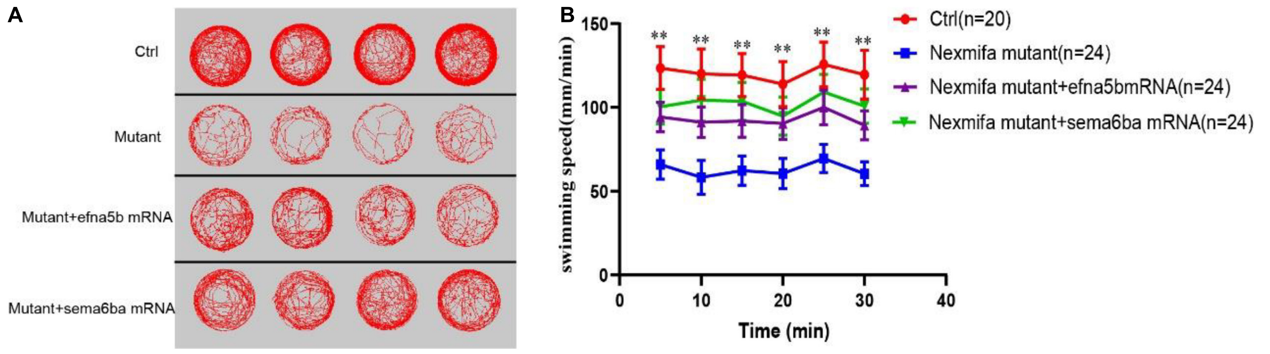

FIGURE 8 | Efna5b and sema6ba overexpression rescues the impaired motility in nexmifa mutant embryos at 7 dpf. **(A)** Thirty minutes of free movement trajectories among control, nexmifa mutants, nexmifa mutant + efna5b mRNA and nexmifa mutant + sema6ba mRNA. **(B)** Quantification of swimming distances among control, nexmifa mutants, nexmifa mutant + efna5b mRNA and nexmifa mutant + sema6ba mRNA at 7 dpf per 5 min (*n* = 20, 24, and 24, respectively). Each point represents the mean ± standard error of the mean (SEM). ***p* < 0.01.

Many genes are involved in motor neuron development via morphogenesis regulation (Dong et al., 2019; Koh et al., 2020). In this study, RNA-sequencing was performed on control and nexmifa morphant embryos to explore nexmifa-mediated morphogenesis mechanisms. Several DEGs were related to CNS development, e.g., DEGs were involved in the axon guidance pathway and various synapse pathways, consistent with mouse data (Ishikawa et al., 2012; Gilbert et al., 2020). This consistency not only indicated successful model establishment (knockdown), but also demonstrated the conserved function of nexmif. Of the 45 down regulated DEGs related to axon guidance, efna5b, bmpr2b and sema6ba are the top three genes with the largest fold changes. Using qRT-PCR at 72 hpf, we found that expression of most DEGs including efna5b and sema6ba were consistent with RNA-sequencing results, thereby proving RNA-sequencing data reliability. Efna5b, or ephrin-A5b, belongs to the family of epha, Eph receptor tyrosine kinases and their cognate ligands. Ephrins are a important class of axon guidance molecules (Lisabeth et al., 2013; Cayuso et al., 2015). EphrinA6 drastically reduces BDNF-induced axon branching (Poopalasundaram et al., 2011), whereas *Caenorhabditis elegans* ephrin EFN-4 promotes primary neurite outgrowth in AIY interneurons and D-class motor neurons (Schwieterman et al., 2016). Sema6ba belongs to the semaphorins (Semas), another large class of proteins that function throughout the nervous system to guide axons. In Sema-2b loss-of-function embryos, specific motor neuron and interneuron axon pathways display guidance defects (Emerson et al., 2013). Sema5A was also expressed in the myotome during the period of motor axon outgrowth, the lack of sema5A in zebrafish result in delayed in motor axon extension into the ventral myotome and aberrant branching of these motor axons (Hilario et al., 2009). We showed that nexmifa deficiency caused a significant decrease in efna5b and sema6ba expression levels. Furthermore, efna5b and sema6ba overexpression rescued the motor neuron defects and inactive swimming behavior in nexmifa mutant embryos. These data suggested that nexmifa regulated motor neuron development, at least in part, by regulating efna5b and sema6ba expression. In the future, we will perform dual-luciferase reporter gene assays to confirm interactions between nexmifa and efna5b and sema6ba.

DATA AVAILABILITY STATEMENT

The datasets presented in this study can be found in online repositories. The names of the repository/repositories and accession number(s) can be found below: NCBI BioProject PRJNA797475.

ETHICS STATEMENT

The animal study was reviewed and approved by Administration Committee of Experimental Animals, Jiangsu Province, China.

AUTHOR CONTRIBUTIONS

HN and Y-JW designed the study. Y-QZ and G-HS performed the experiments. DL and H-YL analyzed the data and are responsible for the statistical analysis. Y-QZ wrote the manuscript. All the authors have reviewed and approved this version of the manuscript.

FUNDING

This work was supported by the National Natural Science Foundation of China (81871024), the 333 Scientific Research Project of Jiangsu Province (BRA2020396), Key medical research project of Jiangsu Provincial Health Commission (ZD2021004), Science and Technology Program of Nantong (MS22020002), Maternal and Child Health Care Association of Jiangsu Province (FYX202125), Nantong Municipal Health Commission (MB2021001 and MB2021002).

SUPPLEMENTARY MATERIAL

The Supplementary Material for this article can be found online at: https://www.frontiersin.org/articles/10.3389/fnmol.2022.848257/full#supplementary-material

Supplementary Figure S1 | Appearance of embryo fish at 72 hpf between Ctrl and nexmifa mutant.

Supplementary Figure S2 | The effect of MO on knocking down nexmifa expression. **(A)** An nexmifa splice-blocking MO was designed to target the exon 2-intron 2 splice donor site. **(B)** RT-PCR analysis of total RNA from 24 hpf embryos treated with or without MO nexmifa (Std MO). **(C)** Schematic and sequencing data showing that 181 bp of intron 2 were added between exons 2 and 3.

Supplementary Figure S3 | Nexmifa affects motor neuron morphogenesis in nexmifa morphant zebrafish embryos. **(A)** Confocal imaging of primary motor neurons in three different groups at 48 and 72 hpf. **(B)** The percentage of embryos with normal PMNs in the three groups at 48 hpf (n = 113, 231, and 218) and 72 hpf (n = 104, 214, and 221, respectively). **(C)** Cap axon lengths in the three groups at 48 hpf (n = 18, 29, and 21, respectively) and 72 hpf (n = 17, 23, and 25, respectively). **(D)** The number of branches per 1 mm Cap axons in the three groups at 48 hpf (n = 7, 9, and 10, respectively) and 72 hpf (n = 8, 10, and 10, respectively). Bars represent the mean ± standard deviation (SD). $^{**}p < 0.01$.

Supplementary Table S1 | Primers and oligos are used in this study.

Supplementary Table S2 | DEGs between Ctrl and morphants.

REFERENCES

Allen Institute for Brain Science (2004). *Allen Mouse Brain Alatas. Experiment 69531127, Gene C77370*. Washington: Allen Institute for Brain Science.

Babin, P. J., Goizet, C., and Raldua, D. (2014). Zebrafish models of human motor neuron diseases: advantages and limitations. *Prog. Neurobiol.* 118, 36–58. doi: 10.1016/j.pneurobio.2014.03.001

Beattie, C. E. (2000). Control of motor axon guidance in the zebrafish embryo. *Brain Res. Bull.* 53, 489–500. doi: 10.1016/s0361-9230(00)00382-8

Beattie, C. E., Granato, M., and Kuwada, J. Y. (2002). Cellular, genetic and molecular mechanisms of axonal guidance in the zebrafish. *Results Probl. Cell Differ.* 40, 252–269. doi: 10.1007/978-3-540-46041-1_13

Brusegan, C., Pistocchi, A., Frassine, A., Della Noce, I., Schepis, F., and Cotelli, F. (2012). Ccdc80-l1 Is involved in axon pathfinding of zebrafish motoneurons. *PLoS One* 7:e31851. doi: 10.1371/journal.pone.0031851

Cantagrel, V., Haddad, M. R., Ciofi, P., Andrieu, D., Lossi, A. M., Maldergem, L., et al. (2009). Spatiotemporal expression in mouse brain of Kiaa2022, a gene disrupted in two patients with severe mental retardation. *Gene Expr. Patterns* 9, 423–429. doi: 10.1016/j.gep.2009.06.001

Cantagrel, V., Lossi, A. M., Boulanger, S., Depetris, D., Mattei, M. G., and Gecz, J. (2004). Disruption of a new X linked gene highly expressed in brain in a family with two mentally retarded males. *J. Med. Genet.* 41, 736–742. doi: 10.1136/jmg.2004.021626

Cayuso, J., Xu, Q., and Wilkinson, D. G. (2015). Mechanisms of boundary formation by Eph receptor and ephrin signaling. *Dev. Biol.* 401, 122–131. doi: 10.1016/j.ydbio.2014.11.013

de Lange, I. M., Helbig, K. L., Weckhuysen, S., Moller, R. S., Velinov, M., and Dolzhanskaya, N. (2016). De novo mutations of KIAA2022 in females cause intellectual disability and intractable epilepsy. *J. Med. Genet.* 53, 850–858. doi: 10.1136/jmedgenet-2016-103909

Dong, Z., Wu, S., Zhu, C., Wang, X., Li, Y., and Chen, X. (2019). Clustered Regularly Interspaced Short Palindromic Repeats (CRISPR)/Cas9-mediated kif15 mutations accelerate axonal outgrowth during neuronal development and regeneration in zebrafish. *Traffic* 20, 71–81. doi: 10.1111/tra.12621

Downes, G. B., and Granato, M. (2004). Acetylcholinesterase function is dispensable for sensory neurite growth but is critical for neuromuscular synapse stability. *Dev. Biol.* 270, 232–245. doi: 10.1016/j.ydbio.2004.02.027

Eisen, J. S., Myers, P. Z., and Westerfield, M. (1986). Pathway selection by growth cones of identified motoneurones in live zebra fish embryos. *Nature* 320, 269–271. doi: 10.1038/320269a0

Emerson, M. M., Long, J. B., and Van Vactor, D. (2013). Drosophila semaphorin2b is required for the axon guidance of a subset of embryonic neurons. *Dev. Dyn.* 242, 861–873. doi: 10.1002/dvdy.23979

Flanagan-Steet, H., Fox, M. A., Meyer, D., and Sanes, J. R. (2005). Neuromuscular synapses can form in vivo by incorporation of initially aneural postsynaptic specializations. *Development* 132, 4471–4481. doi: 10.1242/dev.02044

Gao, T., Li, J., Li, N., Gao, Y., Yu, L., and Zhuang, S. (2020). lncrps25 play an essential role in motor neuron development through controlling the expression of olig2 in zebrafish. *J. Cell Physiol.* 235, 3485–3496. doi: 10.1002/jcp.29237

Gilbert, J., and Man, H. Y. (2016). The X-Linked Autism Protein KIAA2022/KIDLIA Regulates Neurite Outgrowth via N-Cadherin and delta-Catenin Signaling. *eNeuro* 3, ENEURO.238–ENEURO.216. doi: 10.1523/ENEURO.0238-16.2016

Gilbert, J., O'Connor, M., Templet, S., Moghaddam, M., Di Via Ioschpe, A., Sinclair, A., et al. (2020). NEXMIF/KIDLIA Knock-out Mouse Demonstrates Autism-Like Behaviors, Memory Deficits, and Impairments in Synapse Formation and Function. *J. Neurosci.* 40, 237–254. doi: 10.1523/JNEUROSCI.0222-19.2019

Gong, J., Hu, S., Huang, Z., Hu, Y., Wang, X., Zhao, J., et al. (2020). The Requirement of Sox2 for the Spinal Cord Motor Neuron Development of Zebrafish. *Front. Mol. Neurosci.* 13:34. doi: 10.3389/fnmol.2020.00034

Gong, J., Wang, X., Zhu, C., Dong, X., Zhang, Q., Wang, X., et al. (2017). Insm1a Regulates Motor Neuron Development in Zebrafish. *Front. Mol. Neurosci.* 10:274. doi: 10.3389/fnmol.2017.00274

Hao le, T., Duy, P. Q., An, M., Talbot, J., Iyer, C. C., Wolman, M., et al. (2017). HuD and the Survival Motor Neuron Protein Interact in Motoneurons and Are Essential for Motoneuron Development, Function, and mRNA Regulation. *J. Neurosci.* 37, 11559–11571. doi: 10.1523/JNEUROSCI.1528-17.2017

Hilario, J. D., Rodino-Klapac, L. R., Wang, C., and Beattie, C. E. (2009). Semaphorin 5A is a bifunctional axon guidance cue for axial motoneurons in vivo. *Dev. Biol.* 326, 190–200. doi: 10.1016/j.ydbio.2008.11.007

Hilario, J. D., Wang, C., and Beattie, C. E. (2010). Collagen XIXa1 is crucial for motor axon navigation at intermediate targets. *Development* 137, 4261–4269. doi: 10.1242/dev.051730

Ishikawa, T., Miyata, S., Koyama, Y., Yoshikawa, K., Hattori, T., Kumamoto, N., et al. (2012). Transient expression of Xpn, an XLMR protein related to neurite extension, during brain development and participation in neurite outgrowth. *Neuroscience* 214, 181–191. doi: 10.1016/j.neuroscience.2012.04.030

Jin, S. W., Beis, D., Mitchell, T., Chen, J. N., and Stainier, D. Y. (2005). Cellular and molecular analyses of vascular tube and lumen formation in zebrafish. *Development* 132, 5199–5209. doi: 10.1242/dev.02087

Kaur, M., Srinivasan, S., and N Bhat, A. (2018). Comparing motor performance, praxis, coordination, and interpersonal synchrony between children with and without Autism Spectrum Disorder (ASD). *Res. Dev. Disabil.* 72, 79–95. doi: 10.1016/j.ridd.2017.10.025

Koh, A., Tao, S. J., Goh, Y. J., Chaganty, V., See, K., and Purushothaman, K. (2020). A Neurexin2aa deficiency results in axon pathfinding defects and increased anxiety in zebrafish. *Hum. Mol. Genet.* 29, 3765–3780. doi: 10.1093/hmg/ddaa260

Lisabeth, E. M., Falivelli, G., and Pasquale, E. B. (2013). Eph receptor signaling and ephrins. *Cold Spring Harb. Perspect. Biol.* 5:a009159. doi: 10.1101/cshperspect.a009159

Liu, D. W., and Westerfield, M. (1990). The formation of terminal fields in the absence of competitive interactions among primary motoneurons in the zebrafish. *J. Neurosci.* 10, 3947–3959. doi: 10.1523/JNEUROSCI.10-12-03947.1990

Magome, T., Hattori, T., Taniguchi, M., Ishikawa, T., Miyata, S., Yamada, K., et al. (2013). XLMR protein related to neurite extension (Xpn/KIAA2022) regulates cell-cell and cell-matrix adhesion and migration. *Neurochem. Int.* 63, 561–569. doi: 10.1016/j.neuint.2013.09.011

Menelaou, E., Husbands, E. E., Pollet, R. G., Coutts, C. A., Ali, D. W., and Svoboda, K. R. (2008). Embryonic motor activity and implications for regulating motoneuron axonal pathfinding in zebrafish. *Eur. J. Neurosci.* 28, 1080–1096. doi: 10.1111/j.1460-9568.2008.06418.x

Moreno, R. L., and Ribera, A. B. (2009). Zebrafish motor neuron subtypes differ electrically prior to axonal outgrowth. *J. Neurophysiol.* 102, 2477–2484. doi: 10.1152/jn.00446.2009

Myers, P. Z. (1985). Spinal motoneurons of the larval zebrafish. *J. Comp. Neurol.* 236, 555–561. doi: 10.1002/cne.902360411

Myers, P. Z., Eisen, J. S., and Westerfield, M. (1986). Development and axonal outgrowth of identified motoneurons in the zebrafish. *J. Neurosci.* 6, 2278–2289. doi: 10.1523/JNEUROSCI.06-08-02278.1986

Nozawa, K., Lin, Y., Kubodera, R., Shimizu, Y., Tanaka, H., and Ohshima, T. (2017). Zebrafish Mecp2 is required for proper axonal elongation of motor neurons and synapse formation. *Dev. Neurobiol.* 77, 1101–1113. doi: 10.1002/dneu.22498

Poopalasundaram, S., Marler, K. J., and Drescher, U. (2011). EphrinA6 on chick retinal axons is a key component for p75(NTR)-dependent axon repulsion and TrkB-dependent axon branching. *Mol. Cell Neurosci.* 47, 131–136. doi: 10.1016/j.mcn.2011.03.008

Schneider, V. A., and Granato, M. (2006). The myotomal diwanka (lh3) glycosyltransferase and type XVIII collagen are critical for motor growth cone migration. *Neuron* 50, 683–695. doi: 10.1016/j.neuron.2006.04.024

Schwieterman, A. A., Steves, A. N., Yee, V., Donelson, C. J., Bentley, M. R., Santorella, E. M., et al. (2016). The Caenorhabditis elegans Ephrin EFN-4 Functions Non-cell Autonomously with Heparan Sulfate Proteoglycans to Promote Axon Outgrowth and Branching. *Genetics* 202, 639–660. doi: 10.1534/genetics.115.185298

Van Maldergem, L., Hou, Q., Kalscheuer, V. M., Rio, M., Doco-Fenzy, M., Medeira, A., et al. (2013). Loss of function of KIAA2022 causes mild to severe intellectual disability with an autism spectrum disorder and impairs neurite outgrowth. *Hum. Mol. Genet.* 22, 3306–3314. doi: 10.1093/hmg/ddt187

Westerfield, M., McMurray, J. V., and Eisen, J. S. (1986). Identified motoneurons and their innervation of axial muscles in the zebrafish. *J. Neurosci.* 6, 2267–2277. doi: 10.1523/JNEUROSCI.06-08-02267.1986

Xu, M., Liu, D., Dong, Z., Wang, X., Wang, X., Liu, Y., et al. (2014). Kinesin-12 influences axonal growth during zebrafish neural development. *Cytoskeleton* 71, 555–563. doi: 10.1002/cm.21193

Zhu, J., Xu, H., Song, H., Li, X., Wang, N., and Zhao, J. (2021). CRISPR/Cas9-mediated grna gene knockout leads to neurodevelopmental defects and motor behavior changes in zebrafish. *J. Neurochem.* 157, 520–531. doi: 10.1111/jnc.15307

Conflict of Interest: The authors declare that the research was conducted in the absence of any commercial or financial relationships that could be construed as a potential conflict of interest.

Frontiers in Molecular Neuroscience

ORIGINAL RESEARCH
published: 07 April 2022
doi: 10.3389/fnmol.2022.854556

Sema6D Regulates Zebrafish Vascular Patterning and Motor Neuronal Axon Growth in Spinal Cord

Jiajing Sheng[1†], *Jiehuan Xu*[2†], *Kaixi Geng*[1] *and Dong Liu*[1*]

[1] Nantong Laboratory of Development and Diseases, Key Laboratory of Neuroregeneration of Jiangsu and Ministry of Education, School of Life Science, Second Affiliated Hospital, Co-innovation Center of Neuroregeneration, Nantong University, Nantong, China, [2] Medical School, Nantong University, Nantong, China

Vessels and nerves are closely associated in anatomy as well as functions. Accumulating evidences have demonstrated that axon-guiding signals may affect endothelial cells migration and path finding, which is crucial for the patterning of both the complex vascular network and neural system. However, studies regarding the functional overlap between vascular and neuronal orchestrating are still incomplete. Semaphorin6D (Sema6D) belongs to the Semaphorin family and has been identified as an important regulating factor in diverse biological processes. Its roles in vascular development are still unclear. Here, we confirmed that *sema6D* is enriched in neural system and blood vessels of zebrafish embryos by *in situ* hybridization. Then, the deficiency of *sema6D* caused by specific antisense morpholino-oligonucleotides (MO) led to dramatic path finding defects in both intersegmental vessels (ISVs) and primary motor neurons (PMNs) of spinal cord in zebrafish embryos. Furthermore, these defective phenotypes were confirmed in F0 generation of *sema6D* knockouts and rescue experiments by overexpression of *sema6D* mRNA in *sema6D* morphants. These data collectively indicate that *sema6D* regulates zebrafish vascular patterning and motor neuronal axon growth in the spinal cord, which might be of great therapeutical use to regulate vessel and nerve guidance in the relevant diseases that affect both systems.

Keywords: endothelial cells, motor neuronal axon, guidance cues, path finding, zebrafish

Edited by:
Feng Rao,
Peking University People's Hospital,
China

Reviewed by:
Zhen Zhong,
Zhejiang University, China
Matthew B. Veldman,
Medical College of Wisconsin,
United States

****Correspondence:***
Dong Liu
liudongtom@gmail.com;
tom@ntu.edu.cn

[†] These authors have contributed equally to this work

Specialty section:
This article was submitted to Neuroplasticity and Development, a section of the journal Frontiers in Molecular Neuroscience

Received: *14 January 2022*
Accepted: *02 March 2022*
Published: *07 April 2022*

Citation:
Sheng J, Xu J, Geng K and Liu D (2022) Sema6D Regulates Zebrafish Vascular Patterning and Motor Neuronal Axon Growth in Spinal Cord.
Front. Mol. Neurosci. 15:854556.
doi: 10.3389/fnmol.2022.854556

INTRODUCTION

Vascular formation is an early and essential process during the development of vertebrate embryos (Nikolova and Lammert, 2003). Vascular endothelial cells assemble into tubes and then couple into an initial vascular pattern. The stereotypical wiring pattern of vessels is essential for its functions and its abnormality is inextricably related to a wide range of diseases, including atherosclerosis, hypertension, aneurysms, diabetic retinopathy, aneurysms, and tumor (Carmeliet, 2003). Although studies on angiogenesis have made extraordinary progress, the detailed regulatory mechanisms of vascular patterning remain to be fully explored (Patan, 2000; Makanya et al., 2009; Uccelli et al., 2019). Vessels and nerves are closely associated in anatomy as well as functions. Increasing reports have demonstrated that axon-guiding signals may affect endothelial cells migration and path finding, which is crucial for the development of both the vascular and the nervous systems.

However, studies regarding the functional overlap between vascular and neuronal pathways are still limited and need advanced research (Luo et al., 1993; Kolodkin and Tessier-Lavigne, 2011).

Semaphorins that are expressed in most organs and tissues were originally described as axon guidance in the hard wiring of the nervous systems (Bussolino et al., 2006; Suchting et al., 2006). However, increasing reports attested to the significance of Semaphorinsin the development and regulation outside the neuron system (Neufeld and Kessler, 2008; Capparuccia and Tamagnone, 2009). Members of Semaphorins have been found to regulate the cells motility during the development of nervous (Sema3A, 3F, 4D, 6C, 7A), immune (Sema4D), reproductive (Sema3), cancer (Sema3A, 4D) and vascular systems (Sema3A, 3E, 4D; Gherardi et al., 2004; Gu et al., 2005; Sakurai et al., 2012; Acker et al., 2018; Elder et al., 2018; Ferreira et al., 2018). Semaphorins6D (Sema6D) is a member of Semaphorin family and has been identified as an important regulating factor in the development of the spinal cord, optic nerve, heart, and tumor (Toyofuku et al., 2004a; Yazdani and Terman, 2006; Yoshida et al., 2006; Leslie et al., 2011; Peng et al., 2016). Additionally, Sema6D controls endothelial cell migration during heart development, which may imply its potential role in vascular development (Toyofuku et al., 2004a). However, there is so far no data proving the pro-angiogenic effects of Sema6D yet.

Zebrafish intersegmental vessels (ISVs) are an excellent system to trace cell behavior and morphology *in vivo* by expressing the fluorescent protein in transparent embryos (Ellertsdóttir et al., 2010). To further explore the function of *sema6D* in vertebrate development, we investigated the sequence homology, embryonic expression pattern, and function of *sema6D* in zebrafish. The results present in this study have shown that *sema6D* regulates zebrafish vascular patterning and motor neuronal axon growth in spinal cord. The findings might serve as a ground work for studying the molecular mechanism of neurovascular communication, and might be of therapeutically use to guide vessels and nerves in the relevant diseases that affect both systems.

MATERIALS AND METHODS

Zebrafish Husbandry and Breeding

The study was conducted conforming to the local institutional laws and the Chinese law for the protection of animals. All adult zebrafish (*Dario rerio*) were maintained under standard conditions in accordance with our previous protocols (Huang et al., 2013; Xu et al., 2014). The *AB/WT*, *Tg(kdrl:ras-mCherry)* and *Tg(mnx1:EGFP)* zebrafish used in this article have been described previously (Nicoli et al., 2012; Jao et al., 2013). Zebrafish embryos after 24 hpf were treated with 0.2 mM 1-phenyl-2-thio-urea to prevent pigment formation.

Phylogenetic Analysis

The zebrafish *sema6D* protein sequences (NP_998164.3) and zebrafish *sema6dl* sequences (XP_005173705.1) together with other nine species, including *Bos taurus* (XP_024853302.1), *Gallus gallus* (XP_040562440.1), *Homo sapiens* (XP_024305841.1), *Mus musculus* (XP_030105194.1), *Oryctolaguscuniculus* (XP_017203544.1), *Oryziaslatipes* (XP_011486693.1), *Rattus norvegicus* (XP_038960910.1), *Sus scrofa* (XP_020951762.1), and *Xenopus tropicalis* (XP_031753477.1) were got from NCBI and used for phylogenetic analysis. The alignments of these sequences were constructed by MEGA7and the phylogenetic tree was constructed by ML.

RNA Isolation, Reverse Transcription (RT), Polymerase Chain Reaction (PCR), Quantitative RT-PCR, and RNA Probe Transcription

Total RNA of zebrafish embryos at various stages was extracted with TRizol according to the manufacturer's instruction (Invitrogen, Waltham, MA, USA) and genomic contaminations were removed by DNaseI. Quantity of isolated RNA was verified using gel electrophoresis and Nanodrop, followed by cDNA synthesis using Transcriptor First Strand cDNA Synthesis Kit (Roche), and then was stored at −20°C.

Primers for PCR were designed by the Primer Premier six software and listed as following:

sema6D-QF: 5′-CCTCCTCCTATTCCTCTTCTGTT-3′;
sema6D-QR: 5′-ACTACGGTGCGGTTCTTATGA-3′;
ef1a–QF: 5′-GAGTTGTGCCGTACATCAG-3′;
ef1a–QR: 5′-CGTGAGAGTACATGGTCATG-3′.

Quantitative RT-PCR was conducted in a total 20 μl reaction volume with 10 μl SYBR premix (TIANGEN). The relative RNA amounts were calculated with the comparative CT (2-DDCT) method and normalized with elongation factor 1-alpha (ef1a) as the reference. Whole-mount *in situ* hybridization (WISH) with antisense RNA probes was synthesized as described previously (Wang et al., 2016). The cDNA fragments used for *sema6D* RNA probe transcription as templates were amplified using the forward primer 5'-CGACGGCTATCACTTCACTCT-3'and reverse primer 5'-TGGAACATTCTGACGGCTCTT-3'. Then a 548bp sequence of *sema6D* was inserted into pGEM-T-easy vector. Digxigenin (DIG)-labeled sense and antisense probes were performed from the linearized pGEM-T-easy plasmids using the DIG RNA Labeling Kit (Roche).

Whole Mount *In situ* Hybridization

Whole-mount *in situ* hybridization (WISH) was performed according to our previous procedures (Huang et al., 2013). Digoxigenin-labeled antisense probes were constructed as described above. Zebrafish embryos without pigment at different developmental stages were collected and fixed with 4% PFA overnight at 4°C. After incubated with the probe overnight, an alkaline phosphatase-conjugated antibody against digoxigenin and AP-substrate NBT/BCIP solution (Roche, Switzerland) was used to detect the digoxigenin-labeled RNA probe.

Morpholino and mRNA Injections

Splicing-blocking Morpholino (5'- TGTGAGCTGAGTGAA TGCAGACCT -3') that was specific for *sema6D* gene was synthesized by Gene Tools. The Morpholino was diluted to 0.3 mM with RNase-free water. The single cell stage embryos of *Tg(kdrl:ras-mCherry)* and *Tg(mnx1:EGFP)* zebrafish were obtained for microinjections as described previously (Wang et al., 2016). Then, the embryos were raised in E3 medium at 28.5°C for following imaging.

sgRNA/Cas9 mRNA Synthesis and Injections

Cas9 mRNA was obtained by *in vitro* transcription with the linearized plasmid pXT7-Cas9 according to the procedure previously described (Nakayama et al., 2013). The *sema6D* guide RNA (gRNA; 5'-GGCGTGGCAGAAGTAATGAGTGG-3') was designed and synthesized followed the previously reported (Chang et al., 2013). Transgenic zebrafish lines *Tg(kdrl:ras-mCherry)* and *Tg(mnx1:EGFP)* were natural mated to obtain embryos for microinjection. One to two-cell stage zebrafish embryos were injected with 2–3 nl of a solution containing 250 ng/μl Cas9 mRNA and 15 ng/μl sgRNA (Gong et al., 2017). At 72 hpf, 10 zebrafish embryos were randomly collected and mixed for genomic DNA extraction according to the previous methods (Gong et al., 2017). Then, the amplicons from the genomic DNA were cloned into pGEM-T-easy vector and after transformation, 50 clones were selected randomly for sequencing. The inserted fragments were sequenced by using the forward primer 5'-CCTGTGCATATAGATTGTTG-3' and reverse primer 5'-AAGTCTACAGACAGTAACG-3'. The mutation efficiency of Crispr-Cas9 was then calculated based on the sequencing results (Wu et al., 2018).

Rescue Experiments

Full-length and truncated coding sequences of *sema6D* were synthesized and inserted into PCS^{2+} vector as templates for *in vitro* transcription. The mRNA synthesis was carried out by using the mMESSAGEmMACHINESp6 Ultra Kit (Ambion) and purified with the MEGAclearTM Transcription Clean-Up Kit (Ambion) before the injection. Finally, 2 nl capped mRNA was co-injected with *sema6D* Mo into one-cell stage embryos. The *fli1a:sema6D* plasmid was constructed by LR recombination as described in the LifetechMultiste Gateway Manual (Life Technologies, Carls-bad, CA, USA). Then, the construct was injected into one cell stage embryos of *Tg(mnx1:EGFP::kdrl:ras-mcherry)* zebrafish for tissue specific rescue experiments (1 ng per embryo).

Microscopy and Statistical Analysis

After being anesthetized with tricaine, the zebrafish embryos were mounted in 0.8% low melt agarose and then photographed by Leica TCS-SP5 LSM confocal microscope. For the *in situ* hybridization, Photographs were taken using an Olympus stereomicroscope MVX10. Statistical analyses were performed by one-way analysis of variance (ANOVA) and the Mann-Whitney test. Statistical differences were considered significant for *P*-values <0.05.

RESULTS

sema6D Gene Is Evolutionarily Conserved in Vertebrates

To analyze the homology of zebrafish *sema6D* with other homologous genes, the multiple alignments and phylogenetic analyses of *sema6D/sema6Dl* were performed with species including *Danio rerio*, *Bostaurus*, *Gallus gallus*, *Homo sapiens*, *Musmusculus*, *Oryctolaguscuniculus*, *Oryziaslatipes*, *Rattusnorvegicus*, *Sus scrofa*, and *Xenopus tropicalis*. As shown in **Figures 1A,B**, the *sema6D* proteins are significantly conserved during evolution, especially for the sema domain, suggesting their important functions. In addition, zebrafish *sema6D* was clustered in a separate clade with *Oryziaslatipes* and was close to *Xenopus tropicalis* in the phylogenetic tree constructed by complete amino acid sequences of all the *sema6D* proteins above (**Figure 1C**). Interestingly, the *sema6Dl*, a *sema6D* isoform gene in zebrafish, was clustered with *sema6D* from *Oryziaslatipes*, suggesting it may not be functionally related to *sema6D* in zebrafish.

Expression of *sema6D* Genes in Zebrafish

To explore the roles of *sema6D* during zebrafish embryonic development, the expression level of *sema6D* was studied using QRT-PCR and WISH. According to QRT-PCR results, *sema6D* exhibited steady expression from 24 hpf to 96 hpf, with the highest level at 72 hpf, followed by 96 hpf (**Figure 2A**). Then, the spatial expression pattern of *sema6D* in early embryonic development was further studied by WISH. From 24 hpf to 48 hpf, *sema6D* was mainly expressed in the nervous system and also in the blood vessels (**Figures 2B–D**). Its expression in the nervous system is much restricted to the brain and head structures, being very weak in the spinal cord. Its expression in the vascular system was mainly observed in the ISVs. To further analyze the expression of *sema6D* in the zebrafish vessels, the endothelial cells from *Tg(fli1a:EGFP)* were sorted for RT-PCR (**Figure 2E**). The results showed that both fli1a and *sema6D* were detected in the selected endothelial cells, which was consistent with the previously reported single-cell RNA sequencing data of zebrafish endothelial cells (Shi et al., 2020; **Figure 2F**; **Supplementary Table S1**). Besides, mef2aa, which is specifically expressed in somite and heart, was chosen as a negative control to validate the purity of selected cells (Lv et al., 2017). The results showed that no mef2aa signals were detected in the sorted EGFP-positive cells (**Figure 2F**). Taken together, these results suggested that *sema6D* might participate in the development of zebrafish vessels and nerves.

Deficiency of *sema6D* Caused Developmental Defect of PMNs

Considering the significant expression of *sema6D* in the zebrafish brain, it is rational to speculate it might modulate the development of neural system. To validate the hypothesis, specific morpholino antisense oligonucleotide (*sema6D*-MO) was used to knockdown the expression of *sema4D* in *Tg(mnx1:EGFP)* transgenic zebrafish. The results of cDNA amplification provided evidence

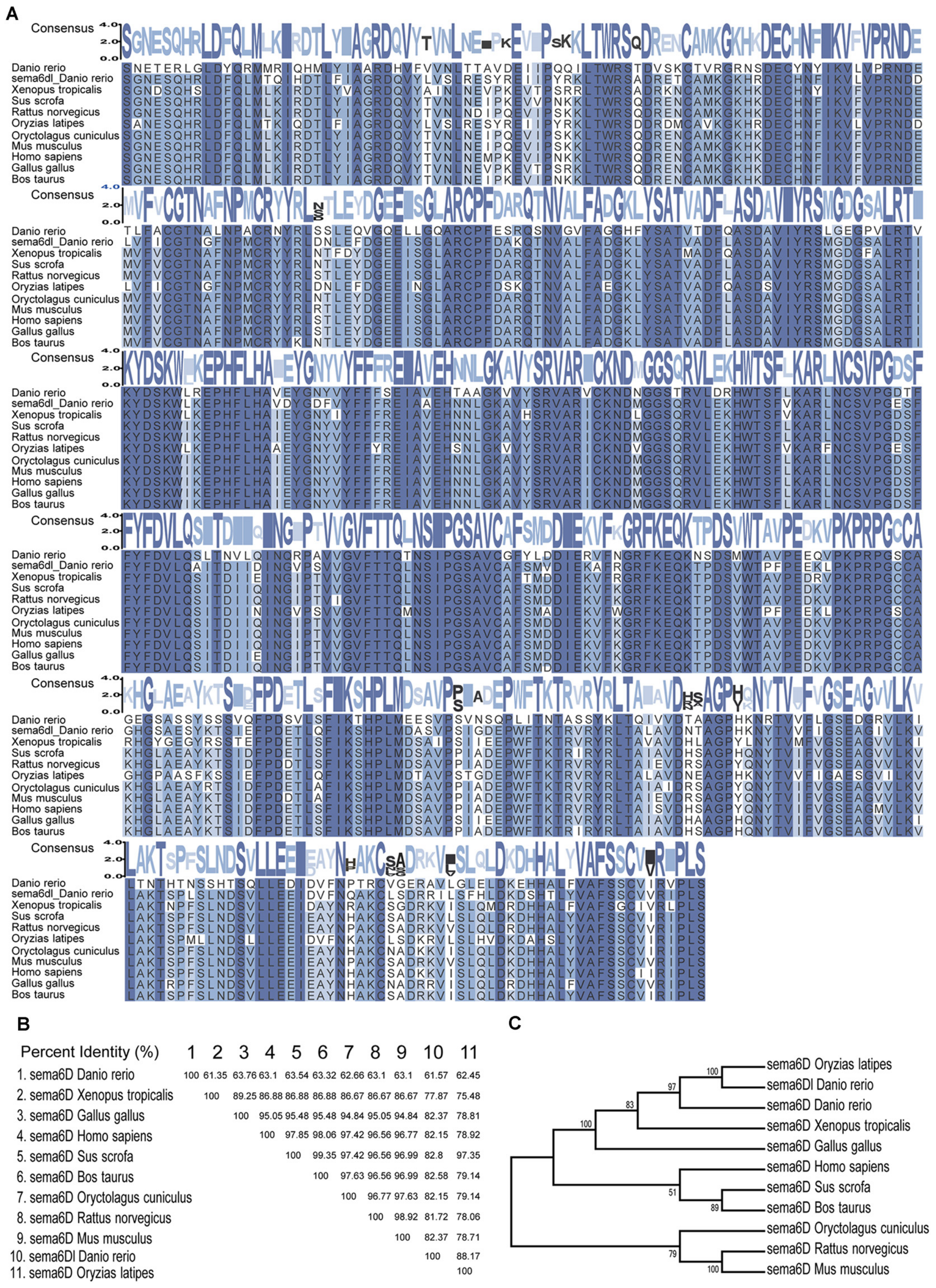

Percent Identity (%)	1	2	3	4	5	6	7	8	9	10	11
1. sema6D Danio rerio	100	61.35	63.76	63.1	63.54	63.32	62.66	63.1	63.1	61.57	62.45
2. sema6D Xenopus tropicalis		100	89.25	86.88	86.88	86.88	86.67	86.67	86.67	77.87	75.48
3. sema6D Gallus gallus			100	95.05	95.48	95.48	94.84	95.05	94.84	82.37	78.81
4. sema6D Homo sapiens				100	97.85	98.06	97.42	96.56	96.77	82.15	78.92
5. sema6D Sus scrofa					100	99.35	97.42	96.56	96.99	82.8	97.35
6. sema6D Bos taurus						100	97.63	96.56	96.99	82.58	79.14
7. sema6D Oryctolagus cuniculus							100	96.77	97.63	82.15	79.14
8. sema6D Rattus norvegicus								100	98.92	81.72	78.06
9. sema6D Mus musculus									100	82.37	78.71
10. sema6Dl Danio rerio										100	88.17
11. sema6D Oryzias latipes											100

FIGURE 1 | *Sema6D* Is highly conserved during evolution. **(A)** Alignment of the amino acid sequences of the sema domain of *sema6D/sema6Dl* in *Danio rerio*, *Bostaurus, Gallus gallus, Homo sapiens, Musmusculus, Oryctolaguscuniculus, Oryziaslatipes, Rattusnorvegicus, Sus scrofa, and Xenopus tropicalis*. Consensus values indicate the similarity of amino acid sequence, and the greater the similarity. These protein sequences were aligned using MEGA7 software and edited by TBtools. **(B)** The amino acid sequence similarity (%) of sema domain in above species. **(C)** Phylogenetic tree of the sema6D protein.

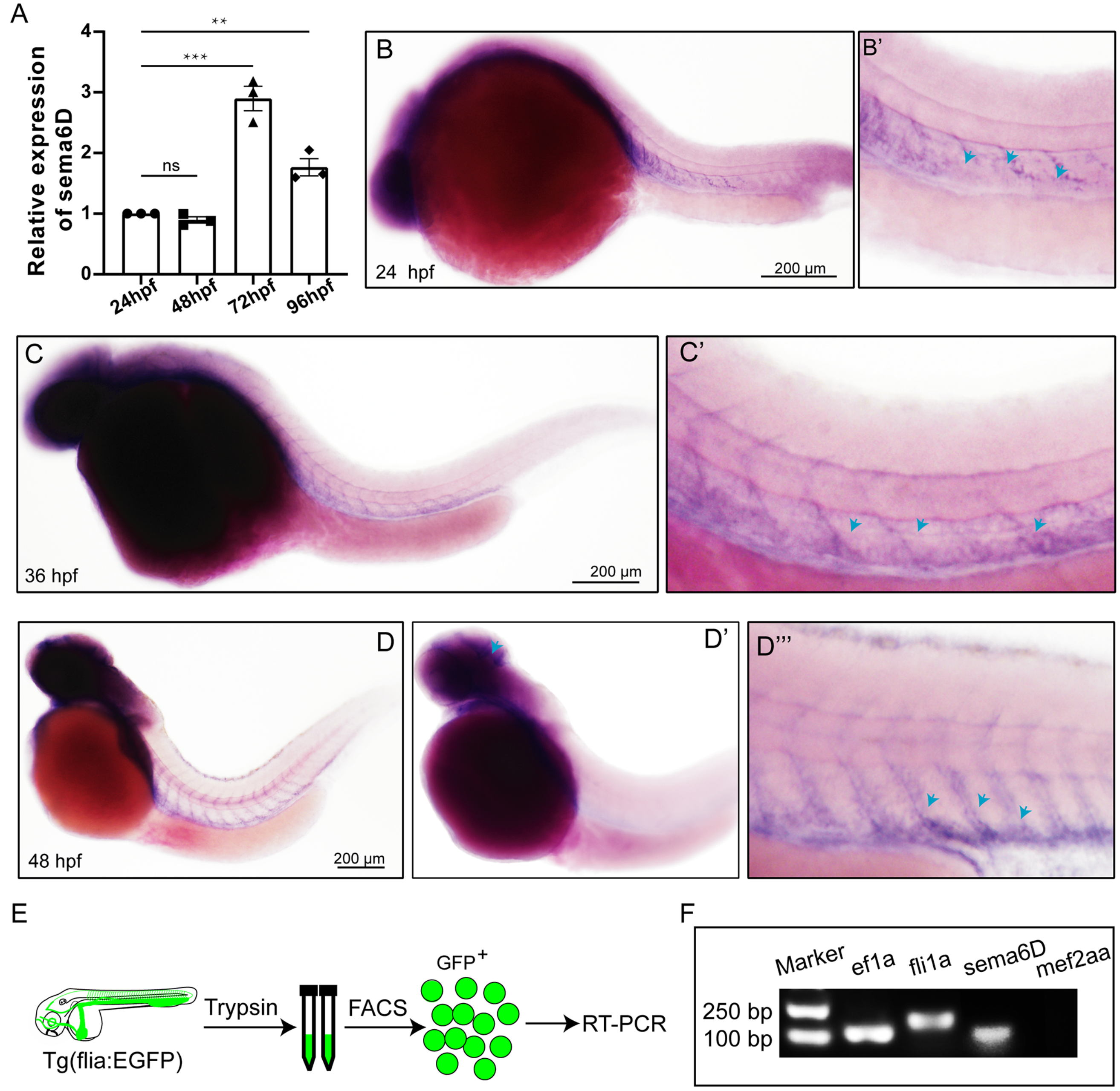

FIGURE 2 | Expression of *sema6D* gene in embryonic zebrafish at different stages. **(A)** QRT-PCR analysis of *sema6D* expression in embryonic zebrafish at different stages ($n = 3$). One-way ANOVA, values with ** and *** above the bars are significantly different ($P < 0.01$ and $P < 0.001$, respectively); value with "ns" above the bars indicated no significantly different. **(B–D)** Whole mount *in situ* hybridization analysis of *sema6D* in zebrafish embryos at different stages, blue arrowheads indicate blood vessels. **(E)** The procedure of the endothelial cells sorting and RT-PCR. **(F)** The agarose gel electrophoresis results of RT-PCR on *fli1a-EGFP* sorted cells.

that the injection of *sema6D*-MO efficiently altered the transcription pattern of *sema6D* (**Supplementary Figure S1**). Themorphology of PMNs was examined by confocal microscopy at 48 and 72 hpf. Although the morphant zebrafish embryos grossly appeared normal, the deficiency of *sema6D* caused dramatic developmental defects of PMNs (**Figure 3A**). Compared with the controls, the development of caudal primary motor neurons (Caps) was significantly inhibited at 48 hpf, where the average length of CaPs in the *sema6D* morphants was particularly shorter than that of the control groups (**Figure 3B**). At 72 hpf, although the length of CaP in the morphants were similar to the controls, the axonal trajectories of PMNs were significantly misled and many of the truncated axons in the *sema6D* deficient zebrafish could not recover completely (**Figure 3C**). Moreover, the number of CaP branches in the morphants decreased obviously at 72 hpf (**Figure 3D**). Taken together, these results suggest that *sema6D* is required for the development and navigation of neural networks.

Deficiency of *sema6D* Caused Developmental Defects of Vascular Pattern

Since *sema6D* was found to express in zebrafish vessels, we speculated that it might participate in the development of blood vessel. To further explore the roles of *sema6D* in blood vessel formation, the morphology of ISVs in *sema6D* knockdown zebrafish was observed by confocal microscopy at different stages. The results showed that the deficiency of *sema6D* resulted in significant path finding defects of zebrafish ISVs, which was consistent with observation in the development of motor neuron. In control groups, ISVs grew from the dorsal aorta and reached the dorsal roof in an orderly manner to form dorsal anastomotic vessels (DLAV). In contrast, the ISVsin *sema6D* deficiency zebrafish grew upwards halfway, then turned to connect with adjacent ISVs disorderly, and could not form complete DLAV (**Figures 4A,B**). In addition, a small number of ISVs which grew only halfway or even less usually failed to cross the horizontal myoseptum in the *sema6D* knockdown zebrafish (**Figure 4C**). These results indicated that *sema6D* seems not necessary for the initial stages of ISVs sprouting, but rather regulates the vascular patterning.

Knockout of *sema6D* Caused Aberrant Patterns of Both Nerves and Vascular System

In order to confirm that *sema6D* is required for the development of PMNs and ISVs, the CRISPR/Cas9 system was utilized to knockout *sema6D* in *Tg(mnx1:EGFP::kdrl:ras-mCherry)* transgenic zebrafish line. In order to ensure complete disruption of functional proteins, the target sites near and downstream of the translation start codon (ATG) of *sema6D* coding sequence were selected for gRNAs design (**Figure 5A**). The editing efficiency and the knockout patterns of the selected gRNA-Cas9 system were identified by sequencing (**Figures 5B,C**). It was found that the phenotypes of PMNs and ISVs in the F0 generation of *sema6D* knockouts were consistent with the deficient morphants by confocal imaging analysis (**Figure 5D**). The PMNs were shorter and the axonal trajectories were apparently misled in the F0 knockouts (**Figure 5E**). Besides, the disorganized vasculature was also observed (**Figure 5F**). Furthermore, injection of *sema6D* gRNA without cas9 caused no obvious developmental defects, confirming the phenotype was a specific consequence of *sema6D* knockdown.

Overexpressing *sema6D* Partially Restored the Defects of ISVs and PMNs in *sema6D* Deficient Embryos

In order to confirm the defects of vascular and neuronal development were specifically caused by *sema6D* deficiency, the *in vitro* synthesized *sema6D* mRNA and *sema6D*-Mo were co-injected into one cell stage zebrafish embryos. Confocal imaging analysis revealed that the overexpression of *sema6D* mRNA could greatly rescue the defective phenotypes of PMNs and ISVs (**Figures 6A–C**) in *sema6D* deficient embryos. In addition, single *sema6D* mRNA injection also caused phenotypes of PMNs and ISVs, which are similar to those in deficient morphant (**Figures 6A–C**). This result validated that *sema6D* could regulate growing guidance of vessels and neurons in zebrafish. To further investigate the consequences of tissue specific rescue, *sema6D* was over-expressed in morphants with the fli1a promoter. Comparing with the morphant, embryos co-injected with *sema6D*-MO and *fli1a:sema6D* plasmid exhibited rescue phenotypes (**Figures 6D–F**). Taken together, these results suggested that endothelial-derived *sema6D* were involved in both neural and vascular development.

DISCUSSION

In this study, we found *sema6D* played a dual role in regulating vascular and neuronal patterning for the first time by using unique advantages of the zebrafish model. First, detailed expression analysis confirmed that *sema6D* is enriched in the neural system as well as blood vessels. Then, the knockdown and knockout of *sema6D* disturbed the pattern of both ISVs and PMNs, suggesting a requirement for *sema6D* in guiding endothelial cells and neurons during zebrafish embryonic development. Furthermore, overexpression of *sema6D* in whole embryos and endothelial cells both significantly relieved the aberrant phenotypes of vessels and nerves in sema6D morphants, validating that endothelial-derived *sema6D* is of great importance to the development and patterning of embryonic nervous and vascular system in zebrafish.

Semaphoring signaling was initially recognized in guiding axon growth (Chisholm and Tessier-Lavigne, 1999; Goodman et al., 1999). However, recent studies have focused its roles outside the neural system. Sema6D belongs to the semaphore in family, which exerts its function in either cell–cell interaction or a long distances manner by releasing its extracellular domains (SEMA+PSI domains) from the cell surface as a secreted cytokine (Toyofuku et al., 2004a,b; Peng et al., 2016). Thus, *sema6D* may perform diverse important functions during development processes. Furthermore, *sema6D* and its receptor Plexin-A1 were found to promote endocardial cells migration during heart development in combination with VEGFR2, suggesting it may function as a proangiogenic factor (Toyofuku et al., 2004a; Sun et al., 2019). However, there is so far no data on the regulation of vascular development by *sema6D*. Here, our WISH results showed that *sema6D* was not only expressed in the nervous system, but also in the ISVs, suggesting *sema6D* may participate in the vascular development of zebrafish. Our knock-down study provides first *in vivo* evidence supporting the expectation. The deficiency of *sema6D* resulted in abnormal ISVs patterning in zebrafish embryo. This result is consistent with previous studies, which have suggested that the organization of vascular system share various common guiding factors involved in nerves network (Sakurai et al., 2012; Zhang et al., 2020). However, there is another *sema6D* related gene in zebrafish, *sema6Dl*, whose

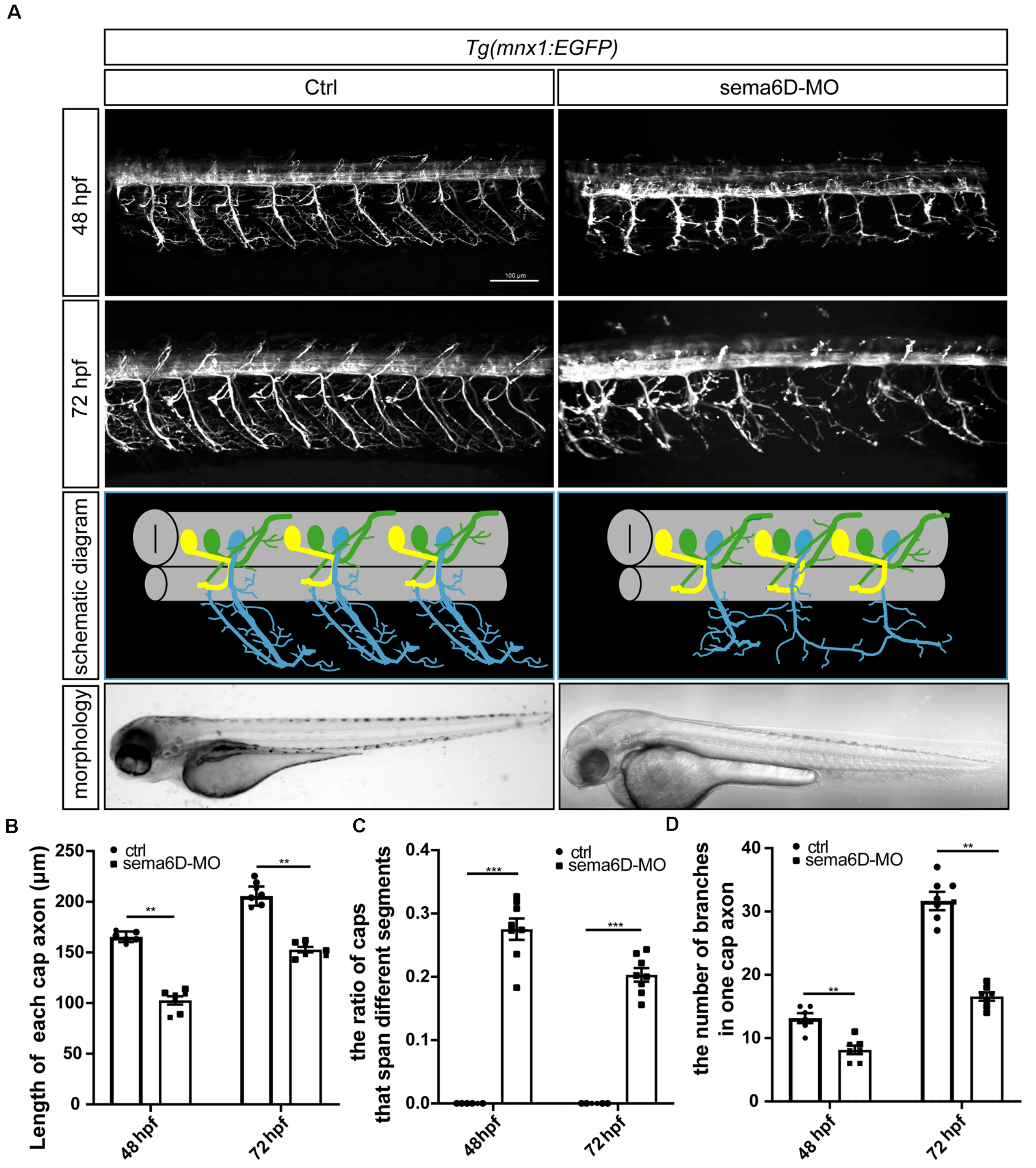

FIGURE 3 | Primary motor neuron morphogenesis defects in the *sema6D* knockout zebrafish. **(A)** Confocal imaging analysis of PMNs in control and *sema6D* knockout groups at 48 and 72 hpf. **(B)** The statistical analysis of the length of each cap axon in the control and *sema6D* morphants at 48 and 72 hpf ($n = 7$). The length of five cap axon was measured in each zebrafish and the average was used. Mann-Whitney test, $P = 0.0012$. Values with ** above the bars are significantly different ($P < 0.01$). **(C)** The statistical analysis of the ratio of Caps across different segments in the control and *sema6D* morphants at 48 and 72 hpf ($n = 8$). Mann-Whitney test, $P = 0.0007$. Values with *** above the bars are significantly different ($P < 0.001$). **(D)** The statistical analysis of the number of branches in one cap axon in the control and *sema6D* morphants at 48 and 72 hpf. The number of branches in each cap axon was measured in five axon of each zebrafish and the average was used. Mann-Whitney test, 48 hpf: $P = 0.0017$; 72 hpf: $P = 0.0012$. Values with ** above the bars are significantly different ($P < 0.01$).

function is unclear. Interestingly, our evolutionary analysis showed that *sema6Dl* did not cluster with *sema6D* in zebrafish but with other species, suggesting it may not be functionally related to *sema6D* in zebrafish. Furthermore, previous reports

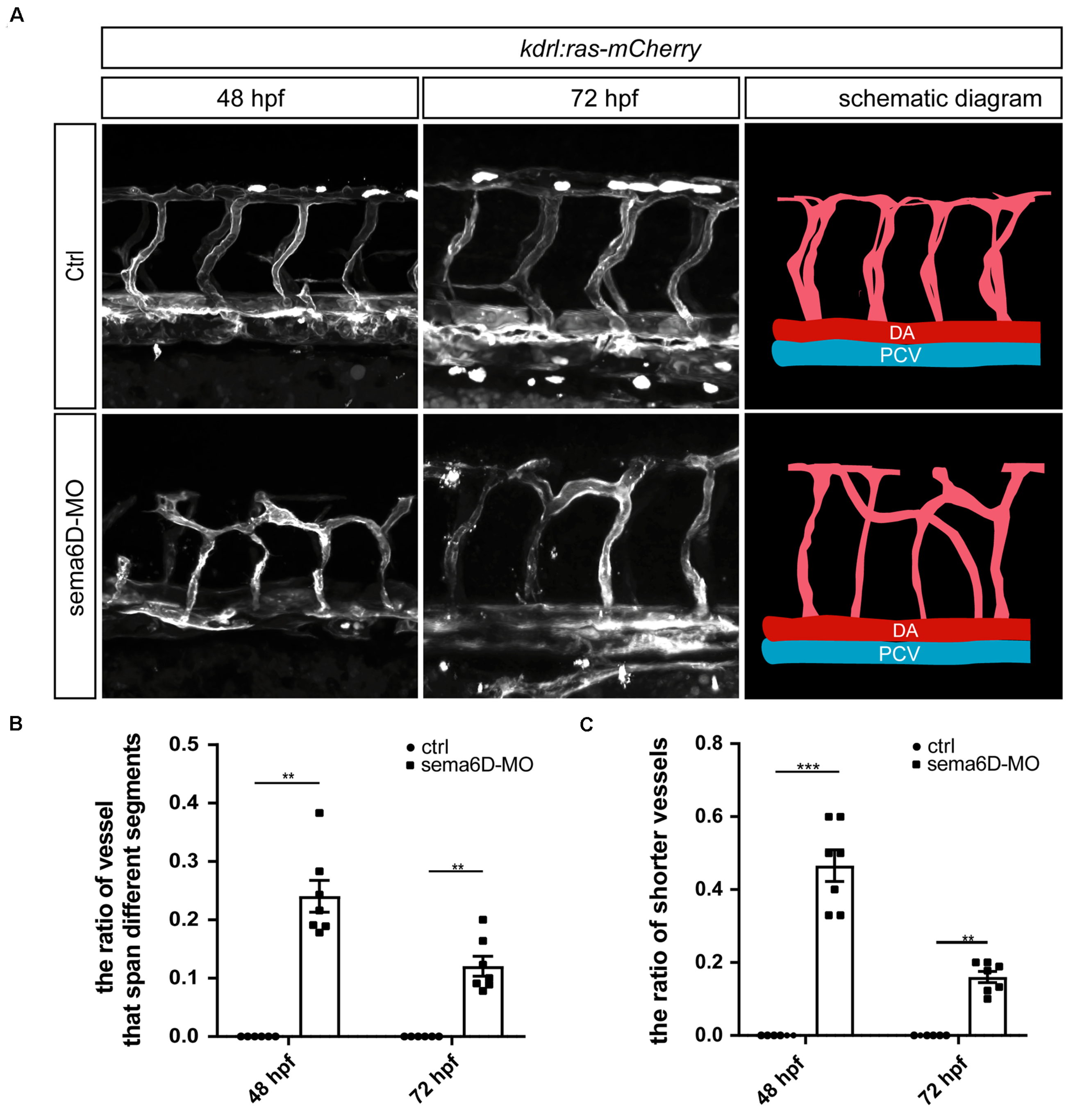

FIGURE 4 | Deficiency of *sema6D* caused aberrant vascular networks. **(A)** Confocal imaging analysis of ISVs in the control and *sema6D*-MO embryos at 48 and 72 hpf. **(B)** The statistical analysis of the ratio of vessels that span different segments in the control and *sema6D* morphants at 48 and 72 hpf ($n = 7$). About 9–12 ISVs were used for statistics per zebrafish. Mann-Whitney test, $P = 0.0012$. Values with ** above the bars are significantly different ($P < 0.01$). **(C)** The statistical analysis of the ratio of shorter vessels in the control and *sema6D* morphants at 48 and 72 hpf ($n = 7$). About 9–12 ISVs were used for statistics per zebrafish. Mann-Whitney test, 48 hpf: $P = 0.0006$; 72 hpf: $P = 0.0012$. Values with ** and *** above the bars are significantly different ($P < 0.01$ and $P < 0.001$, respectively).

have found that *sema6Dl* was mainly expressed in the brain, lens, vagal ganglion, and retinal ganglion cells, but not in the primary motor neurons or the vascular system (**Supplementary Table S1**, Ebert et al., 2012; Shi et al., 2020). It is rational to speculate there is no redundant function between *sema6D* and *sema6Dl* in PMNs and ISVs development. Therefore, our data and previous studies remind us that *sema6D* might contribute to the endothelial cell formation and path finding.

Although *sema6D* has been validated in regulating specific axons projection as a guidance cue, its functional roles in

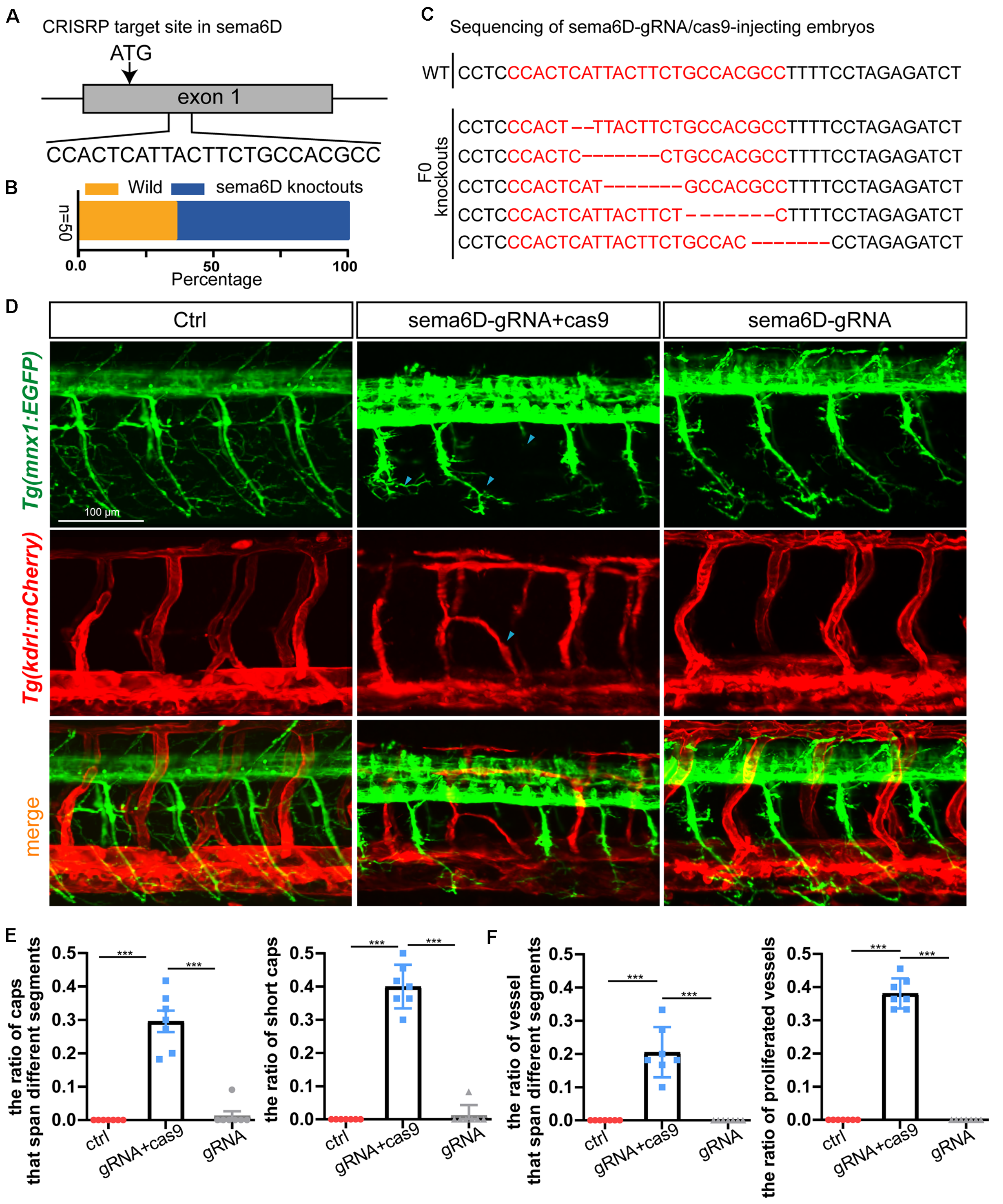

FIGURE 5 | Knockout of *sema6D* caused both aberrant phenotypes in PMNs and ISVs. **(A)** Schematic diagram showing the targeting site of the gRNA on the *sema6D* gene. Starting codon (ATG) site is indicated by arrow. **(B)** The statistics of the ratio of wildtype to mutant sequences ($n = 50$). **(C)** Knockout patterns of *sema6D*-gRNA/cas9-injecting embryos by sequencing. **(D)** Confocal imaging analysis of primary motor neurons and intersegmental vessels in control and the F0 generation of the injected *Tg(mnx1:EGFP::kdrl:ras-mCherry)* zebrafish at 48 hpf, blue arrowheads indicate aberrant PMN and ISV. **(E)** The statistical analysis of the ratio of aberrant axonal projection of Caps ($P = 0.0006$) and short Caps ($P = 0.0006$) in the wild, F0 knockouts, and cas9 negative control at 48 hpf ($n = 7$). About 9–11caps were used for statistics per zebrafish. Mann-Whitney test. Values with *** above the bars are significantly different ($P < 0.001$). **(F)** The statistical analysis of the ratio of vessels that span different segments ($P = 0.0006$) and the ratio of proliferated vessels ($P = 0.006$) in the wild, F0 knockouts, and cas9 negative control at 48 hpf ($n = 7$). About 9–12 ISVs were used for statistics per zebrafish. Mann-Whitney test. Values with *** above the bars are significantly different ($P < 0.001$).

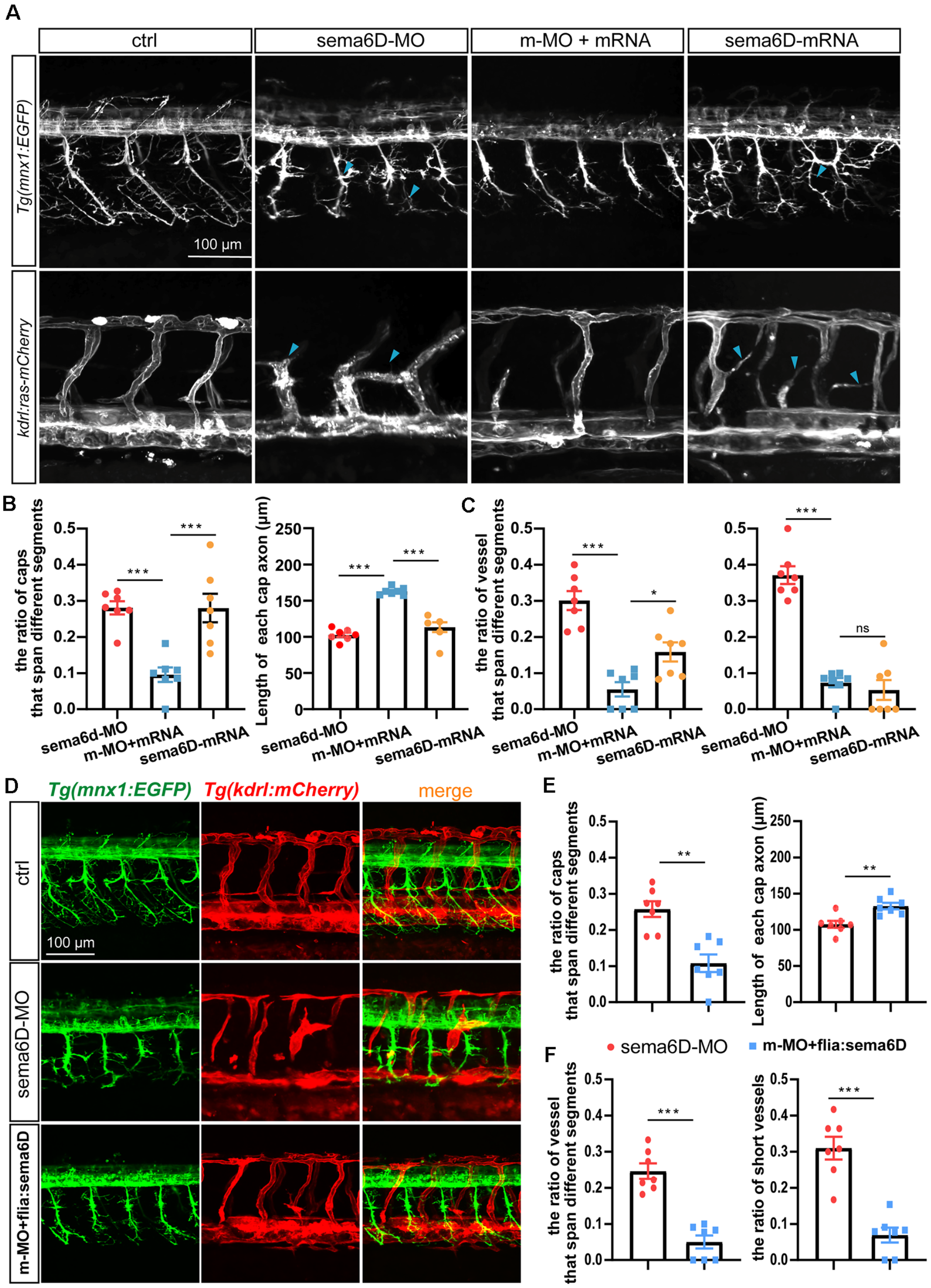

FIGURE 6 | Overexpressing *sema6D* partially restored the defects of PMNs and ISVs in *sema6D*-deficient embryos. **(A)** Confocal imaging analysis of PMNs and ISVs in control, *sema6D*-MO, and *sema6D*-mRNA injected embryos at 48 hpf. Blue arrowheads indicate aberrant PMNs and ISVs. **(B)** The statistical analysis of the ratio of aberrant axonal projection of Caps ($P = 0.0006$) and short Caps ($P = 0.0006$) in *sema6D*-MO, m-MO+*sema6D*-mRNA, and *sema6D*-mRNA injected embryos at 48 hpf ($n = 7$). About 9–11 caps were used for statistics per zebrafish. Mann-Whitney test. Values with *** above the bars are significantly different ($P < 0.001$). **(C)** The statistical analysis of the ratio of vessel that span different segments (***$P = 0.0006$; *$P = 0.0291$) and the ratio of ectopic vessels ($P = 0.0006$) in the *sema6D*-MO, m-MO+*sema6D*-mRNA, and *sema6D*-mRNA injected embryos at 48 hpf ($n = 7$). About 9–12 ISVs were used for statistics per zebrafish. Mann-Whitney test. Values with *** above the bars are significantly different ($P < 0.001$). Value with "ns" above the bars indicated no significantly different. **(D)** Confocal imaging analysis of PMNs and ISVs in control, *sema6D* morphants, and *sema6D* morphants with *fli1a:sema6D* plasmid at 48 hpf. **(E)** The statistical analysis of the ratio of aberrant axonal projection of Caps ($P = 0.0012$) and the length of Caps ($P = 0.0047$) in the *sema6D* morphants and *sema6D* morphants with *fli1a:sema6D* plasmid at 48 hpf ($n = 7$). About 9–11 caps were used for statistics per zebrafish. Mann-Whitney test. Values with ** above the bars are significantly different ($P < 0.01$). **(F)** The statistical analysis of the ratio of vessels that span different segments ($P = 0.0006$) and the ratio of ectopic vessels ($P = 0.0006$) in the *sema6D* morphants and *sema6D* morphants with *fli1a:sema6D* plasmid at 48 hpf ($n = 7$). About 9–12 ISVs were used for statistics per zebrafish. Mann-Whitney test. Values with *** above the bars are significantly different ($P < 0.001$).

animal motor neurons development remain unclear (Kimura et al., 2007; Kuwajima et al., 2012; Key et al., 2013). Here, our study demonstrated that *sema6D* is of great importance to the development of embryonic motor neurons in zebrafish. The deficiency of *sema6D* could lead to obvious motor neuron defects, including the inhibition of Caps growth and reduced branching of CaP axons. Meanwhile, the absence of *sema6D* caused dramatic aberrant patterning of PMNs, suggesting *sema6D* could regulate motor neurons path finding as a guidance signal. Interestingly, the previous report and our *in situ* hybridization results demonstrated that the expression of *sema6D* was not significant in the spinal cord (Kucenas et al., 2009). An important question is how does *sema6D* participate in motor neurons especially Cap axon guidance? From our results, the deficient phenotypes of PMNs are not always accompanied by abnormal ISVs, indicating the motor neurons defects are not the consequence of the aberrant vascular patterning. Another hypothesis is that *sema6D* acts as a guidance cue, which requires the receptors on motor neurons. Accordingly, a recent report demonstrated knockdown of plexin A1 leads to axons defect in somites, which is similar to our phenotypes (Dworschak et al., 2021). Furthermore, previous study in mouse also showed that developing embryonic but not mature adult blood vessels expressed Plexin-A1 andPlexin-A1 injected led a significant number of abnormal angiogenic spouts in zebrafish ISVs (Jacob et al., 2016). Therefore, our data and previous studies remind us that *sema6D* might contribute to the PMNs and ISVs patterning by binding to plexin A1 on motor neurons as well as endothelial cells. To further explore the relationship between the vascular and PMNs phenotypes, the tissue-specific rescue experiments were performed. The results showed that overexpressing *sema6D* in endothelial cells partially rescued the deficient phenotypes in the morphants, indicating endothelial-derived *sema6D* contributes to the development and patterning of embryonic nervous and vascular systems in zebrafish.

In summary, the present study identified the essential and multifunctional roles of *sema6D* during the embryonic nervous and vascular development. Deficiency of *sema6D* could cause deficient neuronal and vascular navigation. Our findings here provided new clues to the synergistically functional and molecular mechanism of *sema6D* underlying the nerves and blood vascular development. It is of great significance to completely dissect the axon guidance signaling network to understand how the nervous and blood vessel system are built up.

DATA AVAILABILITY STATEMENT

The original contributions presented in the study are included in the article/**Supplementary Material**, further inquiries can be directed to the corresponding author.

ETHICS STATEMENT

The animal study was reviewed and approved by Administration Committee of Experimental Animals, Jiangsu Province, China.

AUTHOR CONTRIBUTIONS

DL supervised and designed this project. JS and DL wrote the manuscript and analyzed the data. JS, JX, and KG performed the experiments. All authors contributed to the article and approved the submitted version.

FUNDING

This study was supported by grants from the National Natural Science Foundation of China (81870359, 2018YFA0801004) and Natural Science Foundation of Jiangsu Province (BK20180048).

SUPPLEMENTARY MATERIAL

The Supplementary Material for this article can be found online at: https://www.frontiersin.org/articles/10.3389/fnmol.2022.854556/full#supplementary-material.

REFERENCES

Acker, D. W., Wong, I., Kang, M., and Paradis, S. (2018). Semaphorin 4D promotes inhibitory synapse formation and suppresses seizures *in vivo*. *Epilepsia* 59, 1257–1268. doi: 10.1111/epi.14429

Bussolino, F., Valdembri, D., Caccavari, F., and Serini, G. (2006). Semaphoring vascular morphogenesis. *Endothelium* 13, 81–91. doi: 10.1080/10623320600698003

Capparuccia, L., and Tamagnone, L. (2009). Semaphorin signaling in cancer cells and in cells of the tumor microenvironment-two sides of a coin. *J. Cell Sci.* 122, 1723–1736. doi: 10.1242/jcs.030197

Carmeliet, P. (2003). Angiogenesis in health and disease. *Nat. Med.* 9, 653–660. doi: 10.1038/nm0603-653

Chang, N., Sun, C., Gao, L., Zhu, D., Xu, X., Zhu, X., et al. (2013). Genome editing with RNA-guided Cas9 nuclease in zebrafish embryos. *Cell Res.* 23, 465–472. doi: 10.1038/cr.2013.45

Chisholm, A., and Tessier-Lavigne, M. (1999). Conservation and divergence of axon guidance mechanisms. *Curr. Opin. Neurobiol.* 9, 603–615. doi: 10.1016/S0959-4388(99)00021-5

Dworschak, G. C., Punetha, J., Kalanithy, J. C., Mingardo, E., Erdem, H. B., Akdemir, Z. C., et al. (2021). Biallelic and monoallelic variants in PLXNA1 are implicated in a novel neurodevelopmental disorder with variable cerebral and eye anomalies. *Genet. Med.* 23, 1715–1725. doi: 10.1038/s41436-021-01196-9

Ebert, A. M., Lamont, R. E., Childs, S. J., and Mcfarlane, S. (2012). Neuronal expression of class 6 semaphorins in zebrafish. *Gene Expr. Patterns* 12, 117–122. doi: 10.1016/j.gep.2012.01.007

Elder, A. M., Tamburini, B. A., Crump, L. S., Black, S. A., Wessells, V. M., Schedin, P. J., et al. (2018). Semaphorin 7A promotes macrophage-mediated lymphatic remodeling during postpartum mammary gland involution and in breast cancer. *Cancer Res.* 78, 6473–6485. doi: 10.1158/0008-5472.CAN-18-1642

Ellertsdóttir, E., Lenard, A., Blum, Y., Krudewig, A., Herwig, L., Affolter, M., et al. (2010). Vascular morphogenesis in the zebrafish embryo. *Dev. Biol.* 341, 56–65. doi: 10.1016/j.ydbio.2009.10.035

Ferreira, G. D., Capp, E., Jauckus, J., Strowitzki, T., and Germeyer, A. (2018). Expression of semaphorin class 3 is higher in the proliferative phase on the human endometrium. *Arch. Gynecol. Obstet.* 297, 1175–1179. doi: 10.1007/s00404-018-4719-3

Gherardi, E., Love, C. A., Esnouf, R. M., and Jones, E. Y. (2004). The sema domain. *Curr. Opin. Struct. Biol.* 14, 669–678. doi: 10.1016/j.sbi.2004.10.010

Gong, J., Wang, X., Zhu, C., Dong, X., Zhang, Q., Wang, X., et al. (2017). Insm1a regulates motor neuron development in zebrafish. *Front. Mol. Neurosci.* 10:274. doi: 10.3389/fnmol.2017.00274

Goodman, C., Kolodkin, A., Luo, Y., Püschel, A., and Raper, J. (1999). Unified nomenclature for the semaphorins/collapsins. *Cell* 97, 551–552. doi: 10.1016/s0092-8674(00)80766-7

Gu, C., Yoshida, Y., Livet, J., Reimert, D. V., Mann, F., Merte, J., et al. (2005). Semaphorin 3E and plexin-D1 control vascular pattern independently of neuropilins. *Science* 307, 265–268. doi: 10.1126/science.1105416

Huang, Y., Wang, X., Wang, X., Xu, M., Liu, M., and Liu, D. (2013). Nonmuscle myosin II-B (myh10) expression analysis during zebrafish embryonic development. *Gene Expr. Patterns* 13, 265–270. doi: 10.1016/j.gep.2013.04.005

Jacob, L., Sawma, P., Garnier, N., Meyer, L. A., Fritz, J., Hussenet, T., et al. (2016). Inhibition of PlexA1-mediated brain tumor growth and tumor-associated angiogenesis using a transmembrane domain targeting peptide. *Oncotarget* 7, 57851–57865. doi: 10.18632/oncotarget.11072

Jao, L.-E., Wente, S. R., and Chen, W. (2013). Efficient multiplex biallelic zebrafish genome editing using a CRISPR nuclease system. *Proc. Natl. Acad. Sci. U S A* 110, 13904–13909. doi: 10.1073/pnas.1308335110

Key, B., Matsuoka, R. L., Sun, L. O., Katayama, K.-I., Yoshida, Y., and Kolodkin, A. L. (2013). Sema6B, sema6C and sema6D expression and function during mammalian retinal development. *PLoS One* 8:e63207. doi: 10.1371/journal.pone.0063207

Kimura, M., Taniguchi, M., Mikami, Y., Masuda, T., Yoshida, T., Mishina, M., et al. (2007). Identification and characterization of zebrafish semaphorin 6D. *Biochem. Biophys. Res. Commun.* 363, 762–768. doi: 10.1016/j.bbrc.2007.09.038

Kolodkin, A. L., and Tessier-Lavigne, M. (2011). Mechanisms and molecules of neuronal wiring: a primer. *Cold Spring Harb. Perspect. Biol.* 3:a001727. doi: 10.1101/cshperspect.a001727

Kucenas, S., Wang, W.-D., Knapik, E. W., and Appel, B. (2009). A selective glial barrier at motor axon exit points prevents oligodendrocyte migration from the spinal cord. *J. Neurosci.* 29, 15187–15194. doi: 10.1523/JNEUROSCI.4193-09.2009

Kuwajima, T., Yoshida, Y., Takegahara, N., Petros, T. J., Kumanogoh, A., Jessell, T. M., et al. (2012). Optic chiasm presentation of semaphorin6D in the context of plexin-A1 and Nr-CAM promotes retinal axon midline crossing. *Neuron* 74, 676–690. doi: 10.1016/j.neuron.2012.03.025

Leslie, J. R., Imai, F., Fukuhara, K., Takegahara, N., Rizvi, T. A., Friedel, R. H., et al. (2011). Ectopic myelinating oligodendrocytes in the dorsal spinal cord as a consequence of altered semaphorin 6D signaling inhibit synapse formation. *Development* 138, 4085–4095. doi: 10.1242/dev.066076

Luo, Y., Raible, D., and Raper, J. A. (1993). Collapsin: a protein in brain that induces the collapse and paralysis of neuronal growth cones. *Cell* 75, 217–227. doi: 10.1016/0092-8674(93)80064-l

Lv, F., Zhu, C., Yan, X., Wang, X., and Liu, D. (2017). Generation of a mef2aa:EGFP transgenic zebrafish line that expresses EGFP in muscle cells. *Fish Physiol. Biochem.* 43, 287–294. doi: 10.1007/s10695-016-0286-3

Makanya, A. N., Hlushchuk, R., and Djonov, V. G. (2009). Intussusceptive angiogenesis and its role in vascular morphogenesis, patterning and remodeling. *Angiogenesis* 12, 113–123. doi: 10.1007/s10456-009-9129-5

Nakayama, T., Fish, M. B., Fisher, M., Oomen-Hajagos, J., Thomsen, G. H., and Grainger, R. M. (2013). Simple and efficient CRISPR/Cas9-mediated targeted mutagenesis in *Xenopus tropicalis*. *Genesis* 51, 835–843. doi: 10.1002/dvg.22720

Neufeld, G., and Kessler, O. (2008). The semaphorins: versatile regulators of tumour progression and tumour angiogenesis. *Nat. Rev. Cancer* 8, 632–645. doi: 10.1038/nrc2404

Nicoli, S., Knyphausen, C.-P., Zhu, L. J., Lakshmanan, A., and Lawson, N. D. (2012). miR-221 is required for endothelial tip cell behaviors during vascular development. *Dev. Cell* 22, 418–429. doi: 10.1016/j.devcel.2012.01.008

Nikolova, G., and Lammert, E. (2003). Interdependent development of blood vessels and organs. *Cell Tissue Res.* 314, 33–42. doi: 10.1007/s00441-003-0739-8

Patan, S. (2000). Vasculogenesis and angiogenesis as mechanisms of vascular network formation, growth and remodeling. *J. Neurooncol.* 50, 1–15. doi: 10.1023/a:1006493130855

Peng, Y., Song, L., Li, D., Kesterson, R., Wang, J., Wang, L., et al. (2016). Sema6D acts downstream of bone morphogenetic protein signalling to promote atrioventricular cushion development in mice. *Cardiovasc. Res.* 112, 532–542. doi: 10.1093/cvr/cvw200

Sakurai, A., Doci, C., and Gutkind, J. S. (2012). Semaphorin signaling in angiogenesis, lymphangiogenesis and cancer. *Cell Res.* 22, 23–32. doi: 10.1038/cr.2011.198

Shi, Y., Qian, P., Sheng, J., Zhang, X., Wang, X., Zhao, J., et al. (2020). Single-cell RNA-seq reveals endoimmune cells in zebrafish. *bioRxiv* [Preprint]. doi: 10.1101/2019.12.31.892240

Suchting, S., Bicknell, R., and Eichmann, A. (2006). Neuronal clues to vascular guidance. *Exp. Cell Res.* 312, 668–675. doi: 10.1016/j.yexcr.2005.11.009

Sun, Q., Peng, Y., Zhao, Q., Yan, S., Liu, S., Yang, Q., et al. (2019). SEMA6D regulates perinatal cardiomyocyte proliferation and maturation in mice. *Dev. Biol.* 452, 1–7. doi: 10.1016/j.ydbio.2019.04.013

Toyofuku, T., Zhang, H., Kumanogoh, A., Takegahara, N., Suto, F., Kamei, J., et al. (2004a). Dual roles of Sema6D in cardiac morphogenesis through region-specific association of its receptor, plexin-A1, with off-track and vascular endothelial growth factor receptor type 2. *Genes Dev.* 18, 435–447. doi: 10.1101/gad.1167304

Toyofuku, T., Zhang, H., Kumanogoh, A., Takegahara, N., Yabuki, M., Harada, K., et al. (2004b). Guidance of myocardial patterning in cardiac development by Sema6D reverse signalling. *Nat. Cell Biol.* 6, 1204–1211. doi: 10.1038/ncb1193

Uccelli, A., Wolff, T., Valente, P., Di Maggio, N., Pellegrino, M., Gürke, L., et al. (2019). Vascular endothelial growth factor biology for regenerative angiogenesis. *Swiss Med. Wkly.* 149:w20011. doi: 10.4414/smw.2019.20011

Wang, X., Ling, C. C., Li, L., Qin, Y., Qi, J., Liu, X., et al. (2016). MicroRNA-10a/10b represses a novel target gene mib1 to regulate angiogenesis. *Cardiovasc. Res.* 110, 140–150. doi: 10.1093/cvr/cvw023

Wu, R. S., Lam, I. I., Clay, H., Duong, D. N., Deo, R. C., and Coughlin, S. R. (2018). A rapid method for directed gene knockout for screening in G0 zebrafish. *Dev. Cell* 46, 112–125.e4. doi: 10.1016/j.devcel.2018.06.003

Xu, M., Liu, D., Dong, Z., Wang, X., Wang, X., Liu, Y., et al. (2014). Kinesin-12 influences axonal growth during zebrafish neural development. *Cytoskeleton (Hoboken)* 71, 555–563. doi: 10.1002/cm.21193

Yazdani, U., and Terman, J. R. (2006). The semaphorins. *Genome Biol.* 7:211. doi: 10.1186/gb-2006-7-3-211

Yoshida, Y., Han, B., Mendelsohn, M., and Jessell, T. M. (2006). PlexinA1 signaling directs the segregation of proprioceptive sensory axons in the developing spinal cord. *Neuron* 52, 775–788. doi: 10.1016/j.neuron.2006.10.032

Zhang, C.-L., Hong, C.-D., Wang, H.-L., Chen, A.-Q., Zhou, Y.-F., Wan, Y., et al. (2020). The role of semaphorins in small vessels of the eye and brain. *Pharmacol. Res.* 160:105044. doi: 10.1016/j.phrs.2020.105044

Conflict of Interest: The authors declare that the research was conducted in the absence of any commercial or financial relationships that could be construed as a potential conflict of interest.

frontiers | Frontiers in Molecular Neuroscience

ORIGINAL RESEARCH
published: 14 April 2022
doi: 10.3389/fnmol.2022.859166

Protein Tyrosine Phosphatase Receptor Type D Regulates Neuropathic Pain After Nerve Injury *via* the STING-IFN-I Pathway

Chengkuan Sun, Guangzhi Wu, Zhan Zhang, Rangjuan Cao* and Shusen Cui*

Department of Hand Surgery, China-Japan Union Hospital of Jilin University, Changchun, China

Neuropathic pain is usually caused by injury or dysfunction of the somatosensory system, and medicine is a common way of treatment. Currently, there are still no satisfactory drugs, like opioids and lidocaine, which carry a high risk of addiction. Protein tyrosine phosphatase receptor type D (PTPRD) is a known therapeutic target in addiction pathways and small molecule inhibitors targeting it, such as 7-butoxy illudalic acid analog (7-BIA), have recently been developed to tackle addition. PTPRD is also upregulated in the dorsal root ganglion (DRG) in a rat model of neuropathic pain, but is not yet clear whether PTPRD contributes to the development of neuropathic pain. Here, we established a chronic constriction injury (CCI) and evaluated PTPRD expression and its association with neuropathic pain. PTPRD expression was found to gradually increase after CCI in DRGs, and its expression was concomitant with the progressive development of hypersensitivity as assessed by both mechanical and thermal stimuli. Both PTPRD knockdown and administration of PTPRD inhibitor 7-BIA alleviated CCI-induced neuropathic pain while upregulating STING and IFN-α in the DRG. Treatment with H-151, a STING inhibitor, abolished the analgesic effects of PTPRD knockdown. Taken together, our study suggests that increased levels of PTPRD in the DRG following CCI are involved in the development of neuropathic pain *via* the STING-IFN-I pathway. 7-BIA, a small molecule inhibitor of PTPRD with anti-addiction effects, may represent a novel and safe therapeutic strategy for the clinical management of neuropathic pain without the risk of addiction.

Keywords: protein tyrosine phosphatase receptor type D, neuropathic pain, chronic constriction injury, stimulator of interferon genes, type I interferon

Edited by:
Biqin Lai,
Sun Yat-sen University, China

Reviewed by:
Guang-Yin Xu,
Soochow University, China
Wolfgang Liedtke,
Regeneron Pharmaceuticals, Inc.,
United States

****Correspondence:***
Rangjuan Cao
caorj@jlu.edu.cn
Shusen Cui
cuiss@jlu.edu.cn

Specialty section:
This article was submitted to Neuroplasticity and Development, a section of the journal Frontiers in Molecular Neuroscience

Received: *21 January 2022*
Accepted: *28 February 2022*
Published: *14 April 2022*

Citation:
Sun C, Wu G, Zhang Z, Cao R and Cui S (2022) Protein Tyrosine Phosphatase Receptor Type D Regulates Neuropathic Pain After Nerve Injury via the STING-IFN-I Pathway.
Front. Mol. Neurosci. 15:859166.
doi: 10.3389/fnmol.2022.859166

INTRODUCTION

Neuropathic pain is a type of chronic pain caused by injury or dysfunction of the somatosensory system and can dramatically influence the quality of the life of affected patients (Baron et al., 2010; Cohen and Mao, 2014; Braden et al., 2020). Neuropathic pain is estimated to constitute a fifth of all chronic pain cases (Fillingim et al., 2016; Bouhassira, 2019). Diabetes, nerve compression, infection, or trauma, neuroma, and autoimmune diseases causing ectopic neural activity in the dorsal root ganglion (DRG) or dorsal horn of the spinal cord may induce neuropathic pain (Cohen and Mao, 2014; Wang et al., 2018; Dai et al., 2020). A number of previous studies investigating the mechanisms underlying neuropathic pain (Campbell and Meyer, 2006; Bannister et al., 2020) indicated that the DRG plays a vital role in the progression of neuropathic pain in the peripheral nerve system (Berta et al., 2017). Following peripheral nerve injury, a series of pathological changes involved in sensitization of nociceptive pathways occur in the DRG, including activation of ion channels, glial, and immune cells (Scholz and Woolf, 2007; Yeh et al., 2020; Finnerup et al., 2021). Treatment of neuropathic pain remains a challenge, as patients often only experience insufficient pain relief. This might be due to a heterogeneity of chronic neuropathic pain mechanisms. Additionally, some patients prescribed opioids such as morphine exhibit severe side effects, including drug addiction (Cooper et al., 2017). Therefore, novel satisfactory treatment options for the clinical management of neuropathic pain are urgently required.

Protein tyrosine phosphatase receptor type D (PTPRD), a member of the leukocyte common antigen-related receptor (LAR) family located on human chromosome 9, was first discovered in 1990 (Krueger et al., 1990). PTPRD is a transmembrane protein with extracellular immunoglobulin and fibronectin domains and contributes to cell adhesion and synaptic specificity (Pulido et al., 1995; Song et al., 2016). Previous studies have shown that PTPRD may be involved in several disorders of the central nervous system, including Alzheimer's disease, mood lability, restless legs syndrome, and vulnerability to addiction (Wang and Bixby, 1999; Ensslen-Craig and Brady-Kalnay, 2004; Vellieux and d'Ortho, 2020). Inhibition of the phosphatase activity of PTPRD has previously been shown to reduce addiction to cocaine (Uhl et al., 2018), suggesting that PTPRD could represent a therapeutic target for addiction disorders.

Interestingly, PTPRD is also significantly upregulated in DRGs following chronic constriction injury (CCI) in rats (Cao et al., 2019; Sun et al., 2020). CCI represents a classical model for neuropathic pain, following which animals exhibit hypersensitivity to mechanical and thermal stimuli (Decosterd and Woolf, 2000; Challa, 2015; Gopalsamy et al., 2019; Guida et al., 2020). Despite initial insights into an upregulation of PTPRD in DRGs following CCI, the temporal dynamics of expression changes and whether PTPRD was involved in development and onset neuropathic pain remained unknown. In this study, we found that PTPRD expression gradually increased in DRG after CCI in mice, consistent with previous reports in rats, and PTPRD upregulation coincided with the onset of hypersensitivity. PTPRD inhibition using shRNA or small molecule inhibitor 7-butoxy illudalic acid analog (7-BIA) ameliorated neuropathic pain which suggested that PTPRD played a key role in mediating neuropathic pain following nerve injury. As PTPRD has previously been identified as a target for addiction treatment, our study suggests that it may represent a safe analgesic therapeutic strategy for the clinical management of neuropathic pain with low addiction risk.

MATERIALS AND METHODS

Animals

All animal experiments were approved by the Institutional Animal Care and Use Committee in Jilin University and complied with relevant ethical guidelines. C57BL/6 male mice weighing 18–20 g were purchased from the Animal Centre of Jilin University. All mice were housed at 25°C in a humidity-controlled room on a 12 h light–dark cycle with *ad libitum* to food and water. Experiments were conducted on mice aged between 8 and 12 weeks old. Animals were randomly assigned to a treatment group and were allowed to acclimatize to experimental conditions for 3 days before the experiments.

Reagents and Drug Delivery

Our study used H-151 (10 nM, MedChemExpress, HY-112693) and 7-BIA (10 or 20 mg/kg, MedChemExpress, HY-115496). Both reagents (H-151, 7-BIA) were diluted in 10% DMSO and 90% corn oil. H-151 was administered *via* intrathecal injection. All intrathecal injections were performed under brief anesthesia induced by isoflurane. Briefly, a small area was shaved on the back of the animal and a spinal puncture was carried out at L4–L5 using a microsyringe needle to deliver a maximum of 10 μl reagents into the subarachnoid space. A tail movement confirmed a successful intrathecal injection. 7-BIA was administrated by intraperitoneal injection.

Chronic Constriction Injury

The CCI neuropathic pain model was induced in 8- to 10-week-old male C57 mice under isoflurane anesthesia, as previously described (Bennett and Xie, 1988; Gopalsamy et al., 2019). Briefly, the right thigh was shaved and sterilized with iodophor. A transverse incision was made under the long head of the biceps femoris and the sciatic nerve was exposed *via* blunt dissection. Under a microscope, three ligatures (8-0 Prolene) were placed around the sciatic nerve 1 mm apart from proximal to the trifurcation. Ligatures were loosely tied to prevent an arrest of the epineural blood flow. In the sham group, the same procedure was performed without ligation of the sciatic nerve.

Behavioral Testing in Mice

All sensory behavioral testing in mice was performed between 9 am and 6 pm in an isolated experimental room maintained at 21–25°C. Mice were placed in the experimental room at least 3 day prior to baseline behavioral testing and all tests were performed by the same experimenter who was blinded to treatment. To assay mechanical sensitivity, the paw withdrawal threshold (PWT) of the hind paw was recorded using a series of von Frey filaments (from 0.16 to 2.0 g, Aesthesio, UGO) by perpendicular stimulation of the central plantar surface of the paw at resting state. A positive response was recorded if the paw was sharply withdrawn. To test the 50% PWT, we used the up–down method, as previously described (Michaelidou et al., 2013). Typically, 0.16 g filaments do not elicit paw withdrawal in mice and were used to test the paw withdrawal frequency (PWF). Mice were repeatedly stimulated 10 times, in 1 min intervals (Aesthesio, UGO).

To assay temperature sensitivity, thermal paw withdrawal latency (PWL) was assessed using a hot plate (BIO-CHP-ER, Bioseb). Briefly, the mice were placed on a 52°C metallic plate surrounded by an acrylic container. A sensory response was recorded by flinching, licking one of the hind paws, or jumping.

The test was stopped if the paw was not withdrawn within 20 s. The hot plate test was repeated three times for each mouse, with at least 20 min intervals between each repetition.

Motor coordination was evaluated by rotarod testing (Panlab, LE8505), as previously described (Bohlen et al., 2009). Rotarods were accelerated from 4 to 40 rpm over 300 s. Over the course of 3 days, each mouse underwent three trials per day separated by 15 min intervals. The fall latency was recorded on the third day.

Lentiviral Transduction

Two different target shRNAs were designed using BLOCK-iT^{TM} RNAi Designer and cloned into the lentiviral EGFP-expressing PLL3.7 plasmid. The shRNA sequences were as follows: shPTPRD1, 5′-GGTTCAGATGACTCCGGTTAC-3′; shPTPRD2, 5′-GGTTGAAAGCAAATGATAA-3′. For lentiviral packaging, plasmids containing shRNAs (including shRNAs against PTPRD and scrambled shRNA) were transfected into the packaging cell line 293T with the packaging plasmid psPAX2 (#12260, Addgene) and the envelop plasmid pMD2.G (#12259, Addgene) at a ratio of 4:3:1. Viruses were harvested 48 or 72 h later by filtering cell lysates with 0.45 μm filters (Millipore) followed by ultracentrifugation for 4 h at 25,000 rpm (Beckman SW28 rotor) and resuspension in phosphate-buffered saline (PBS, 50 μl). The efficiency of the two shRNAs in 293T cells was tested using quantitative real-time PCR (qRT-PCR) and Western blotting.

Dorsal Root Ganglion Injection

DRG injections were performed as previously described (Fischer et al., 2011). L4 and L5 vertebrae were exposed by a 2 cm longitudinal incision and blunt dissection of multifidus and longissimus lumborum muscles. The processus accessorius and parts of the left processus transversus were removed to expose L4/L5 DRGs. The spinal column was fixed in a stereotaxic frame and lentiviruses (300 nL for each DRG) were injected at 30 nL/min using a 36 G NanoFil needle on a NanoFil syringe, controlled by a micropump (World Precision Instruments, Sarasota, FL, United States).

Immunohistochemistry

Mice were deeply anesthetized with isoflurane and perfused *via* injection of 20 mL PBS followed by 4% paraformaldehyde (PFA) into the ascending aorta. After perfusion, L–L5 DRGs were removed and fixed in the pre-cooled 4% PFA. DRG samples were dehydrated in a 30% sucrose solution, and 12 μm transverse sections were cut using a cryostat microtome (CM1950, Leica, Germany). After washing sections three times in PBS, tissues were permeabilized in 1% Triton X-100 at room temperature and blocked with 5% BSA in PBS containing 0.5% Tween 20 (PBS-T). Samples were incubated with the following primary antibodies overnight at 4°C: rabbit anti-PTPRD (1:200; Novus, NBP2-94767), rabbit anti-NeuN (1:100, CST, D4G40), mouse anti-Tuj1 (1:1000, Abcam, 2G10), mouse anti-S100β (1:1000, Sigma, S2532), or mouse anti-GFAP (1:200, Abmart, MB0345S). The following day, sections were washed three times in PBS-T, and primary antibodies were visualized using secondary antibodies labeled with Alexa-488 and Alexa-546 (1:800; Invitrogen). Fluorescence (DM4B, Leica, Germany) and laser scanning confocal microscopes (A1HD25, Nikon, Japan) were used to capture images.

Western Blotting

Mice were deeply anesthetized with isoflurane and L4–L5 DRGs were dissected and placed in RIPA assay lysis buffer (C50008, Sangon Biotech). Protein concentration was measured using a bicinchoninic acid (BCA) assay (P0010, Beyotime Biotechnology, China). Proteins were separated by 10% SDS-PAGE and transferred onto PVDF membranes. PVDF membranes were blocked for 90 min at room temperature using 5% BSA in TBS-T and subsequently probed with the following primary antibodies at 4°C overnight: rabbit anti-PTPRD (1:1000, Novus, NBP2-94767), rabbit anti-STING (1:1000, CST, D2P2F), or mouse anti-GAPDH (1:1000, TransGen Biotech). The membranes were subsequently incubated with horseradish peroxidase (HRP)-conjugated secondary antibodies (1:1000, Beyotime) for 120 min at room temperature. Finally, images were acquired using a GS800 Densitometer Scanner. The optical density of protein bands was quantified using ImageJ, with GAPDH used as the loading control to normalize protein expression levels. Each experiment was repeated three times.

Quantitative Real-Time PCR Analysis

Total RNA from L4 to L5 DRGs or cells was extracted using the Eastep^{TM} Super Total RNA Extraction Kit (LS1040, Promega), and cDNA was synthesized using the Tranc-Script One-Step cDNA Synthesis SuperMix (AT311, TransGen Biotech, China). Primers (shown in **Supplementary Table 1**) were synthesized by Genewiz Biotech. For PCR reactions, the TB Green^{TM} Premix Ex Taq^{TM} (RR420A, TaKaRa) mix was used. PCR reactions were carried out on a Real-Time PCR System (CFX96, Bio-Rad, United States), and the $2^{-\Delta\ \Delta\ Ct}$ method was used to calculate relative mRNA expression. mRNA levels were normalized to *Gapdh*.

Enzyme-Linked Immunosorbent Assay

Levels of inflammatory cytokines IL-6, IL-1β, TNF-α, IL-10, and IFN-α in DRG tissues were determined by enzyme-linked immunosorbent assay (ELISA) according to the manufacturer's instructions (Anoric Bio-technology Co., Ltd., Tianjin, China). Absorbance at 450 nm was measured using a microplate reader (Thermo Fisher K3, United States). Each experiment was performed three times.

Statistical Analysis

Statistical analysis was performed using SPSS 21.0 for windows (SPSS, Inc., Chicago, IL, United States). All data are presented as mean ± SEM. Behavioral data were analyzed using two-way ANOVAs followed by *post hoc* Tukey's tests to compare multiple groups. Unpaired Student's *t*-tests were used for comparisons between two groups. All experiments were performed at least three times independently. *P*-values less than 0.05 were considered statistically significant. Asterisks correspond to the following significance levels: $^{*}p < 0.05$, $^{**}p < 0.01$, $^{***}p < 0.001$.

RESULTS

Protein Tyrosine Phosphatase Receptor Type D Expression Is Increased in DRGs After Chronic Constriction Injury

RNA sequencing (RNA-seq) experiments previously indicated that PTPRD is upregulated in rat DRGs 14 days after CCI (Zhou et al., 2017; Cao et al., 2019; Sun et al., 2020). To confirm these findings in mice and further investigate the role of PTPRD in neuropathic pain, we established a mouse CCI model (**Figure 1A**). Behavioral testing confirmed that the hot plate test PWL was decreased after CCI surgery, indicating that the induction of the neuropathic pain model was successful. Likewise, von Frey filament tests demonstrated that the PWT decreased, while the PWF increased, from day 3 to day 21 after CCI surgery (**Figures 1B–D**). The above behavioral results indicated a successful induction of neuropathic pain in mice following CCI.

We next evaluated which cells in the DRG expressed PTPRD by co-staining sections from 7 days post CCI with PTPRD and astrocyte marker GFAP, satellite glial cell marker S100β, or neuronal marker Tuj1. This revealed that PTPRD was exclusively expressed in DRG neurons (**Figure 1E**).

To investigate the temporal dynamics of PTPRD expression in more detail, we conducted immunohistochemical staining on sections collected before surgery (day 0) and on days 1, 3, 7, and 14 after CCI surgery. PTPRD exhibited only low expression in the uninjured DRG (before surgery), but expression significantly increased by day 7 and 14 after CCI (**Figure 2A**). We next validated our immunohistochemistry results by Western blotting. Western blotting indicated that PTPRD expression was slightly elevated by day 3 and significantly increased by days 7 and 14 after CCI (**Figures 2B,C**). Importantly, the expression of PTPRD in contralateral DRGs did not change and was maintained at basal levels for each timepoint we evaluated (**Figures 2D,E**). These results suggested a potential correlation between elevated PTPRD protein levels and the onset of neuropathic pain.

Knockdown of Protein Tyrosine Phosphatase Receptor Type D Ameliorates Chronic Constriction Injury-Induced Neuropathic Pain

To confirm whether PTPRD participated in the development neuropathic pain following CCI, we generated lentiviruses containing one of two PTPRD-targeting shRNAs (shPTPRD-1 and shPTPRD-2) or a control shRNA (shCtrl). The silencing efficiency of the two shPTPRDs was assessed by qRT-PCR (**Supplementary Figure 1A**) and Western blotting (**Supplementary Figures 1B,C**), and shPTPRD-2 was chosen for subsequent experiments as it performed better. Viruses containing shCtrl or shPTPRD-2 (shPTPRD in short hereafter) were injected into L4-L5 DRGs. DRGs were isolated and stained 14 days after transfection, which revealed that the majority of NeuN$^+$ DRG neurons were successfully transfected (**Figure 3A**). qRT-PCR confirmed an *in vivo* PTPRD mRNA silencing efficiency of 75.11 ± 2.55% (**Figure 3B**). The silencing ability of shPTPRD was further tested by Western blotting, which showed a 46.83 ± 4.12% decrease in PTPRD protein levels (**Figures 3C,D**). These results showed that the lentiviral shRNA delivery successfully knocked down RNA and protein levels of PTPRD in DRG tissues *in vivo*.

We next went on to assess the impact of PTPRD knockdown on development of neuropathic pain. Fourteen days before CCI, baseline performance (BL) in the von Frey and heat plate tests was recorded, after which lentiviruses containing shRNAs were administered. After injection, mice were allowed to recover for 14 days. Behavioral tests were then again conducted prior to CCI surgery (day 0) or 1, 3, 5, 7, 14, and 21 days after surgery (**Figure 3E**). shPTPRD did not influence mechanical or thermal sensitivity prior to CCI, with animals showing similar PWT, PWL, and PWF compared to shCtrl-injected animals 14 days after lentiviral injection, which suggested that PTPRD did not participate in modulating or inducing neuropathic pain under physiological condition. In the shCtrl group, mechanical and thermal hypersensitivity were observed as early as 1 day after CCI and lasted for 21 days, when animals were sacrificed. Conversely, PTPRD silencing significantly attenuated mechanical and thermal hypersensitivity (**Figures 3F–H**). Knockdown of PTPRD did not alter motor behaviors (**Supplementary Figure 2A**). The above results suggested that upregulation of PTPRD participated in the development of neuropathic pain following CCI in mice.

Protein Tyrosine Phosphatase Receptor Type D Knockdown Increases IFN-α Levels in the Dorsal Root Ganglion After Chronic Constriction Injury

We subsequently aimed to investigate the molecular mechanism through which PTPRD contributed to the development of neuropathic pain. Previous studies suggested that inflammation and the balance of pro- and anti-inflammatory cytokines play an important role in regulating neuropathic pain in injured nerves (Xu et al., 2018; Zheng et al., 2019). We hypothesized that the amelioration of neuropathic pain following PTPRD knockdown in CCI mice was associated with changes in neuroinflammation. To test this hypothesis, we evaluated levels of multiple inflammatory cytokines 7 days after CCI using ELISA (**Figure 4A**). DRG levels of IL-6, IL-1β, TNF-α, and IL-10 were not significantly altered following PTPRD knockdown (**Figures 4B–E**). Conversely, levels of IFN-α were significantly increased (**Figure 4F**) compared to shCtrl DRGs. These results were confirmed by qRT-PCR (**Figure 4G**). Based on this finding, we aimed to determine how PTPRD was involved in the regulation of IFN-α expression in the DRG after CCI. Previous reports have described that mitochondrial antiviral signaling protein (MAVs), acid-inducible gene I (RIG-I), stimulator of interferon genes (STING), Toll-like receptor-7 (TLR-7), and Toll/IL-1 receptor domain-containing adaptor (TRIF) can promote the release of IFN-1. We therefore assessed mRNA levels of these potential upstream regulators by qRT-PCR and found that the expression of STING, but not MAVs, RIG-1, TLR-7, or TRIF, was increased after PTPRD knockdown

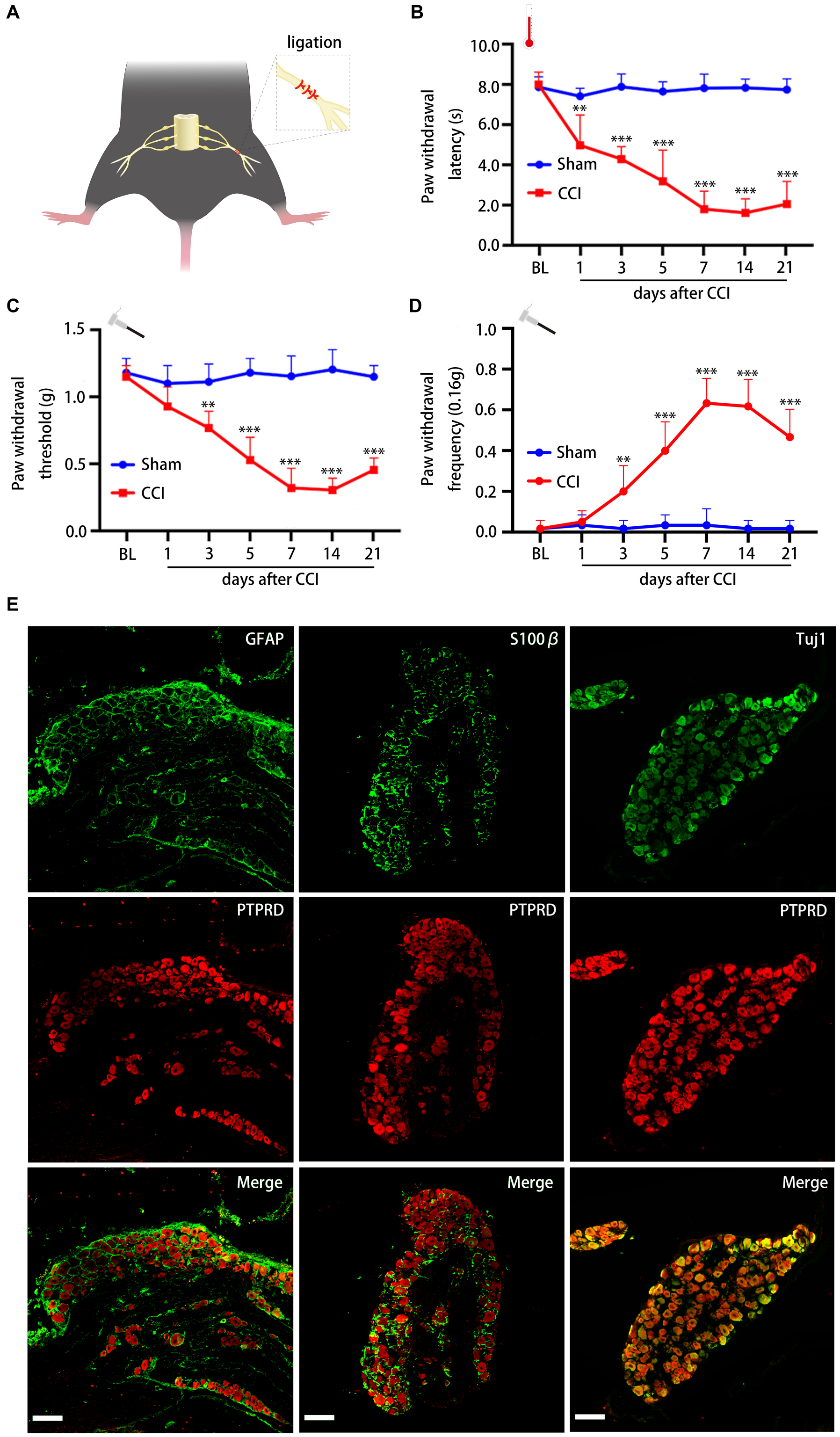

FIGURE 1 | Chronic constriction injury induces neuropathic pain and PTPRD is expressed in DRG neurons. **(A)** Schematic overview of the CCI-induced neuropathic pain model. **(B–D)** Paw withdrawal latency (PWL), paw withdrawal threshold (PWT), and paw withdrawal frequency (PWF) before the surgery (BL) and 1, 3, 5, 7, 14, and 21 days after CCI. $N = 6$ mice per group, $^{**}p < 0.01$, $^{***}p < 0.001$. **(E)** Representative images of PTPRD co-staining with GFAP, S100β, or Tuj1 in DRG sections 7 days after CCI. Scale bars, 100 μm. Statistical comparisons were performed by two-way ANOVA with Tukey's *post hoc* test **(B–D)**.

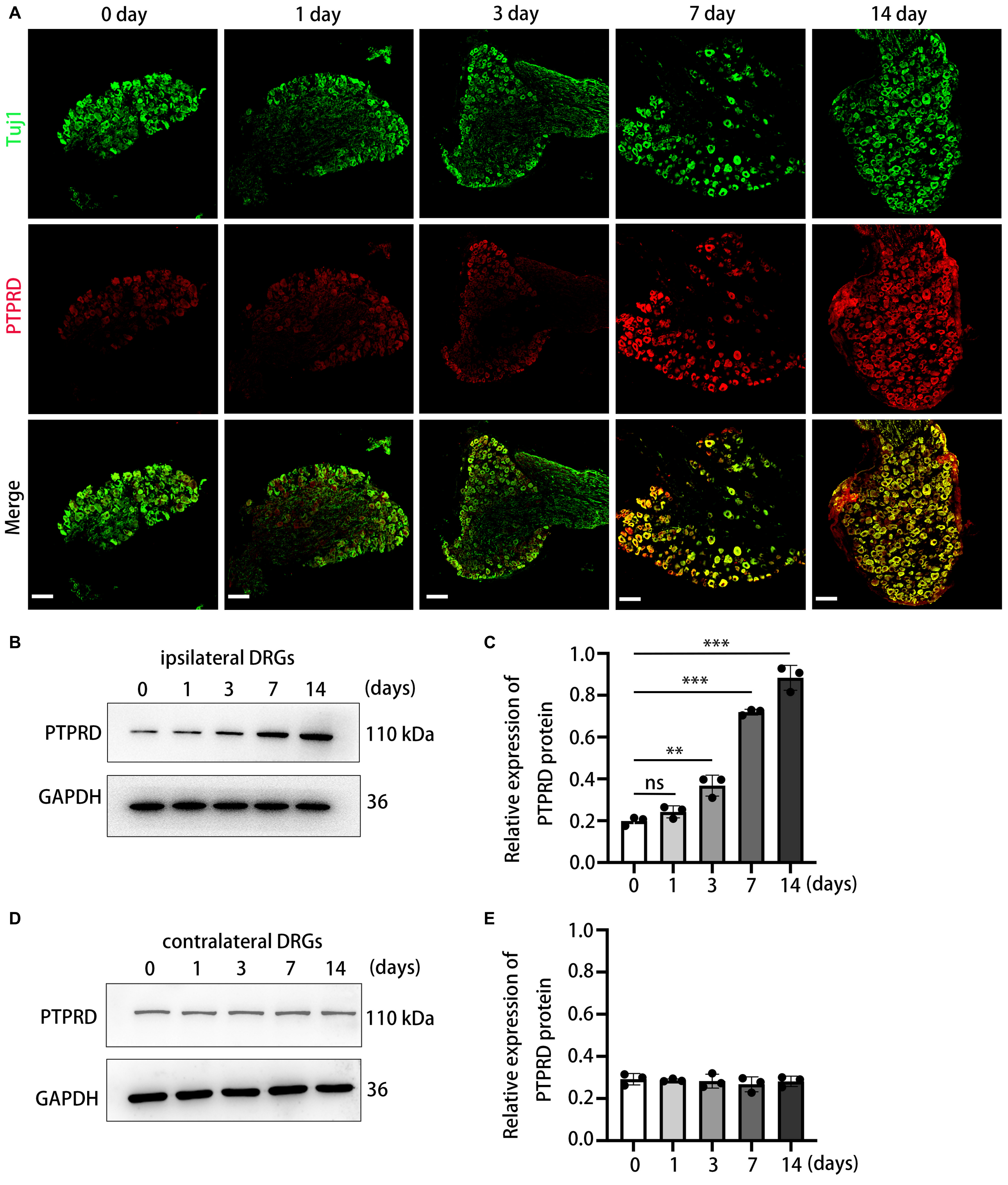

FIGURE 2 | Protein tyrosine phosphatase receptor type D expression levels are increased in the DRG after CCI. **(A)** Representative images of DRG sections stained for PTPRD (red) and Tuj1 (green) in the indicated groups. Scale bars, 100 μm. **(B)** Western blot of PTPRD levels in ipsilateral DRGs (L4–L5) at 0, 1, 3, 7, and 14 days after CCI. Each experiment was repeated three times. **(C)** Quantitative analysis of data in **(B)**. $N = 3$, $^{**}p < 0.01$, $^{***}p < 0.001$. **(D)** Western blot of PTPRD levels in contralateral DRGs (L4–L5) at 0, 1, 3, 7, and 14 days after CCI. Each experiment was repeated three times. **(E)** Quantitative analysis of data in **(D)**. $N = 3$, $p > 0.05$. Statistical comparisons were performed by unpaired Student's *t*-test **(C,E)**.

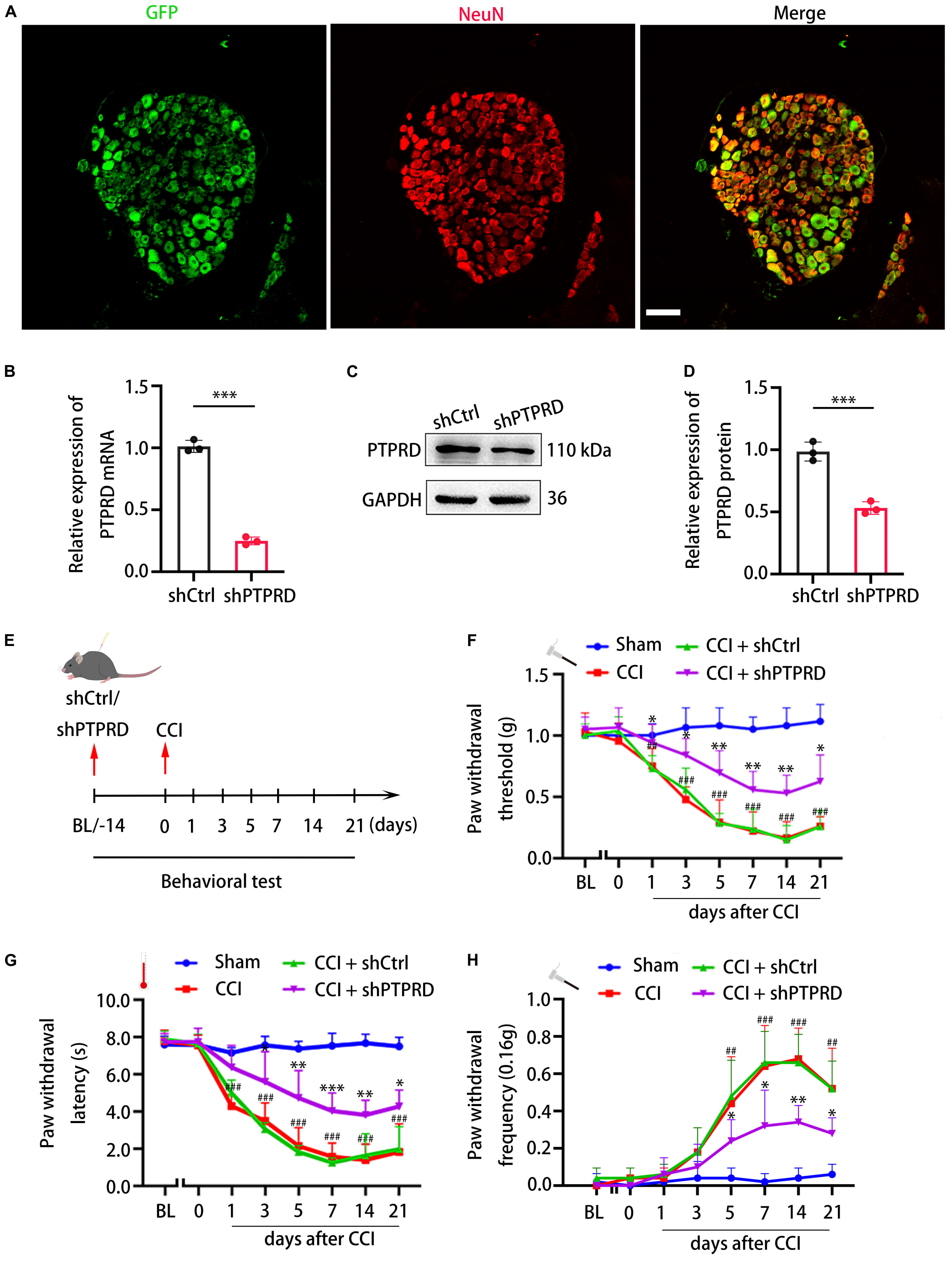

FIGURE 3 | Protein tyrosine phosphatase receptor type D knockdown attenuates neuropathic pain following CCI. **(A)** Representative images of GFP (green) and NeuN staining (red) 14 days after shPTPRD injection in the DRG. Scale bar, 100 μm. **(B)** qRT-PCR analysis of the relative expression of PTPRD in DRGs transfected with shCtrl or shPTPRD after CCI. $N = 3$, $^{***}p < 0.001$. **(C)** Western blot of PTPRD in DRG tissues transfected with shCtrl or shPTPRD after CCI. Each experiment was repeated three times. **(D)** Quantitative analysis of data in **(C)**. GAPDH served as the loading control. $N = 3$, $^{***}p < 0.001$. **(E)** Schedule of lentivirus administration, surgery, and behavioral testing. **(F–H)** Paw withdrawal threshold, paw withdrawal latency, and paw withdrawal frequency prior to virus injection (BL), on the day of surgery, or 1, 3, 5, 7, 14, and 21 days after CCI. $N = 6$ mice per group. CCI + shPTPRD vs. CCI + shCtrl, $^{*}p < 0.05$, $^{**}p < 0.01$, $^{***}p < 0.001$. CCI vs. sham, $^{\#}p < 0.05$, $^{\#\#}p < 0.01$, $^{\#\#\#}p < 0.001$. Statistical comparisons were performed using unpaired Student's *t*-test **(B,D)** or two-way ANOVA with Tukey's *post hoc* test **(F–H)**.

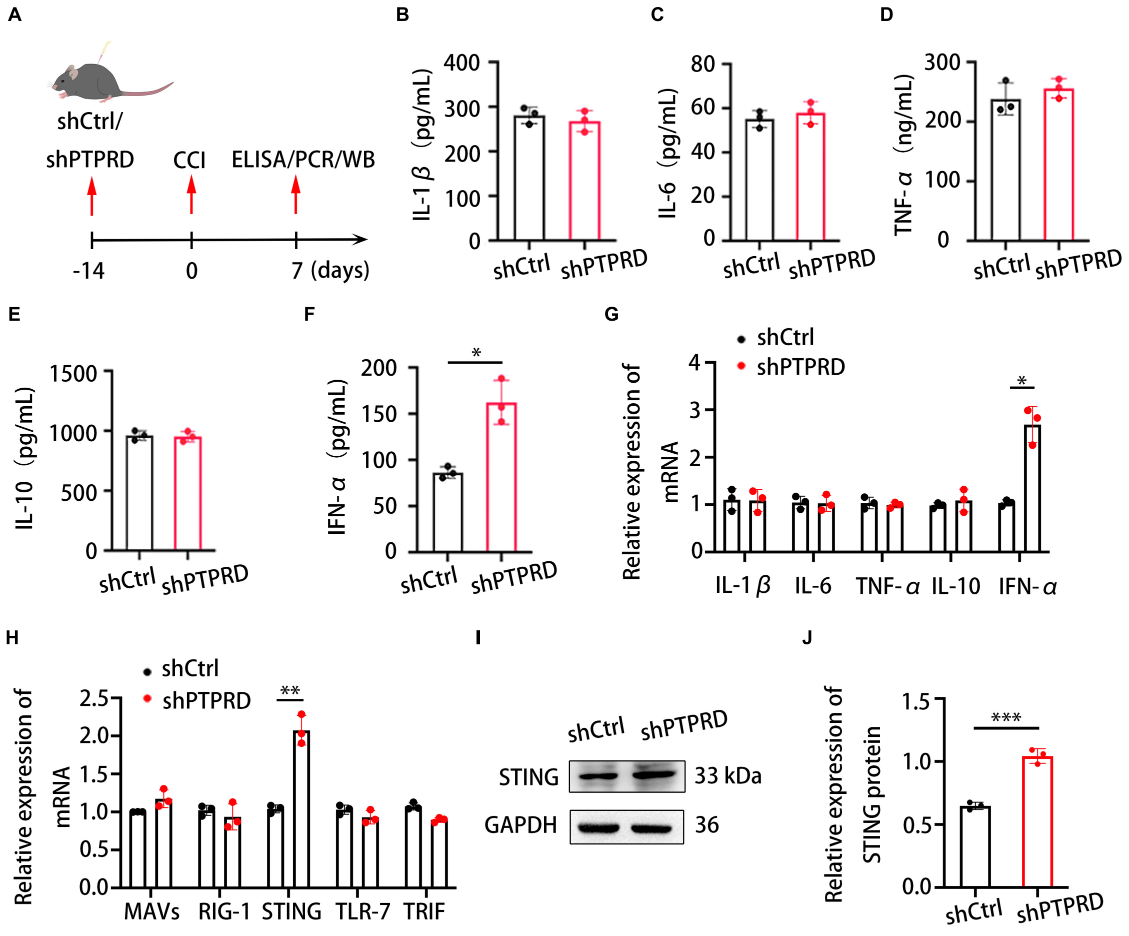

FIGURE 4 | Protein tyrosine phosphatase receptor type D knockdown increases IFN-α and STING levels in the DRG after CCI. **(A)** Schedule of lentivirus administration, surgery, ELISA, qRT-PCR, and Western blotting. **(B–F)** ELISA assessing IL-1β, IL-6, TNF-α, IL-10, and IFN-α levels in the DRG after shCtrl or shPTPRD virus injection. CCI + shPTPRD vs. CCI + shCtrl, *N* = 3. For IFN-α, $*p < 0.05$. **(G)** qRT-PCR analysis of the relative expression of IL-1β, IL-6, TNF-α, IL-10, and IFN-α in the DRG after shCtrl or shPTPRD virus injection. CCI + shPTPRD vs. CCI + shCtrl, *N* = 3. For IFN-α, $*p < 0.05$. **(H)** qRT-PCR analysis of the relative expression of MAVS, RIG-1, STING, TLR-7, and TRIF in the DRG after shCtrl or shPTPRD administration. CCI + shPTPRD vs. CCI + shCtrl, *N* = 3. For STING, $**p < 0.01$. **(I)** Western blot evaluation of the DRG levels of STING after shCtrl or shPTPRD treatment. Experiment was repeated three times. **(J)** Quantitative analysis of data in **(H)**. CCI + shPTPRD vs. CCI + shCtrl, *N* = 3, $***p < 0.001$. Statistical comparisons were performed by unpaired Student's *t*-test **(B–H,J)**.

(**Figure 4H**). Consistently, Western blotting also demonstrated an enhanced protein expression of STING in shPTPRD DRGs (**Figures 4I,J**).

Protein Tyrosine Phosphatase Receptor Type D Regulates Chronic Constriction Injury-Induced Neuropathic Pain *via* the STING-IFN-I Pathway

To confirm whether the development of neuropathic pain caused by PTPRD was mediated *via* the STING-IFN-I pathway, we intrathecally administered animals with the STING-specific palmitoylation inhibitor H-151 at 7 days after CCI, when hypersensitivity had typically already improved in PTPRD knockdown mice (**Figure 5A**). As early as 4 h after the injection, the attenuation of hypersensitivity in shPTPRD animals was reversed and no differences in PWT, PWL, and PWF were observed between the control and shPTPRD + H-151 groups. This effect lasted for 48 h (**Figures 5B–D**). Therefore, H-151 administration disrupted the increased expression and secretion of IFN-α (**Figures 5E,F**), suggesting that PTPRD mediated neuropathic pain *via* the STING-IFN-I pathway in mice following CCI.

Protein Tyrosine Phosphatase Receptor Type D Inhibitor 7-Butoxy Illudalic Acid Analog Alleviates Neuropathic Pain in Mice Following Chronic Constriction Injury

7-Butoxy illudalic acid analog is a small molecule drug recently synthesized to specifically target PTPRD as part of addiction therapy. Here, we investigated whether 7-BIA could also serve as a treatment for neuropathic pain. Seven days after CCI

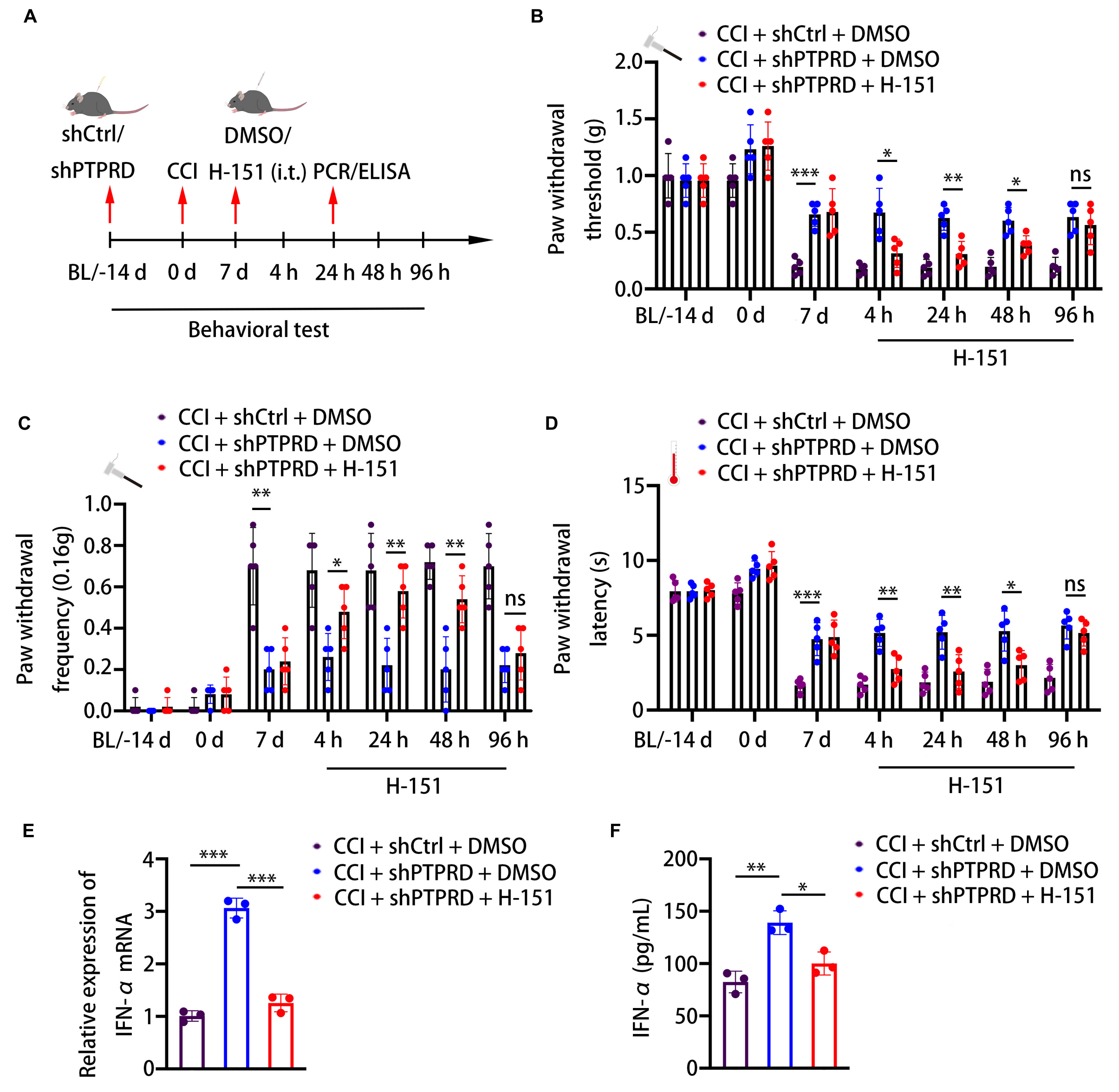

FIGURE 5 | Protein tyrosine phosphatase receptor type D regulates CCI-induced neuropathic pain *via* the STING-IFN-α pathway. **(A)** Schedule of the virus injection, surgery, STING inhibitor (H-151, 10 nM, i.t.) administration, behavioral testing, qRT-PCR, and ELISA. **(B–D)** Paw withdrawal threshold, paw withdrawal latency, and paw withdrawal frequency before virus injection (BL), the day of surgery, 7 days after the surgery, or 4, 24, 48, and 96 h after H-151 treatment. $N = 5$ mice per group, $^{*}p < 0.05$, $^{**}p < 0.01$, $^{***}p < 0.001$. **(E)** qRT-PCR analysis of the relative expression of IFN-α. $N = 3$, $^{***}p < 0.001$. **(F)** ELISA analysis of the expression of IFN-α. $N = 3$, $^{*}p < 0.05$, $^{**}p < 0.01$. Statistical comparisons were performed using two-way ANOVA with Tukey's *post hoc* test **(B–D)** or unpaired Student's *t*-test **(E,F)**.

surgery, we intraperitoneally (i.p.) administered 7-BIA at 10 and 20 mg/kg and performed behavioral testing at 1.5, 6, 24, and 48 h after injection (**Figure 6A**). 7-BIA elicited a dose-dependent analgesic effect in CCI mice as early as 1.5 h after i.p. injection and lasted for 24 h, reducing both mechanical and thermal sensitivity (**Figures 6B–D**). Additionally, 7-BIA treatment resulted in increased DRG IFN-α levels after CCI (**Figure 6E**) as well as significantly increased protein levels of STING in the DRG (**Figures 6F,G**). Animals exhibited no changes in motor coordination (**Supplementary Figure 2B**). Together, these results suggested that PTPRD might be involved in the development of neuropathic pain, and its specific small molecule inhibitor 7-BIA could represent a novel and safe treatment for the clinical management of neuropathic pain without addiction risk.

DISCUSSION

Previous studies have reported an involvement of PTPRD in various central nervous system disorders, including addiction (Baron et al., 2010; Cohen and Mao, 2014), but there have been few reports on the role of PTPRD in the peripheral

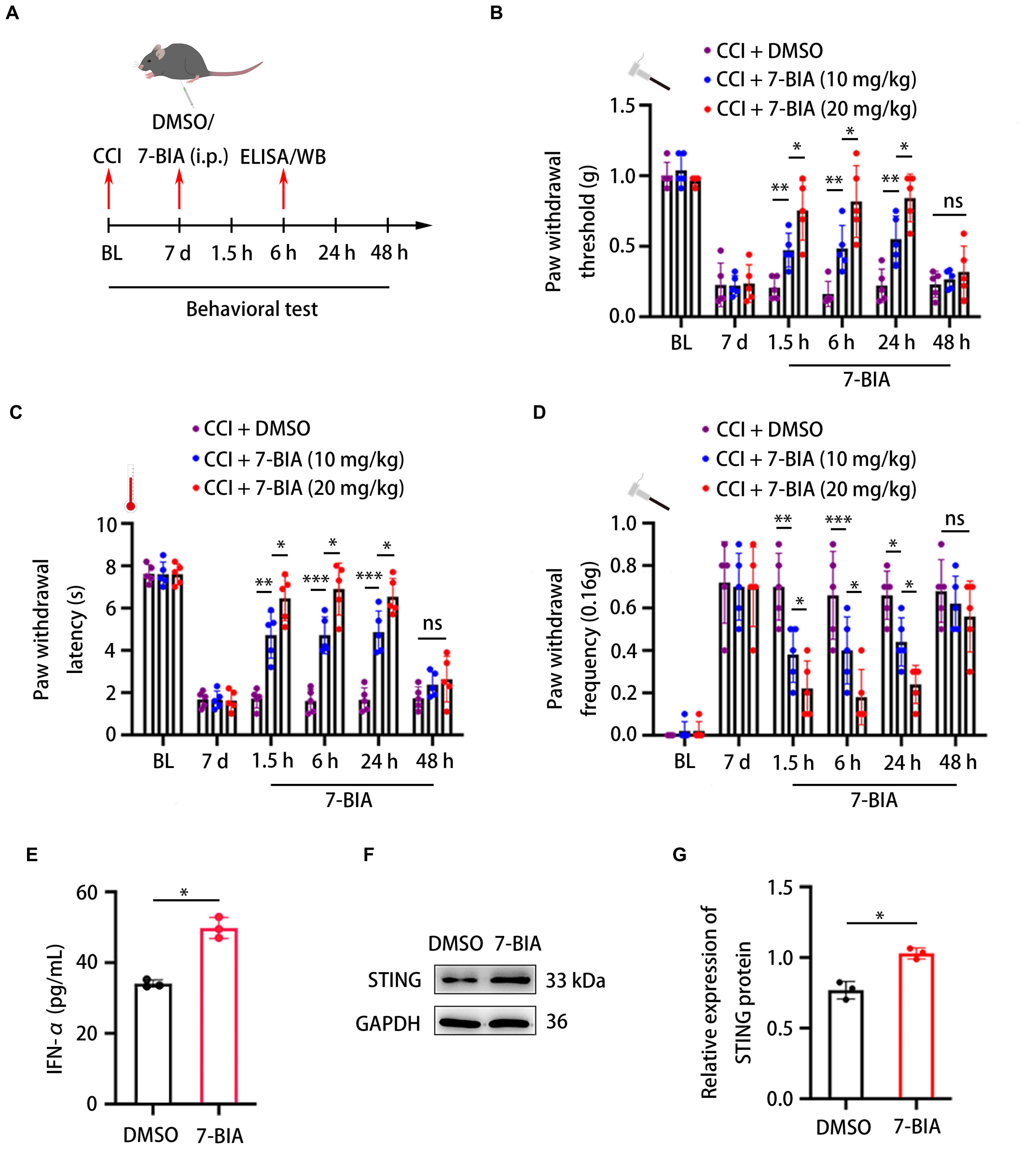

FIGURE 6 | Protein tyrosine phosphatase receptor type D inhibitor 7-BIA alleviates neuropathic pain in mice following CCI. **(A)** Schedule of surgery, 7-BIA treatment (10 or 20 mg/kg, i.p.), behavioral testing, ELISA, and Western blotting. **(B–D)** Paw withdrawal threshold, paw withdrawal latency, and paw withdrawal frequency before CCI (BL), 7 days after the surgery, or 1.5, 6, 24, and 48 h after 7-BIA treatment. $N = 5$ mice per group, $^{*}p < 0.05$, $^{**}p < 0.01$, $^{***}p < 0.001$. **(E)** ELISA analysis of the expression of IFN-α in the DRG after treatment with 7-BIA or DMSO. CCI + 7-BIA vs. CCI + DMSO, $N = 3$, $^{*}p < 0.05$. **(F)** Western blot analysis of the expression of STING in DRGs treated with 7-BIA or DMSO. Experiment was repeated three times. **(G)** Quantitative analysis of data in **(F)**. CCI + 7-BIA vs. CCI + DMSO, $N = 3$, $^{*}p < 0.05$. Statistical comparisons were performed using two-way ANOVA with Tukey's *post hoc* test **(B–D)** or unpaired Student's *t*-test **(E,G)**.

nervous system. A previous RNA-seq study found a significant upregulation of PTPRD 14 days after induction of a chronic pain model in rats, but it remained unknown whether this change in expression was biologically meaningful and whether PTPRD contributed to chronic neuropathic pain. In the present study, we found that PTPRD was typically located in the cytoplasm of Tuj1^{+} neurons in the DRG and confirmed a significant upregulation of PTPRD after CCI. Concomitantly with increased expression of PTPRD, we observed behavioral changes and found an increased sensitivity to mechanical and thermal stimuli, which suggested that PTPRD expression levels might be associated with the development of neuropathic pain following CCI. To confirm this hypothesis, we performed PTPRD knockdown using shRNA (shPTPRD) or the small molecule inhibitor 7-BIA, which revealed that a reduction of PTPRD levels following CCI effectively ameliorated neuropathic pain. Further investigating the mechanisms underlying the involvement of PTPRD in neuropathic pain, we found that PTPRD regulated this process *via* the STING-IFN-I pathway. Baseline PWT, PWL, and PWF levels were unaltered after PTPRD knockdown prior to CCI, but significantly increased (PWT, PWL) or reduced (PWF) after CCI surgery following shPTPRD treatment. DRG expression levels of PTPRD were low under physiological levels and therefore a knockdown may have had little influence on physiological function. Conversely, the analgesic effect was observed after CCI when expression of PTPRD was significantly upregulated and maintained at high levels. These results indicated that PTPRD might not participate in the regulation of pain sensitivity under physiological conditions, but instead was only involved in regulation of neuropathic pain following injury. There are many neuropathic pain models including surgical models like CCI, chemical pain models, and inflammatory pain models. Here, we investigated the role of PTPRD in the CCI-induced neuropathic pain, as CCI exhibits a similar pathophysiologic mechanism with carpal tunnel syndrome, which is the most common peripheral nerve chronic compression disease. However, it will be necessary to further test the function of PTPRD in other pain models in the later study.

Previous studies have shown that the development of neuropathic pain is closely related to neuroinflammation (Penas and Navarro, 2018; Yi et al., 2021). The expression of TNF-α, IL-6, and other pro-inflammatory factors in the DRG have been found to be increased after peripheral nerve injury (Sommer et al., 2018). Our results showed that IFN-α was significantly increased in DRG after both PTPRD knockdown or 7-BIA administration, while levels of IL-6, IL-1β, TNF-α, and IL-10 were not affected. IFN-α is a type I interferon which acts as an anti-inflammatory factor. Donnelly et al. (2021) previously found that intrathecal injection of IFN-α following CCI in mice prevented mechanical and thermal hypersensitivity. While these results indicated that PTPRD might regulate neuropathic pain *via* IFN-α. PTPRD is a phosphatase that is not thought to directly regulate the release of IFN-α. STING is a DNA receptor located in the intracellular endoplasmic reticulum (Rodero and Crow, 2016; Kwon and Bakhoum, 2020; Shi et al., 2021) and is involved in the regulation of IFN-α release in the DRG. Interestingly, the STING-IFN-I pathway has previously been shown to be a classic pathway involved in the regulation of neuropathic pain (Donnelly et al., 2021). We found that the expression of STING was significantly increased after either PTPRD knockdown or 7-BIA treatment, and therefore reasoned that PTPRD may influence IFN-α levels *via* STING. Further investigation of the relationship between PTPRD and STING will be of critical importance. PTPRD consists of an extracellular domain, a transmembrane protein structure, and an intracellular domain. The intracellular domain of PTPRD acts as a phosphatase which can lead to dephosphorylation of factors such as STAT3, PDGFRβ, and TBK1, amongst others (Tonks, 2006). Intriguingly, STING and TBK1 have been shown to form oligomers and STING can be phosphorylated by TBK1 (Bai and Liu, 2019). Based on these prior findings, we propose an indirect relationship between PTPRD and STING, for instance *via* TBK1, but this will need to be confirmed in future studies.

7-Butoxy illudalic acid analog is a small molecule drug targeting PTPRD that specifically inhibits the intracellular phosphatase activity of PTPRD (Uhl et al., 2018). Animal studies have confirmed the safety of 7-BIA, demonstrating repeated intraperitoneal injections were neither toxic nor addictive. Previous studies have shown that treatment of 7-BIA may relieve cocaine addiction in mice (Uhl et al., 2018). In our study, 7-BIA treatment significantly increased the PWT and PWL, while reducing the PWF following CCI in mice and exhibited an analgesic effect, consistent with results from PTPRD knockdown. The results of our study suggest that 7-BIA may represent a potential drug for the clinical management of neuropathic pain without addiction risk.

CONCLUSION

In conclusion, we found a critical role for elevated DRG PTPRD levels in the development of CCI-induced neuropathic pain in mice. Our results suggest that PTPRD knockdown improved neuropathic pain *via* the STING-IFN-I pathway. A small molecule-specific inhibitor of PTPRD, 7-BIA, effectively prevented hypersensitivity after CCI and may represent a novel therapeutic agent for clinical management of neuropathic pain.

DATA AVAILABILITY STATEMENT

The original contributions presented in the study are included in the article/**Supplementary Material**, further inquiries can be directed to the corresponding authors.

ETHICS STATEMENT

The animal study was reviewed and approved by the Institutional Animal Care and Use Committee of Jilin University.

AUTHOR CONTRIBUTIONS

CS and RC performed the main experiments, summarized the results, and wrote the manuscript. GW and ZZ analyzed the data. RC and SC provided the supervision and comments on the manuscript. All authors read and approved the final manuscript.

FUNDING

This work was supported by the Jilin Special Project of Health Researchers (2019SCZ002), Excellent Young Teacher Training Program of Jilin University, Jilin Scientific and Technological Development Program (20190905003SF), and Industrial Independent Innovation Capability Project of Jilin Development, and Reform Commission (2019C005).

SUPPLEMENTARY MATERIAL

The Supplementary Material for this article can be found online at: https://www.frontiersin.org/articles/10.3389/fnmol.2022.859166/full#supplementary-material

REFERENCES

Bai, J., and Liu, F. (2019). The cGAS-cGAMP-STING Pathway: a Molecular Link Between Immunity and Metabolism. *Diabetes* 68, 1099–1108. doi: 10.2337/dbi18-0052

Bannister, K., Sachau, J., Baron, R., and Dickenson, A. H. (2020). Neuropathic Pain: mechanism-Based Therapeutics. *Annu. Rev. Pharmacol. Toxicol.* 60, 257–274. doi: 10.1146/annurev-pharmtox-010818-021524

Baron, R., Binder, A., and Wasner, G. (2010). Neuropathic pain: diagnosis, pathophysiological mechanisms, and treatment. *Lancet Neurol.* 9, 807–819. doi: 10.1016/s1474-4422(10)70143-5

Bennett, G. J., and Xie, Y. K. (1988). A peripheral mononeuropathy in rat that produces disorders of pain sensation like those seen in man. *Pain* 33, 87–107. doi: 10.1016/0304-3959(88)90209-6

Berta, T., Qadri, Y., Tan, P. H., and Ji, R. R. (2017). Targeting dorsal root ganglia and primary sensory neurons for the treatment of chronic pain. *Expert Opin. Ther. Targets* 21, 695–703. doi: 10.1080/14728222.2017.1328057

Bohlen, M., Cameron, A., Metten, P., Crabbe, J. C., and Wahlsten, D. (2009). Calibration of rotational acceleration for the rotarod test of rodent motor coordination. *J. Neurosci. Methods* 178, 10–14. doi: 10.1016/j.jneumeth.2008.11.001

Bouhassira, D. (2019). Neuropathic pain: definition, assessment and epidemiology. *Rev. Neurol.* 175, 16–25. doi: 10.1016/j.neurol.2018.09.016

Braden, K., Giancotti, L. A., Chen, Z., DeLeon, C., Latzo, N., Boehn, T., et al. (2020). GPR183-Oxysterol Axis in Spinal Cord Contributes to Neuropathic Pain. *J. Pharmacol. Exp. Ther.* 375, 367–375. doi: 10.1124/jpet.120.000105

Campbell, J. N., and Meyer, R. A. (2006). Mechanisms of neuropathic pain. *Neuron* 52, 77–92. doi: 10.1016/j.neuron.2006.09.021

Cao, S., Yuan, J., Zhang, D., Wen, S., Wang, J., Li, Y., et al. (2019). Transcriptome Changes In Dorsal Spinal Cord Of Rats With Neuropathic Pain. *J. Pain Res.* 12, 3013–3023. doi: 10.2147/jpr.S219084

Challa, S. R. (2015). Surgical animal models of neuropathic pain: pros and Cons. *Int. J. Neurosci.* 125, 170–174. doi: 10.3109/00207454.2014.922559

Cohen, S. P., and Mao, J. (2014). Neuropathic pain: mechanisms and their clinical implications. *BMJ* 348:f7656. doi: 10.1136/bmj.f7656

Cooper, T. E., Chen, J., Wiffen, P. J., Derry, S., Carr, D. B., Aldington, D., et al. (2017). Morphine for chronic neuropathic pain in adults. *Cochrane Database Syst. Rev.* 5:Cd011669. doi: 10.1002/14651858.CD011669.pub2

Dai, W. L., Bao, Y. N., Fan, J. F., Li, S. S., Zhao, W. L., Yu, B. Y., et al. (2020). Levo-corydalmine attenuates microglia activation and neuropathic pain by suppressing ASK1-p38 MAPK/NF-κB signaling pathways in rat spinal cord. *Reg. Anesth. Pain Med.* 45, 219–229. doi: 10.1136/rapm-2019-100875

Decosterd, I., and Woolf, C. J. (2000). Spared nerve injury: an animal model of persistent peripheral neuropathic pain. *Pain* 87, 149–158. doi: 10.1016/s0304-3959(00)00276-1

Donnelly, C. R., Jiang, C., Andriessen, A. S., Wang, K., Wang, Z., Ding, H., et al. (2021). STING controls nociception *via* type I interferon signalling in sensory neurons. *Nature* 591, 275–280. doi: 10.1038/s41586-020-03151-1

Ensslen-Craig, S. E., and Brady-Kalnay, S. M. (2004). Receptor protein tyrosine phosphatases regulate neural development and axon guidance. *Dev. Biol.* 275, 12–22. doi: 10.1016/j.ydbio.2004.08.009

Fillingim, R. B., Loeser, J. D., Baron, R., and Edwards, R. R. (2016). Assessment of Chronic Pain: domains, Methods, and Mechanisms. *J. Pain* 17, T10–T20. doi: 10.1016/j.jpain.2015.08.010

Finnerup, N. B., Kuner, R., and Jensen, T. S. (2021). Neuropathic Pain: from Mechanisms to Treatment. *Physiol. Rev.* 101, 259–301. doi: 10.1152/physrev.00045.2019

Fischer, G., Kostic, S., Nakai, H., Park, F., Sapunar, D., Yu, H., et al. (2011). Direct injection into the dorsal root ganglion: technical, behavioral, and histological observations. *J. Neurosci. Methods* 199, 43–55. doi: 10.1016/j.jneumeth.2011.04.021

Gopalsamy, B., Sambasevam, Y., Zulazmi, N. A., Chia, J. S. M., Omar Farouk, A. A., Sulaiman, M. R., et al. (2019). Experimental Characterization of the Chronic Constriction Injury-Induced Neuropathic Pain Model in Mice. *Neurochem. Res.* 44, 2123–2138. doi: 10.1007/s11064-019-02850-0

Guida, F., De Gregorio, D., Palazzo, E., Ricciardi, F., Boccella, S., Belardo, C., et al. (2020). Behavioral, Biochemical and Electrophysiological Changes in Spared Nerve Injury Model of Neuropathic Pain. *Int. J. Mol. Sci.* 21:3396. doi: 10.3390/ijms21093396

Krueger, N. X., Streuli, M., and Saito, H. (1990). Structural diversity and evolution of human receptor-like protein tyrosine phosphatases. *EMBO J.* 9, 3241–3252. doi: 10.1002/j.1460-2075.1990.tb07523.x

Kwon, J., and Bakhoum, S. F. (2020). The Cytosolic DNA-Sensing cGAS-STING Pathway in Cancer. *Cancer Discov.* 10, 26–39. doi: 10.1158/2159-8290.Cd-19-0761

Michaelidou, K., Tzovaras, A., Missitzis, I., Ardavanis, A., and Scorilas, A. (2013). The expression of the CEACAM19 gene, a novel member of the CEA family, is associated with breast cancer progression. *Int. J. Oncol.* 42, 1770–1777. doi: 10.3892/ijo.2013.1860

Penas, C., and Navarro, X. (2018). Epigenetic Modifications Associated to Neuroinflammation and Neuropathic Pain After Neural Trauma. *Front. Cell Neurosci.* 12:158. doi: 10.3389/fncel.2018.00158

Pulido, R., Serra-Pagès, C., Tang, M., and Streuli, M. (1995). The LAR/PTP delta/PTP sigma subfamily of transmembrane protein-tyrosine-phosphatases: multiple human LAR, PTP delta, and PTP sigma isoforms are expressed in a tissue-specific manner and associate with the LAR-interacting protein LIP.1. *Proc. Natl. Acad. Sci. U. S. A.* 92, 11686–11690. doi: 10.1073/pnas.92.25.11686

Rodero, M. P., and Crow, Y. J. (2016). Type I interferon-mediated monogenic autoinflammation: the type I interferonopathies, a conceptual overview. *J. Exp. Med.* 213, 2527–2538. doi: 10.1084/jem.20161596

Scholz, J., and Woolf, C. J. (2007). The neuropathic pain triad: neurons, immune cells and glia. *Nat. Neurosci.* 10, 1361–1368. doi: 10.1038/nn1992

Shi, F., Su, J., Wang, J., Liu, Z., and Wang, T. (2021). Activation of STING inhibits cervical cancer tumor growth through enhancing the anti-tumor immune response. *Mol. Cell Biochem.* 476, 1015–1024. doi: 10.1007/s11010-020-03967-5

Sommer, C., Leinders, M., and Üçeyler, N. (2018). Inflammation in the pathophysiology of neuropathic pain. *Pain* 159, 595–602. doi: 10.1097/j.pain.0000000000001122

Song, L., Jiang, W., Liu, W., Ji, J. H., Shi, T. F., Zhang, J., et al. (2016). Protein tyrosine phosphatases receptor type D is a potential tumour suppressor gene inactivated by deoxyribonucleic acid methylation in paediatric acute myeloid leukaemia. *Acta Paediatr.* 105, e132–e141. doi: 10.1111/apa.13284

Sun, W., Kou, D., Yu, Z., Yang, S., Jiang, C., Xiong, D., et al. (2020). A Transcriptomic Analysis of Neuropathic Pain in Rat Dorsal Root Ganglia Following Peripheral Nerve Injury. *Neuromolecular Med.* 22, 250–263. doi: 10.1007/s12017-019-08581-3

Tonks, N. K. (2006). Protein tyrosine phosphatases: from genes, to function, to disease. *Nat. Rev. Mol. Cell Biol.* 7, 833–846. doi: 10.1038/nrm2039

Uhl, G. R., Martinez, M. J., Paik, P., Sulima, A., Bi, G. H., Iyer, M. R., et al. (2018). Cocaine reward is reduced by decreased expression of receptor-type protein tyrosine phosphatase D (PTPRD) and by a novel PTPRD antagonist. *Proc. Natl. Acad. Sci. U. S. A.* 115, 11597–11602. doi: 10.1073/pnas.1720446115

Vellieux, G., and d'Ortho, M. P. (2020). [Restless legs syndrome]. *Rev. Med. Interne* 41, 258–264. doi: 10.1016/j.revmed.2020.01.001

Wang, B., Zhang, G., Yang, M., Liu, N., Li, Y. X., Ma, H., et al. (2018). Neuroprotective Effect of Anethole Against Neuropathic Pain Induced by Chronic Constriction Injury of the Sciatic Nerve in Mice. *Neurochem. Res.* 43, 2404–2422. doi: 10.1007/s11064-018-2668-7

Wang, J., and Bixby, J. L. (1999). Receptor tyrosine phosphatase-delta is a homophilic, neurite-promoting cell adhesion molecular for CNS neurons. *Mol. Cell Neurosci.* 14, 370–384. doi: 10.1006/mcne.1999.0789

Xu, L., Liu, Y., Sun, Y., Li, H., Mi, W., and Jiang, Y. (2018). Analgesic effects of TLR4/NF-κB signaling pathway inhibition on chronic neuropathic pain in rats following chronic constriction injury of the sciatic nerve. *Biomed. Pharmacother.* 107, 526–533. doi: 10.1016/j.biopha.2018.07.116

Yeh, T. Y. I, Luo, W., Hsieh, Y. L., Tseng, T. J., Chiang, H., and Hsieh, S. T. (2020). Peripheral Neuropathic Pain: from Experimental Models to Potential Therapeutic Targets in Dorsal Root Ganglion Neurons. *Cells* 9:2725. doi: 10.3390/cells9122725

Yi, M. H., Liu, Y. U., Liu, K., Chen, T., Bosco, D. B., Zheng, J., et al. (2021). Chemogenetic manipulation of microglia inhibits neuroinflammation and neuropathic pain in mice. *Brain Behav. Immun.* 92, 78–89. doi: 10.1016/j.bbi.2020.11.030

Zheng, Y., Hou, X., and Yang, S. (2019). Lidocaine Potentiates SOCS3 to Attenuate Inflammation in Microglia and Suppress Neuropathic Pain. *Cell Mol. Neurobiol.* 39, 1081–1092. doi: 10.1007/s10571-019-00703-6

Zhou, J., Fan, Y., and Chen, H. (2017). Analyses of long non-coding RNA and mRNA profiles in the spinal cord of rats using RNA sequencing during the progression of neuropathic pain in an SNI model. *RNA Biol.* 14, 1810–1826. doi: 10.1080/15476286.2017.1371400

Conflict of Interest: The authors declare that the research was conducted in the absence of any commercial or financial relationships that could be construed as a potential conflict of interest.

frontiers | Frontiers in Molecular Neuroscience

BRIEF RESEARCH REPORT
published: 26 April 2022
doi: 10.3389/fnmol.2022.891463

Co-targeting B-RAF and PTEN Enables Sensory Axons to Regenerate Across and Beyond the Spinal Cord Injury

Harun N. Noristani[1]*, Hyukmin Kim[1], Shuhuan Pang[1], Jian Zhong[2] and Young-Jin Son[1]

[1] Shriners Hospitals Pediatric Research Center and Center for Neural Repair, Lewis Katz School of Medicine, Temple University, Philadelphia, PA, United States, [2] Burke Medical Research Institute, Weill Cornell Medical College of Cornell University, White Plains, NY, United States

Primary sensory axons in adult mammals fail to regenerate after spinal cord injury (SCI), in part due to insufficient intrinsic growth potential. Robustly boosting their growth potential continues to be a challenge. Previously, we showed that constitutive activation of B-RAF (rapidly accelerated fibrosarcoma kinase) markedly promotes axon regeneration after dorsal root and optic nerve injuries. The regrowth is further augmented by supplemental deletion of PTEN (phosphatase and tensin homolog). Here, we examined whether concurrent B-RAF activation and PTEN deletion promotes dorsal column axon regeneration after SCI. Remarkably, genetically targeting B-RAF and PTEN selectively in DRG neurons of adult mice enables many DC axons to enter, cross, and grow beyond the lesion site after SCI; some axons reach ∼2 mm rostral to the lesion by 3 weeks post-injury. Co-targeting B-RAF and PTEN promotes more robust DC regeneration than a pre-conditioning lesion, which additively enhances the regeneration triggered by B-RAF/PTEN. We also found that post-injury targeting of B-RAF and PTEN enhances DC axon regeneration. These results demonstrate that co-targeting B-RAF and PTEN effectively enhances the intrinsic growth potential of DC axons after SCI and therefore may help to develop a novel strategy to promote robust long-distance regeneration of primary sensory axons.

Keywords: spinal cord injury, primary afferents, glial scar, DRG, dorsal column axons, sensory axon regeneration, conditioning lesion

Edited by:
Qi Han,
Shanghai Jiao Tong University, China

Reviewed by:
Yongcheol Cho,
Daegu Gyeongbuk Institute of Science and Technology (DGIST), South Korea
Barbara Hausott,
Innsbruck Medical University, Austria

Correspondence:
Harun N. Noristani
harun.noristani@temple.edu

Specialty section:
This article was submitted to Neuroplasticity and Development, a section of the journal Frontiers in Molecular Neuroscience

Received: *07 March 2022*
Accepted: *30 March 2022*
Published: *26 April 2022*

Citation:
Noristani HN, Kim H, Pang S, Zhong J and Son Y-J (2022) Co-targeting B-RAF and PTEN Enables Sensory Axons to Regenerate Across and Beyond the Spinal Cord Injury. Front. Mol. Neurosci. 15:891463. doi: 10.3389/fnmol.2022.891463

INTRODUCTION

Adult mammalian central nervous system (CNS) neurons fail to regenerate their axons after spinal cord injury (SCI). This regeneration failure is due to extrinsic inhibitory cues and glial scar formation that hinder axonal re-growth by imposing physical and chemical barriers [for reviews see Silver and Miller (2004), Geoffroy and Zheng (2014)]. The lack of a sufficiently robust intrinsic regenerative response also substantially contributes to the inability of adult CNS neurons to regenerate their severed axons across and beyond the lesion site [for reviews see Mar et al. (2014), He and Jin (2016), Curcio and Bradke (2018)].

The pseudounipolar sensory neurons within the dorsal root ganglia (DRG) project a peripheral branch that innervates muscle, skin, and joints and a central branch [also referred to as dorsal column (DC) axons] that transmits information to the spinal cord and brainstem. In adults, a lesion to the peripheral branch prior to a lesion to the central branch, known as a pre-conditioning lesion, initiates an intrinsic regenerative response that enhances limited regeneration of DC axons (McQuarrie and Grafstein, 1973; Richardson and Issa, 1984; Richardson and Verge, 1986; Neumann and Woolf, 1999).

Studies over the past decade have identified several molecules that regulate intrinsic regeneration, including: phosphatase and tensin homolog (PTEN) (Park et al., 2008; Liu et al., 2010), rapidly accelerated fibrosarcoma kinase (B-RAF) (O'Donovan et al., 2014), suppressor of cytokine signaling 3 (SOCS3) (Smith et al., 2009), Krüppel-like factors (KLFs) (Moore et al., 2009; Blackmore et al., 2012), c-myc (Belin et al., 2015), SRY-Box Transcription Factor 11 (*Sox11*) (Wang et al., 2015; Norsworthy et al., 2017), and Lin28 (Wang et al., 2018; Nathan et al., 2020). However, the limited efficacy with which these molecules promote DC axon regeneration following SCI emphasizes the urgent need to identify additional molecules that can powerfully stimulate robust, lengthy axon re-growth.

B-RAF is critical for neurotrophin-induced sensory axon outgrowth (Markus et al., 2002; Zhong et al., 2007). We demonstrated previously that constitutive, selective activation of B-RAF in adult DRG neurons enables their axons to regenerate into the spinal cord in adult mice after dorsal root injury (O'Donovan et al., 2014). B-RAF activation also enhances regeneration of the optic nerves. Importantly, concomitant B-RAF activation and PTEN deletion synergistically increases regeneration of both optic nerve (O'Donovan et al., 2014) and dorsal root (Kim, Noristani et al., in preparation). No studies have yet examined the effects of concurrently targeting B-RAF and PTEN on DC axon regeneration after SCI. Here we demonstrate that simultaneous B-RAF activation and PTEN deletion enables DC axons to regenerate up to 2,000 μm rostral to the lesion site by 3 weeks post SCI. The extent of this regrowth is significantly greater than that enabled by a pre-conditioning lesion, which, however, additively enhances the regeneration stimulated by B-RAF/PTEN. We also report that concomitant B-RAF activation and PTEN deletion immediately after SCI promotes DC axon regeneration. These results identify concurrent B-RAF activation and PTEN deletion as a promising strategy to heighten intrinsic regeneration of adult sensory neurons and to promote axon regeneration after SCI.

RESULTS

Concomitant B-RAF Activation and PTEN Deletion Promotes Dorsal Column Axon Regeneration Across the Spinal Cord Lesion

To examine whether simultaneous B-RAF activation and PTEN deletion enhances DC axon regeneration after SCI, we used inducible transgenic mice expressing constitutively active B-RAF with PTEN deletion selectively in dorsal root ganglia (DRG) neurons: *LSL-kaBRAF:PTEN*$^{f/f}$*:Brn3a-CreER*^{T2}*:R26-TdT* (hereafter as kaBRAF/PTEN iTg). We used 6-weeks-old kaBRAF/PTEN iTg and age-matched *Brn3a-CreER*^{T2}-negative littermates as controls (WT). To induce kaBRAF expression and PTEN deletion, we administered tamoxifen for 5 consecutive days, 2 weeks prior to SCI (**Figure 1A**). We visualized ascending DC axons by microinjecting the recombinant self-complementary Adeno-Associated Virus serotype 2 expressing enhanced green fluorescent protein (scAAV2-eGFP) into the lumbar level (L) 4 and L5 DRGs. Recently, we have shown that AAV2-eGFP injections in the DRG predominantly label proprioceptive and mechanoreceptive axons (Zhai et al., 2021). Using GFAP immunostaining, we first assessed the lesion area in all sagittal sections with DC axons. The lesion area ranged between 0.093–0.192 mm^2 in WT and 0.028–0.172 mm^2 in kaBRAF/PTEN iTg mice (**Figure 1B**), suggesting that our SCI model produced relatively wide lesions. Mice with unusually enlarged or narrow lesion areas were excluded from the analysis. The lesion width at the injury epicenter ranged between 145–230 μm in WT and 100–220 μm in kaBRAF/PTEN iTg mice. Quantification of lesion area showed no significant differences between WT and kaBRAF/PTEN iTg groups (**Figure 1B**). We then determined the total number of regenerating DC axons at specific distances rostral to the lesion epicenter using a consecutive series of GFP and GFAP overlay images (**Figures 1C,D** and **Supplementary Figure 1**).

In WT mice most DC axons stopped at the astroglial border caudal to the injury site with very few axons growing over the astrocytic bridge and then abruptly stopping within 200 μm of the lesion epicenter (**Figure 1C**). DC axons in WT mice displayed characteristic dieback from the lesion epicenter, and individual axons had several retraction bulbs that appeared as bulbous swellings in their axonal tips (**Figures 1C,C′**). In all WT mice examined, DC axons failed to reach the rostral border of the lesion (**Figure 1C″**) or extend rostrally across the astroglial border (**Figure 1C‴**). Remarkably, in kaBRAF/PTEN iTg mice numerous DC axons crossed the caudal astroglial border and penetrated the lesion epicenter (**Figure 1D**). In most kaBRAF/PTEN iTg mice, regenerating DC axons that entered the lesion epicenter appeared preferentially to grow on the surface of the spinal cord (**Figure 2D**). Regenerating DC axons extending along the spinal cord surface frequently penetrated the CNS parenchyma rostral to the lesion site (**Figure 2D‴**). In a few kaBRAF/PTEN iTg mice, dramatic rostral growth was also found across the astroglial border (**Figures 1D″,D‴**). DC axons in the kaBRAF/PTEN iTg group exhibited a characteristic regenerative morphology with tortuous trajectories (**Figure 1D**). Most DC axonal tips in kaBRAF/PTEN iTg mice were thin and continuous with the axonal shaft resembling growth cones (**Figures 1D′–D‴**). Quantification revealed a significant increase in regenerating DC axons $> 2{,}000$ μm rostral to the lesion site in kaBRAF/PTEN iTg mice compared to the WT group (**Figure 1E**). Using GFAP immunostaining, we next specifically examined regenerating DC axons within the CNS parenchyma. Around two-thirds of regenerating DC axons in kaBRAF/PTEN iTg mice appeared within the CNS parenchyma i.e., the area with GFAP-positive astrocytes, while the remaining regenerating DC axons projected along the spinal cord surface. Quantification of regenerating DC axons within the CNS parenchyma confirmed a significant increase $> 2{,}000$ μm across the lesion epicenter in

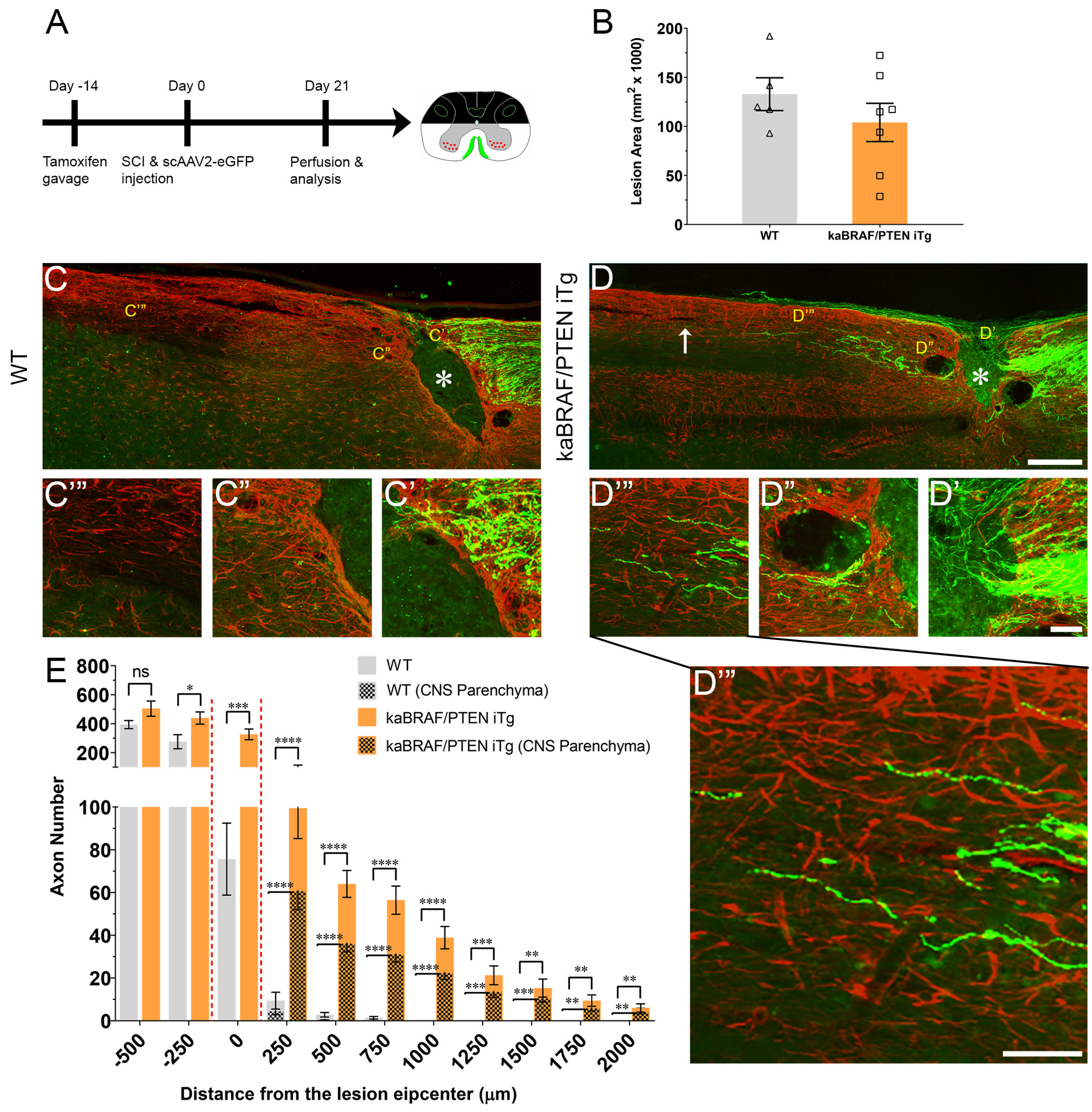

FIGURE 1 | Concomitant B-RAF activation and PTEN deletion promotes DC axon regeneration. **(A)** Schematic diagram showing the experimental timeline. Two weeks after the first tamoxifen gavage WT and kaBRAF/PTEN iTg mice underwent dorsal SCI and scAAV2-eGFP injection into the right lumbar (L) 4 and L5 DRGs to label regenerating DC axons. **(B)** Quantitative analysis of the lesion area after dorsal SCI in kaBRAF/PTEN iTg versus WT mice. **(C–C′′′)** Representative images of a WT mouse spinal cord showing most DC axons stopping at the caudal astroglial border of the injury site and very few growing along the astrocytic bridge that also terminates ~200 μm from the lesion epicenter. * Indicates lesion epicenter. **(D–D′′′)** Representative images of a kaBRAF/PTEN iTg mouse spinal cord showing increased DC axon regeneration. Many regenerating DC axons penetrate the lesion epicenter; several extend directly across the rostral astroglial border of the injury site. * Indicates lesion epicenter. **(E)** Quantitative analysis of total numbers of regenerated DC axons in kaBRAF/PTEN iTg versus WT mice. DC axon regeneration is significantly greater in kaBRAF/PTEN iTg mice at multiple distances measured from the lesion epicenter: –250 μm: *P = 0.0133, df = 10; 0 μm: ***P = 0.0009, df = 10; 250 μm: ****P < 0.0001, df = 10; 500 μm: ****P < 0.0001, df = 10; 750 μm: ****P < 0.0001, df = 10; 1,000 μm: ****P < 0.0001, df = 10; 1,250 μm: ***P = 0.0003, df = 10; 1,500 μm: **P = 0.0029, df = 10; 1,750 μm: **P = 0.0037, df = 10; 2,000 μm: **P = 0.0081, df = 10; two-way ANOVA with repeated measures. ~75% of regenerating DC axons in kaBRAF/PTEN iTg mice enter the CNS parenchyma (the area with GFAP-positive astrocytes); the remaining 25% grow along the spinal cord surface. [**(E)** patterned] Quantitative comparison of DC axons regenerated into CNS parenchyma in kaBRAF/PTEN iTg versus WT mice. Regenerating DC axons within CNS parenchyma are significantly increased at several distances rostral to the SCI in kaBRAF/PTEN iTg mice. 250 μm: ****P < 0.0001, df = 10; 500 μm: ****P < 0.0001, df = 10; 750 μm: ****P < 0.0001, df = 10; 1,000 μm: ****P < 0.0001, df = 10; 1,250 μm: ***P = 0.0004, df = 10; 1,500 μm: ***P = 0.0003, df = 10; 1,750 μm: **P = 0.0034, df = 10; 2,000 μm: **P = 0.0053, df = 10; two-way ANOVA with repeated measures. n = 5 (WT), and 7 (kaBRAF/PTEN iTg). Scale bars, 250 μm **(C,D)**, 50 μm **(C′–C′′′,D′–D′′′)**.

kaBRAF/PTEN iTg mice compared to the WT group (**Figure 1E**). Therefore, concomitant B-RAF activation and PTEN deletion powerfully promotes regeneration of DC axons, enabling them to extend up to ∼2 mm beyond the lesion within 3 weeks after SCI.

Concomitant B-RAF Activation and PTEN Deletion Enhances DC Axon Regeneration More Effectively Than a Pre-conditioning Lesion

It is firmly established that sciatic nerve injury enhances the regenerative capacity of adult DRG neurons following a subsequent injury of DC axons. This injury is known as a "pre-conditioning" lesion (Richardson and Issa, 1984; Richardson and Verge, 1986). To compare the extent of DC axon regeneration between kaBRAF/PTEN iTg mice and mice with a pre-conditioning lesion, we crushed the right sciatic nerve of another group of WT mice 10 days before SCI (**Figure 2A**). The lesion area in pre-conditioning mice ranged between 0.06–0.137 mm^2 and was not significantly different from that in kaBRAF/PTEN iTg mice (**Figure 2B**). Like kaBRAF/PTEN iTg mice, all mice examined in the pre-conditioning group showed numerous DC axons that crossed the caudal astroglial border and entered the lesion epicenter. However, they rarely penetrated across the rostral border of the lesion (**Figure 2C″**). In contrast, axons frequently penetrated the rostral border and extended rostrally in kaBRAF/PTEN iTg mice (**Figures 2D″,D‴**). In addition, more numerous axons extended rostrally along the spinal cord surface in kaBRAF/PTEN iTg mice than in pre-conditioning mice (**Figures 2C‴,D‴**). Regenerating DC axons preferentially extended rostrally along the spinal cord surface in both groups, but more frequently penetrated the CNS parenchyma in kaBRAF/PTEN iTg mice (**Figures 2C‴,D‴**). Axon quantification revealed no significant difference in regenerating DC axon numbers within the lesion epicenter between kaBRAF/PTEN iTg and the pre-conditioning group (**Figure 2E**). Importantly, kaBRAF/PTEN iTg mice showed a significant increase in regenerating DC axons between 250–2,000 μm across the lesion site compared to the pre-conditioning group. Quantification of regenerating DC axons within the CNS parenchyma also confirmed a significant increase between 250–2,000 μm across the lesion epicenter in kaBRAF/PTEN iTg mice compared to the pre-conditioning group (**Figure 2E**).

Supplemental Pre-conditioning Lesion Enhances Further the Stimulatory Effect of Concomitant B-RAF Activation and PTEN Deletion

To determine whether there is an additive effect of concurrent B-RAF activation and PTEN deletion with pre-conditioning lesion, we crushed the right sciatic nerves at 10 days before SCI in another group of kaBRAF/PTEN iTg mice (kaBRAF/PTEN iTg + Pre-Conditioning, **Figure 3A**). The lesion area in kaBRAF/PTEN iTg + Pre-Conditioning mice ranged between 0.079–0.116 mm^2 and was not significantly different compared to kaBRAF/PTEN iTg mice (**Figure 3B**). Notably, in contrast to mice with kaBRAF/PTEN iTg or pre-conditioning alone, all kaBRAF/PTEN iTg + Pre-Conditioning mice showed lesion epicenters that were densely populated by numerous DC axons that crossed the astroglial border caudal to the lesion site (**Figures 3C′,D′**). Although most axons extended along the spinal cord surface, more axons penetrated the rostral astroglial border in kaBRAF/PTEN iTg + Pre-Conditioning mice than in the kaBRAF/PTEN iTg group (**Figures 3C″,D″**). The number of regenerating DC axons extending rostrally along the spinal cord surface was also higher in the kaBRAF/PTEN iTg + Pre-Conditioning group than in kaBRAF/PTEN iTg mice and these axons often penetrated the CNS parenchyma (**Figures 3C‴,D‴**). Axon quantification revealed a significant increase in DC axon number at 250 μm caudal to the lesion and within the lesion epicenter in the kaBRAF/PTEN iTg + Pre-Conditioning group compared to the kaBRAF/PTEN iTg group (**Figure 3E**). However, there was no statistically significant increase in the number of regenerating DC axons rostral to the lesion, perhaps because of the great variability among mice (**Figure 3E**). Similarly, quantification of DC axons within the CNS parenchyma showed no statistically significant difference between kaBRAF/PTEN iTg + Pre-Conditioning and kaBRAF/PTEN iTg groups (**Figure 3E**). We interpret these results to suggest that a pre-conditioning lesion has an additive role on the stimulatory effect of B-RAF activation and PTEN deletion, resulting in more extensive DC axon regrowth. However, most axons preferentially extended along the spinal cord, rather than directly penetrating the rostral border of the lesion.

Co-targeting B-RAF and PTEN Immediately After SCI Promotes DC Axon Regeneration

To model a clinically relevant setting more closely, we next examined whether concomitant B-RAF activation and PTEN deletion immediately post-SCI can promote DC axon regeneration.

To specifically activate B-RAF and delete PTEN in sensory neurons, we injected scAAV2-Cre unilaterally into the L4 and L5 DRGs in *LSL-kaBRAF:PTEN*$^{f/f}$*:R26-TdT* transgenic mice that carry floxed alleles for kaBRAF with PTEN (hereafter as kaBRAF/PTEN/TdTom$^{+/+}$). This transgenic line also expresses Rosa 26-TdTomato (*R26-TdT*) upon Cre-mediated recombination, which enables identification of fluorescent DC axons. We used *R26-TdT* (hereafter as TdTom$^{+/+}$) mice as control.

We first confirmed the efficiency of scAAV2-Cre-mediated recombination and transfection using TdTom$^{+/+}$ mice (**Supplementary Figure 2**). Single unilateral microinjection of scAAV2-Cre into L4 and L5 DRGs resulted in high TdTom expression in transfected neuron somata (**Supplementary Figure 2A**) and DC axons (**Figure 4C**), confirming effective Cre-mediated recombination. To examine transfection efficiency, we co-stained microinjected DRGs with a mature neuronal marker (NeuN) and found that 63.6% (1,351/2,123, $n = 3$ mice, 6 DRGs) of sensory neurons were transfected (**Supplementary Figures 2A,B**). We further characterized scAAV2-Cre-labeled DRG neuron subtypes using immunohistochemistry

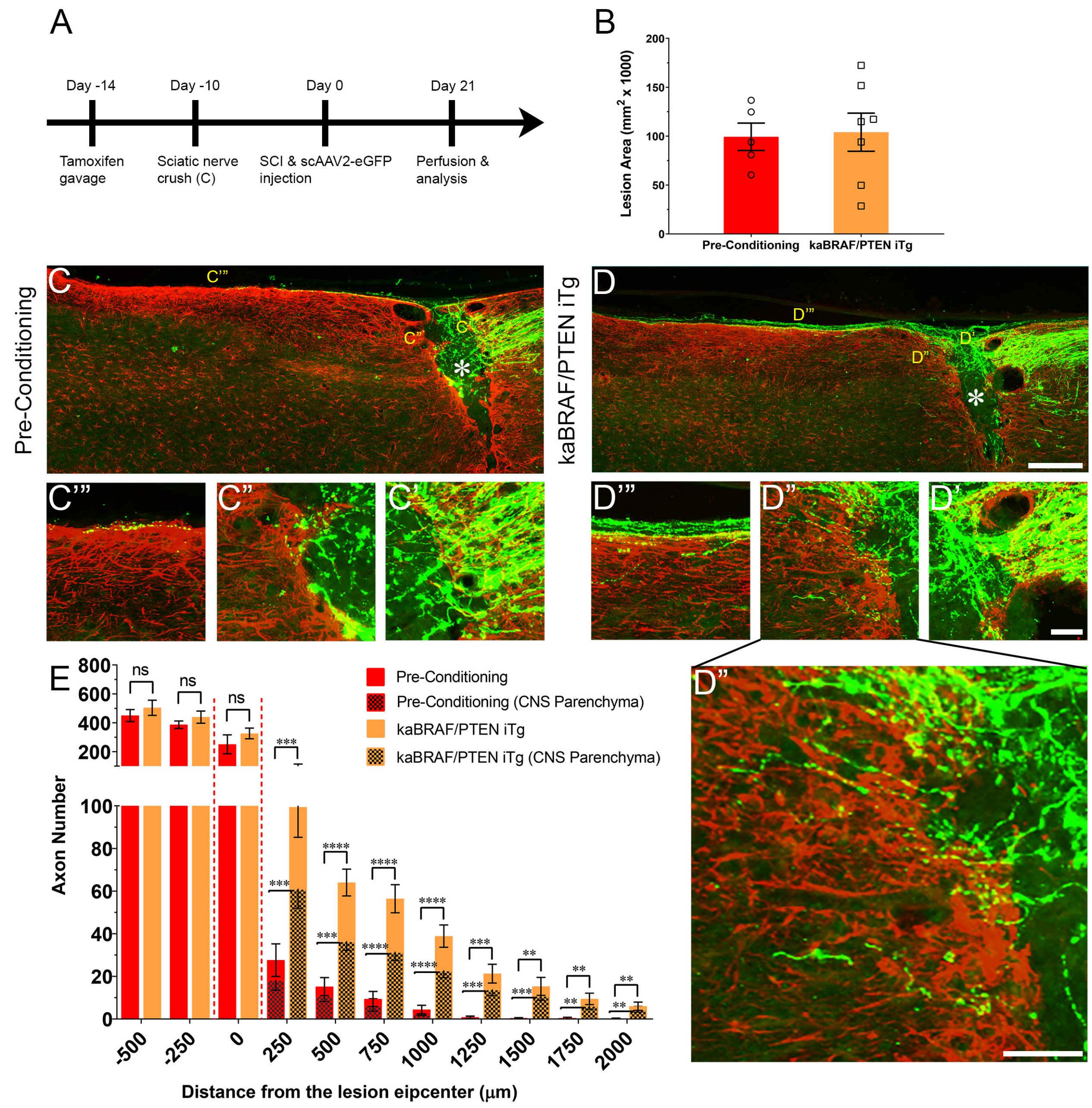

FIGURE 2 | Concomitant B-RAF activation and PTEN deletion enhances DC axon regeneration more effectively than a pre-conditioning lesion. **(A)** Schematic diagram showing the experimental timeline. Four days after the first tamoxifen gavage one group of WT mice underwent right sciatic nerve crush (pre-conditioning lesion). WT mice with a pre-conditioning lesion and kaBRAF/PTEN iTg mice without pre-conditioning lesion underwent dorsal SCI and scAAV2-eGFP injection into the right L4 and L5 DRGs to label regenerating DC axons 2 weeks after the first tamoxifen gavage. **(B)** Quantitative analysis of the SCI lesion area in kaBRAF/PTEN iTg group versus pre-conditioning group. **(C–C‴)** Representative images of a pre-conditioning mouse spinal cord showing regenerating DC axons reaching the lesion epicenter with a few terminating just rostral to the lesion site. * Indicates lesion epicenter. **(D–D‴)** Representative images of a kaBRAF/PTEN iTg mouse spinal cord showing robust DC axon regeneration. Many regenerating DC axons penetrate the lesion epicenter and extend long distances rostral to the lesion site. * Indicates lesion epicenter. **(E)** Quantitative comparison of regenerated DC axons in kaBRAF/PTEN iTg mice versus WT pre-conditioning lesion group. Significantly greater DC axon regeneration is evident at multiple distances rostral to the lesion in kaBRAF/PTEN iTg mice. 250 μm: ***$P = 0.0004$, df = 10; 500 μm: ****$P < 0.0001$, df = 10; 750 μm:****$P < 0.0001$, df = 10; 1,000 μm: ****$P < 0.0001$, df = 10; 1,250 μm: ***$P = 0.0005$, df = 10; 1,500 μm: **$P = 0.0035$, df = 10; 1,750 μm: **$P = 0.005$, df = 10; 2,000 μm: **$P = 0.0100$, df = 10; two-way ANOVA with repeated measures. **[(E)** patterned] Quantitative analysis of regenerated DC axons in CNS parenchyma rostral to the injury site in kaBRAF/PTEN iTg mice versus WT pre-conditioning lesion group. Significantly increased DC axon regeneration is evident at multiple distances up to 2,000 μm rostral to the lesion in kaBRAF/PTEN iTg mice. 250 μm: ***$P = 0.0008$, df = 10; 500 μm: ***$P = 0.0001$, df = 10; 750 μm: ****$P < 0.0001$, df = 10; 1,000 μm: ****$P < 0.0001$, df = 10; 1,250 μm: ***$P = 0.0006$, df = 10; 1,500 μm: ***$P = 0.0004$, df = 10; 1,750 μm: **$P = 0.0054$, df = 10; 2,000 μm: **$P = 0.0071$, df = 10; two-way ANOVA with repeated measures. $n = 5$ (pre-conditioning), and 7 (kaBRAF/PTEN iTg). Scale bars, 250 μm **(C,D)**, 50 μm **(C′–C‴,D′–D‴)**, ns, not significant.

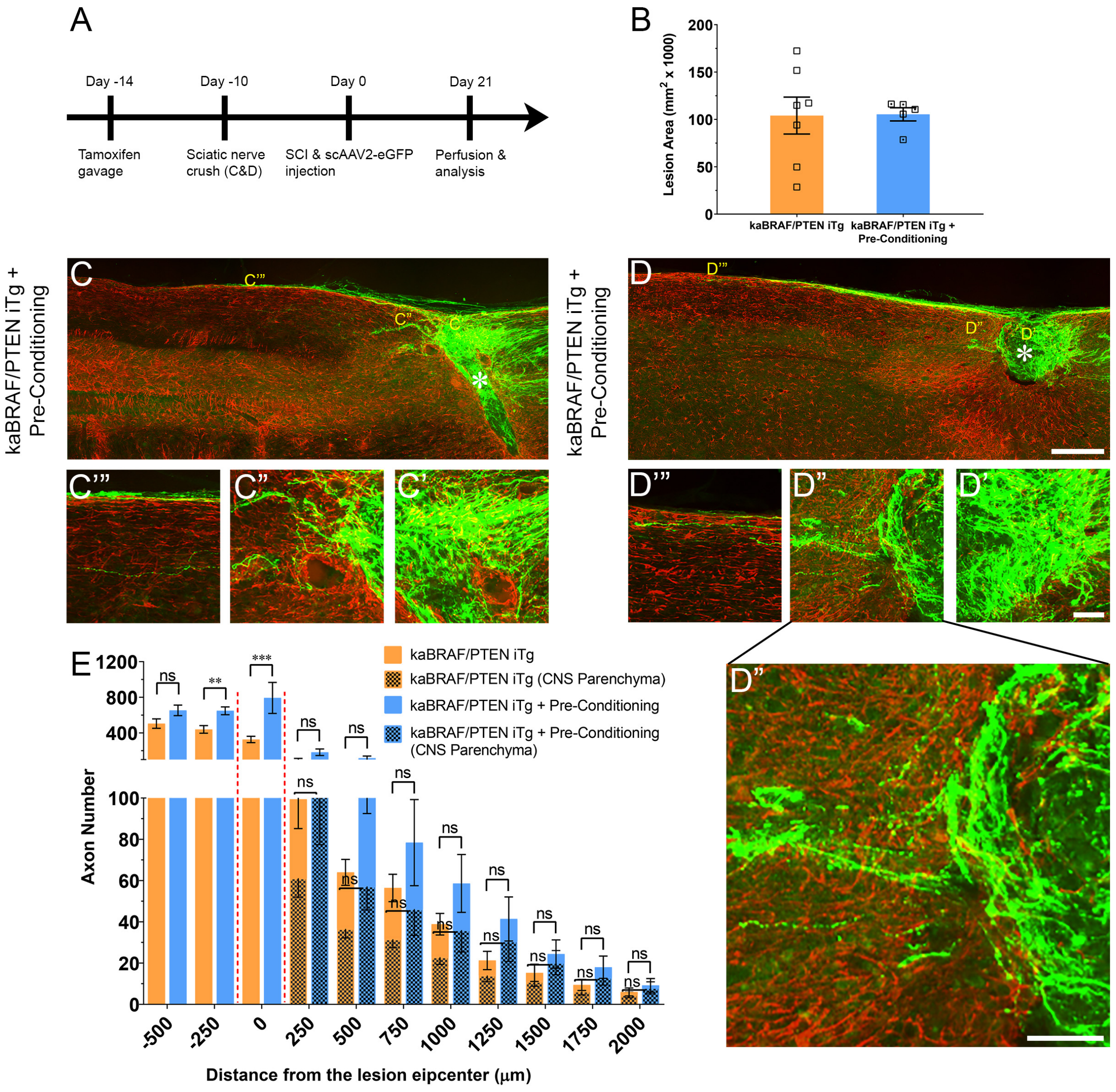

FIGURE 3 | Additive effect of pre-conditioning lesion and concomitant B-RAF activation and PTEN deletion in promoting DC axon regeneration. **(A)** Schematic diagram showing the experimental timeline. Four days after the first tamoxifen gavage a group of kaBRAF/PTEN iTg mice underwent right sciatic nerve crush (kaBRAF/PTEN iTg + Pre-Conditioning). Both kaBRAF/PTEN iTg + Pre-Conditioning and kaBRAF/PTEN iTg mice then underwent dorsal SCI and scAAV2-eGFP injection into the right L4 and L5 DRGs to label regenerating DC axons 2 weeks after the first tamoxifen gavage. **(B)** Quantitative analysis of the lesion area after SCI in kaBRAF/PTEN iTg versus kaBRAF/PTEN iTg + Pre-Conditioning mice. **(C–D′′′)** Representative images of two kaBRAF/PTEN iTg + Pre-Conditioning lesion mouse spinal cords showing a large number of regenerating DC axons immediately caudal to the lesion and numerous axons within the lesion epicenter. * Indicates lesion epicenter. **(E)** Quantitative comparison of regenerated DC axons in kaBRAF/PTEN iTg group versus kaBRAF/PTEN iTg + Pre-Conditioning lesion group. Significantly increased DC axon regeneration is evident at 250 µm caudal to the lesion in the combined group (***P* = 0.0037, df = 10), and at the lesion epicenter (0 µm: ****P* < 0.001, df = 10). Two-way ANOVA with repeated measures. *n* = 7 (kaBRAF/PTEN iTg) and 5 (kaBRAF/PTEN iTg + Pre-Conditioning). [**(E)** patterned] Quantitative comparison of regenerated DC axons within the CNS parenchyma rostral to the SCI in kaBRAF/PTEN iTg versus kaBRAF/PTEN iTg + Pre-Conditioning group. Scale bars, 250 µm **(C,D)**, 50 µm **(C′–C′′′,D′–D′′′)**, ns, not significant.

(**Supplementary Figures 2A,C**). TdTom$^+$ DRG neurons represented 80.4% (1132/1408) of large-diameter NF$^+$ neurons, 39.6% (349/881) of CGRP$^+$ peptidergic neurons, and 14.9% (126/848) of IB4$^+$ non-peptidergic neurons (**Supplementary Figure 2C**), suggesting that scAAV2-Cre predominantly transfects large-diameter sensory neurons. Single unilateral microinjection of scAAV2-Cre into kaBRAF/PTEN/TdTom$^{+/+}$ mice DRGs also downregulated PTEN protein expression in sensory neurons, further confirming efficient Cre-mediated recombination (**Supplementary Figure 2D**).

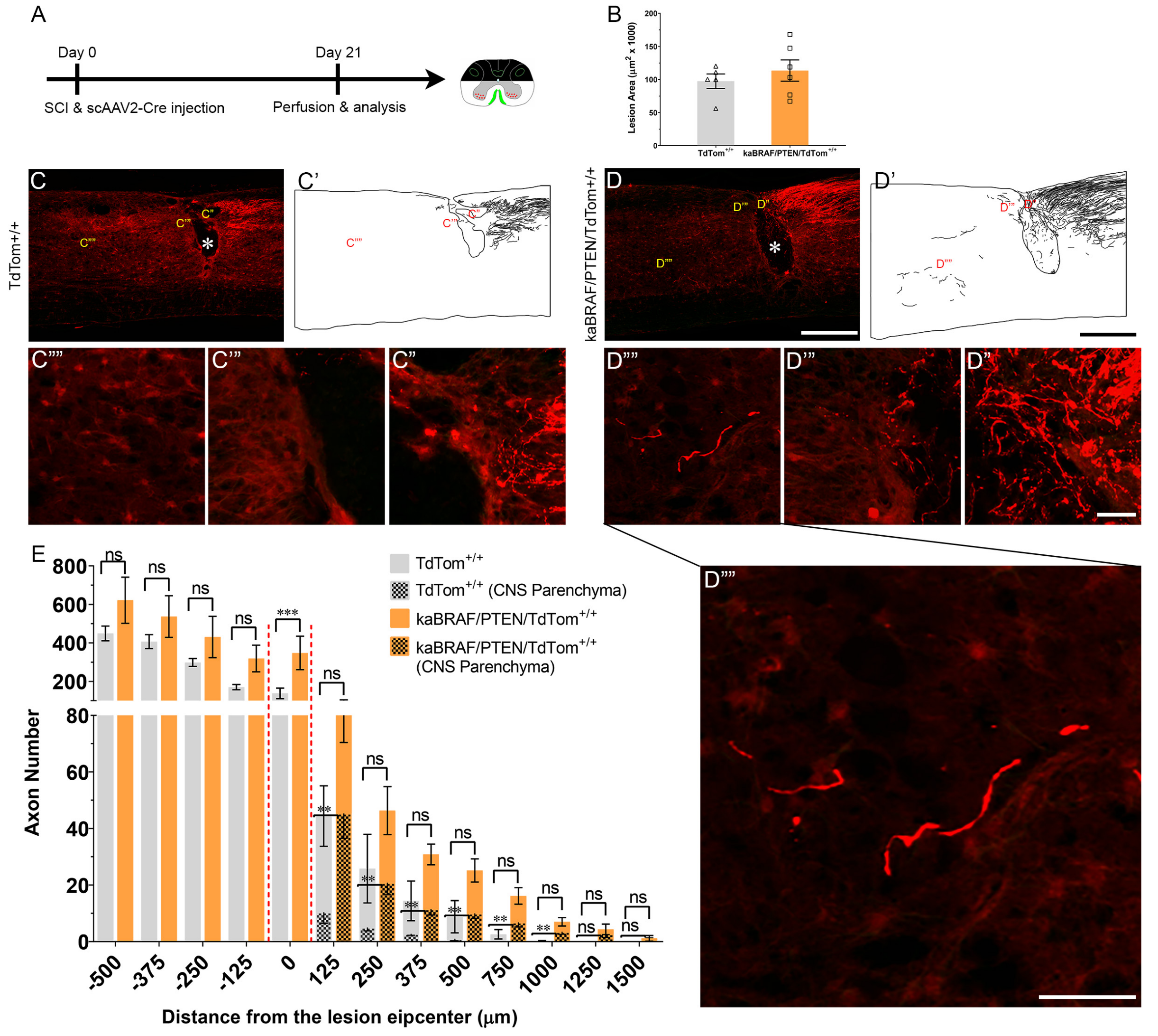

FIGURE 4 | Co-targeting of B-RAF and PTEN immediately after SCI promotes DC axon regeneration. **(A)** Schematic diagram showing the experimental timeline. Immediately following dorsal SCI scAAV2-Cre was injected into the right L4 and L5 DRGs to induce B-RAF activation and PTEN deletion in *LSL-kaBRAF:PTEN$^{f/f}$:R26-TdT* mice. scAAV2-Cre induction is also used to label regenerating DC axons *via* TdTomato expression upon Cre-mediated recombination in experimental (*LSL-kaBRAF:PTEN$^{f/f}$:R26-TdT*) and control (*R26-TdT*) mice. **(B)** Quantitative analysis of the SCI lesion area in *LSL-kaBRAF:PTEN$^{f/f}$:R26-TdT* versus *R26-TdT* mice. **(C–C′′′′)** Representative images of a *R26-TdT* mouse spinal cord showing lack of DC axon regeneration within the lesion epicenter. Most axons stop at the caudal astroglial border of the injury site and rarely penetrate the lesion epicenter. * Indicates lesion epicenter. **(D–D′′′′)** Representative images of an *LSL-kaBRAF:PTEN$^{f/f}$:R26-TdT* mouse spinal cord showing increased DC axon regeneration. Some regenerating DC axons penetrate the lesion epicenter, and a few extend directly across the rostral astroglial border of the injury site. * Indicates lesion epicenter. **(E)** Quantitative comparison of regenerated DC axons in *LSL-kaBRAF:PTEN$^{f/f}$:R26-TdT* versus *R26-TdT* mice. Significantly increased DC axon regeneration is evident at the lesion epicenter (0 µm: ****$P < 0.0001$, df = 9). Two-way ANOVA with repeated measures. [**(E)** patterned] Quantitative comparison of regenerated DC axons within CNS parenchyma rostral to the DC crush in *LSL-kaBRAF:PTEN$^{f/f}$:R26-TdT* versus *R26-TdT* mice. Regenerating DC axons are significantly more numerous in *LSL-kaBRAF:PTEN$^{f/f}$:R26-TdT* mice at distances > 1,000 µm rostral to the lesion. 125 µm: **$P = 0.0082$, df = 9; 250 µm: **$P = 0.0079$, df = 9; 375 µm: **$P = 0.0046$, df = 9; 500 µm: **$P = 0.0019$, df = 9; 750 µm: **$P = 0.0058$, df = 9; 1,000 µm: **$P = 0.0075$, df = 9; two-way ANOVA with repeated measures. $n = 5$ (*R26-TdT*), and 6 (*LSL-kaBRAF:PTEN$^{f/f}$:R26-TdT*). Scale bars, 500 µm **(C,C′,D,D′)**, 50 µm **(C′–C′′′′,D′′–D′′′′)**, ns, not significant.

We then injected scAAV2-Cre into the L4 and L5 DRGs immediately after SCI in TdTom$^{+/+}$ control and kaBRAF/PTEN/TdTom$^{+/+}$ mice (**Figure 4A**). The lesion area ranged between 0.056–0.120 mm^2 in TdTom$^{+/+}$ control and 0.067–0.168 mm^2 in kaBRAF/PTEN/TdTom$^{+/+}$ mice (**Figure 4B**). Quantification of the lesion size showed no differences in lesion area between TdTom$^{+/+}$ and kaBRAF/PTEN/TdTom$^{+/+}$ groups (**Figure 4B**). At 3 weeks after SCI in TdTom$^{+/+}$ mice, most DC axons stopped at the astroglial border caudal to the injury site. DC axons were rarely observed in the lesion epicenter (**Figures 4C–C′**). Most DC axons in TdTom$^{+/+}$ animals displayed characteristic dieback from the lesion site and individual axons had several retraction bulbs (**Figure 4C′′**). In all TdTom$^{+/+}$ mice examined, DC axons failed to extend a notable distance rostrally across the astroglial border (**Figures 4C′′′,C′′′′**). Remarkably, in kaBRAF/PTEN/TdTom$^{+/+}$ animals many DC axons penetrated the lesion epicenter and several axons extended considerable distances rostrally over 1,000 μm (**Figures 4D–D′′′′**). Individual DC axons in kaBRAF/PTEN/TdTom$^{+/+}$ mice exhibited a distinctive regenerative morphology, including tortuous trajectories (**Figure 4D′′′′**). Quantification of DC axons revealed a significant increase in regenerating DC axons at the lesion epicenter in kaBRAF/PTEN/TdTom$^{+/+}$ mice compared to the TdTom$^{+/+}$ group (**Figure 4E**). Rostral to the lesion, around 50% of regenerating DC axons in kaBRAF/PTEN/TdTom$^{+/+}$ mice entered the CNS parenchyma (**Figure 4D′′′′**). Quantification of regenerating DC axons in the CNS parenchyma showed a significant increase in axons that grew more than 1,000 μm across the lesion epicenter in kaBRAF/PTEN/TdTom$^{+/+}$ mice compared to the TdTom$^{+/+}$ group (**Figure 4E**). Altogether, these results demonstrate that scAAV2-Cre predominantly labels large-diameter sensory neurons and that concomitant B-RAF and PTEN targeting immediately post-SCI enhances DC axon regeneration, although it is less vigorous compared to animals that were transduced 2 weeks before injury.

DISCUSSION

Dorsal column crush causes complete destruction of the dorsal spinal cord parenchyma and totally disrupts ascending DC axons (Zhang et al., 1996). In line with earlier studies (Inman and Steward, 2003; Cafferty et al., 2004), we observed only a few DC axons approaching and entering the site of injury in WT mice (**Figure 1C**). In contrast, mice with concomitant B-RAF activation and PTEN deletion either before or immediately after SCI demonstrated many more axons regenerating into the lesion and densely populating its epicenter. Although most of these regenerating axons preferentially grew along the surface of the spinal cord, many extended directly across and beyond the lesion, and some even reached distances greater than 2,000 μm rostral to the lesion by 3 weeks after SCI. These observations demonstrate that co-targeting B-RAF and PTEN powerfully enhances the intrinsic capacity of DC axons to regenerate after SCI.

Previous studies reported limited efficacy in promoting DC axon regeneration after SCI through targeting single (Seijffers et al., 2007; Bareyre et al., 2011; Yu et al., 2011; Wang et al., 2015, 2017) or multiple (Bomze et al., 2001; Fagoe et al., 2015) intrinsic pro-regenerative pathways. For instance, constitutive overexpression of activating transcription factor 3 (*Atf3*) failed to promote DC axon regeneration 4 weeks following thoracic 10 (T10) dorsal hemisection in mouse (Seijffers et al., 2007). Similarly, pre-injury overexpression of signal transducer and activator of transcription 3 (*Stat3*) increased DC axon sprouting at 2 days post-lesion but did not enhance their regeneration at 10 days after cervical dorsal hemisection in mice (Bareyre et al., 2011). Pre-injury overexpression of *Klf7* (Wang et al., 2017) or *Sox11* (Wang et al., 2015) reduced DC axonal dieback without inducing regenerative growth up to 8 weeks after cervical 5 (C5) dorsal hemisection in mice. Comparable results have been reported for rat. In one recent example, pre-injury overexpression of the proto-oncogene *Myc* prevented DC axon retraction but failed to promote their rostral outgrowth by 4 weeks after T9 dorsal hemisection (Shin et al., 2021). Equally, pre-injury overexpression of DNA binding 2 (*Id2*) enabled DC axons to reach the injury site without extending beyond the lesion epicenter by 2 weeks following T10 dorsal hemisection in mice (Yu et al., 2011). Constitutive neuronal overexpression of two growth cone proteins (GAP-43 and CAP-23) triggered DC axon regeneration over 5 mm into the sciatic nerve grafted within the lesion site by 4 months following cervico-thoracic dorsal hemisection in mice (Bomze et al., 2001). Notably, neither GAP-43 nor CAP-23 overexpression alone could promote DC axon regeneration into a graft (Bomze et al., 2001). However, simultaneous pre-injury overexpression of four transcription factors (*Atf3*, *c-Jun*, *Stat3*, and *Smad1*) failed to enhance DC axon regeneration 4 weeks after C4 dorsal hemisection in rats (Fagoe et al., 2015).

Pre-injury overexpression of CREB promoted DC axon regeneration into the lesion site by 4 weeks after T6-T7 dorsal hemisection in rats (Gao et al., 2004). Similarly, overexpression of BMP4 either before injury or immediately post-SCI triggered DC axon regeneration into the lesion epicenter but not rostral to the lesion by 4 weeks after T8 dorsal hemisection in mice (Parikh et al., 2011). Equally, enforced α9 integrin expression immediately post-SCI stimulated DC axon regeneration into the lesion epicenter by 6 weeks following C5/C6 dorsal column crush in rats (Andrews et al., 2009).

Among the multiple axon growth repressors identified to date, only GSK3β has been targeted to enhance DC axon regeneration after SCI. Constitutive complete or partial GSK3β deletion promoted DC regeneration that extended within the lesion site by 5 weeks after T9/T10 dorsal hemisection in mice (Liz et al., 2014). Co-deleting two intrinsic axon growth repressors, SOCS3 and PTEN, induced modest peripheral sensory axon regeneration after sciatic nerve crush in mice (Gallaher and Steward, 2018); whether this strategy will enhance DC axon regeneration after SCI is unknown.

Other studies targeting extrinsic inhibitors (Shields et al., 2008; Lee et al., 2010) and intrinsic and extrinsic molecules in combination (Wang et al., 2017) also reported promoting DC axon regeneration after SCI with moderate efficacy. Sustained chondroitinase ABC (ChABC) release within the lesion site blocked chondroitin sulfate proteoglycans (CSPGs)-mediated inhibition and prevented DC axonal dieback but failed to promote their rostral re-growth at 6 weeks after T10 dorsal hemisection in rats (Lee et al., 2010). Intrathecal ChABC injection mildly enhanced DC axon regeneration toward the lesion site, but only a few axons extended rostrally at 5 weeks after C3 dorsal hemisection in rats (Shields et al., 2008). Combined intraparenchymal ChABC injection and *Klf7* overexpression stimulated DC axon regeneration toward the lesion site without enhancing their regenerative growth within or across the lesion site by 8 weeks after C4/C5 dorsal hemisection in mice (Wang et al., 2017). Concomitant ChABC and neurotrophin-3 treatments induced DC axon extension beyond 500 μm rostral to the lesion at 6 weeks following T10 dorsal over-hemisection in rats (Lee et al., 2010). Our observation that DC axons regenerate farther than 2,000 μm rostral to a bilateral dorsal column crush injury by 3 weeks highlights the increased potency of concomitantly targeting B-RAF and PTEN, although differences in injury models may also contribute to these differences.

Although we did not examine the extent of DC regeneration elicited by individually activating B-RAF or deleting PTEN, we examined them in the context of DR injury. We found that B-RAF activation, but not PTEN deletion, enables DR axons to regenerate into the spinal cord, and that supplemental PTEN deletion markedly enhances B-RAF elicited regeneration (O'Donovan et al., 2014; Kim, Noristani et al., in preparation). These findings suggest that B-RAF activation enhances growth potential of DRG neurons more strongly than PTEN deletion, and that this individual effect can be augmented further by supplemental PTEN deletion. Based on these findings, we surmise that PTEN deletion alone would modestly increase DC regeneration and that B-RAF activation alone would produce a stronger increase, which would be substantially boosted by combined PTEN deletion.

Multiple studies reported additive or synergistic increases in CNS regeneration by simultaneous targeting of growth promoters or inhibitors. Synergistic increase in optic nerve regeneration has been reported with SOCS3/*Klf4* co-deletion (Qin et al., 2013), PTEN/SOCS3 co-deletion (Sun et al., 2011), SOCS3 deletion with ciliary neurotrophic factor (CNTF) (Smith et al., 2009), PTEN deletion with cAMP and zymosan (de Lima et al., 2012), and PTEN deletion with cAMP and CNTF (Yungher et al., 2015). Synergistic increases in corticospinal tract regeneration have also been observed with PTEN deletion combined with hyper-interleukin-6 overexpression (Leibinger et al., 2021), and with co-expression of insulin like growth factor 1 and osteopontin (Liu et al., 2017). The effects of these combinatorial approaches on DC regeneration have yet to be tested.

The mechanisms by which B-RAF activation with PTEN deletion powerfully and synergistically promotes DC axon regeneration remain unclear. A recent transcriptomic study combining data from several independent laboratories has provided a comprehensive list of regeneration- associated genes (RAGs) that are responsible for sensory axon regeneration after pre-conditioning lesion (Chandran et al., 2016). *In silico* examination of this list did not implicate a downstream mediator of B-RAF as a RAG, including *Braf*, *Mapk1*, *Map3k2*, *Map2k1*, *Creb1*, and *Rps6ka1* (Chandran et al., 2016). Downstream mediators of PTEN, including *Rps6*, *Rps6kb1*, and *Mtor* were also not identified as RAGs, suggesting that pre-conditioning lesion and B-RAF/PTEN co-targeting depend on distinct underlying mechanisms. In addition, as mentioned earlier, enforced expression of multiple identified RAGs (*Sox11*, *Atf3*, *Jun*, *Stat3*, and *Smad1*) in sensory neurons either individually (Seijffers et al., 2007; Bareyre et al., 2011; Wang et al., 2015) or in combination (Fagoe et al., 2015) did not promote robust DC axon regeneration after SCI, suggesting that different molecules are responsible. Furthermore, our findings that concomitant B-RAF and PTEN targeting induces significantly greater DC axon regeneration than a pre-conditioning lesion (**Figure 2**), and that a supplemental pre-conditioning lesion has an additive, rather than a synergic, effect on B-RAF/PTEN-mediated DC axon regeneration (**Figure 3**), provide additional evidence that their underlying mechanisms are likely to differ. Consistent with this notion, pre-conditioning injury in kaBRAF/PTEN iTg animals increased DC axon regeneration in the same region as in WT mice: within and 250 μm caudal to the lesion. Therefore, it remains an important challenge to identify growth-promoting pathways or downstream signaling effectors that are uniquely activated upon concomitant B-RAF activation and PTEN deletion in the injured sensory neurons. These studies may reveal novel signaling pathways or effectors that drive the remarkable synergistic effect of concomitant B-RAF and PTEN targeting on DC axon regeneration.

MATERIALS AND METHODS

Animals

All procedures, including animal care and maintenance, complied with the National Institute of Health guidelines regarding the care and use of experimental animals and were approved by the Institutional Animal Care and Use Committee of Temple University, Philadelphia, PA, United States. Male and female mice, aged 6 weeks and weighing over 20 g, were used in all experiments and were maintained on the C57/BL6 background. *LSL-kaBRAF:PTEN*$^{f/f}$*:brn3a-CreER*^{T2}*:R26-TdT* (kaBRAF/PTEN iTg) transgenic lines were kindly provided by Jian Zhong (Cornell University). The *LSL-kaBRAF* and *Brn3a-CreER*^{T2} deleter mouse lines were generated and genotyped as described previously (Eng et al., 2001; O'Donovan et al., 2014). Cre-negative (*LSL-kaBRAF:PTEN*) mice from the same litter were used as control (WT). Transgenic *Rosa26(R26)-TdT* mice were purchased from the Jackson Laboratory (Stock # 007914).

Genotyping

Genotyping was performed by polymerase chain reaction (PCR) using the following primer pairs: *Braf* = 5′-GCCCAGGCTCTTTATGAGAA-3′ (common forward), 5′-AGTCAATCATCC ACAGAGACCT-3′ (reverse, mutant allele), 5′GCTTGGCTGGACGTAAACTC-3′ (reverse, wildtype allele), *Rosa26* = 5′-AAGGGAGCTGCAGTGGAGTA-3′ (forward, wildtype allele), 5′-CCGAAAATCTGTGGGAAGTC-3′ (reverse, wildtype), 5′-GGCATTAAAGCAGCATATCC-3′ (reverse, mutant allele), 5′-CTGTTCCTGTACGGCATGG-3 (forward, mutant allele), *Brn3aCre* = 5′-CGCGGACTTTGCGAGTGTTTTGTGGA-3′ (forward), 5′-GTGAAACAGCATTGCTGTCACTT-3′ (reverse), *Pten* = 5′-CAAGCACTCTGCGAACTGAG-3′ (forward), and 5′-AAGTTTTTGAAGGCAAGATGC-3′ (reverse).

Tamoxifen Administration

A 10 mg/ml tamoxifen solution was prepared in 10:1 sunflower oil:100% ethanol. 50 μl tamoxifen (10 mg/ml) was given *via* oral gavage for five consecutive days, 2 weeks prior to injury.

To account for the possible effects of tamoxifen, we also applied the same tamoxifen administration paradigm to WT and preconditioning groups.

Surgical Procedure

Two weeks following the first tamoxifen gavage, mice underwent dorsal column injury. They were anesthetized by intraperitoneal (i.p.) injection of ketamine (8 mg/kg), and xylazine (120 mg/kg). Supplements were given during the surgical procedure as needed. Small animal hair clippers (Oster Professional Products) were used to remove the hair overlying the surgical site. A 2–3 cm incision was made in the skin overlying the thoracic region, the spinal musculature was reflected, and the T10-T11 spinal cord segments were exposed by laminectomy. The cavity made by the laminectomy was continuously perfused with warm sterile Ringer's solution. Lidocaine (2%) was added dropwise ($\sim$2–3 drops) to the exposed spinal cord region. The dorsal part of the spinal cord was completely crushed for 2 s with a modified #5 forceps (Dumont, Fine Science Tools, Inc., Foster City, CA, United States). The 4–5 mm of the forceps adjacent to the tip were thinned to a width of 0.1 mm. The spinal dura and the dorsal spinal vein remained intact after crushing. For preconditioning lesion, the right sciatic nerve was crushed 10 days prior to the SCI, as we described previously (Di Maio et al., 2011). Following SCI, a piece of biosynthetic membrane (Biobrane, UDL Laboratories, Inc., Sugarland, TX, United States) was placed over the injured site. Muscles were then sutured with sterile 5-0 sutures (Ethicon, Cincinnati, OH, United States), and the midline incision closed with wound clips (Fine Science Tools, Inc., Foster City, CA, United States).

Adeno-Associated Virus Vector Injection

Recombinant self-complementary adeno-associated virus serotype 2 expressing enhanced green fluorescent protein under the control of a CMV-enhanced chicken β-actin (CAG) promoter (scAAV2-eGFP, Vector Biolabs, catalog #7072, 1×10^{13} genomic copy/ml) was used to label regenerating DC axons. We also used scAAV2 carrying Cre (scAAV2-Cre, 1×10^{12} genomic copy/ml kindly provided by George M. Smith, Temple University) to transduce DRG neurons in *LSL-kaBRAF:PTEN*$^{f/f}$*:R26-TdT* and *R26-TdT* mice. Immediately after SCI, the right L4 and L5 DRGs were exposed, and the mice were placed in a stereotaxic holder with spinal cord clamps (STS-A, Narishige Group, Tokyo, Japan). Either scAAV2-eGFP or scAAV2-Cre was microinjected using a micropipette pulled to a diameter of 0.05 mm and a nanoinjector (World Precision Instruments, Inc., Sarasota, FL, United States). For each injection, the micropipette was introduced 0.5 mm into the DRGs, and 1 μl of the virus was injected over a 10 min period (100 nl/min). The glass needle was left in place for three additional min following each injection to allow adequate virus diffusion within the DRGs. Following virus injection, a piece of biosynthetic membrane (Biobrane, UDL Laboratories, Inc., Sugarland, TX, United States) was placed over the exposed spinal cord and dura to minimize scar formation. The musculature was closed with 5-0 sterile silk sutures (Ethicon) and the skin with wound clips (Fine Science Tools, Inc., Foster City, CA, United States). To avoid dehydration, mice were given subcutaneous injections of lactated Ringer's solution and kept on a heating pad until fully recovered from anesthesia. Buprenorphine (0.05 mg/kg) was given intramuscularly for 2 consecutive days after SCI.

Immunohistochemistry, Fluorescence, and Confocal Microscopy

Three weeks following SCI and virus injection, the mice were anesthetized with a lethal dose of 10% Euthasol (Virbac, Westlake, TX, United States) in 0.9% saline and perfused transcardially with 4% paraformaldehyde (PFA) in PBS. The spinal cord containing injected DRs was dissected out, post-fixed in 4% PFA for 2 additional hours and stored in 30% sucrose in 1 × PBS, pH 7.4, overnight at 4°C for cryoprotection. Tissues were frozen-embedded in cryoprotectant medium (M-1 Embedding Matrix, Thermo Fisher Scientific, Waltham, MA, United States) in isomethylbutane at −80°C. Serial sagittal spinal cord sections (20 μl) were cut using a cryostat (Leica Microsystems, Wetzlar, Germany) and collected directly onto Superfrost Plus glass slides. To ensure the absence of spared DC axons, we examined all spinal cord and sagittal sections and confirmed that there were no GFP$^+$ or TdTom$^+$ axons over 4 mm rostral to the lesion site (data not shown). For immunolabeling, sections were rehydrated by rinsing in three changes, 10 min each, of 1 × PBS, incubated in 0.1 M glycine in 1 × PBS for 15 min, and subsequently blocked in 0.2% Triton X-100, 2% bovine serum albumin (BSA) in 1 × PBS for 15 min. Sections were incubated with primary antibodies overnight at 4°C, washed with 2% BSA in PBS three times, 10 min each, and incubated with secondary antibodies for 1 hr. Primary antibodies were used at the following concentrations for immunohistochemistry: rabbit anti-CGRP (1:1,000, Peninsula Labs, Burlingame, CA, United States, T-4032), mouse anti SMI312 (1:1,000, Biolegend, San Diego, CA, United States, 83790), chicken anti-GFP (1:1,000, Avés Labs Inc., Tigard, OR, United States, 1020), rabbit anti-GFAP (1:500, Dako, Santa Clara, CA, United States, Z0334), mouse anti-GFAP (1:500, Sigma-Aldrich, Burlington, MA, United States, G3893), mouse anti NeuN (1:1,000, MilliporeSigma, Burlington, MA, United States, MAB377), rabbit anti red fluorescent protein (1:5,000, Rockland, Limerick, PA, United States, 600-401-379), and rabbit anti-PTEN (1:200, Cell Signaling, Danvers, MA, United States, 9559). Secondary antibodies used were Alexa Fluor 647 goat anti-mouse IgG1 (1:400, Molecular Probes, Eugene, OR, United States, A-21240), Alexa Fluor 568 goat anti-rabbit IgG (1:400, Molecular Probes, Eugene, OR, United States, A-11011), Alexa Fluor 647 goat anti-rabbit IgG (1:400, Molecular Probes, Eugene, OR, United States, A-21244), Fluorescein-conjugated donkey anti-rabbit IgG (1:400, Jackson ImmunoResearch Labs Inc., West Grove, PA, United States, 711-096-152), Fluorescein-conjugated goat anti-rabbit IgG (1:400, Chemicon International, Temecula, CA, United States, AP307F), and Alexa Fluor 488 donkey anti-chicken IgG (1:400, Jackson ImmunoResearch Labs Inc., West Grove, PA, United States, 703-545-155).

For Isolectin B4 (IB4) immunostaining, sections were first post-fixed in 4% PFA, rehydrated in 1 × PBS, quenched in

0.1 M glycine in 1 × PBS, and permeabilized with 0.2% Triton X-100/PBS (PBST). Sections were then incubated with an IB4-biotin conjugate (1:200, Sigma-Aldrich, Burlington, MA, United States, L2140) prepared in 5% normal goat serum (NGS)/PBST overnight at room temperature. Sections were then blocked with 5% NGS/PBS and incubated with rhodamine (TRITC) streptavidin (1:400, Jackson ImmunoResearch Labs Inc., West Grove, PA, United States, 016-020-084) prepared in 1 × PBS for 1 hr. DAPI nucleic acid stain (1:1,000, Invitrogen, Waltham, MA, United States, D-1306) was used to counterstain prior to the final washes in 1 × PBS. All antibodies were diluted in 2% BSA in PBS. Sections were washed in three changes of 1 × PBS, 10 min each, and mounted with Vectashield mounting medium (Vector Laboratories, Burlingame, CA, United States).

Conventional fluorescence microscopy was performed using Olympus BX53 and Zeiss Axio Imager microscopes. Images were captured using a Zeiss Axio Imager upright fluorescence microscope with a 10 × 0.45 NA or 20 × 0.8 NA objective. Z stacked images were acquired using the AxioVision (Zeiss) software. We also used a SP8 confocal microscope (Leica Microsystems, Wetzlar, Germany) with either a 40 × 1.3 NA or 63 × 1.4 NA objective and Leica proprietary software. Acquired stacks were assembled using the maximum projection tool. All images were processed using Imaris (Bitplane, Zürich, Switzerland), and figures were prepared using Adobe Photoshop (Adobe, San Jose, CA, United States).

Quantification of ScAAV2-Cre Labeled Neurons

The number of NeuN/scAAV2-Cre, SMI312/scAAV2-Cre, CGRP/scAAV2-Cre, and IB4/scAAV2-Cre co-labeled neurons in L4 and L5 DRGs was counted in 20 non-adjacent sections from 3 independent mice. Co-labeled neurons were averaged from all 20 sections for each mouse.

Quantification of Regenerating DC Axons and Lesion Area After SCI

We used a consecutive series of 20 μm thick sagittal sections to determine the total number of regenerating DC axons at different distances from the lesion epicenter, which was identified based on GFAP immunostaining (**Figure 1C**). Perpendicular lines were drawn on to the sagittal plane at the lesion epicenter and at 0.25 mm intervals from 0.5 mm caudal to 2 mm rostral to the lesion epicenter. All GFP$^+$ or TdTom$^+$ axons crossing the perpendicular lines at each distance were counted manually using the ImageJ Cell Counter plug-in. The total number of axons at a given distance was summed from all immunostained sections containing GFP$^+$ or TdTom$^+$ axons. Based on overlay images of GFP and GFAP or TdTom and GFAP, regenerating axons in the rostral segments of the spinal cord were sub-divided into two groups: (i) associated with GFAP-positive astrocytes: either grew directly across the lesion site or entered the GFAP-positive territories of the spinal cord above the lesion site, and (ii) not associated with GFAP-positive astrocytes: circumvented the lesion site and grew along the surface of the spinal cord. Lesion area was quantified using ImageJ based on GFAP staining in all consecutive sagittal sections in which regenerating DC axons were quantified. Lesion area was quantified based on GFAP staining using ImageJ software on 7–10 sagittal sections and then averaged to estimate the final lesion area in μ m^2.

Statistical Analysis

Statistical significance of axon regeneration was assessed by 2-way ANOVA with repeated measures using Statistical Analysis System (SAS) software (SAS Institute Inc., Cary, NC, United States) and GraphPad Prism 6.0 (GraphPad, San Diego, CA, United States). Data were split between rostral and caudal to the lesion before carrying out 2-way ANOVA with repeated measures. Lesion area was assessed by un-paired *t*-test using GraphPad Prism 6.0 (GraphPad, San Diego, CA, United States). All data are presented as mean ± standard error of the mean (SEM). Sample sizes are as described in the figure legends. Results were considered statistically significant if the p-value was < 0.05.

DATA AVAILABILITY STATEMENT

The original contributions presented in the study are included in the article/**Supplementary Material**, further inquiries can be directed to the corresponding author/s.

ETHICS STATEMENT

The animal study was reviewed and approved by Institutional Animal Care and Use Committee of Temple University, Philadelphia, PA, United States.

AUTHOR CONTRIBUTIONS

HN: data curation, formal analysis, and writing—original draft. HK: investigation and methodology. SP: resources and investigation. JZ: resources and methodology. Y-JS: conceptualization, supervision, funding acquisition, investigation, project administration, and writing—review and editing. All authors contributed to the article and approved the submitted version.

FUNDING

This work was supported by Shriners Children's (257487 and 268980 to Y-JS; 84600 to HN), and NIH NINDS (NS253020 to Y-JS).

ACKNOWLEDGMENTS

We thank all members of Son laboratory for critical reading of the manuscript. We also thank Huaqing Zhao, and Xiaoning Lu for statistical analysis.

SUPPLEMENTARY MATERIAL

The Supplementary Material for this article can be found online at: https://www.frontiersin.org/articles/10.3389/fnmol.2022.891463/full#supplementary-material

Supplementary Figure 1 | Serial sections from the kaBRAF/PTEN iTg mouse spinal cord shown in **Figure 1D**. Numerous regenerating sensory axons penetrate the lesion epicenter and extend long distances rostral to the lesion site at 3 weeks after SCI. DC axons are labeled by injecting scAAV2-eGFP into right L4 and L5 DRGs. #16 image is also shown in **Figure 1D**. Scale bar: 200 μ m.

Supplementary Figure 2 | Viral and genetic targeting of B-RAF and PTEN. **(A)** Representative image of a *R26-TdT* mouse DRG microinjected with scAAV2-Cre and co-stained with the global mature neuronal marker NeuN, large-diameter neuron marker NF, small-diameter peptidergic neuron marker CGRP, and small diameter non-peptidergic neuron marker IB4. **(B)** Quantitative analysis of transfected [$NeuN^+$/$TdTom^+$, arrowheads in panel **(A)**] mature neurons as a percentage of total ($NeuN^+$) DRG neurons. Single unilateral microinjection of scAAV2-Cre into *R26-TdT* mice transfected > 63.6% of mature neurons in the DRG. **(C)** Quantitative analysis of transfected large diameter (NF^+/$TdTom^+$), peptidergic ($CGRP^+$/$TdTom^+$), and non-peptidergic [$IB4^+$/$TdTom^+$, arrowheads in panel **(A)**] DRG neurons. Single unilateral microinjection of a scAAV2-Cre into *R26-TdT* mice transfected > 79.4% of NF^+ large-diameter neurons, 39.6% of small-diameter peptidergic $CGRP^+$ neurons, and 15% of small-diameter non-peptidergic $IB4^+$ neurons in the DRG. **(D)** Representative image of an *LSL-kaBRAF:PTEN*$^{f/f}$*:R26-TdT* mouse DRG microinjected with scAAV2-Cre and co-stained with the PTEN antibody showing high TdTom expression and PTEN deletion (arrowheads) in sensory neurons upon Cre-mediated recombination. PTEN deletion is particularly evident in large-diameter neurons. Scale bar, 50 μm **(A)**.

REFERENCES

Andrews, M. R., Czvitkovich, S., Dassie, E., Vogelaar, C. F., Faissner, A., Blits, B., et al. (2009). alpha 9 Integrin Promotes Neurite Outgrowth on Tenascin-C and Enhances Sensory Axon Regeneration. *J. Neurosci.* 29, 5546–5557. doi: 10.1523/JNEUROSCI.0759-09.2009

Bareyre, F. M., Garzorz, N., Lang, C., Misgeld, T., Büning, H., and Kerschensteiner, M. (2011). *In vivo* imaging reveals a phase-specific role of STAT3 during central and peripheral nervous system axon regeneration. *Proc. Natl. Acad. Sci. U.S.A.* 108, 6282–6287. doi: 10.1073/pnas.1015239108

Belin, S., Nawabi, H., Wang, C., Tang, S., Latremoliere, A., Warren, P., et al. (2015). Injury-induced decline of intrinsic regenerative ability revealed by quantitative proteomics. *Neuron* 86, 1000–1014. doi: 10.1016/j.neuron.2015.03.060

Blackmore, M. G., Wang, Z., Lerch, J. K., Motti, D., Zhang, Y. P., Shields, C. B., et al. (2012). Krüppel-like Factor 7 engineered for transcriptional activation promotes axon regeneration in the adult corticospinal tract. *Proc. Natl. Acad. Sci. U.S.A.* 109, 7517–7522. doi: 10.1073/pnas.1120684109

Bomze, H. M., Bulsara, K. R., Iskandar, B. J., Caroni, P., and Skene, J. H. (2001). Spinal axon regeneration evoked by replacing two growth cone proteins in adult neurons. *Nat. Neurosci.* 4, 38–43. doi: 10.1038/82881

Cafferty, W. B., Gardiner, N. J., Das, P., Qiu, J., Mcmahon, S. B., and Thompson, S. W. (2004). Conditioning injury-induced spinal axon regeneration fails in interleukin-6 knock-out mice. *J. Neurosci.* 24, 4432–4443. doi: 10.1523/JNEUROSCI.2245-02.2004

Chandran, V., Coppola, G., Nawabi, H., Omura, T., Versano, R., Huebner, E. A., et al. (2016). A Systems-Level Analysis of the Peripheral Nerve Intrinsic Axonal Growth Program. *Neuron* 89, 956–970. doi: 10.1016/j.neuron.2016.01.034

Curcio, M., and Bradke, F. (2018). Axon Regeneration in the Central Nervous System: facing the Challenges from the Inside. *Annu. Rev. Cell Dev. Biol.* 34, 495–521. doi: 10.1146/annurev-cellbio-100617-062508

de Lima, S., Koriyama, Y., Kurimoto, T., Oliveira, J. T., Yin, Y., Li, Y., et al. (2012). Full-length axon regeneration in the adult mouse optic nerve and partial recovery of simple visual behaviors. *Proc. Natl. Acad. Sci. U.S.A.* 109, 9149–9154. doi: 10.1073/pnas.1119449109

Di Maio, A., Skuba, A., Himes, B. T., Bhagat, S. L., Hyun, J. K., Tessler, A., et al. (2011). *In vivo* imaging of dorsal root regeneration: rapid immobilization and presynaptic differentiation at the cns/pns border. *J. Neurosci.* 31, 4569–4582. doi: 10.1523/JNEUROSCI.4638-10.2011

Eng, S. R., Gratwick, K., Rhee, J. M., Fedtsova, N., Gan, L., and Turner, E. E. (2001). Defects in sensory axon growth precede neuronal death in Brn3a-deficient mice. *J. Neurosci.* 21, 541–549. doi: 10.1523/JNEUROSCI.21-02-00541.2001

Fagoe, N. D., Attwell, C. L., Kouwenhoven, D., Verhaagen, J., and Mason, M. R. (2015). Overexpression of ATF3 or the combination of ATF3, c-Jun, STAT3 and Smad1 promotes regeneration of the central axon branch of sensory neurons but without synergistic effects. *Hum. Mol. Genet.* 24, 6788–6800. doi: 10.1093/hmg/ddv383

Gallaher, Z. R., and Steward, O. (2018). Modest enhancement of sensory axon regeneration in the sciatic nerve with conditional co-deletion of PTEN and SOCS3 in the dorsal root ganglia of adult mice. *Exp. Neurol.* 303, 120–133. doi: 10.1016/j.expneurol.2018.02.012

Gao, Y., Deng, K., Hou, J., Bryson, J. B., Barco, A., Nikulina, E., et al. (2004). Activated CREB is sufficient to overcome inhibitors in myelin and promote spinal axon regeneration *in vivo*. *Neuron* 44, 609–621. doi: 10.1016/j.neuron.2004.10.030

Geoffroy, C. G., and Zheng, B. (2014). Myelin-associated inhibitors in axonal growth after CNS injury. *Curr. Opin. Neurobiol.* 27, 31–38. doi: 10.1016/j.conb.2014.02.012

He, Z., and Jin, Y. (2016). Intrinsic Control of Axon Regeneration. *Neuron* 90, 437–451. doi: 10.1016/j.neuron.2016.04.022

Inman, D. M., and Steward, O. (2003). Ascending sensory, but not other long-tract axons, regenerate into the connective tissue matrix that forms at the site of a spinal cord injury in mice. *J. Comp. Neurol.* 462, 431–449. doi: 10.1002/cne.10768

Lee, H., Mckeon, R. J., and Bellamkonda, R. V. (2010). Sustained delivery of thermostabilized chABC enhances axonal sprouting and functional recovery after spinal cord injury. *Proc. Natl. Acad. Sci. U.S.A.* 107, 3340–3345. doi: 10.1073/pnas.0905437106

Leibinger, M., Zeitler, C., Gobrecht, P., Andreadaki, A., Gisselmann, G., and Fischer, D. (2021). Transneuronal delivery of hyper-interleukin-6 enables functional recovery after severe spinal cord injury in mice. *Nat. Commun.* 12:391. doi: 10.1038/s41467-020-20112-4

Liu, K., Lu, Y., Lee, J. K., Samara, R., Willenberg, R., Sears-Kraxberger, I., et al. (2010). PTEN deletion enhances the regenerative ability of adult corticospinal neurons. *Nat. Neurosci.* 13, 1075–U64. doi: 10.1038/nn.2603

Liu, Y., Wang, X., Li, W., Zhang, Q., Li, Y., Zhang, Z., et al. (2017). A Sensitized IGF1 Treatment Restores Corticospinal Axon-Dependent Functions. *Neuron* 95, 817.e–833.e. doi: 10.1016/j.neuron.2017.07.037

Liz, M. A., Mar, F. M., Santos, T. E., Pimentel, H. I., Marques, A. M., Morgado, M. M., et al. (2014). Neuronal deletion of GSK3β increases microtubule speed in the growth cone and enhances axon regeneration *via* CRMP-2 and independently of MAP1B and CLASP2. *BMC Biol.* 12:47. doi: 10.1186/1741-7007-12-47

Mar, F. M., Bonni, A., and Sousa, M. M. (2014). Cell intrinsic control of axon regeneration. *EMBO Rep.* 15, 254–263. doi: 10.1002/embr.201337723

Markus, A., Zhong, J., and Snider, W. D. (2002). Raf and akt mediate distinct aspects of sensory axon growth. *Neuron* 35, 65–76. doi: 10.1016/s0896-6273(02)00752-3

McQuarrie, I. G., and Grafstein, B. (1973). Axon outgrowth enhanced by a previous nerve injury. *Arch. Neurol.* 29, 53–55. doi: 10.1001/archneur.1973.00490250071008

Moore, D. L., Blackmore, M. G., Hu, Y., Kaestner, K. H., Bixby, J. L., Lemmon, V. P., et al. (2009). KLF family members regulate intrinsic axon regeneration ability. *Science* 326, 298–301. doi: 10.1126/science.1175737

Nathan, F. M., Ohtake, Y., Wang, S., Jiang, X., Sami, A., Guo, H., et al. (2020). Upregulating Lin28a Promotes Axon Regeneration in Adult Mice with Optic Nerve and Spinal Cord Injury. *Mol. Ther*. 28, 1902–1917. doi: 10.1016/j.ymthe.2020.04.010

Neumann, S., and Woolf, C. J. (1999). Regeneration of dorsal column fibers into and beyond the lesion site following adult spinal cord injury. *Neuron* 23, 83–91. doi: 10.1016/s0896-6273(00)80755-2

Norsworthy, M. W., Bei, F., Kawaguchi, R., Wang, Q., Tran, N. M., Li, Y., et al. (2017). Sox11 Expression Promotes Regeneration of Some Retinal Ganglion Cell Types but Kills Others. *Neuron* 94, 1112.e–1120.e. doi: 10.1016/j.neuron.2017.05.035

O'Donovan, K. J., Ma, K. J., Guo, H. C., Wang, C., Sun, F., Han, S. B., et al. (2014). B-RAF kinase drives developmental axon growth and promotes axon regeneration in the injured mature CNS. *J. Exp. Med.* 211, 801–814. doi: 10.1084/jem.20131780

Parikh, P., Hao, Y., Hosseinkhani, M., Patil, S. B., Huntley, G. W., Tessier-Lavigne, M., et al. (2011). Regeneration of axons in injured spinal cord by activation of bone morphogenetic protein/Smad1 signaling pathway in adult neurons. *Proc. Natl. Acad. Sci. U.S.A.* 108, E99–E107. doi: 10.1073/pnas.1100426108

Park, K. K., Liu, K., Hu, Y., Smith, P. D., Wang, C., Cai, B., et al. (2008). Promoting Axon Regeneration in the Adult CNS by Modulation of the PTEN/mTOR Pathway. *Science* 322, 963–966. doi: 10.1126/science.1161566

Qin, S., Zou, Y., and Zhang, C. L. (2013). Cross-talk between KLF4 and STAT3 regulates axon regeneration. *Nat. Commun.* 4:2633. doi: 10.1038/ncomms3633

Richardson, P. M., and Issa, V. M. (1984). Peripheral injury enhances central regeneration of primary sensory neurones. *Nature* 309, 791–793. doi: 10.1038/309791a0

Richardson, P. M., and Verge, V. M. (1986). The induction of a regenerative propensity in sensory neurons following peripheral axonal injury. *J. Neurocytol.* 15, 585–594. doi: 10.1007/BF01611859

Seijffers, R., Mills, C. D., and Woolf, C. J. (2007). ATF3 increases the intrinsic growth state of DRG neurons to enhance peripheral nerve regeneration. *J. Neurosci.* 27, 7911–7920. doi: 10.1523/JNEUROSCI.5313-06.2007

Shields, L. B., Zhang, Y. P., Burke, D. A., Gray, R., and Shields, C. B. (2008). Benefit of chondroitinase ABC on sensory axon regeneration in a laceration model of spinal cord injury in the rat. *Surg. Neurol.* 69, 568–577. doi: 10.1016/j.surneu.2008.02.009

Shin, H. Y., Kwon, M. J., Lee, E. M., Kim, K., Oh, Y. J., Kim, H. S., et al. (2021). Role of Myc Proto-Oncogene as a Transcriptional Hub to Regulate the Expression of Regeneration-Associated Genes following Preconditioning Peripheral Nerve Injury. *J. Neurosci.* 41, 446–460. doi: 10.1523/JNEUROSCI.1745-20.2020

Silver, J., and Miller, J. H. (2004). Regeneration beyond the glial scar. *Nat. Rev. Neurosci.* 5, 146–156. doi: 10.1038/nrn1326

Smith, P. D., Sun, F., Park, K. K., Cai, B., Wang, C., Kuwako, K., et al. (2009). SOCS3 deletion promotes optic nerve regeneration *in vivo*. *Neuron* 64, 617–623. doi: 10.1016/j.neuron.2009.11.021

Sun, F., Park, K. K., Belin, S., Wang, D., Lu, T., Chen, G., et al. (2011). Sustained axon regeneration induced by co-deletion of PTEN and SOCS3. *Nature* 480, 372–375. doi: 10.1038/nature10594

Wang, X. W., Li, Q., Liu, C. M., Hall, P. A., Jiang, J. J., Katchis, C. D., et al. (2018). Lin28 Signaling Supports Mammalian PNS and CNS Axon Regeneration. *Cell Rep.* 24, 2540.e–2552.e. doi: 10.1016/j.celrep.2018.07.105

Wang, Z., Reynolds, A., Kirry, A., Nienhaus, C., and Blackmore, M. G. (2015). Overexpression of Sox11 promotes corticospinal tract regeneration after spinal injury while interfering with functional recovery. *J. Neurosci.* 35, 3139–3145. doi: 10.1523/JNEUROSCI.2832-14.2015

Wang, Z., Winsor, K., Nienhaus, C., Hess, E., and Blackmore, M. G. (2017). Combined chondroitinase and KLF7 expression reduce net retraction of sensory and CST axons from sites of spinal injury. *Neurobiol. Dis.* 99, 24–35. doi: 10.1016/j.nbd.2016.12.010

Yu, P., Zhang, Y. P., Shields, L. B., Zheng, Y., Hu, X., Hill, R., et al. (2011). Inhibitor of DNA binding 2 promotes sensory axonal growth after SCI. *Exp. Neurol.* 231, 38–44. doi: 10.1016/j.expneurol.2011.05.013

Yungher, B. J., Luo, X., Salgueiro, Y., Blackmore, M. G., and Park, K. K. (2015). Viral vector-based improvement of optic nerve regeneration: characterization of individual axons' growth patterns and synaptogenesis in a visual target. *Gene Ther.* 22, 811–821. doi: 10.1038/gt.2015.51

Zhai, J., Kim, H., Han, S. B., Manire, M., Yoo, R., Pang, S., et al. (2021). Co-targeting myelin inhibitors and CSPGs markedly enhances regeneration of GDNF-stimulated, but not conditioning-lesioned, sensory axons into the spinal cord. *Elife* 10:e63050. doi: 10.7554/eLife.63050

Zhang, Z., Fujiki, M., Guth, L., and Steward, O. (1996). Genetic influences on cellular reactions to spinal cord injury: a wound-healing response present in normal mice is impaired in mice carrying a mutation (WldS) that causes delayed Wallerian degeneration. *J. Comp. Neurol.* 371, 485–495. doi: 10.1002/(SICI)1096-9861(19960729)371:3<485::AID-CNE10>3.0.CO;2-I

Zhong, J., Li, X., Mcnamee, C., Chen, A. P., Baccarini, M., and Snider, W. D. (2007). Raf kinase signaling functions in sensory neuron differentiation and axon growth *in vivo*. *Nat .Neurosci.* 10, 598–607. doi: 10.1038/nn1898

Conflict of Interest: The authors declare that the research was conducted in the absence of any commercial or financial relationships that could be construed as a potential conflict of interest.

ORIGINAL RESEARCH
published: 19 May 2022
doi: 10.3389/fnmol.2022.848185

Neuroprotective Effects of the Pannexin-1 Channel Inhibitor: Probenecid on Spinal Cord Injury in Rats

Qi Qi[2,4†], Xiao-Xuan Wang[2,3†], Jing-Lu Li[1,2], Yu-Qing Chen[2,3], Jian-Rong Chang[2], Jin Xi[2], He-Zuo Lü[1,2,3] and Yu-Xin Zhang[2,3*]*

[1] Clinical Laboratory, The First Affiliated Hospital of Bengbu Medical College, Bengbu, China, [2] Anhui Key Laboratory of Tissue Transplantation, Bengbu Medical College, Bengbu, China, [3] School of Laboratory Medicine, Bengbu Medical College, Bengbu, China, [4] School of Basic Medicine, Bengbu Medical College, Bengbu, China

Proinflammatory immune cell subsets constitute the majority in the local microenvironment after spinal cord injury (SCI), leading to secondary pathological injury. Previous studies have demonstrated that inflammasomes act as an important part of the inflammatory process after SCI. Probenecid, an inhibitor of the Pannexin-1 channel, can inhibit the activation of inflammasomes. This article focuses on the effects of probenecid on the local immune microenvironment, histopathology, and behavior of SCI. Our data show that probenecid inhibited the expression and activation of nucleotide-binding oligomerization domain receptor pyrindomain-containing 1 (NLRP1), apoptosis-associated speck-like protein containing a CARD (ASC) and caspase-1, interleukin-1β (IL-1β), and caspase-3 proteins associated with inflammasomes, thereby suppressing the proportion of M1 cells. And consequently, probenecid reduced the lesion area and demyelination in SCI. Moreover, the drug increased the survival of motor neurons, which resulted in tissue repair and improved locomotor function in the injured SC. Altogether, existing studies indicated that probenecid can alleviate inflammation by blocking Pannexin-1 channels to inhibit the expression of caspase-1 and IL-1β, which in turn restores the balance of immune cell subsets and exerts neuroprotective effects in rats with SCI.

Keywords: probenecid, spinal cord injury, inflammasome, macrophages polarization, immune microenvironment

Edited by:
Biqin Lai,
Sun Yat-sen University, China

Reviewed by:
Xuecheng Qiu,
Xuzhou Medical University, China
Yuanhuan Ma,
Guangzhou First People's Hospital, China

***Correspondence:**
He-Zuo Lü
lhz233003@163.com
Yu-Xin Zhang
zyx5460@aliyun.com

†These authors have contributed equally to this work

Specialty section:
This article was submitted to Neuroplasticity and Development, a section of the journal Frontiers in Molecular Neuroscience

***Received:** 04 January 2022*
***Accepted:** 01 April 2022*
***Published:** 19 May 2022*

Citation:
Qi Q, Wang X-X, Li J-L, Chen Y-Q, Chang J-R, Xi J, Lü H-Z and Zhang Y-X (2022) Neuroprotective Effects of the Pannexin-1 Channel Inhibitor: Probenecid on Spinal Cord Injury in Rats. Front. Mol. Neurosci. 15:848185. doi: 10.3389/fnmol.2022.848185

INTRODUCTION

Spinal cord injury (SCI) is damage to the spinal cord caused by a sports accident, traffic accident, or fall from a height, which results in the loss of motor or sensory function, leading to a decrease in the quality of life and a heavy medical burden on the family and society (Gaojian et al., 2020). The treatment of SCI has been a challenge for the medical community because of the poor regenerative capacity of neurons after SCI and the rapid appearance of glial scarring, which makes it difficult to repair and reconstruct the spinal cord tissue and function (Wang et al., 2019). Therefore, it is significant to explore effective treatments for SCI to improve patients' quality of life and reduce the medical burden for families and society.

Spinal cord injury contains two phases, the primary phase and the secondary phase (the main phase). The mechanisms of secondary injury after SCI are complex and include neuroinflammatory response, ischemia and hypoxia, lipid peroxidation, apoptosis, etc. (Wu and Xu, 2016).

Among them, the neuroinflammatory response has been regarded as an important factor in the pathological process leading to secondary injury (Scholtes et al., 2012). The pathophysiological processes of secondary injury, such as apoptosis, edema, glial scarring, and inflammation in the injured tissue, severely impact the conduction function of nerves in the corresponding spinal cord segments. The inflammatory response during SCI includes local immune cell activation of the injury, the infiltration of peripheral immune cells, and the production of proinflammatory factors, which ultimately lead to spinal cord dysfunction (Sun et al., 2016). Effective and early use of anti-inflammatory drugs is of considerable importance to improve the local immune microenvironment and promote neuronal regeneration and recovery of spinal cord function.

Probenecid, a sulfonamide derivative approved for use in 1951, has been used to treat gout and its adverse effects, and pharmacokinetics have been intensively studied (Baranova et al., 2004; Papadopoulos and Verkman, 2008). One study found that oxidative stress in nerve cells can be effectively inhibited by probenecid (Cheng and Kim, 2020). Another study showed that probenecid also acts as a pannexin-1 channel inhibitor and may inhibit the activation of inflammasomes (Silverman et al., 2009). Inflammasomes are multiprotein complexes that mainly consist of intracellular pattern recognition receptors (PRRs), apoptosis-associated speck-like protein containing a card (ASC), and pro-caspase-1 (Christgen et al., 2020). The pannexin-1 channel presents mainly in the brain, spinal cord, and thyroid gland (Bruzzone et al., 2003). It has a great effect on the activation of inflammasomes. In a study of a rat brain model of cognitive impairment, probenecid was found to inhibit the activation of nucleotide-binding oligomerization domain receptor pyrindomain-containing 1 (NLRP1) inflammasomes and reduce the activation of caspase-1, which in turn reduced the degree of cognitive impairment in rats (Mawhinney et al., 2011). Several studies have reported that probenecid can also reduce neuropathic pain in the spinal cord (Pineda-Farias et al., 2013; Bravo et al., 2014). These reports suggest that during the injury process of the central nervous system (CNS), probenecid has a neuroprotective and restorative effect on CNS injury, SCI has a similar process; however, it has not been reported whether this drug is useful for the treatment of SCI.

In the immune microenvironment at the site of SCI, there are generally M1 and M2 two phenotypes of macrophages. They appear in all stages from SCI to recovery, especially playing an indispensable part in the secondary inflammatory response of SCI (Martinez et al., 2008; Milich et al., 2019; Zhang et al., 2020). M1 cells can produce high levels of proinflammatory cytokines, such as secreting proinflammatory factors, like tumor necrosis factor α (TNF-α) and interleukin-1β (IL-1β), which induce the production of inflammatory cascade responses. M2 cells can secrete anti-inflammatory factors like IL-4, IL-10, and other factors, which reduce the inflammatory response and promote wound healing (Gensel and Zhang, 2015). Whether probenecid affects the polarization of microglia/macrophages to exert neuroprotective effects on SCI is an important research value to explore new mechanisms of SCI pathology and find new targets for treatment.

MATERIALS AND METHODS

Experimental Animals

In this experiment, a total of 98 SPF-grade women standard deviation (SD) rats (weight, 200–220 g; age, 8 weeks old) were used. All these rats were provided by Jinan Pengyue Experimental Animal Breeding Co., Ltd., Jinan, China, under license No. SCXK (Lu) 2019-0003. All surgical operations and postoperative care of SD rats during the experiment were approved by the Committee on the Laboratory Animal Care and Use of Bengbu Medical College.

Experimental Methods

Preparation of Spinal Cord Injury Models in Adult Rats

Before performing the test, SD rats were housed in an environment with the appropriate humidity and temperature and given adequate feed and water for 5–7 days. Before surgery, the required surgical instruments were soaked in 75% alcohol (Shangdong Lierkang Co., Dezhou, China) for 30 min and sterilized with UV light for 30 min. During the operation, firstly, SD rats were anesthetized with 10% trichloroacetaldehyde intraperitoneally, then the rat hair around the T9 vertebral plate on the back of the rats was removed, the skin, fascia, and muscles of the corresponding part of T9 were cut open with a scalpel (Shanghai Medical Equipment Co., Shanghai, China), the T9 spinous process was removed with a bite forceps, and the vertebral plate was bitten along the interspinal foramen between T9 and T10 to fully expose the spinal cord, forming a circular opening of about 2.5 mm in diameter. Then, we use a 10-g weight falling directly from a certain height of about 25 mm to impact the exposed spinal cord. After surgery, the rats were grouped into different groups. For the sham-operated group [sham group], the rats received the same surgical procedure but without spinal cord damage and pharmacological treatment. SD rats after SCI were randomly divided into solvent control group [SCI (vector) group] (intraperitoneal injection within 3 h after surgery, followed by daily injection of PBS buffer (Biosharp) and the probenecid (Sigma) administration group [SCI (Prob) group; intraperitoneal injection of probenecid within 3 h after surgery, followed by daily injection (1 mg/kg)]. To prevent infection, the rats were given intraperitoneal injections of penicillin for 7 days. SD rats were given manual bladder emptying three times daily until the recovery of the bladder function.

Western Blot

Three days after SCI surgery, the rats were anesthetized with 10% trichloroacetaldehyde and then perfused with PBS, and total protein was extracted from the spinal cord tissue of the injury site (0.5-cm spinal cord segments containing the injury epicenter and the same segments for the sham group) and treated with RIPA lysis (Beyotime). We use the BCA kit (CWBIO) to detect the protein concentration and then use the SDS-PAGE gel kit (Beyotime) with the corresponding concentration to separate the protein, and then transfer it to polyvinylidene fluoride (PVDF) membranes (Millipore). The PVDF membranes were blocked with 5% skim milk for 2 h, then the primary antibodies incubated PVDF membranes overnight at 4°C. After that, the PVDF membranes were incubated for 2 h with horseradish peroxidase-(HRP-) conjugated secondary antibody. Proteins were detected with Immobilon western chemilum HRP substrate (Millipore) and observed with an electrochemiluminescence gel imager (Bio-Rad). Primary and secondary antibody information is listed in **Supplementary Table 1**. Finally, the expression of each protein was quantified using Image J.

Immunofluorescence Staining

At 7 days following surgery, the rats were anesthetized with 10% trichloroacetaldehyde, as described in the western blot protocol. And, the rats were cardiac perfused with PBS followed by 4% pre-cooled paraformaldehyde (PFA) at 4°C until the rats' limbs were rigid, 1-cm spinal cord segments containing the injury epicenter were removed and postfixed overnight in 4% PFA before being transferred to 30% sucrose in 0.01 M PBS (pH 7.4) at 4°C overnight. Spinal cords were embedded in an OCT compound embedding medium (TissueTek, Miles, Elkart) and 10-μm serial frozen sections were prepared using a frozen microtome (Leica), followed by thaw-mounting on poly-L-lysine-coated slides. For the immunohistochemical assay, firstly, the tissue sections were incubated with the primary antibody overnight at 4°C. After that, the sections were washed with PBS and then incubated with the secondary antibody for 2 h. Next, the tissue sections were washed with PBS, and then we used blue nuclear dye (Hoechst 33342; Abcam) to stain the cell nuclei, and the tissue sections were covered with coverslips for use. **Supplementary Table 2** shows the details of the antibodies. Photographs were taken with a fluorescent microscope (Zeiss). In the quantitative experiment of immunofluorescence, the spinal cord cross-sections of six rats were used for evaluation. We took multiple pictures around the center of the SCI. Double-positive cells in each picture were counted by the blinded observer, and the average value was divided by the picture area. A smaller area in each group of pictures was selected as the representative picture.

Flow Cytometry

Rats were anesthetized with 10% trichloroacetaldehyde and then perfused with PBS after 7 days of SCI. Then, 0.5-cm spinal cords, including the injury epicenter or the same segments for the sham group, were removed. The spinal cords were then grounded and centrifuged to obtain a single-cell suspension. Then, mononuclear cells were isolated by Percoll (Solarbio) gradient centrifugation. Briefly, 70% Percoll solution, 30% Percoll solution, and cell suspensions were added to a 15 ml conical tube in sequence, the cells were centrifuged at 300 g for 30 min at 20°C. After centrifugation, the cell debris layer was discarded and the rest parts were washed two times before their use. Then, the primary antibodies were incubated with the cells for 30 min; after that, the cells were washed with PBS and then fixed with 0.5 ml of 1% PFA (MACKLIN); finally, they were detected by BD FACSVerse flow cytometer (BD Bioscience). We used isotype control antibodies to estimate the non-specific staining that was subtracted from the specific staining results. **Supplementary Table 3** shows the details of the antibodies. We use FlowJo 7.6 software (FlowJo) to analyze the data.

Histological Analysis

The remaining rats were anesthetized with 10% trichloroacetaldehyde at 6 weeks post-SCI, and cardiac perfusion was performed with PBS followed by precooled PFA at 4°C. Spinal cords were collected, fixed, and cut into 10 μm serial frozen sections using a frozen microtome (Leica), as described in the immunofluorescence protocol. According to the manufacturer's instructions, the slides were stained with the desired staining. Hematoxylin-eosin (HE, Beyotime) and Luxol Fast Blue (LFB, Sigma-Aldrich) staining were performed to measure the lesion area and the preservation of myelination (LFB-positive area) of the spinal cord. Lesion and myelinated area measurements were performed in an unbiased stereological manner using ImageJ software. Cavitation and LFB-positive tissue at the injury epicenter and the epicenter to rostral and caudal 1, 2, 3, and 4 mm in axial sections were quantified and normalized to the percentage of intact spinal cord area. Nissl staining (Beyotime) was used to identify surviving motor neurons by the existence of the Nissl substance and euchromatic nuclei. Surviving motor neurons were quantified by counting all such cells in the ventral horn. The three staining methods were described previously (Chen et al., 2020).

Behavioral Analysis

Three methods were used to assess the behavior of SCI rats. The Basso, Beattie, and Bresnahan (BBB) locomotor rating scale ranging from 0 to 21 points was used to assess the behavior of SCI rats. The BBB locomotor rating scale was performed by the double-blind method at 1, 3, 5, 7, 14, 28, 35, and 42 days after SCI, when the rats walked freely on the open-field surface for 4 min. The footprint analysis and the Grid walk test were performed as previously described (Metz et al., 2000). Information from the BBB locomotor rating scale and footprint analysis is listed in **Supplementary Tables 4** and **5**.

Statistical Analyses

Data are presented as mean ± SD. Histological data were analyzed by a two-way ANOVA followed by Bonferroni's multiple comparisons test, and the BBB locomotor rating scale was analyzed by repeated-measures two-way ANOVA followed by Tukey's multiple comparisons test. A one-way ANOVA with a Tukey's multiple comparisons test and student's *t*-tests were used to evaluate the other data. $p < 0.05$ was considered statistically significant. Data were analyzed with Graphpad Prism software v.9.0.

RESULTS

Probenecid Inhibits the Expression and Activation of Inflammasome-Associated Molecules After Spinal Cord Injury

To prove the effect of probenecid on the expression and activation of inflammasome-associated molecules, we performed

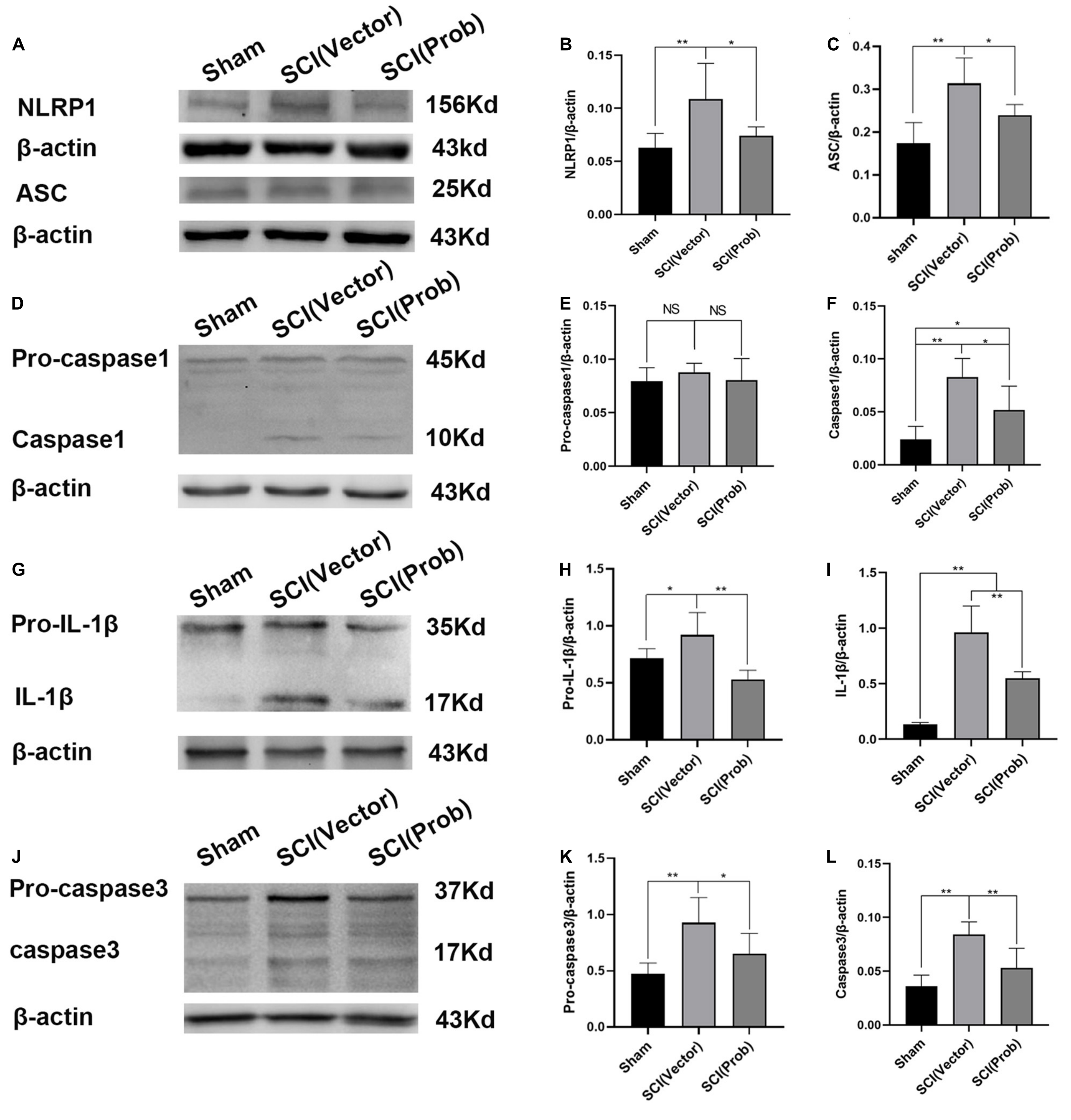

FIGURE 1 | Probenecid inhibits the expression of inflammasome-associated molecules at 3 days following spinal cord injury (SCI). **(A,D,G,J)** Representative pictures of WB results of the expression of NLRP1 and ASC **(A)**, pro-caspase-1and caspase-1 **(D)**, pro-interleukin-1β (pro-IL-1β) and IL-1β **(G)**, pro-caspase-3 and caspase-3 **(J)**. **(B,C,E,F,H,I,K,L)** Quantitative results of the expression of inflammasome-associated molecules ($^*p < 0.05$, $^{**}p < 0.01$ $n = 6$).

western blotting on spinal cord homogenate extracts obtained from sham, SCI (vector), and SCI (Prob) groups. ASC and NLRP1 were significantly increased in the SCI (vector) group, whereas they were significantly reduced in the SCI (Prob) group compared with the SCI (vector) group (**Figures 1A–C**). Pro-caspase-1 levels were unchanged among the three groups (**Figures 1D–F**). However, caspase-1 levels were significantly decreased in the SCI (Prob) group compared with the SCI (vector) group. Pro-IL-1β and IL-1β levels were significantly decreased after probenecid treatment compared with the SCI (vector) group (**Figures 1G–I**). The levels of the pro-caspase-3 and the caspase-3 were significantly decreased in

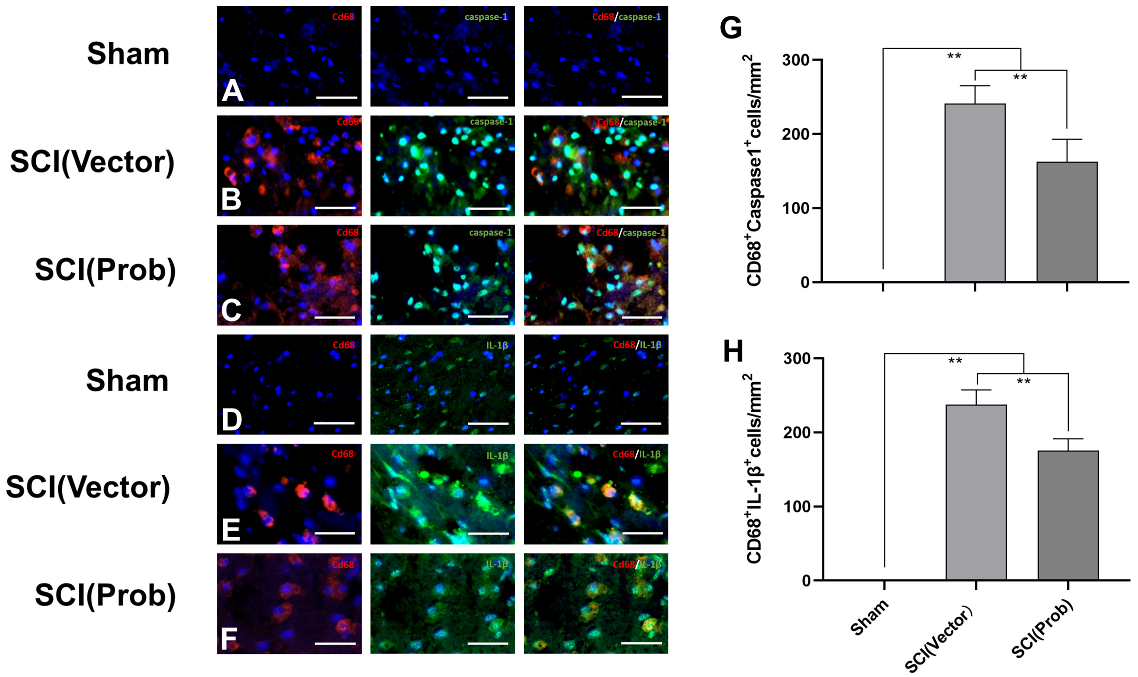

FIGURE 2 | Inhibitory effects of Probenecid on the expression of inflammasome-associated molecules at 7 days following SCI: immunofluorescence detection. Representative images of CD68 (red, rhodamine staining) and caspase-1 [green, fluorescein isothiocyanate (FITC) staining] co-stained **(A–C)**, CD68 and IL-1β (green, FITC staining) co-stained **(D–F)**. Hoechst 33342 (blue) was used to counterstain cells to visualize nuclei. **(G,H)** Quantitative analysis of CD68^{+}caspase-1^{+} **(G)**, and CD68^{+} IL-1β^{+} **(H)**, (**$p < 0.01$ $n = 6$) scale bar: 50 µm.

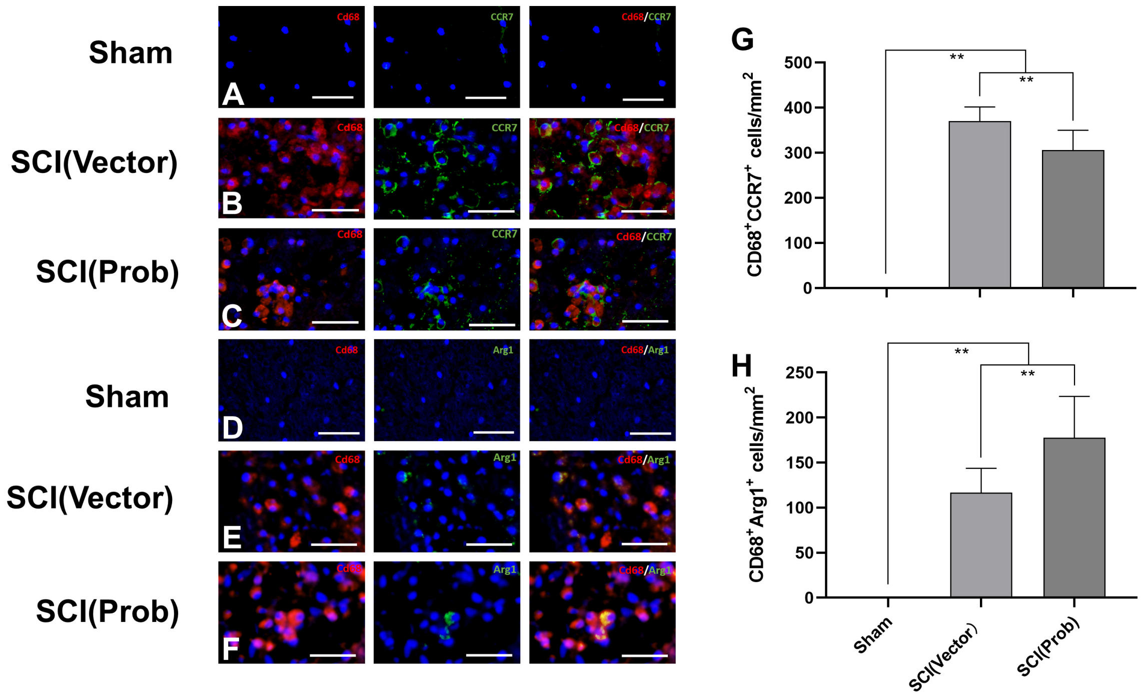

FIGURE 3 | Effects of Probenecid on M1 and M2 cells in the injured spinal cord as distinguished by immunofluorescence. Representative images of CD68 (red, rhodamine staining) and CCR7 (green, FITC staining) co-stained M1 cells **(A–C)**, CD68 (red, rhodamine staining) and Arg1 (green, FITC staining) co-stained M2 cells **(D–F)**. Cells were counterstained with Hoechst 33342 (blue) to visualize nuclei. **(G,H)** Quantitative analysis of CD68^{+} CCR7^{+} **(G)**, and CD68^{+} Arg1^{+} (**H**; **$p < 0.01$ $n = 6$), scale bar: 50 µm.

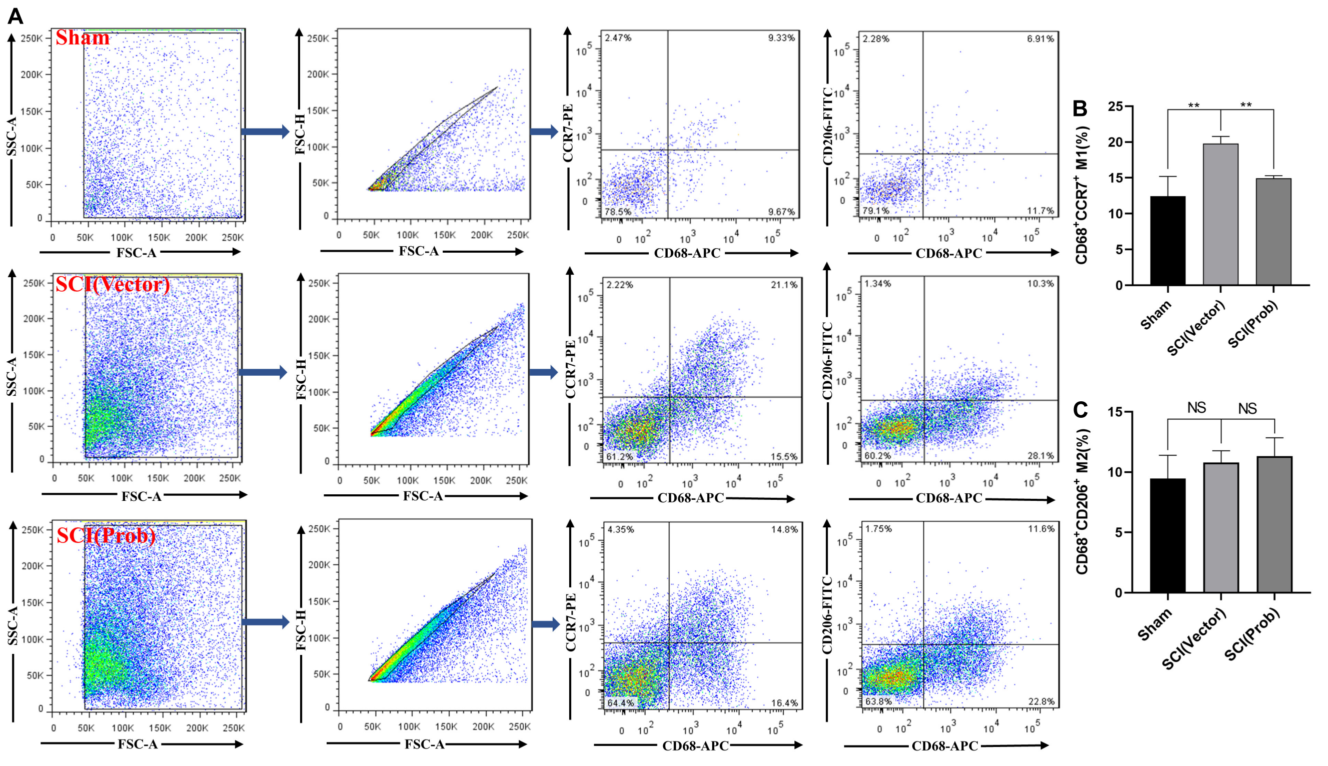

FIGURE 4 | Effects of Probenecid on Polarization of M1 and M2 in the injured spinal cord as distinguished by flow cytometr (FCM). $CD68^+CCR7^+$ and $CD68^+CD206^+$ cells were defined as M1 and M2, respectively. **(A)** Flow cytometry pictures of cells derived from spinal cord homogenate. **(B,C)** Statistical charts ($^{**}p < 0.01$ $n = 4$).

the SCI (Prob) group compared with the SCI (vector) group (**Figures 1J–L**).

The immunofluorescence assay was used to detect the effect of probenecid on the expression and activation of inflammasome-associated molecules. We used double immunofluorescence staining to label CD68 with caspase-1 and IL-1β, respectively (**Figures 2A–F**). CD68 is the marker of activated microglia/macrophages. The number of $CD68^+$ Caspase-1^+ cells and $CD68^+$ IL-$1\beta^+$ cells was significantly decreased in the SCI (Prob) group compared with the SCI (vector) group (**Figures 2G,H**). The results could indicate that probenecid inhibits the expression and activation of inflammasome-associated molecules after SCI.

Probenecid Inhibits Spinal Cord Injury-Induced Polarization of Microglia/macrophages Into M1 Cells and Increases the Polarization of Microglia/macrophages Into M2 Cells

To verify the effect of probenecid on M1 and M2 phenotype cells, we used the immunofluorescence assay to detect the specific markers of M1 ($CD68^+CCR7^+$) and M2 cells ($CD68^+Arg1^+$; **Figures 3A–F**). The number of $CD68^+CCR7^+$ (M1) cells was significantly decreased and the number of $CD68^+Arg1^+$ (M2) cells was significantly increased in the SCI (Prob) group compared with the SCI (vector) group (**Figures 3G,H**).

M1 and M2 cells in the injured spinal cords were also analyzed by flow cytometry. $CD68^+CCR7^+$ and $CD68^+CD206^+$ cells were defined as M1 and M2 cells, respectively (**Figure 4A**). Although the proportions of M2 cells did not differ between the SCI (Prob) and SCI (vector) group (**Figure 4C**), the proportions of M1 cells were significantly increased in the SCI (vector) compared with the sham group while the proportions of M1 cells after probenecid treatment were significantly decreased compared with the SCI (vector) group (**Figure 4B**). This is enough to indicate that probenecid can improve the local immune microenvironment of SCI.

Probenecid Reduces Spinal Cord Tissue Damage, Increases Myelination and the Number of Residual Neurons, and Promotes Functional Recovery

To verify the effect of probenecid on histopathology and behavior after SCI, myelin preservation, the area of lesion, and motor neuron survival were examined by LFB, HE, and Nissl staining, respectively. **Figures 5A**, **6A** are the representative pictures of HE and LFB staining in the 2-mm transverse sections rostral to the epicenter of spinal cords. Lesion areas in the center of

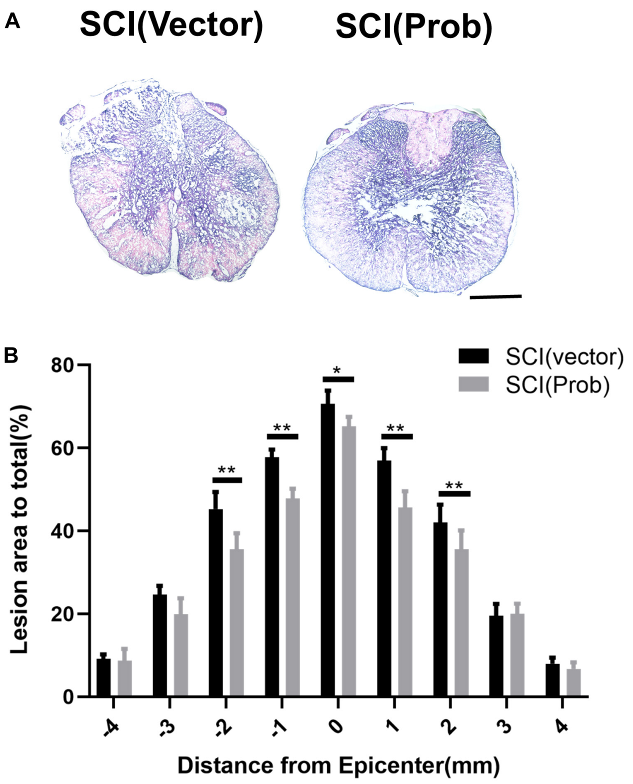

FIGURE 5 | Quantitative analysis of the effect of Probenecid on lesion areas. **(A)** Representative pictures of hematoxylin-eosin (HE) staining in the transverse sections of 2 mm rostral to the epicenter of spinal cords. **(B)** Quantitative analysis of lesion areas in different groups at different distances from the epicenter (0 mm) and 1, 2, 3, and 4 mm rostral (+) and caudal (–) from the epicenter ($^*p < 0.05$, $^{**}p < 0.01$ $n = 6$). Scale bar: 500 μm.

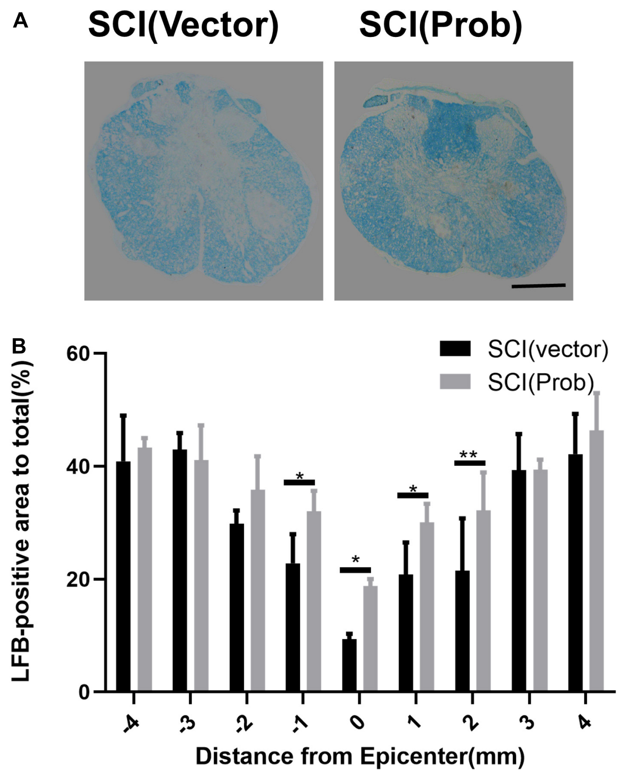

FIGURE 6 | Quantitative analysis of the effect of Probenecid on myelin preservation. **(A)** Representative pictures of LFB staining in the transverse sections of 2 mm rostral to the epicenter of spinal cords. **(B)** Quantitative analysis of residual myelination in different groups at different distances from the epicenter (0 mm) and 1, 2, 3, and 4 mm rostral (+) and caudal (–) from the epicenter ($^*p < 0.05$, $^{**}p < 0.01$ $n = 6$). Scale bar: 500 μm.

injury, 1 and 2 mm rostral and caudal to the epicenter were smaller in the SCI (Prob) group than in the SCI (vector) group (**Figure 5B**). The LFB-positive areas at the lesion epicenter, 1 mm rostral and caudal, and 2 mm rostral to the epicenter in the SCI (Prob) group were larger than those in the SCI (vector) group (**Figure 6B**). **Figure 7A** is a representative Nissl-staining image of neurons in the ventral horn 3 mm rostral to the lesion at 6 weeks post SCI. The number of residual ventral horn motoneurons 3 and 4 mm rostral and caudal to the injury center in the SCI (Prob) group were more than those in the SCI (vector) group (**Figure 7B**).

To research the effect of probenecid on behavioral recovery after SCI, BBB scores were performed at 1, 3, 5, 7, 10, 14, 21, 28, 35, and 42 days after SCI. Both the sham group and the pre-injury score were 21, and there was no significant difference between the SCI (Prob) group and the SCI (vector) group from 1 to 10 days post-injury. At 14, 28, 35, and 42 days, scores were higher in the SCI (Prob) group than in the SCI (vector) group (**Figure 8A**). At 6 weeks following SCI, a grid walk test and the footprint analysis were also used to evaluate the effects of neuroprotection and motor function recovery. The SCI (Prob) group had less footfall errors compared to the SCI (vector) group (**Figure 8B**). Similarly, in the footprint analysis, the scores of the SCI (vector) group were lower than those of the SCI (Prob) group (**Figures 8C,D**).

DISCUSSION

Spinal cord injury is a direct or indirect injury to the spinal cord, which has a high incidence and disability rate, causing pain and suffering to the patient and a heavy burden to the family and society. The pathogenesis of SCI is complex and has not yet been precisely elucidated. It has been reported that a series of cascade reactions, including neuroinflammation, apoptosis, and free radical production, occur during the development of SCI (Rong et al., 2019; Zhu et al., 2020). In this experiment, we establish SCI models in SD rats to investigate the function of probenecid in SCI and its possible mechanism.

Probenecid is a compound with a molecular weight of 285.36 Da, and its molecular formula is $C_{13}H_{19}NO_4S$, which has been used for the treatment of gout clinically (Cheng and Kim, 2020). Probenecid has been found to inhibit oxidative stress in neuronal cells (Cheng and Kim, 2020) and also acts as a pannexin-1 channel inhibitor, which may inhibit the

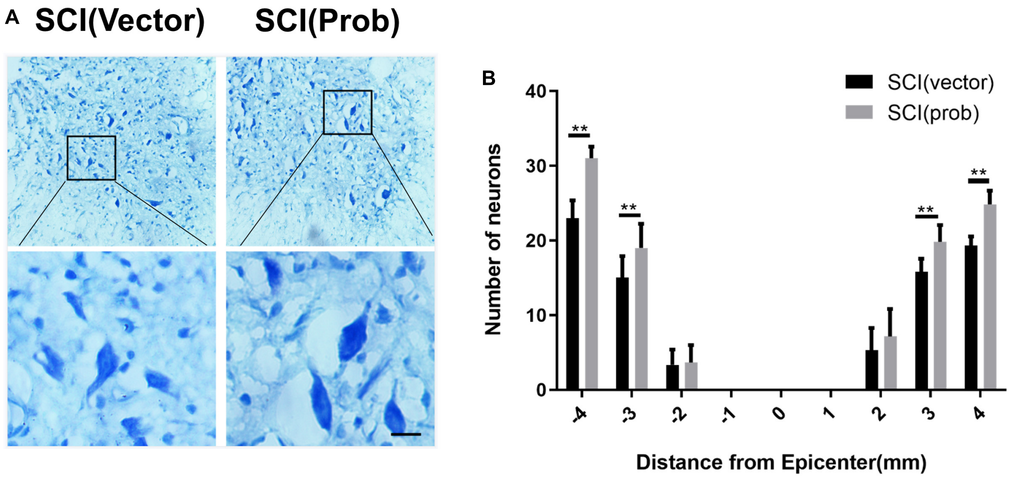

FIGURE 7 | Quantitative analysis of the effect of Probenecid on the number of residual ventral horn neurons. **(A)** Nissl-stained images of neurons in the ventral horn 3 mm rostral to the epicenter at 6 weeks post-SCI. Scale bar: 50 μm. **(B)** Quantitative analysis of residual ventral horn neurons in different groups at different distances from the epicenter of the injury (0 mm) and 1, 2, 3, and 4 mm rostral (+) and caudal (–) from the epicenter. (***p* < 0.01 *n* = 6).

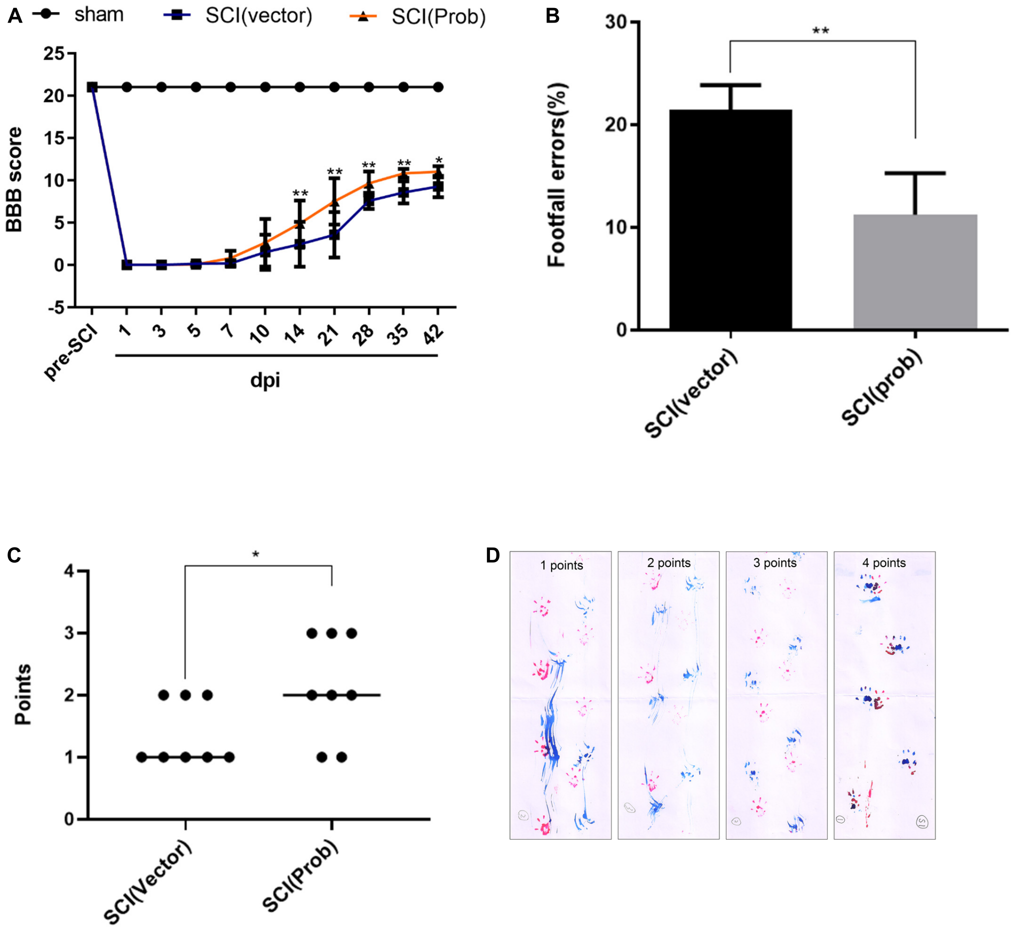

FIGURE 8 | Effects of Probenecid on behavior recovery following SCI. Motor function was evaluated by the BBB scoring, footprint analysis, and grid walk in the SCI (Prob) and SCI (vector) group. **(A)** The BBB scores of the three groups. **(B)** Grid walk test post SCI. **(C)** Footprint analysis post SCI. **(D)** Representative pictures of footprints of different points (**p* < 0.05, ***p* < 0.01 *n* = 8).

activation of inflammasomes (Silverman et al., 2009), as well as being protective in a rat model of cognitive impairment (Cheng and Kim, 2020). These reports suggest that probenecid is therapeutic for CNS injury. Recently, we also found that some signal pathways associated with inflammatory responses can be inhibited by the application of probenecid after SCI *via* the RNA-sequencing analysis (Zhang et al., 2020). Therefore, we hypothesize that probenecid may have anti-inflammatory and neuroprotective effects. The pannexin-1 channel is mainly found in the brain, spinal cord, and thyroid and is the most widely studied channel due to its key role in the activation of inflammasomes (Bruzzone et al., 2003). The literature suggested that it was involved in many diseases, such as Alzheimer's disease, type II diabetes, and atherosclerosis (Karasawa and Takahashi, 2017; Sepehri et al., 2017; White et al., 2017). Some of the inflammasomes involved in pannexin-1 channels, like NLRP1, NLRP2, and NLRP3, have been shown to exert effects in inflammation due to CNS injury (de Rivero Vaccari et al., 2014; Mortezaee et al., 2018). During the process of natural immune defense, the activation of caspase-1 can be regulated by inflammasomes and foster the creation of IL-1β and IL-18 (Lamkanfi and Dixit, 2012; Strowig et al., 2012), ultimately leading to the generation of a series of downstream inflammatory cascade responses. We hypothesized that the pannexin-1 channel could act as an important part to inhibit the activation of inflammasomes, thereby improving the immune microenvironment of SCI and reducing spinal cord nerve injury. It has been shown that probenecid can treat neuropathic pain due to its inhibition of pannexin-1 channels (Bravo et al., 2014). Our experimental results showed that probenecid inhibits the expression and activation of pannexin-1 channel-related molecules, like ASC, NLRP1, IL-1β, and caspase-1 after SCI. The results indicated that probenecid can affect the expression of inflammatory factors downstream of inflammasomes by inhibiting pannexin-1 channels in SCI rat models. Following SCI, inflammatory cells at the site of injury are activated and increased, producing large amounts of inflammatory factors and forming an inflammatory microenvironment, eventually resulting in spinal cord dysfunction (Sun et al., 2016). It has been proven that, under natural conditions, inflammatory cell subsets (e.g., M1) constitute the majority in the local immune microenvironment of SCI, while anti-inflammatory cell subsets (e.g., M2) are fewer (Zhou et al., 2014; Ma et al., 2015; Ahmed et al., 2018), which is an important mechanism for the pathological damage that occurs after SCI. As probenecid inhibits pannexin-1 channels, suppresses the stimulation of inflammasomes, and reduces proinflammatory factors, we hypothesize that probenecid may improve the local immune microenvironment and exert effects to protect the nerve. We used flow cytometry to investigate the effects of probenecid on local immune cell subsets in SCI by detecting CD68, a universal marker of activated microglia/macrophages, and specific markers of M1 ($CCR7^+$) and M2 subtype cells ($CD206^+$). The results showed a significant increase in M1-type macrophages after SCI, which is consistent with the pattern that M1-type macrophages promote the development of inflammatory responses. In the SCI (Prob) group, we found that there was a decrease in M1 cells, which may be the result of prohibiting inflammasome activation by probenecid. We also used the immunofluorescence assay to investigate the effects of probenecid on local immune cell subsets by detecting the specific markers of M1 (CCR-7) and M2 cells (Arg1). Our study indicated that probenecid lessened the number of M1 cells and rose the number of M2 cells compared with the SCI (vector) group. Therefore, we hypothesize that probenecid could affect the polarization of microglia/macrophages, thereby affecting the local immune microenvironment.

These findings suggested that the inhibition of inflammasome activation might reduce M1 cells and increase M2 cells (Ślusarczyk et al., 2018; Su et al., 2020). Taken together, probenecid could inhibit the activation of inflammasomes, thereby affecting microglia/macrophage cell polarization to improve the limited immune microenvironment. These findings supported the possibility that probenecid may provide neuroprotection and improve motor function. Morphological and behavioral tests were also performed to determine whether probenecid has such effects. In the SCI (Prob) group, a meaningful decline in the demyelinating area of spinal cord, a rise in residual ventral horn motor neurons and a considerable improvement in motor function were observed.

CONCLUSION

In summary, the present experimental results indicate that probenecid is restorative in the SCI model in SD rats. The possible mechanism is that probenecid improves rat SCI by inhibiting the activation of inflammasomes, reducing the production of proinflammatory factors, improving the local immune microenvironment, reducing the early inflammatory response, and reducing secondary SCI through the inhibition of Pannexin-1 channels, and the early use of probenecid may be a meaningful strategy for the treatment of SCI.

DATA AVAILABILITY STATEMENT

The raw data supporting the conclusions of this article will be made available by the authors, without undue reservation.

ETHICS STATEMENT

The animal study was reviewed and approved by Committee on the Laboratory Animal Care and Use of the Bengbu Medical College.

AUTHOR CONTRIBUTIONS

Y-XZ participated in literature search, study design, and writing. H-ZL participated in the study design and data interpretation. QQ and X-XW performed experimental procedures and statistically analyzed the data. J-LL, Y-QC, J-RC, and JX conducted data analysis and figures. All authors read and approved the final manuscript.

FUNDING

This work was supported by the National Natural Science Foundation of China (Nos. 81772321 and 82072416); Program of Natural Science Foundation of the Anhui Higher Education Institutions (No. KJ2020A0587); and Research Innovation Program for Graduate Students of Bengbu Medical College (No. Byycx21003).

ACKNOWLEDGMENTS

We are grateful to Jian-Guo Hu for helpful comments, as well as to Lin Shen and Rui Wang for their generous contributions to this article.

SUPPLEMENTARY MATERIAL

The Supplementary Material for this article can be found online at: https://www.frontiersin.org/articles/10.3389/fnmol.2022.848185/full#supplementary-material

REFERENCES

Ahmed, A., Patil, A. A., and Agrawal, D. K. (2018). Immunobiology of spinal cord injuries and potential therapeutic approaches. *Mol. Cell. Biochem.* 441, 181–189. doi: 10.1007/s11010-017-3184-9

Baranova, A., Ivanov, D., Petrash, N., Pestova, A., Skoblov, M., Kelmanson, I., et al. (2004). The mammalian pannexin family is homologous to the invertebrate innexin gap junction proteins. *Genomics* 83, 706–716. doi: 10.1016/j.ygeno.2003.09.025

Bravo, D., Ibarra, P., Retamal, J., Pelissier, T., Laurido, C., Hernandez, A., et al. (2014). Pannexin 1: a novel participant in neuropathic pain signaling in the rat spinal cord. *Pain* 155, 2108–2115. doi: 10.1016/j.pain.2014.07.024

Bruzzone, R., Hormuzdi, S. G., Barbe, M. T., Herb, A., and Monyer, H. (2003). Pannexins, a family of gap junction proteins expressed in brain. *Proc. Natl. Acad. Sci. U.S.A.* 100, 13644–13649. doi: 10.1073/pnas.2233464100

Chen, Y. Q., Wang, S. N., Shi, Y. J., Chen, J., Ding, S. Q., Tang, J., et al. (2020). CRID3, a blocker of apoptosis associated speck like protein containing a card, ameliorates murine spinal cord injury by improving local immune microenvironment. *J. Neuroinflammation* 17:255. doi: 10.1186/s12974-020-01937-8

Cheng, M. H., and Kim, S. J. (2020). Inhibitory effect of probenecid on osteoclast formation via JNK, ROS and COX-2. *Biomol. Ther. (Seoul.)* 28, 104–109. doi: 10.4062/biomolther.2019.047

Christgen, S., Place, D. E., and Kanneganti, T. D. (2020). Toward targeting inflammasomes: insights into their regulation and activation. *Cell Res.* 30, 315–327. doi: 10.1038/s41422-020-0295-8

de Rivero Vaccari, J. P., Dietrich, W. D., and Keane, R. W. (2014). Activation and regulation of cellular inflammasomes: gaps in our knowledge for central nervous system injury. *J. Cereb. Blood Flow Metab.* 34, 369–375. doi: 10.1038/jcbfm.2013.227

Gaojian, T., Dingfei, Q., Linwei, L., Xiaowei, W., Zheng, Z., Wei, L., et al. (2020). Parthenolide promotes the repair of spinal cord injury by modulating M1/M2 polarization via the NF-κB and STAT 1/3 signaling pathway. *Cell Death Discov.* 6, 97. doi: 10.1038/s41420-020-00333-8

Gensel, J. C., and Zhang, B. (2015). Macrophage activation and its role in repair and pathology after spinal cord injury. *Brain Res.* 1619, 1–11. doi: 10.1016/j.brainres.2014.12.045

Karasawa, T., and Takahashi, M. (2017). Role of NLRP3 inflammasomes in atherosclerosis. *J. Atheroscler. Thromb.* 24, 443–451. doi: 10.5551/jat.RV17001

Lamkanfi, M., and Dixit, V. M. (2012). Inflammasomes and their roles in health and disease. *Annu. Rev. Cell Dev. Biol.* 28, 137–161. doi: 10.1146/annurev-cellbio-101011-155745

Ma, S. F., Chen, Y. J., Zhang, J. X., Shen, L., Wang, R., Zhou, J. S., et al. (2015). Adoptive transfer of M2 macrophages promotes locomotor recovery in adult rats after spinal cord injury. *Brain Behav. Immun.* 45, 157–170. doi: 10.1016/j.bbi.2014.11.007

Martinez, F. O., Sica, A., Mantovani, A., and Locati, M. (2008). Macrophage activation and polarization. *Front. Biosci.* 13, 453–461. doi: 10.2741/2692

Mawhinney, L. J., de Rivero Vaccari, J. P., Dale, G. A., Keane, R. W., and Bramlett, H. M. (2011). Heightened inflammasome activation is linked to age-related cognitive impairment in Fischer 344 rats. *BMC Neurosci.* 12:123. doi: 10.1186/1471-2202-12-123

Metz, G. A., Merkler, D., Dietz, V., Schwab, M. E., and Fouad, K. (2000). Efficient testing of motor function in spinal cord injured rats. *Brain Res.* 883, 165–177. doi: 10.1016/s0006-8993(00)02778-5

Milich, L. M., Ryan, C. B., and Lee, J. K. (2019). The origin, fate, and contribution of macrophages to spinal cord injury pathology. *Acta Neuropathol.* 137, 785–797. doi: 10.1007/s00401-019-01992-3

Mortezaee, K., Khanlarkhani, N., Beyer, C., and Zendedel, A. (2018). Inflammasome: its role in traumatic brain and spinal cord injury. *J. Cell. Physiol.* 233, 5160–5169. doi: 10.1002/jcp.26287

Papadopoulos, M. C., and Verkman, A. S. (2008). Potential utility of aquaporin modulators for therapy of brain disorders. *Prog. Brain Res.* 170, 589–601. doi: 10.1016/S0079-6123(08)00446-9

Pineda-Farias, J. B., Pérez-Severiano, F., González-Esquivel, D. F., Barragán-Iglesias, P., Bravo-Hernández, M., Cervantes-Durán, C., et al. (2013). The L-kynurenine-probenecid combination reduces neuropathic pain in rats. *Eur. J. Pain* 17, 1365–1373. doi: 10.1002/j.1532-2149.2013.00305.x

Rong, Y., Liu, W., Zhou, Z., Gong, F., Bai, J., Fan, J., et al. (2019). Harpagide inhibits neuronal apoptosis and promotes axonal regeneration after spinal cord injury in rats by activating the Wnt/β-catenin signaling pathway. *Brain Res. Bull.* 148, 91–99. doi: 10.1016/j.brainresbull.2019.03.014

Scholtes, F., Brook, G., and Martin, D. (2012). Spinal cord injury and its treatment: current management and experimental perspectives. *Adv. Tech. Stand. Neurosurg.* 38, 29–56. doi: 10.1007/978-3-7091-0676-1_2

Sepehri, Z., Kiani, Z., Afshari, M., Kohan, F., Dalvand, A., and Ghavami, S. (2017). Inflammasomes and type 2 diabetes: An updated systematic review. *Immunol. Lett.* 192, 97–103. doi: 10.1016/j.imlet.2017.10.010

Silverman, W. R., de Rivero Vaccari, J. P., Locovei, S., Qiu, F., Carlsson, S. K., Scemes, E., et al. (2009). The pannexin 1 channel activates the inflammasome in neurons and astrocytes. *J. Biol. Chem.* 284, 18143–18151. doi: 10.1074/jbc.M109.004804

Ślusarczyk, J., Trojan, E., Głombik, K., Piotrowska, A., Budziszewska, B., Kubera, M., et al. (2018). Targeting the NLRP3 inflammasome-related pathways via tianeptine treatment-suppressed microglia polarization to the M1 phenotype in lipopolysaccharide-stimulated cultures. *Int. J. Mol. Sci.* 19:1965. doi: 10.3390/ijms19071965

Strowig, T., Henao-Mejia, J., Elinav, E., and Flavell, R. (2012). Inflammasomes in health and disease. *Nature* 481, 278–286. doi: 10.1038/nature10759

Su, X. Q., Wang, X. Y., Gong, F. T., Feng, M., Bai, J. J., Zhang, R. R., et al. (2020). Oral treatment with glycyrrhizin inhibits NLRP3 inflammasome activation and promotes microglial M2 polarization after traumatic spinal cord injury. *Brain Res. Bull.* 158, 1–8. doi: 10.1016/j.brainresbull.2020.02.009

Sun, X., Jones, Z. B., Chen, X. M., Zhou, L., So, K. F., and Ren, Y. (2016). Multiple organ dysfunction and systemic inflammation after spinal cord injury: a complex relationship. *J. Neuroinflammation* 13:260. doi: 10.1186/s12974-016-0736-y

Wang, Y., Yuan, Y., Gao, Y., Li, X., Tian, F., Liu, F., et al. (2019). MicroRNA-31 regulating apoptosis by mediating the phosphatidylinositol-3 kinase/protein kinase B signaling pathway in treatment of spinal cord injury. *Brain Dev.* 41, 649–661. doi: 10.1016/j.braindev.2019.04.010

White, C. S., Lawrence, C. B., Brough, D., and Rivers-Auty, J. (2017). Inflammasomes as therapeutic targets for Alzheimer's disease. *Brain Pathol.* 27, 223–234. doi: 10.1111/bpa.12478

Wu, X., and Xu, X. M. (2016). RhoA/Rho kinase in spinal cord injury. *Neural Regen. Res.* 11, 23–27. doi: 10.4103/1673-5374.169601

Zhang, Y. X., Wang, S. N., Chen, J., Hu, J. G., and Lü, H. Z. (2020). A transcriptomic study of probenecid on injured spinal cords in mice. *PeerJ* 8:e8367. doi: 10.7717/peerj.8367

Zhou, X., He, X., and Ren, Y. (2014). Function of microglia and macrophages in secondary damage after spinal cord injury. *Neural Regen. Res.* 9, 1787–1795. doi: 10.4103/1673-5374.143423

Zhu, N., Ruan, J., Yang, X., Huang, Y., Jiang, Y., Wang, Y., et al. (2020). Triptolide improves spinal cord injury by promoting autophagy and inhibiting apoptosis. *Cell Biol. Int.* 44, 785–794. doi: 10.1002/cbin.11273

Conflict of Interest: The authors declare that the research was conducted in the absence of any commercial or financial relationships that could be construed as a potential conflict of interest.

frontiers | Frontiers in Molecular Neuroscience

ORIGINAL RESEARCH
published: 17 June 2022
doi: 10.3389/fnmol.2022.888351

Premature Neural Progenitor Cell Differentiation Into Astrocytes in Retinoic Acid-Induced Spina Bifida Rat Model

Marc Oria[1,2]*, Bedika Pathak[1], Zhen Li[1], Kenan Bakri[1], Kara Gouwens[1], Maria Florencia Varela[1], Kristin Lampe[1], Kendall P. Murphy[1,3], Chia-Ying Lin[3] and Jose L. Peiro[1,2]

[1] Center for Fetal and Placental Research, Cincinnati Children's Hospital Medical Center (CCHMC), Cincinnati, OH, United States, [2] Department of Surgery, College of Medicine, University of Cincinnati, Cincinnati, OH, United States, [3] Department of Orthopaedic Surgery, College of Medicine, University of Cincinnati, Cincinnati, OH, United States

During embryonic spinal cord development, neural progenitor cells (NPCs) generate three major cell lines: neurons, oligodendrocytes, and astrocytes at precise times and locations within the spinal cord. Recent studies demonstrate early astrogenesis in animal models of spina bifida, which may play a role in neuronal dysfunction associated with this condition. However, to date, the pathophysiological mechanisms related to this early astrocytic response in spina bifida are poorly understood. This study aimed to characterize the development of early astrogliosis over time from Pax6+, Olig2+, or Nkx2.2+ NPCs using a retinoic acid-induced spina bifida rat model. At three gestational ages (E15, E17, and E20), spinal cords from fetuses with retinoic acid-induced spina bifida, their healthy sibling controls, or fetuses treated with the vehicle control were analyzed. Results indicated that premature astrogliosis and astrocytic activation were associated with an altered presence of Pax6+, Olig2+, and Nkx2.2+ NPCs in the lesion compared to the controls. Finally, this response correlated with an elevation in genes involved in the Notch-BMP signaling pathway. Taken together, changes in NPC patterning factor expression with Notch-BMP signaling upregulation may be responsible for the altered astrogenesis patterns observed in the spinal cord in a retinoic acid-induced spina bifida model.

Keywords: neural tube defect (NTD), spina bifida (SB), neural progenitor cell (NPC), astrogenesis, Pax6, Olig2, Nkx2.2

Edited by:
Lingyan Xing,
Nantong University, China

Reviewed by:
Jiajing Sheng,
Nantong University, China
Vladimir Kenis,
Turner Scientific Research Institute
for Children's Orthopedics, Russia

***Correspondence:**
Marc Oria
Marc.Oria@cchmc.org

Specialty section:
This article was submitted to
Neuroplasticity and Development,
a section of the journal
Frontiers in Molecular Neuroscience

Received: 02 March 2022
Accepted: 16 May 2022
Published: 17 June 2022

Citation:
Oria M, Pathak B, Li Z, Bakri K, Gouwens K, Varela MF, Lampe K, Murphy KP, Lin C-Y and Peiro JL (2022) Premature Neural Progenitor Cell Differentiation Into Astrocytes in Retinoic Acid-Induced Spina Bifida Rat Model. Front. Mol. Neurosci. 15:888351. doi: 10.3389/fnmol.2022.888351

INTRODUCTION

Spina bifida, characterized by the failure of the neural tube to close fully during embryonic development, is a defect that leads to neurological and physiological disabilities in the fetus, including motor, urinary, intestinal, and sexual dysfunctions, as well as impaired mental development (Mitchell et al., 2004). Often referred as the "two-hit" hypothesis, the primary neural tube defect is followed by *in utero* neurodegeneration secondary to mechanical and chemical trauma (Meuli and Moehrlen, 2014). The components of the amniotic fluid, such as meconium, likely contribute to this neurodegeneration with advancing gestation, which is supported by the significant neurologic improvement observed after *in utero* repair of the defect (Adzick et al., 2011; Moldenhauer and Adzick, 2017). A better understanding of this neural injury's progression will aid in the development of targeted therapeutics that can combat neurodegeneration.

During normal spinal cord development in the fetus, the ventricular zone (VZ) contains multipotent neural progenitor cells (NPCs) that generate three major cell lineages: neurons, oligodendrocytes, and astrocytes. Moreover, the fate of each cell type depends on the time in which NPCs are initiated to differentiate and their location in the neuroepithelial (Temple, 2001). In normal conditions, neurogenesis occurs in the early embryonic stage, and astrogenesis and oligodendrogenesis occur later in development and even after birth (Reemst et al., 2016). However, recent studies demonstrate that astrocyte differentiation, proliferation, and activation occur earlier in the spinal cord of animals with chemically induced spina bifida (Oria et al., 2018). This early astrocytic reaction may play a role in the impaired neurogenesis and, therefore, the decline in overall neural tissue function. To date, the pathophysiological mechanisms related to this early astrocytic response in spina bifida are poorly understood. However, we anticipate that the regulation of NPC differentiation plays a critical role in this reaction.

Complex interactions between intracellular transcriptional regulators and extracellular signals define the timing and the location of NPC differentiation. For example, transcription factors in the ID and Hes gene families have been implicated as master regulators of normal astrocyte differentiation (Bertrand et al., 2002). Additionally, homeodomain factors, including Pax6 and Nkx2.2, and basic helix loop helix factor, Olig2, determine the differentiation fate of NPCs located on the dorsoventral wall. Moreover, NPCs located on the dorsoventral wall also differentiate depending on bone morphogenetic proteins (BMPs), produced by the roof plate, and sonic hedgehog (Shh), produced by the floor plate (Ulloa and Briscoe, 2007; Molofsky et al., 2012). These morphogens are key regulators of NPC differentiation potential toward neuron and glia cell lineages (Dennis et al., 2019). Interestingly, changes in these transcriptional and extracellular signals may be a possible mechanism for earlier astrocyte presence in spina bifida; however, this has not yet been investigated.

This study characterizes the expression of transcription factors and extracellular signals that regulate NPC differentiation at three time points during gestation (E15, E17, and E20) in a retinoic acid (RA)-induced rat model of *in utero* spina bifida. Importantly, we demonstrate a possible implication of Pax6, Nkx2.2, and Olig2 transcription factors, as well as factors in the Notch-BMP signaling pathway, in the premature shift of NPCs into astrocytes in fetuses with RA-induced spina bifida. These results may lead to new possible therapeutic targets for regulating neurogenesis and gliogenesis in patients with spina bifida.

MATERIALS AND METHODS

The experimental protocols were in agreement with the National Institutes of Health Guidelines for Care and Use of Laboratory Animals and were approved by the Institutional Animal Care and Use Committee at Cincinnati Children's Hospital Medical Center (IACUC 2019-0081).

Congenital Retinoic Acid-Induced Spina Bifida Animal Model and Experimental Design

The study was performed using 36 timed-pregnant Sprague-Dawley rats weighing 200–250 g (Charles River Laboratories, Inc., Wilmington, MA, United States) and housed at 22°C in a standard dark:light cycle (10:14 h) (light 7:00–19:00) with access to water and standard food *ad libitum*. Mating date was defined as E1 and plug day as E0. Trans-retinoic acid (RA) (Sigma-Aldrich Chemical, St. Louis, MO, United States) was solubilized in olive oil (vehicle) at room temperature, protected from light, and used within 1 h of preparation. Twenty rats were gavaged with RA (100 mg/kg) and 16 rats with an equal volume of the vehicle on E10 at 10 a.m. With this model, 70% of fetuses in each liter were diagnosed with spina bifida (Oria et al., 2018).

The following groups were assessed at three gestational ages (E15, E17, and E20):

1. MMC: open spinal cords from fetuses with RA-induced spina bifida ($n = 6–8$ per time point).
2. Control: spinal cords from non-affected siblings of RA-treated rats ($n = 6–8$ per time point).
3. Vehicle: spinal cords from fetuses whose mothers received vehicle (olive oil) ($n = 6–8$ per time point).

Tissue Processing

At each gestational time point (E15, E17, and E20), spinal cords from vehicle, control, and MMC fetuses were dissected, snap-frozen, and stored at −80°C until analyzed for gene expression. For histological analysis, spinal cords were dissected and fixed in 4% paraformaldehyde for 24 h and processed for paraffin embedding.

RNA Extraction and RT-qPCR Analysis

Frozen spinal cords were suspended in RLT buffer and then homogenized using an IkaT10 basic Ultra-Turrax homogenizer. RNA was extracted using the RNeasy Plus Mini Kit (Qiagen Science, Hilden, Germany) following manufacturer's protocol and RNA quantity was assessed through spectrophotometric analysis using an Epoch Biotek spectrophotometer (Biotek Instruments, Winooski, VT, United States). Utilizing the RT^2 First Strand Kit (Qiagen Sciences, MD, United States), 1 μg RNA/sample was reverse transcribed into cDNA. A 1-μg cDNA sample was then used as a template for RT-qPCR employing TaqMan® gene expression assays (Applied Biosystems, Foster City, CA, United States) (**Supplementary Table 1**) in the 7500 Fast Real-Time PCR System. Samples were ran in duplicate for target genes and were normalized using HPRT1 as an endogenous control. Relative quantification of transcript expression was performed using the $2^{-\Delta\Delta Ct}$ method where C_t represents the threshold cycle.

RNA-seq Data Processing and Analysis

Raw FastQ files from the RNA-seq data Sequence Read Archive (SRA)[1] and BioProject (PRJNA683230) and SRA (PRJNA683793)

---

[1] https://ncbi.nlm.nih.gov/sra/

published by Murphy et al. (2021) were processed through the AltAnalyze package v2.0[2] (Emig et al., 2010). The GOseqR package was used to perform gene ontology (GO) enrichment analysis and GO terms with a corrected *p*-value less than 0.05 were considered statistically significant. This analysis identified differentially expressed genes between control, vehicle, and MMC groups at E15, E17, and E20 (Emig et al., 2010). The analysis was conducted according to the functional annotation in "Neurogenesis" genes in the GO database (GO:0022008). Additionally, analysis was conducted according to the functional annotation "Astrocyte Differentiation" genes in the GO database (GO:0048708) and "Oligodendrocyte Differentiation" in the GO database (GO:0048709), sub-classifications within the "Neurogenesis" GO database.

Immunostaining

Sections were deparaffinized, rehydrated, and incubated in sodium citrate buffer (pH 6) for 30 min at 95°C to retrieve antigens. Sections were permeabilized with 0.5% Triton X-100 (Sigma-Aldrich, St. Louis, MO, United States) in phosphate-buffered saline (PBS) and incubated in 3% peroxide for 15 min at room temperature. Non-specific binding was blocked for 1 h with 5% BSA in PBS at room temperature, and sections were then incubated overnight at 4°C in a humidity chamber with the following primary antibodies: anti-Olig2 (Millipore, #AB9610 Rabbit and #ABE1024, Guinea Pig) (1:1,000), anti-GFAP (Abcam, #AB4674, Chicken) (1:500), anti-Pax6 (Abcam #ab5790, Rabbit) (1:1,000), anti-Nkx2.2 (Novus Biological, #NBP2-34799, Mouse) (1:500), anti-Nestin (BD Biosciences, #556309, Rat) (1:50), anti-Vimentin (Sigma, #V6630, Mouse) (1:200), BMP-4 (Invitrogen, #PA5-19683, Rabbit) (1:800), BMP-2 (Invitrogen, #PA5-78874, Rabbit) (1:250), S100b (Sigma, #SAB4200671, Mouse) (1:500), Tubulin β III (TUBB3) (Abcam, #ab18207, Rabbit) (1:500) Aldh1l1 (Novus Biological #NBP2-50045, Mouse) (1:1,000), AQP4 (Sigma #A4971, Rabbit) and Doublecortin (DCX) (Invitrogen #PA5-17428, Rabbit) (1:200). Sections were washed and incubated for 1 h with Alexa Fluor 488 (#1531671, Donkey and #1531669 Goat, #1990462, Goat), Alexa Fluor 568 (#1691230, Goat, #1398018, Goat, #1504529, Goat), or Alexa Fluor 647 (#1445259, Goat, #1608641, Donkey) conjugated secondary antibodies (Life Technologies) (1:1,000) in the dark at room temperature in a humidity chamber. Slides were washed, covered with mounting media containing DAPI (Southern Biotech, Birmingham, AL, United States), and visualized with a Nikon fluorescent microscope (Nikon Inc., Melville, NY, United States).

Immunolabeled Cell and Area Quantification

Pax6+, Olig2+, Nkx2.2+ cell counts, and GFAP+ immunostained area measurement was done using NIS Elements AR 4.5 software (Nikon Instruments Inc.). Quantification was conducted using more than ten random high magnification images per spinal cord section in three consecutives sections from each animal. This analysis was conducted in 4–6 animals per group. Cell count data is reported as the percentage of immuno-positive cells compared to the total number of cells in each area. Area is reported as the positively stained area in square pixels as a percentage of the total area. All quantifications were performed by an investigator blinded to the experimental groups.

Statistical Analysis

All statistical analysis and graphs were performed in Graph Pad Prism 9 software (GraphPad Software Inc., La Jolla, CA, United States). Differences among multiple groups were analyzed by one-way analysis of variances (ANOVA) using Turkey's *post hoc* test. Differences among the same group at different time points were analyzed by two-way ANOVA using Tukey's *post hoc* test. Results are reported as means ± standard error (SE) for the relative gene expression ($2^{-\Delta\Delta Ct}$) and means ± standard deviation (SD) for all cell counting analysis. A p-value < 0.05 was considered statistically significant.

RESULTS

Precautious Astrocyte Generation in Spina Bifida

Altered cell quantification of astrocytes (GFAP) and neurons (NeuN) expression has been described in spina bifida *in utero* (Reis et al., 2007; Danzer et al., 2011; Oria et al., 2018), but the correlation with the NPC which are the origin of these differentiated cell types it is not understood in spina bifida physiopathology. In previous mentioned works neuronal numbers decreased during gestation in spina bifida. To determine the neuronal fate and the distribution of premature neurons, we stained spinal cords with Class III β-tubulin and Doublecortin (Dcx) markers of progenitor cells committed to a neuronal fate. In rat fetuses, spina bifida led to extensive loss of Class III β-tubulin and Dcx as gestation progresses suggesting decrease in the expression of premature neurons compared to the controls with normal development (**Supplementary Figure 1**).

Motivated by evidence that neural cell fate differentiation processes are impacted, with decreased neurogenesis, decreased oligodendrogenesis, and increased astrogenesis, as the RNA-seq (Murphy et al., 2021) and previous work in spina bifida in rats (Oria et al.,. 2018) are described; we investigated how astrocyte presence in the fetal spinal cord at various time points was affected by exposure of the NPC to the amniotic fluid in spina bifida. Not only has GFAP been used in immunohistochemical studies to characterize changes in reactive astrocytosis, but it has also been used in developmental studies as a major mature-astrocyte marker (Koyama, 2014) and therefore was our primary indicator of astrocytes. Interestingly, we observed significant robust upregulation of astrocyte marker, glial fibrillary acidic protein (GFAP), gene expression in MMC fetuses compared to vehicle and control at each studied time point ($^{***}p < 0.001$) (**Figure 1A**). Similarly observed in the RNA-seq results with upregulated GFAP expression at all three time points (E15, E17, and E20) but not significant at E17 and E20 (**Supplementary Table 2**). Immunofluorescent staining indicates that this upregulation correlates with an elevation in

---

[2] http://www.altanalyze.org

the area stained with GFAP in MMC at E15 and E17 before any GFAP-positive cells are detected in normal control groups suggesting the accelerated gliogenesis altered process by spina bifida immature spinal cord ($^{*}p < 0.05$, $^{**}p < 0.01$, $^{***}p < 0.001$) (**Figures 1B,C**). As observed in normal development (Yoon et al., 2017) after E18.5 but mostly at E21 and postnatal, astrocytes beneath the pial surface begin expressing GFAP, which is evident in control and vehicle fetuses where more area is positive for GFAP at E20 compared to E15 and E17 ($^{\#}p < 0.05$, control and vehicle E20 vs. E15 and E17) (**Figures 1B,C**). Importantly, early expression of GFAP is observed in the open spinal cords of MMC fetuses that are exposed to the amniotic fluid (**Figure 1B**). This area corresponds to the VZ and sub-ventricular zone (SVZ), where NPCs are normally located and responsible for neural development processes. In this VZ, we observed distribution of GFAP-hypertrophic positive astrocytes appeared as numerous aggregates throughout the lesion near the exposed neural tissue in spina bifida fetuses. In addition, glial cells (GFAP) do not express in the VZ of control group and the expression in the white matter are not hypertrophic and showed elongated bodies and long filamentous projection (**Figures 1B,D**).

Next, we investigated the reactivity of this GFAP+ astrocyte population in spinal cord sections from MMC and control groups, as reactivity is a major feature of spinal cord injury. This reactivity was determined based on co-expression of GFAP, vimentin, and nestin after immunostaining. Under normal spinal cord development, early neuroepithelial progenitors in the spinal cord and radial glial cells express nestin and vimentin, as we observed in vehicle control and RA control spinal cord tissue sections at E15 (**Figure 2**). Numerous processes in the dorsal and ventral halves radiating from the central canal, corresponding to radial glial, express vimentin, and nestin (Barry and McDermott, 2005) (**Figures 2A,B**). Although you only see that during embryonic development (radial glial) and then very rarely in adult neurogenic zones. At E20 in healthy fetal spinal cords, GFAP is highly expressed in the white matter; however, GFAP+ cells (green) are deemed unreactive as GFAP staining does not co-localize completely with nestin and vimentin. In these representative sections, nestin and vimentin are predominantly expressed in the white matter's radial astrocytes and attenuated radial glial cells of the gray matter. In contrast, we observed hypertrophic and reactive astroglia in MMC fetal spinal cords as indicated by GFAP co-localization with vimentin and nestin (yellow) as early as E15 but is a prominent response by E20 (**Figure 2B**, white arrows). GFAP co-localization with nestin and vimentin was observed in focal points at E15 and E17 when GFAP expression was not detected in control/vehicle tissues.

In addition, this reactive astroglia was predominantly found in the VZ as well as the medial septum and radial processes, areas directly exposed to the amniotic fluid as a result of the defect and different expression pattern was evident compared to control groups (**Figures 2A,B**, white arrows). Furthermore, immunofluorescent staining indicates an increase in the area stained with GFAP + Nestin and GFAP + Vimentin in MMC fetuses at the different time points even before any GFAP-positive cells are detected in normal control groups (E15 and E17) suggesting the accelerated gliogenesis and activation process by spina bifida immature spinal cord ($^{**}p < 0.01$, $^{***}p < 0.001$) (**Figure 2C**). In normal development at E21 astrocytes beneath the pial surface in the white matter begin expressing GFAP, also some area is positive for GFAP + Nestin or GFAP + Vimentin compared control but also the distribution is not the same location as in MMC is located in the VZ. This increase in co-expression of GFAP and Nestin or Vimentin also is increased at the end of gestation compared to E15 and E17 ($^{\#}p < 0.05$, control and vehicle E20 vs. E15 and E17) (**Figure 2C**).

To further validate the expression of astrocytic markers and astroglia reactivity in the VZ exposed to the amniotic fluid in MMC fetuses were determined using immunostaining with other premature astrocyte markers as Aldh1l1 and Aquaporin 4 (AQP4). Using both markers we observed and increase of expression at E17 gestational age (**Figures 3**, **4**). The expression of AQP4 and Aldh1l1 decreased at E20 which correlated with the increase of GFAP expression, used as more mature astrocyte marker (**Figures 3**, **4**). The expression of both Aldh1l1 and AQP4 were observed in the VZ, niche of the NPC and exposed to the amniotic fluid in MMC fetuses.

Gene Ontology Functional Analysis of Differential Expressed Genes in Neurogenesis

To gain molecular insights into the injury responses that are mediated by the exposure of the neural tissue to the amniotic fluid in spina bifida *in utero*, we conducted transcriptome analysis of existing RNA-seq datasets from lumbar spinal cords of fetuses in each experimental group at E15, E17, and E20 (Murphy et al., 2021). Gene expression levels were compared between fetuses with MMC and their control siblings (control) or those that received olive oil (vehicle). Hierarchical cluster analysis of differentially expressed genes demonstrated transcriptome-wide expression patterns that were similar between spinal cords collected from vehicle and control fetuses compared to those from MMC at all three gestational ages: E15, E17, and E20 days (**Figure 5A**) as published by Murphy et al. (2021). An analysis from the RNA-seq study was conducted according to the functional annotation in "Neurogenesis" genes in the GO database (GO:0022008). From the 4,975 annotations, we identified 388 genes that were expressed differently between MMC and the two control groups at E15 (**Supplementary Table 3** and **Figure 5B**), 39 genes were expressed differently between MMC and the two control groups at E17 (**Supplementary Table 4** and **Figure 5B**), and 12 genes were expressed differently between MMC and the two control groups at E20 (**Supplementary Table 5** and **Figure 5B**). Finally, only seven genes were differentially expressed in the neurogenesis GO between vehicle and control at E15 (**Supplementary Table 3** and **Figure 5B**), zero at E17 (**Figure 5B**), and one at E20 (**Supplementary Table 5** and **Figure 5B**).

Analysis of two sub-classifications within the Neurogenesis GO, Oligodendrocyte Differentiation (GO:0048709), and Astrocyte Differentiation (GO:0048708), was conducted to elucidate the early changes in gene expression that could change the NPC fate. Within Oligodendrocyte Differentiation

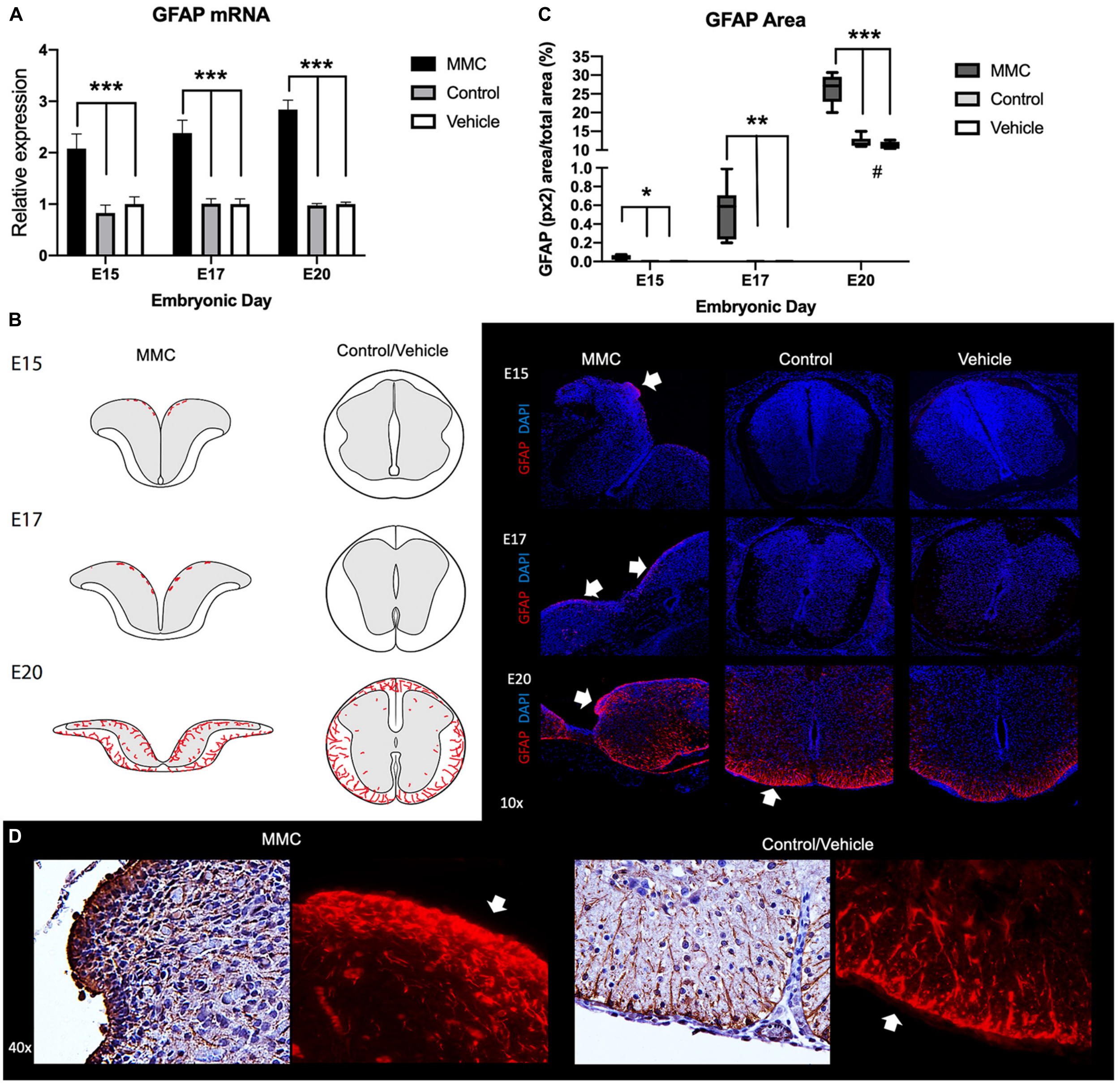

FIGURE 1 | Progressive immunoreactive astrocytes in spina bifida fetuses. **(A)** GFAP relative expression increased in spina bifida (MMC) compared with control and vehicle spinal cords. Values (means ± SE, 6 fetuses/group) of relative expression ($2^{-\Delta\Delta Ct}$) for RA-treated and time-matched controls (***$p < 0.001$). **(B)** Schematic representation of GFAP distribution in MMC and control fetal spinal cords at E15, E17, and E20 (left). GFAP staining (right) in MMC, control, and vehicle fetal spinal cords at E15, E17, and E20. Progressive GFAP+ (red) DAPI+ (blue) immunoreactive astrocyte cells at E15, E17, and E20 in exposed spina bifida (arrows) (10× images). **(C)** GFAP stained area/total picture area in all groups at three gestational ages E15, E17, and E20 (means ± SD, *$p < 0.05$, **$p < 0.01$, ***$p < 0.001$, $^{\#}p < 0.05$ between control and vehicle groups at E20 compared to E15 and E17). **(D)** GFAP-immunoreactive astrocytes in spina bifida (MMC) VZ exposed to the amniotic fluid compared to filamentous astrocyte projections in white matter control spinal cords at E20 (40X).

(GO:0048709), we identified 31 genes differentially expressed between MMC and control groups at E15, 5 at E17 and 3 at E20 from the 174 annotations. At early stages, E15, we identified changes in genes in oligodendrocyte differentiation (Olig1, Olig2, Slc8a3, Sox10, Tmem98, Bmp4, Dusp10, Dusp15, Eif2b2, Enpp2, Errbb2, Gsx2, Hdac1, Hes1, Il34, Mag, Mdk, Med12, Nkx6-1, Notch1, and Ntrkn1), oligodendrocyte development (Tcf7l2 and Ascl1), myelinization (Cntnap1) when compared to controls (**Figure 1C**). Additionally, within Astrocyte Differentiation (GO:0048708), we identified 41 genes dysregulated in MMC vs. control groups at E15, 4 genes at E17 and 2 genes at E20 (**Figure 5C**) from the 424 annotations. Examining the differentially expressed genes in the Astrocyte Differentiation GO, we observed early

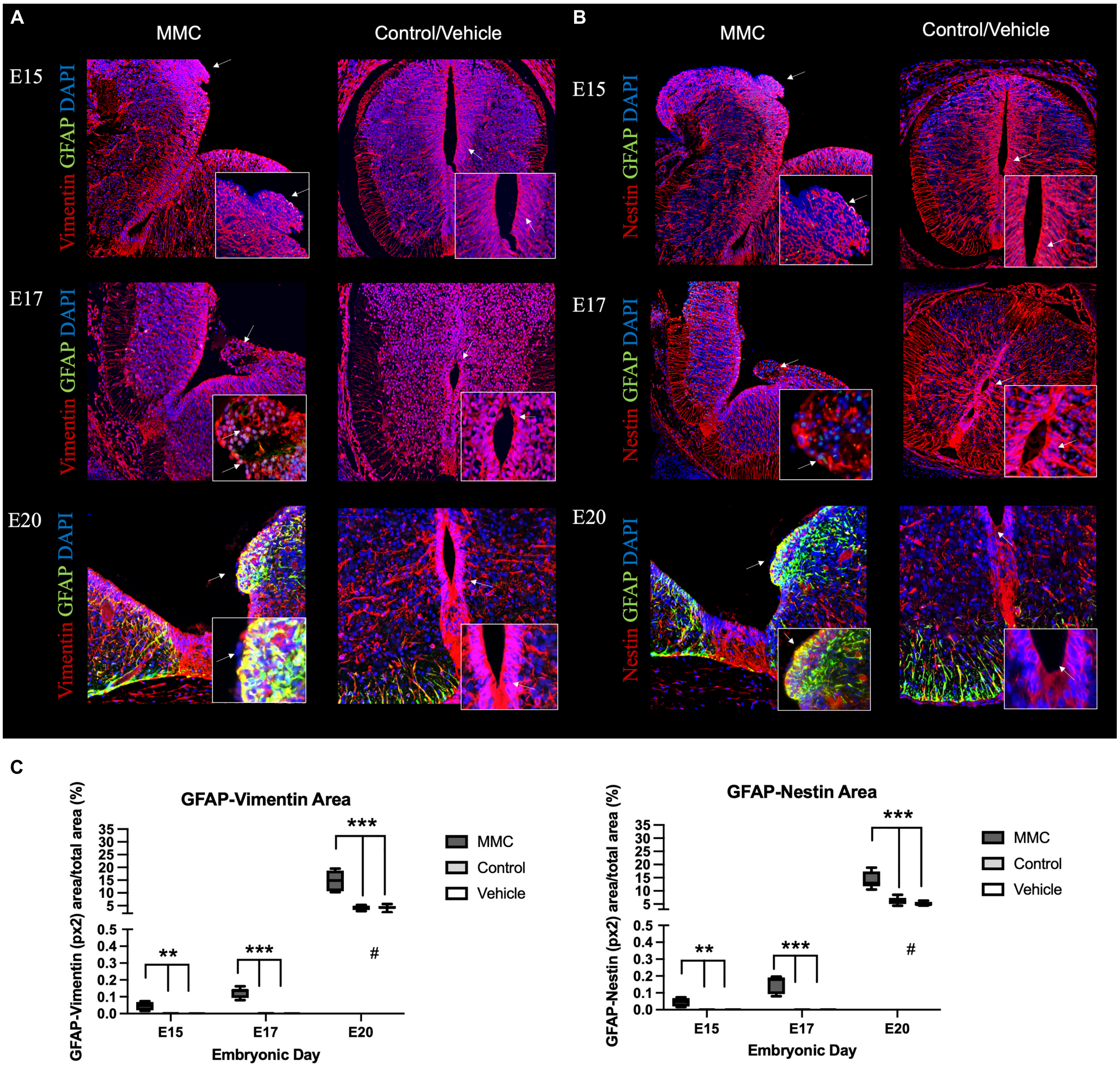

FIGURE 2 | *In utero* progressive astrogliosis in spina bifida. Progressive early astrogliosis in spina bifida (MMC) at E15, E17, and E20 compared with control spinal cords. Progressive GFAP (green) immunoreactive astrocyte cells, **(A)** vimentin (red) and **(B)** nestin (red) reactive astrocytes co-localization (yellow) and DAPI (blue) at E15, E17, and E20 in spina bifida (arrows) (20×). Control/Vehicle immunoreactive GFAP (green) astrocytes in white matter beneath the pial surface at E20 in normal spinal cords (20×). Astrocytes GFAP (green) co-localized with **(A)** vimentin (red) and **(B)** nestin (red) in spina bifida fetuses at in the VZ region compared with controls/vehicle with no expression of GFAP in the VZ nor central canal (arrow). **(C)** GFAP + Nestin and GFAP + Vimentin-stained area/total picture area in all groups at three gestational ages E15, E17, and E20 (means ± SD, $^{**}p < 0.01$, $^{***}p < 0.001$, $^{\#}p < 0.05$ between control and vehicle groups at E20 compared to E15 and E17).

changes at E15 in genes involved in the regulation of glial cell proliferation (Gfap, Notch1, Vim, Abcc8, Adyap1, and E2f1), glial cells differentiation (Ascl1, Dner, Erbb2, Gap43, Hes1, Igf1, Klf15, Lef1, Metrn, Mmp24, Plp1, and Bmp4), glial cell migration (Cspg4, Efemp1, Fn1, Idh2, lamb1, P2ry12, Tspo, and Vcan) glial cell projection (Cspg5 and Mdk), glial cell fate commitment (Hes5), glial cell development (Lgi4), astrocyte differentiation (Dll3, Hes1, Hes5, Hmga2, Mag, Notch1, Ntrk3, and Sox6), astrocyte activation (Egfr, Ldrl, and Smo), astrocyte development (Mt3, Plp1, Pou3f2, Ror1, and Vim), and astrocyte commitment (Sox9) compared to controls (**Figure 5C**). Validation of the RNA-seq data was performed using RT-qPCR for some of the key genes in astrogenesis (**Supplementary Table 2**).

Altered Patterning Factors in the Ventricular Zone in Spina Bifida

In the developing spinal cord, the VZ is divided into three domains along the dorsoventral axis: Pax6 (p0-2), Olig2

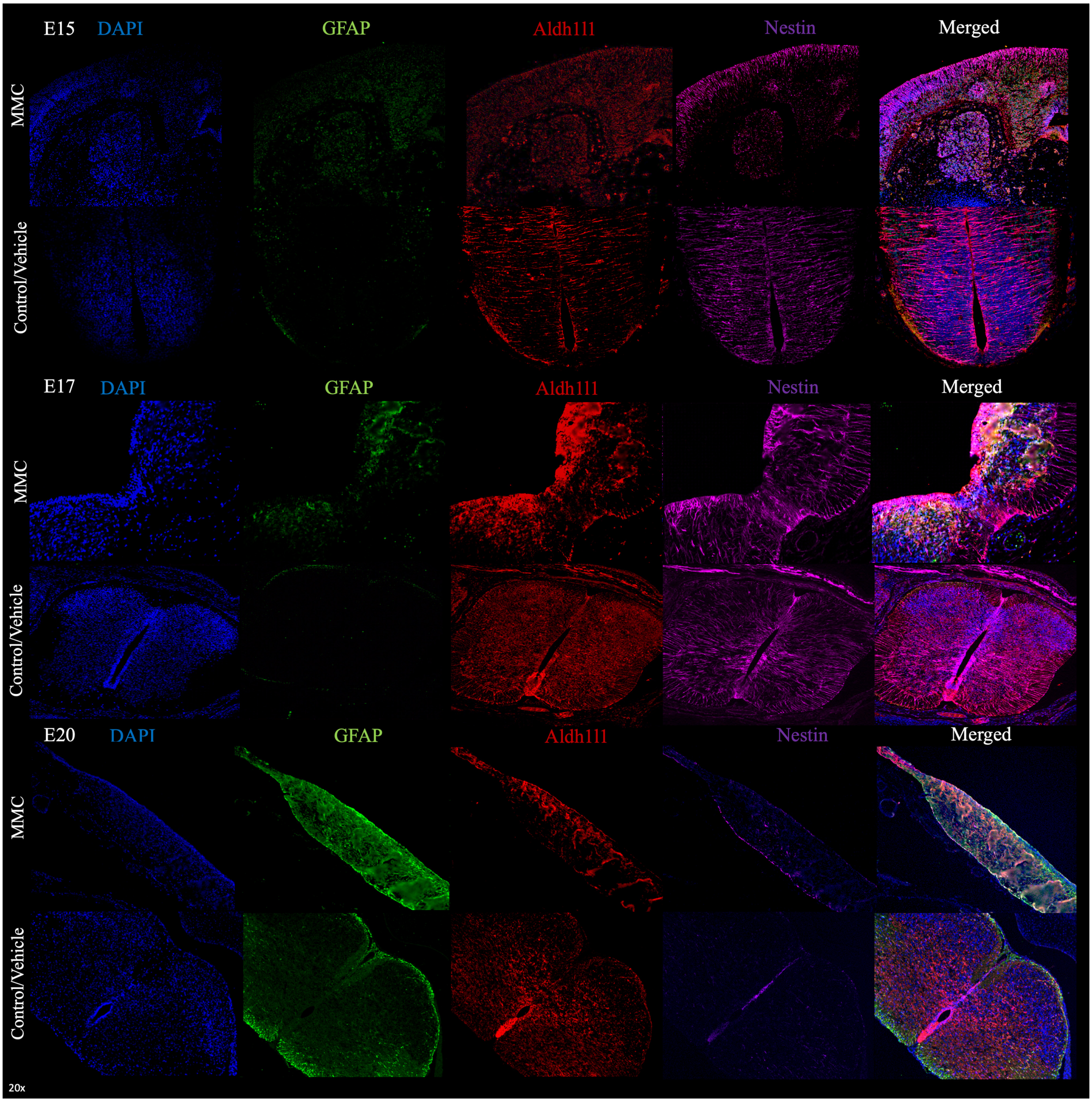

FIGURE 3 | Premature astrocytes in spina bifida. Progressive early astrogliosis in spina bifida (MMC) at E15, E17, and E20 compared with control spinal cords. GFAP (green), Aldh1l1 (red), Nestin (magenta), and DAPI (blue) premature astrocytes localization in VZ exposed to amniotic fluid at E15, E17, and E20 in spina bifida (20×).

(pMN), and Nkx2.2 (p3) domains (Shirasaki and Pfaff, 2002). During spinal cord development, these patterning domains are established early in gestation, by E11, and their expression remains during the course of neuro- and gliogenesis until astrogenesis begins in the end stages of gestation (Sugimori et al., 2007). We hypothesize that treating rats with RA at E10 will modulate the spinal cord's patterning domains. Therefore, to assess the impact of RA-induced spina bifida on NPC differentiation, we characterized Pax6, Olig2, and Nkx2.2 expression in fetal spinal cords during gestation because in spina bifida the spinal cord is open and unfolded exposing the VZ and the progenitor cells to the amniotic fluid. First, Pax6 gene expression was upregulated in MMC at E15 and E17 compared to control and vehicle groups but returns to normal levels by E20 ($^{*}p < 0.05$, $^{**}p < 0.01$) (**Figure 6A**). At E15 and E17, Pax6+ NPCs are located in the VZ in all groups; however, those found in the MMC group are directly in contact with the amniotic fluid as a result of the defect. At E20, Pax6 expression is restricted to the ependyma located in the central canal in fetuses from both control and vehicle groups; in contrast, Pax6+ cells in

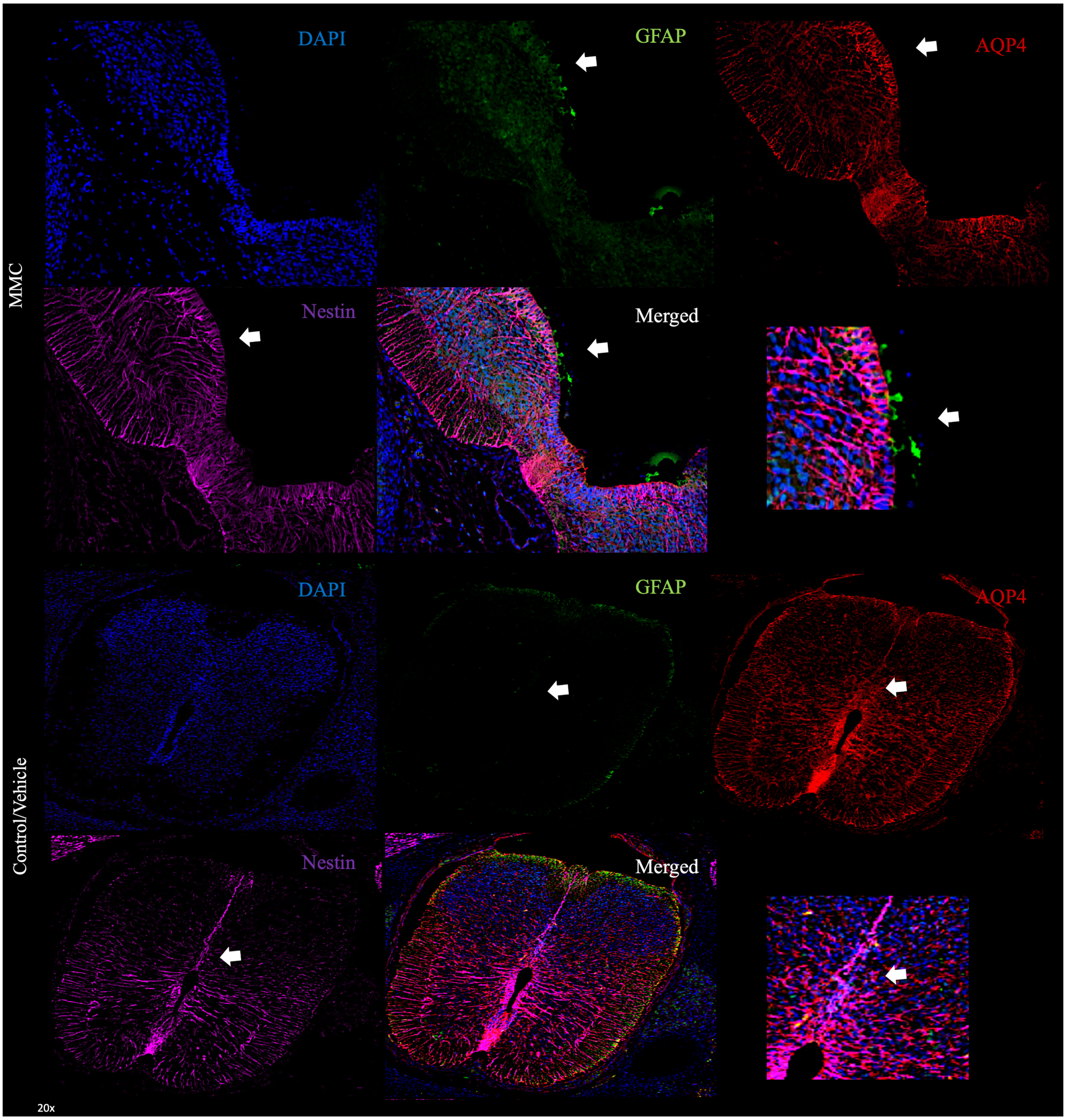

FIGURE 4 | Aquaporin 4 astrocytes in ventricular zone spina bifida fetuses. Generation of mature astrocytes in MMC compared with control spinal cords at E17. AQP4+ GFAP+ cells located in the VZ exposed to the amniotic fluid in spina bifida at E17 (20×). Magnification of VZ in MMC and control/vehicle animals (arrow).

MMC fetuses are spread throughout the gray matter in both halves of the spinal cord (**Figure 6B**). Upon quantification of immunofluorescence staining, we observed a significant increase in Pax6+ cells in MMC fetal spinal cords compared to the control groups at each time point ($^{*}p < 0.05$, $^{**}p < 0.01$, $^{**}p < 0.001$) (**Figure 6C**). Interestingly, by E20, the percentage of Pax6+ cells decreased in control and vehicle compared to E15 ($^{\#}p < 0.05$) following the normal decrease in expression during spinal cord development associated with oligodendrogenesis and astrogenesis (Sugimori et al., 2007) (**Figure 6C**). The percentage of Pax6+ cells in the MMC group also decreased during gestation ($^{\#}p < 0.05$ E15 vs. E20), however, it still was significantly higher compared to the other groups (**Figure 6C**).

Down-regulation of Olig2 patterning factor was observed in MMC fetuses compared with control and vehicle animals at each time point studied ($^{**}p < 0.01$, $^{***}p < 0.001$) (**Figure 7A**), similarly observed in the RNA-seq results (**Supplementary Tables 3–5**). During spinal cord development, Olig2+ cells migrate from the pMN domain to the rest of the spinal cord, as observed in control and vehicle fetuses at E15, E17, and E20

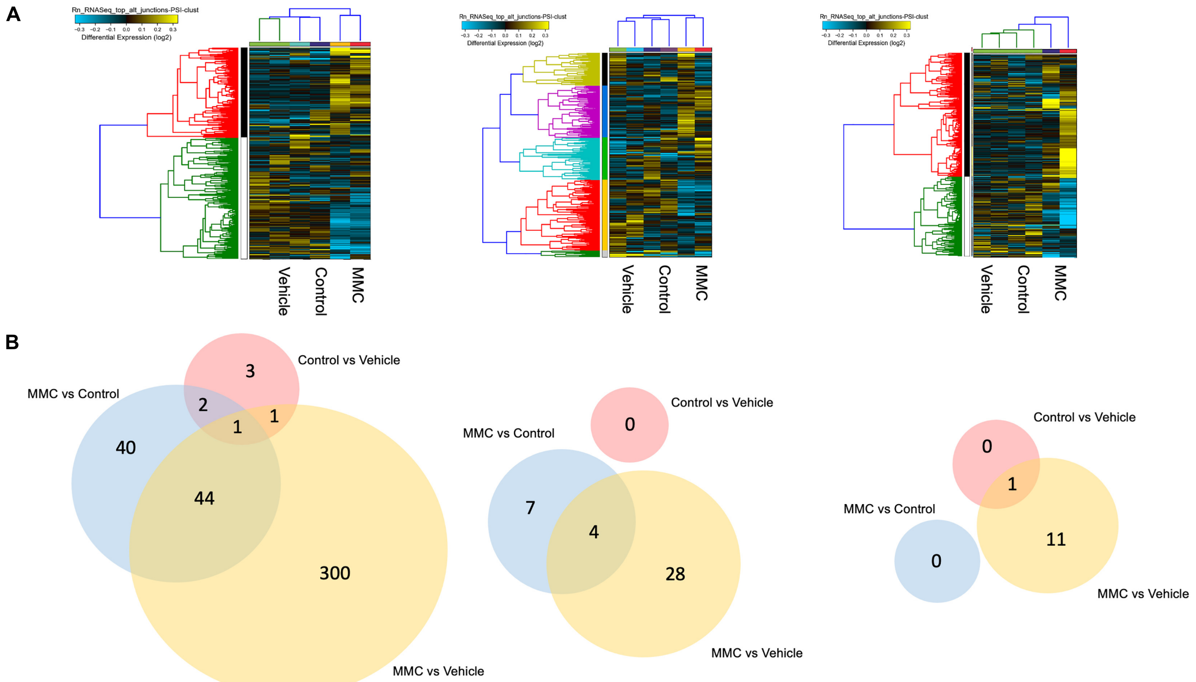

C

Gestational Time	Neurogenesis GO:0022008	Gliogenesis: Astrogenesis Differentiation GO:0048708	Gliogenesis: Oligodendrocyte Differentiation GO:0048709
E15	**346 genes (Supp Table 2)** Abcc8, Ablim1, Acsl6, Ady1, Adyap1, Amigo1Olig1, Olig2, Ngn1-3-4, Id1-2. Hes1-5-6, Dcx, Apoe, Map2, Notch1, Gsx1-2 ...	**41 genes** Abcc8, Adyap1, Ascl1, Cspg4, Cspg5, Dll3, Dner, Egfr, E2f1, Efemp1, Erbb2, Fn1, Gap43, Gfap, Hes1, Hes5, Hmga2, Ldlr,, Idh2, Igf1, Klf15, Lamb1, Lef1, Lg14, Mag, Mt3, Mdk, Metrn, Mmo24, Notch1, Ntrk3, P2ry12, Plp1, Pou3f4, Ror1, Smo, Sox6, Sox9, Tspo, Vcan, Vim	**31 genes** Ascl1, Erbb2, Gsx2, Hdac1, Hes1, Hdac1, Hdac11, Mdk, Notch1, Ntrk2, Olig1, olig2, Scl8a3, Scl45a3 Sox10, Tcf7l2, Tmem98, Ptn, Ptpra, Plp1, Omg, Bmp4, Cntnap1, Dusp10, Dusp15, Egfr, Eif2b2, Enpp2, Sox9, Sox6, Vtn,
E17	**32 genes (Supp Table 3)** Adra2b, Bmp6, Cit, Cbx1, Dll3, Dmart3, Ephra10, Gabra5, Gas1, Heyl, Hoxc10, Hoxc8, Hoxd9, Irx3, Map1a, Nefh, Nefl, Neuog1, Neurog2, Nrtn, Omg, Plppr4, Plxnd1, Robo3. Scn1b, Slc4a10, Sox14, Syt2, Thy1, Tmem98, Vsx2.	**4 Genes** Dll3, Mag, Hes1, Mt3	**5 genes** Tmem98, Ascl1, Cntnap1, Hes1, Mag
E20	**12 genes (Supp Table 4)** Chat, Gpr37l1, Grin2a, Hdac6, Kcnj10, Nefh, Nkx6.2, Ntrk1, Olig2, Plp1, pou4f3, Prdm12	**2 Genes** Nkx6.2, Plp1	**3 genes** Kcnj10, Nkx6.2, Olig2

FIGURE 5 | Cluster analysis of differentially expressed genes. **(A)** Hierarchical cluster analysis of differentially expressed genes showed transcriptome-wide expression patterns similar between the control and vehicle groups compared to MMC samples in all three gestational ages E15, E17, and E20 days. **(B)** Venn diagram of the DEGs in different comparisons. The numbers indicate unique and common DEGs in two duplicates for different comparisons MMC vs. VC, MMC vs. NC and NC vs. VC. **(C)** Analysis of two sub-classifications within the Neurogenesis GO, Oligodendrocyte Differentiation (GO:0048709), and Astrocyte Differentiation (GO:0048708) DEGs between the control and vehicle groups compared to MMC at E15, E17, and E20 days.

($^{###}p < 0.001$, E20 vs. E15 and E17) (**Figures 7B,C**). In contrast, with MMC fetuses, Olig2+ cells remained as tight clusters in the VZ over this gestational period and were exposed to the amniotic fluid (**Figure 7B**). Furthermore, down-regulation of Olig2 mRNA and clustering of Olig2+ cells within the VZ observed in MMC is associated with a decrease in the number of Olig2+ cells at E17 and E20 as compared to control and vehicle ($^{*}p < 0.05$) (E15, E17, and E20) (**Figure 7C**). There was no difference in the percentage of Olig2+ cells between groups at mid gestation (E15). Interestingly, the Olig2 (pMN) domain was exposed to the amniotic fluid in most samples which may lead to this response.

In spina bifida fetuses Nkx2.2 transcription factor was upregulated at E15 and E17 when compared to vehicle spinal cords and upregulated at E20 when compared to control ($^{*}p < 0.05$) (**Figure 8A**). In normal development, Nkx2.2 cells are restricted to the p3 domain of the ventromedial column in early gestational ages. As our data supports, during normal development, NPCs begin to migrate to the ventral spinal cord as early as E13 and by E15, Nkx2.2 cells can be detected in the ventral gray matter (to differentiate into ventral interneurons) and in the white matter (to differentiate into oligodendrocytes). By the end of gestation, Nkx2.2 cells can be detected mostly in the ventral region (McMahon, 2000; Qi et al., 2001; **Figure 8B**). Even with the defect early in gestation, Nkx2.2. cells remain restricted to the p3 domain at E15 in the MMC group; however, they begin to migrate at E17, and are ultimately found throughout

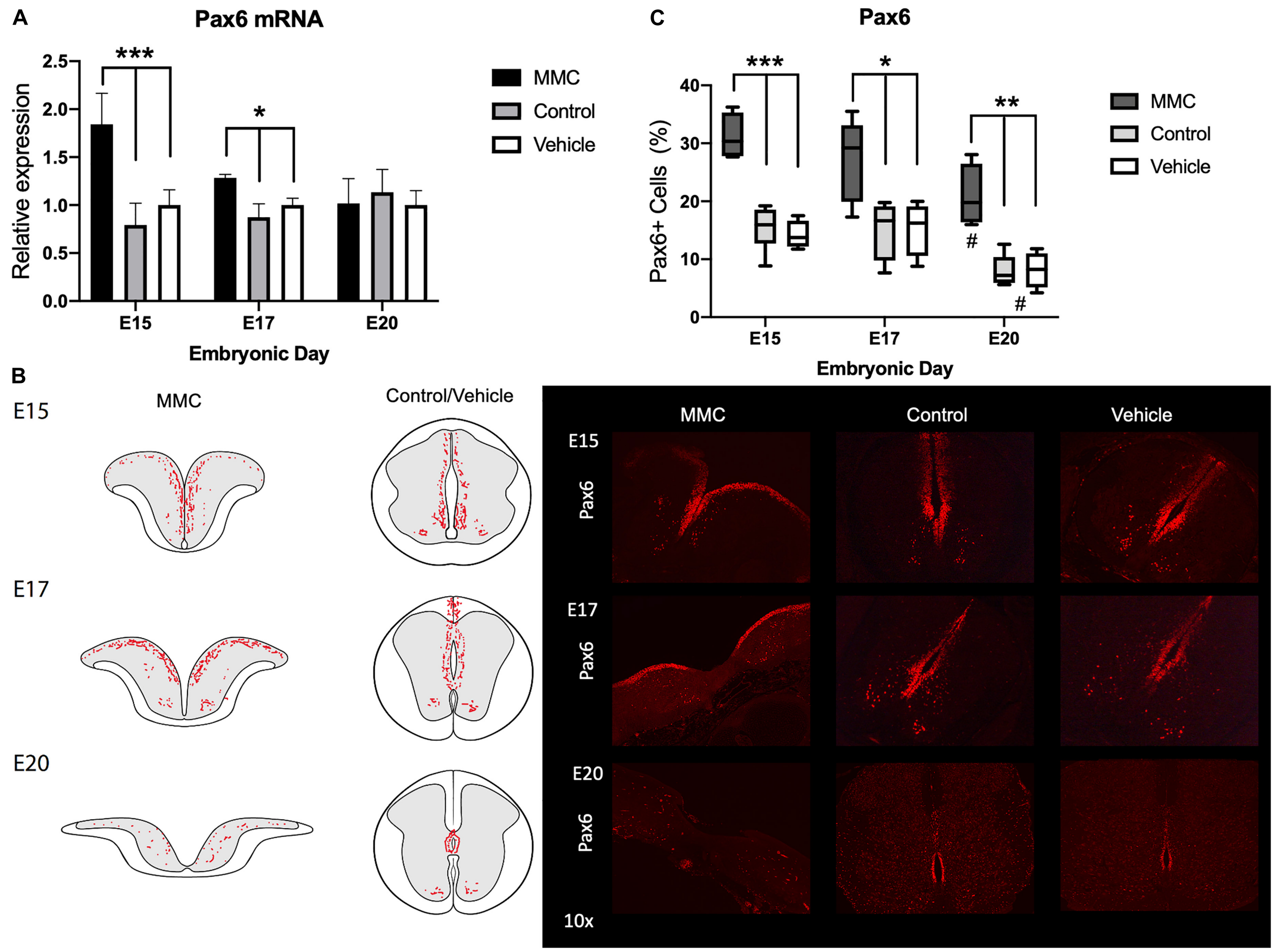

FIGURE 6 | Pax6 expression and distribution in spina bifida. **(A)** Pax6 relative expression increased in spina bifida (MMC) compared with control and vehicle spinal cords at E15 and E17. Values (means ± SE, 6 fetuses/group) of relative expression ($2^{-\Delta\Delta Ct}$) for RA-treated and time-matched controls ($^{*}p < 0.05$, $^{***}p < 0.001$). **(B)** Schematic representation of Pax6 distribution in MMC and control fetal spinal cords at E15, E17, and E20 (left). Pax6+ staining in MMC, control, and vehicle spinal cords at E15, E17, and E20 (right) (10×). Pax6+ (red) immunoreactive NPC cells exposed at E15, E17, and E20 in spina bifida (10×). **(C)** % Pax6+ NPC in spina bifida, control and vehicle spinal cords determined by Pax6 stained cells/total cells at three gestational ages E15, E17, and E20 (means ± SD, $^{*}p < 0.05$, $^{**}p < 0.01$, $^{*}p < 0.001$, $^{\#}p < 0.05$ between E20 and E15).

the entire spinal cord by E20 (**Figure 8B**). In addition, upon quantification of immunofluorescence staining, we observed a significant increase in Nkx2.2+ cells during development ($^{\#}p < 0.05$) (**Figure 8C**, E20 vs. E15 and E17), and an increase in MMC compared to both control groups at E20 ($^{*}p < 0.05$) (**Figure 8C**). As shown in previous studies (Mizuguchi et al., 2001; Sugimori et al., 2007), the down-regulation of Olig2 resulted in up-regulation of Nkx2.2 and dorsal expansion of Nkx2.2 + domain. Consequently, more Nkx2.2 cells and fewer Olig2+ cells were detected at E17 and E20 in the spinal cord of MMC fetuses compared with Control and Vehicle spinal cords ($^{*}p < 0.05$) (E15, E17, and E20) (**Figures 8B,C**).

Origin of Premature Astrocyte Population

Next, we sought to examine the developmental origin of the glial cells in the VZ exposed to amniotic fluid in MMC fetuses by assessing the co-expression of GFAP and patterning factors, Pax6, Olig2, and Nkx2.2, at each time point studied. At E15 and E17, astrocytes (GFAP+ cells) located in the VZ of MMC fetal spinal cords were exposed to amniotic fluid and expressed Olig2 or Pax6 (**Figure 9A**). At these time points, GFAP expression was not observed in Nkx2.2+ cells around the p0 domain (**Figure 9A**) (arrows). As previously observed, GFAP expression was not detected in control and vehicle spinal cords at these time points (**Figure 9B**). At E20, GFAP+ astrocytes found in the VZ of MMC fetal spinal cords expressed Pax6, Olig2, and Nkx2.2 (**Figure 9A**). On the contrary, GFAP+ cells were found in the white matter at the sub-pial region in control and vehicle spinal cords and did not express Pax6, Olig2, or Nkx2.2 (**Figure 9B**). This increase in co-expression of GFAP and Pax6, Olig2, and Nkx2.2 compared to controls ($^{*}p < 0.05$, $^{**}p < 0.01$, $^{***}p < 0.001$) (also is increased at the end of gestation compared to E15 and E17 ($^{\#}p < 0.05$, control and vehicle E20 vs. E15 and E17) (**Figure 9C**). These results demonstrate the expression of an astrocyte marker (GFAP) in VZ

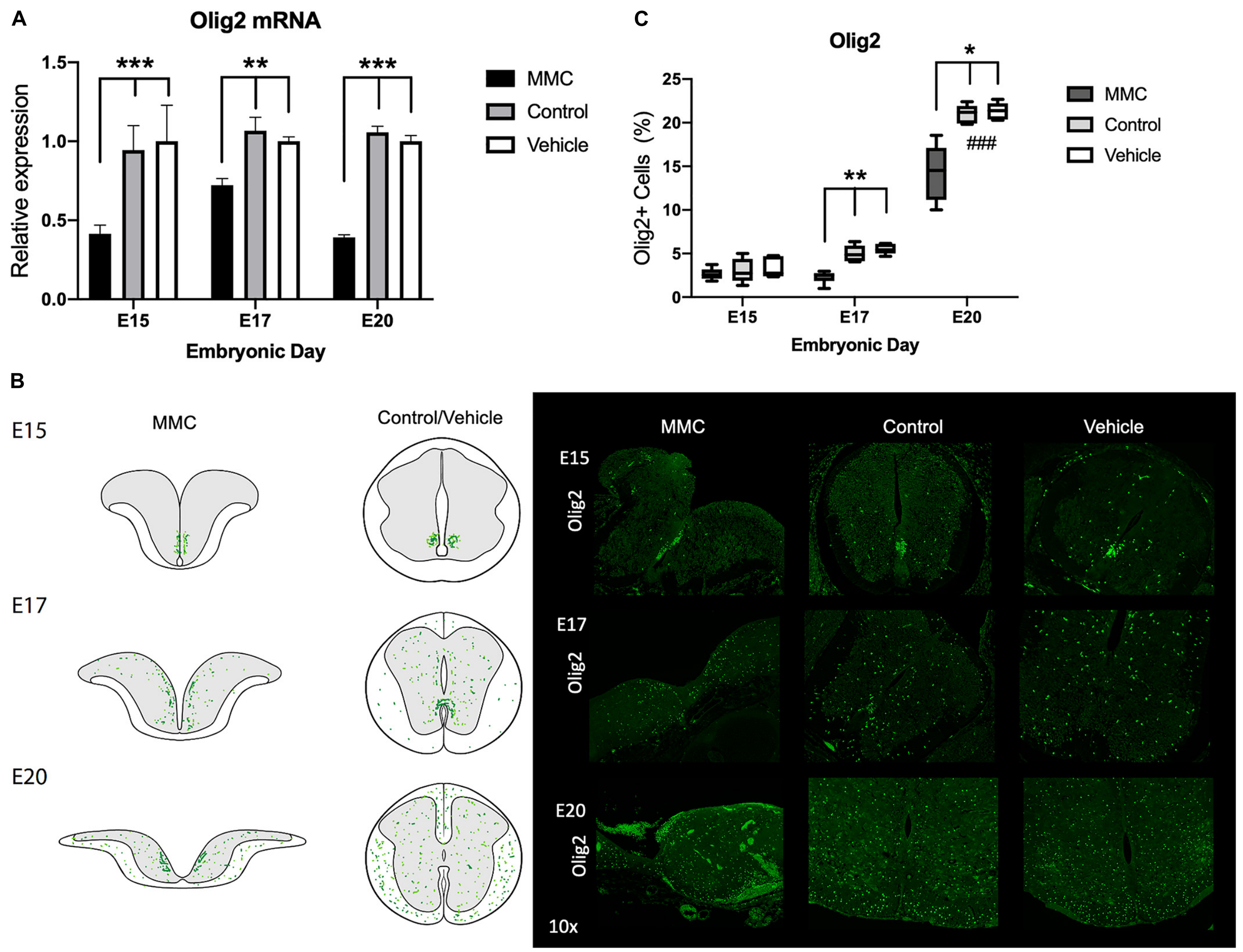

FIGURE 7 | Olig2 expression and distribution in spina bifida. **(A)** Olig2 relative expression increased in spina bifida (MMC) compared with control and vehicle spinal cords at E15 and E17. Values (means ± SE, 6 fetuses/group) of relative expression ($2^{-\Delta\Delta Ct}$) for RA-treated and time-matched controls ($^{*}p < 0.05$, $^{**}p < 0.01$, $^{***}p < 0.001$). **(B)** Schematic representation of Olig2 distribution in MMC and control spinal cords at E15, E17, and E20 (left). Olig2+ staining in MMC, control, and vehicle spinal cords at E15, E17, and E20 (right) (10×). Olig2 (green) immunoreactive NPC cells exposed at E15, E17, and clustering at E20 in spina bifida (10×). **(C)** % Olig2+ NPC in spina bifida (MMC), control, and vehicle fetal spinal cords determined by Olig2 stained cells/total cells at three gestational ages E15, E17, and E20 (means ± SD, $^{*}p < 0.05$, $^{**}p < 0.01$, $^{\#\#\#}p < 0.001$ between control and vehicle groups at E20 compared to E15 and E17).

NPC (Pax6, Olig2, and Nkx2.2) that could lead to astrogenesis in the VZ exposed to the amniotic fluid in MMC fetuses.

Notch Bone Morphogenetic Protein Pathway Involvement in Neural Progenitor Cell Fate in Spina Bifida

During neural development, Notch plays a crucial role in regulating NPC differentiation into astrocytes by activating different signaling pathways such as Notch, Sox9, and BMP (Fulghum, 2005; Xin et al., 2006). BMP signaling has been shown to be a key player in many events in the central nervous system (CNS) development. For example, BMP2 has been demonstrated to promote astrocytes fate both *in vivo* and *in vitro* (Gross et al., 1996; Bonaguidi et al., 2005). Also, BMP4 has been previously reported to repress oligodendrogenesis and promote astrogenesis during CNS maturation (Gross et al., 1996; Mabie et al., 1999). RNA-seq analysis indicated alterations in BMP signaling earlier in gestation (E15); therefore, in order to determine the involvement of BMP signaling in accelerated astrogenesis in RA-induced spina bifida we assessed the expression of Sox9, Notch1, BMP2, and BMP4 in MMC fetal spinal cords compared to control and vehicle fetal spinal cords. Gene expression of Sox9, Notch1, BMP4, and BMP2 were upregulated in MMC fetal spinal cords compared to control and vehicle groups at E15 and E17 ($^{**}p < 0.01$, $^{***}p < 0.001$); however, there were no differences between groups at E20 (**Figure 10A**).

Finally, using immunofluorescence, we investigated if astrocytes were potentially responsible for elevations in BMP-2 and BMP-4 expression. As a marker of early astrocyte maturation, expression of S100b was detected and located in the amniotic fluid exposed layers and the radial glial in MMC samples with almost no expression of S100b in the control groups at this gestational age (E17) (**Figure 10B**). In corroboration with the

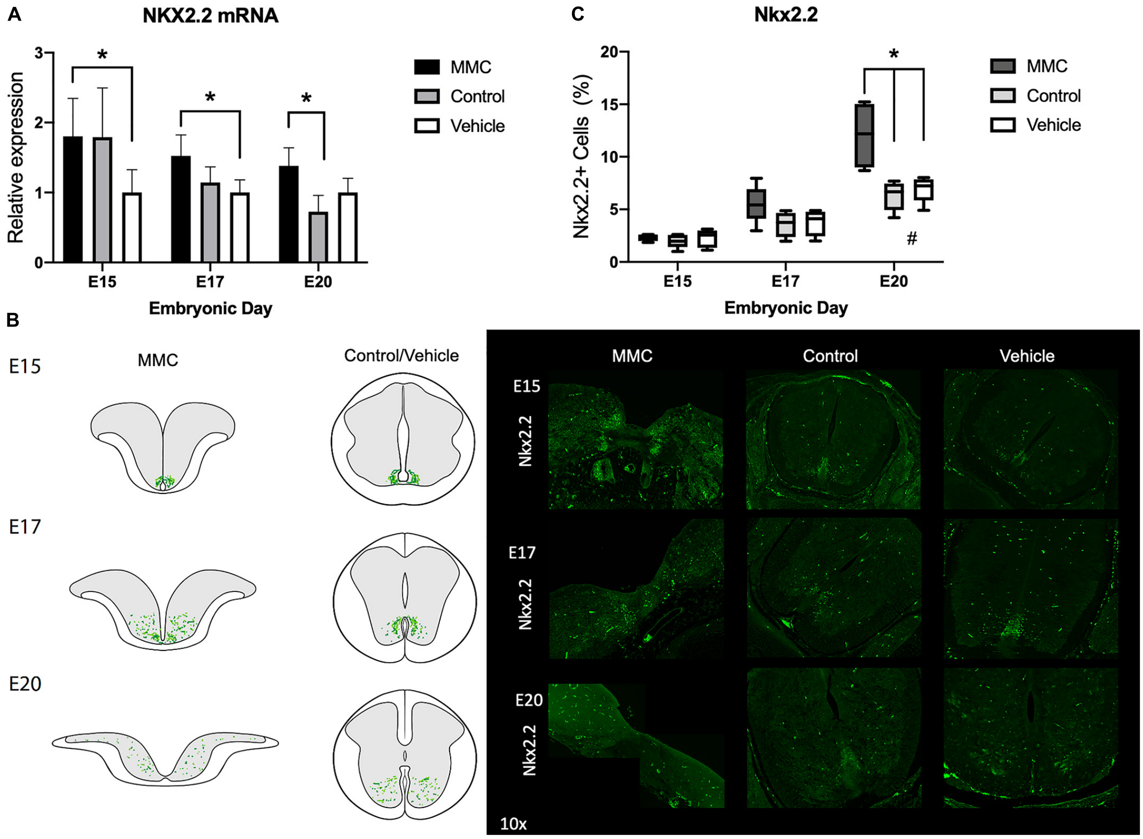

FIGURE 8 | Nkx2.2 expression and distribution in spina bifida. **(A)** Nkx2.2 relative expression increased in spina bifida compared with control and vehicle spinal cords at E15 and E17. Values (means ± SE, 6 fetuses/group) of relative expression ($2^{-\Delta\Delta Ct}$) for RA-treated and time-matched controls ($^*p < 0.05$). **(B)** Schematic representation of Nkx2.2 distribution in MMC and control spinal cords at E15, E17, and E20 (left). Nkx2.2+ staining in MMC, control, and vehicle spinal cords at E15, E17, and E20 (right) (10×). Nkx2.2 (green) immunoreactive NPC cells at E15, E17, and E20 in spina bifida (10×). **(C)** % Nkx2.2+ NPC in MMC, control, and vehicle spinal cords determined by Nkx2.2 stained cells/total cells at three gestational ages E15, E17, and E20 (means ± SD, $^*p < 0.005$, $^{\#}p < 0.05$ between control and vehicle groups at E20 compared to E15 and E17).

gene expression results (**Figure 10A**), BMP-2 and BMP-4 were more expressed in MMC samples compared to the control groups at the same gestational age (**Figure 10B**). Moreover, BMP-2 and BMP-4 expressions were primarily located in the gray matter and co-localized with S100b positive cells in the MMC group. In comparison, BMP-2 and BMP-4 expression was diminished and primarily located in the spinal cords ventro-lateral horn in the control groups. Furthermore, observing BMP-4 was high expressed in MMC and using Aldh1l1 as a premature astrocytes marker we observed co-expression of these two markers in MMC fetuses at E17 gestational age (**Figure 10C**). These results indicate that early S100b and Aldh1l1 positive astrocytes may play a role in BMP-2 and BMP-4 induced premature astrogliosis in MMC fetuses.

DISCUSSION

In this report, we aimed to elucidate a mechanism behind the premature reactive astrogliosis that occurs in a RA-induced spina bifida rat model with the goal of identifying potential therapeutic targets to repair the prenatal neurodegenerative damage that occurs in the spinal cord after exposure to the intrauterine environment. Our data suggests that neurogenesis changes and reactive astrogliosis occurs earlier in the VZ of spinal cords from fetuses with RA-induced spina bifida compared to control groups.

Astrocyte precursors are generated by differentiation of radial glial cells in early development (Seo et al., 2008) and from migratory progenitors that emerge from the sub-VZ at later in gestation (Levison and Goldman, 1993). Based on our data, we propose that NPCs become committed to the astrocyte lineage due the direct exposure to the amniotic fluid in spina bifida by dysregulation in patterning factors, Pax6, Olig2, and Nkx2.2 and potentially downregulating neurogenesis and oligodendrogenesis. Furthermore, we present the involvement of Notch1, Sox9, and BMP signaling in NPC cell fate during gestation and their role in self-propelling earlier astrogliosis observed in spina bifida. Excitingly, our results suggest that inhibiting NPC differentiation into astrocytes through modulation of Notch/BMP signaling or patterning factors could be a promising neuroprotective strategy.

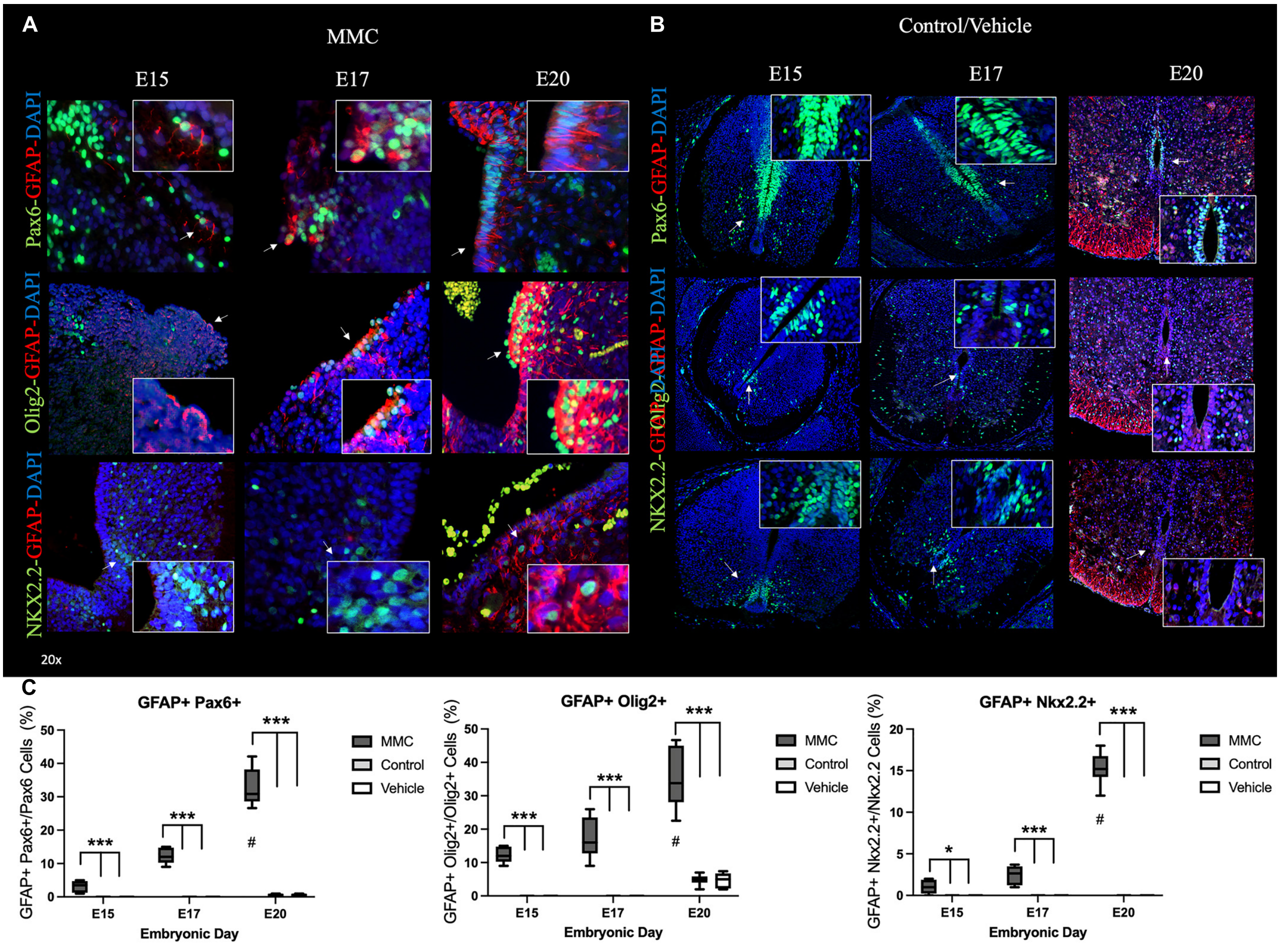

FIGURE 9 | Early NPC differentiation into astrocytes in spina bifida. Progressive early generation of reactive astrocytes in **(A)** MMC compared with **(B)** control spinal cords at E15, E17, and E20. **(A)** Pax6 + GFAP+ cells located in the VZ exposed to the amniotic fluid in spina bifida at E15, E17, and E20 (upper) (arrow). Olig2 + GFAP+ cells located in the VZ exposed to the amniotic fluid in spina bifida at E15, E17, and E20 (center) (arrow). Nkx2.2 + GFAP+ cells located in the VZ exposed to the amniotic fluid in spina bifida at E20 (bellow) (arrow). **(B)** Ventricular zone (VZ) is divided into three domains along the dorsoventral axis: Pax6 (p0-2), Olig2 (pMN), and Nkx2.2 (p3) domains and GFAP sub-pial expression in normal spinal cords. Pax6 (green), Olig2 (green), Nkx2.2 (green), GFAP (red), and DAPI (blue) (20× images). **(C)** % GFAP Pax6+, GFAP+ Olig2+ and % GFAP+ Nkx2.2 astrocytes in spina bifida, control and vehicle spinal cords determined by GFAP and Pax6, Olig2, or Nkx2.2 stained cells/Pax6, Olig2, or Nkx2.2 at three gestational ages E15, E17, and E20 (means ± SD, $^{*}p < 0.05$, $^{***}p < 0.001$, $^{\#}p < 0.05$ between E20 and E15).

Astrocytosis has been described previously in other spina bifida animal models (Reis et al., 2007, 2008; Oria et al., 2018); however, the response to injury as early as E15 has not been investigated until now. Therefore, the gestation time points chosen (E15, E17, and E20), when comparing groups studied in this report, provide significant knowledge about the timeline of astrocytosis in spina bifida. Indeed, we demonstrated changes in astrogenesis in spinal cords of fetuses with spina bifida with the presence of differentiated (GFAP) astroglial cells as early as E15 that progressively increase throughout the rest of gestation. This maturation is much earlier than what is observed in healthy conditions, as NPC begins to differentiate into astrocytes around E16.5 and express GFAP, a astroglial marker, by E18.5, which agrees with the timeline of GFAP in our control groups (Ge et al., 2012; Han et al., 2020). These changes were also supported by RNA-seq in which 19 genes were dysregulated at E15, 4 genes at E17, and 2 genes at E20 other than GFAP in the "Neurogenesis" and sub-classification "Astrocyte Differentiation" GO pathway. Additionally, astroglial cells expressed vimentin and nestin in addition to GFAP, AQP4, and Aldh1l1, indicating that the new astrocytes are also reactive (Pekny and Nilsson, 2005; Koyama, 2014; Sofroniew, 2015; Verkhratsky and Parpura, 2016). We propose that exposure to amniotic fluid plays a role in this early and progressive astrogenesis and astrocyte activation affecting neurogenesis and oligodendrogenesis. As a result of failed neural tube closure, a peculiarly variable shaped, uncovered spinal cord is observed, where the dorsal VZ and often the central canal are completely open and directly exposed to the amniotic fluid. Interestingly, differentiated, and reactive astroglial cells were found in the VZ from spina bifida. Astrocytes respond

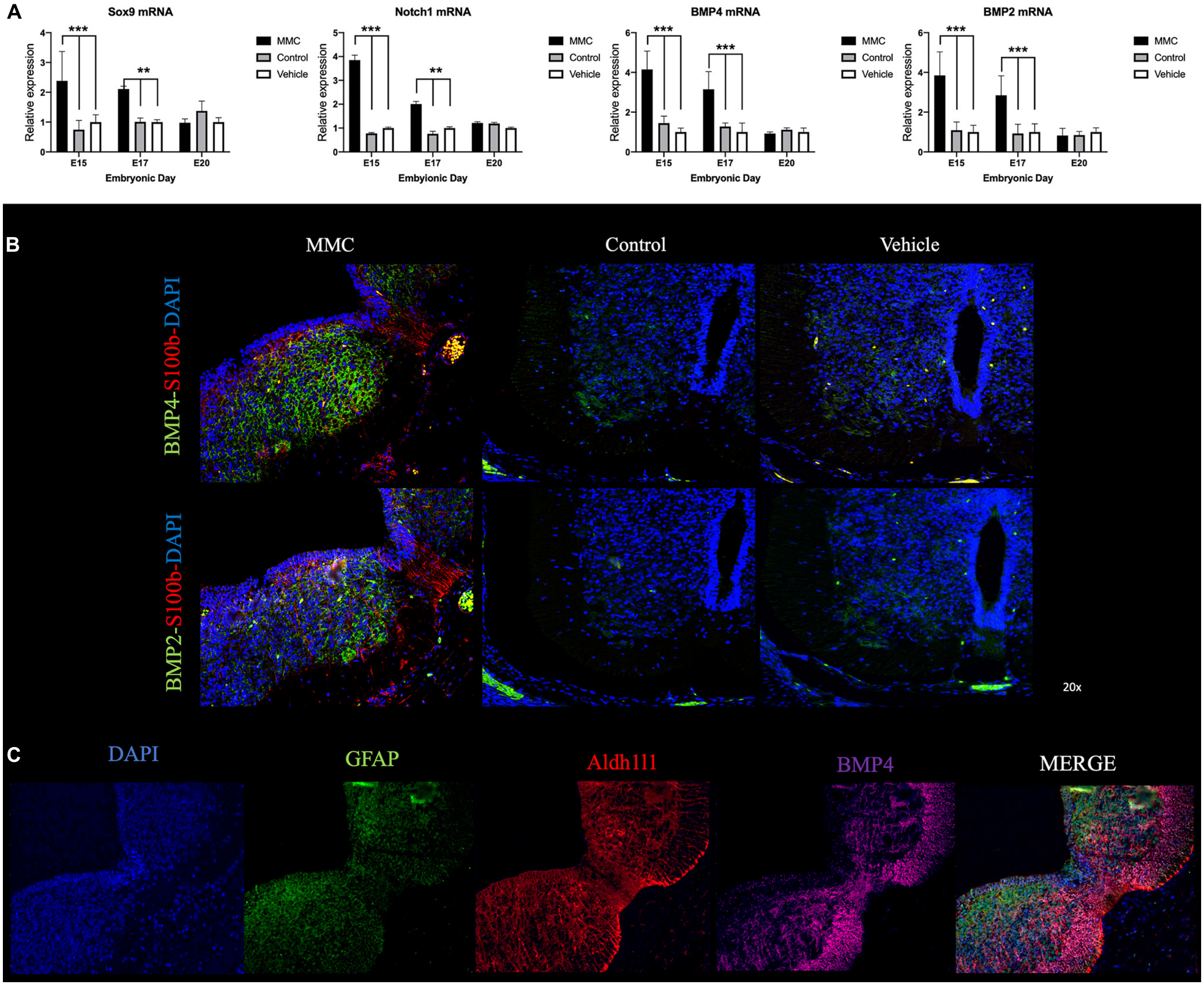

FIGURE 10 | Notch-BMP signaling activation in spina bifida. **(A)** Relative expression of Sox9, Notch1, BMP2, and BMP4 in MMC, control, and vehicle fetuses at E15, E17, and E20. Means ± SE ($n = 6$ fetuses/group) of relative expression ($2^{-\Delta\Delta Ct}$) for RA-treated and time-matched controls; (**$p < 0.01$, ***$p < 0.001$). **(B)** Co-staining of BMP-2 (green), BMP-4 (green), S100b (red), and DAPI (blue) in spinal cords collected from MMC, control, and vehicle fetuses at E17 (20× images). **(C)** Co-staining of BMP-4 (magenta), Aldh1l1 (red), GFAP (green), and DAPI (blue) in spinal cords collected from MMC at E17 (20× images).

to stress or tissue damage within the CNS by proliferating, activating, and interacting with other cell types through signaling molecules (Alonso, 2005). Therefore, it is possible that these cells are responding to the tissue damage induced by the enzymatic action of the amniotic fluid insult (Botto et al., 1999; Copp et al., 2013; Copp and Greene, 2013; Oria et al., 2019); however, the mechanism behind this reaction remains unclear and should be a focus of future pre-clinical studies.

Next, we focused on understanding how NPC patterning factors and signaling pathways that dictate differentiation fate were altered in spina bifida. NPCs are responsible for normal neurogenesis, oligodendrogenesis, and gliogenesis in the spinal cord during development. Neural cell diversity is a complex process during spinal cord development that is determined by a dorsal and ventral gradient of transcription factors and patterning domains such as Olig2, Pax6, and Nkx2.2 (Jessell, 2000; Rowitch, 2004; Rowitch and Kriegstein, 2010). Our data suggest that this process is altered in fetuses with spina bifida due to modifications in Pax6, Olig2, and Nkx2.2 expression throughout the time points studied. We observed dysregulation in genes involved in the "Astrocyte Differentiation" GO pathway, and the data was validated by measuring specific patterning factors and morphogens by RT-qPCR. Specifically, we observed an upregulation of Pax6 and Nkx2.2 gene expression and an elevated number of Pax6 or Nkx2.2 positive cells in spina bifida fetuses compared to the control groups. In addition, Olig2 patterning domain was downregulated in spina bifida during gestation, and this correlated with fewer Olig2 positive cells. These results relate to previous reports indicating that these modifications lead to enhanced astrogenesis while hindering neurogenesis and oligodendrogenesis in other types of spinal cord injuries. While Pax6 is a proneural patterning factor, its overexpression accelerates neural maturation into early neuronal committed cells but is not associated with net neurogenesis over time. In fact, Pax6 overexpression correlated with a loss of NPCs over time (Klempin et al., 2012). In MMC animals, we demonstrated upregulation of Pax6 in early gestational stages, which correlated with an increase in the number of Pax6+ cells committed to astrocytes, potentially at the cost of neurogenesis. Furthermore, Nkx2.2 has a primary role in ventral neuronal patterning and it has been shown to direct neural cell identity toward the glial lineage (Briscoe et al., 1999; Gorris et al., 2015; Yun et al., 2020). Upregulation of Nkx2.2 has been previously reported in other types of spinal cord injuries (Chang et al., 2009). Olig2 is essential for neurogenesis and oligodendrogenesis; therefore, it is possible that reduction in Olig2 led to enhanced astroglial differentiation as shown previously (Mizuguchi et al., 2001; Zhou et al., 2001; Zhou and Anderson, 2002; Hack et al., 2004; Klempin et al., 2012). In addition to patterning factors, BMP signaling has been shown to regulate astrocyte commitment in the CNS (Furuta et al., 1997; Mehler et al., 1997). In fact, up-regulation of proteins involved in this pathway have been extensively shown to direct NPCs to astroglial fate (Gross et al., 1996; Mabie et al., 1999; Bonaguidi et al., 2005; Miyagi et al., 2012). Our results further support this evidence as Sox9, Notch1, and BMP2/4 gene expression was upregulated at the time of early astrogliosis in spina bifida, and BMP2/4 expression with S100b and Aldh1l1, an early astrocyte markers. Therefore, dysregulation of patterning factors, Olig2, Pax6, and Nkx2.2 in combination with upregulation of Notch/BMP signaling may be a plausible mechanism for the early NPC differentiation into astrocytes as a protective mechanism after injury induced by amniotic fluid exposure.

To date, the neuropathological alterations reported in this congenital RA-induced rat model of spina bifida are (1) presence of early astroglia and progressive astrocytosis (Reis et al., 2007; Danzer et al., 2011; Oria et al., 2018), (2) progressive loss of neurons (Reis et al., 2007; Oria et al., 2018), and (3) neuro-inflammatory response associated with reactive microgliosis (Oria et al., 2018). Future studies are aimed to determine the impact of early astrocytosis on neurons and oligodendrocytes function, as it is hypothesized that NPCs differentiate into astrocytes at the cost of neurogenesis and oligodendrogenesis. If this is the case, developing strategies to prevent premature astrocytosis could improve neural function and overall outcomes in spina bifida patients. Furthermore, our present work identifies several transcriptional targets that would be a promising method to inhibit this astrocytic response.

CONCLUSION

In conclusion, spina bifida is one of the most permanently disabling congenital birth defects, and despite fetal surgery to repair or cover the spinal cord at mid-gestation, significant alterations have already been established before the intervention. Identifying the altered mechanism in glio/neurogenesis in response to fetal spinal cord injury in spina bifida is crucial for the development of new therapeutic strategies to improve functional outcomes in these patients. Our results suggest that targeting patterning factors, Pax6, Olig2, and Nkx2.2, as well as BMP/Notch signaling is a promising strategy to impede early gliogenesis in a chemically induced spina bifida rat model.

DATA AVAILABILITY STATEMENT

The datasets presented in this study can be found in online repositories. The names of the repository/repositories and accession number(s) can be found in the article/**Supplementary Material**.

ETHICS STATEMENT

The animal study was reviewed and approved by the IACUC 2019-0081.

AUTHOR CONTRIBUTIONS

MO and JLP: study concept, design, and supervision. MO, BP, ZL, KB, KG, MV, and KL: acquisition of data. KM, MO, and JLP: analysis and interpretation of data and drafting of the manuscript. KM, MV, MO, C-YL, and JLP: critical revision of the manuscript for important intellectual content. MO: statistical analysis. C-YL and JLP: obtained funding. MO, KM, and KL: technical or material support. All authors contributed to the article and approved the submitted version.

FUNDING

This study was supported by the NIH/NINDS 1R01NS103992 to JLP and C-YL by the Cincinnati Children's Hospital Medical Center and University of Cincinnati.

ACKNOWLEDGMENTS

We greatly appreciate Matthijs W. van Hoogdalem for his scientific illustrations.

SUPPLEMENTARY MATERIAL

The Supplementary Material for this article can be found online at: https://www.frontiersin.org/articles/10.3389/fnmol.2022.888351/full#supplementary-material

Supplementary Figure 1 | Decrease of early neurons in spina bifida *in utero*. Full scan spinal cords Immunohistochemistry for **(A)** Doublecortin (DCX) and **(B)** Tubulin β III showed a decrease in early neuron expression in MMC fetuses. In MMC spinal cords DCX and Tubulin β III is exposed and in contact with the amniotic fluid during gestation.

REFERENCES

Adzick, N. S., Thom, E. A., Spong, C. Y., Brock, J. W., Burrows, P. K., Johnson, M. P., et al. (2011). A Randomized trial of prenatal versus postnatal repair of myelomeningocele. *N. Engl. J. Med.* 364, 993–1004.

Alonso, G. (2005). NG2 proteoglycan-expressing cells of the adult rat brain: possible involvement in the formation of glial scar astrocytes following stab wound. *Glia* 49, 318–338. doi: 10.1002/glia.20121

Barry, D., and McDermott, K. (2005). Differentiation of radial glia from radial precursor cells and transformation into astrocytes in the developing rat spinal cord. *Glia* 50, 187–197. doi: 10.1002/glia.20166

Bertrand, N., Castro, D. S., and Guillemot, F. (2002). Proneural genes and the specification of neural cell types. *Nat. Rev. Neurosci.* 3, 517–530. doi: 10.1038/nrn874

Bonaguidi, M. A., McGuire, T., Hu, M., Kan, L., Samantha, J., and Kessler, J. A. (2005). LIF and BMP signaling generate separate and discrete types of GFAP-expressing cells. *Development* 132, 5503–5514. doi: 10.1242/dev.02166

Botto, L. D., Moore, C. A., Khoury, M. J., and Erickson, J. D. (1999). Neural-tube defects. *N. Engl. J. Med.* 341, 1509–1519. doi: 10.1056/NEJM199911113412006

Briscoe, J., Sussel, L., Serup, P., Hartigan-O'Connor, D., Jessell, T. M., Rubenstein, J. L. R., et al. (1999). Homeobox gene Nkx2.2 and specification of neuronal identity by graded Sonic hedgehog signalling. *Nature* 398, 622–627. doi: 10.1038/19315

Chang, Y. W., Goff, L. A., Li, H., Kane-Goldsmith, N., Tzatzalos, E., Hart, R. P., et al. (2009). Rapid induction of genes associated with tissue protection and neural development in contused adult spinal cord after radial glial cell transplantation. *J. Neurotrauma* 26, 979–993. doi: 10.1089/neu.2008.0762

Copp, A. J., and Greene, N. D. E. (2013). Neural tube defects-disorders of neurulation and related embryonic processes. *Wiley Interdiscip. Rev. Dev. Biol.* 2, 213–227. doi: 10.1002/wdev.71

Copp, A. J., Stanier, P., and Greene, N. D. E. (2013). Neural tube defects: recent advances, unsolved questions, and controversies. *Lancet Neurol.* 12, 799–810. doi: 10.1016/S1474-4422(13)70110-8

Danzer, E., Zhang, L., Radu, A., Bebbington, M. W., Liechty, K. W., Adzick, N. S., et al. (2011). Amniotic fluid levels of glial fibrillary acidic protein in fetal rats with retinoic acid induced myelomeningocele: a potential marker for spinal cord injury. *Am. J. Obstet. Gynecol.* 204, 178.e1–11. doi: 10.1016/j.ajog.2010.09.032

Dennis, D. J., Han, S., and Schuurmans, C. (2019). bHLH transcription factors in neural development, disease, and reprogramming. *Brain Res.* 1705, 48–65. doi: 10.1016/j.brainres.2018.03.013

Emig, D., Salomonis, N., Baumbach, J., Lengauer, T., Conklin, B. R., and Albrecht, M. (2010). AltAnalyze and DomainGraph: analyzing and visualizing exon expression data. *Nucleic Acids Res.* 38, W755–W762. doi: 10.1093/nar/gkq405

Fulghum, D. A. (2005). Up a notch. *Aviat. Week Sp. Technol.* 162:86.

Furuta, Y., Piston, D. W., and Hogan, B. L. M. (1997). Bone morphogenetic proteins (BMPs) as regulators of dorsal forebrain development. *Development* 124, 2203–2212. doi: 10.1242/dev.124.11.2203

Ge, W. P., Miyawaki, A., Gage, F. H., Jan, Y. N., and Jan, L. Y. (2012). Local generation of glia is a major astrocyte source in postnatal cortex. *Nature* 484, 376–380. doi: 10.1038/nature10959

Gorris, R., Fischer, J., Erwes, K. L., Kesavan, J., Peterson, D. A., Alexander, M., et al. (2015). Pluripotent stem cell-derived radial glia-like cells as stable intermediate for efficient generation of human oligodendrocytes. *Glia* 63, 2152–2167. doi: 10.1002/glia.22882

Gross, R. E., Mehler, M. F., Mabie, P. C., Zang, Z., Santschi, L., and Kessler, J. A. (1996). Bone morphogenetic proteins promote astroglial lineage commitment by mammalian subventricular zone progenitor cells. *Neuron* 17, 595–606. doi: 10.1016/s0896-6273(00)80193-2

Hack, M. A., Sugimori, M., Lundberg, C., Nakafuku, M., and Götz, M. (2004). Regionalization and fate specification in neurospheres: the role of Olig2 and Pax6. *Mol. Cell. Neurosci.* 25, 664–678. doi: 10.1016/j.mcn.2003.12.012

Han, D., Kwon, M., Lee, S. M., Pleasure, S. J., and Yoon, K. (2020). Non-cell autonomous promotion of astrogenesis at late embryonic stages by constitutive YAP activation. *Sci. Rep.* 10:7041. doi: 10.1038/s41598-020-63890-z

Jessell, T. M. (2000). Neuronal specification in the spinal cord:inductive signals and transcriptional codes. *Nat. Rev. Genet.* 1, 20–29. doi: 10.1038/35049541

Klempin, F., Marr, R. A., and Peterson, D. A. (2012). Modification of Pax6 and Olig2 expression in adult hippocampal neurogenesis selectively induces stem cell fate and alters both neuronal and glial populations. *Stem Cells* 30, 500–509. doi: 10.1002/stem.1005

Koyama, Y. (2014). Signaling molecules regulating phenotypic conversions of astrocytes and glial scar formation in damaged nerve tissues. *Neurochem. Int.* 78, 35–42. doi: 10.1016/j.neuint.2014.08.005

Levison, S. W., and Goldman, J. E. (1993). Both oligodendrocytes and astrocytes develop from progenitors in the subventricular zone of postnatal rat forebrain. *Neuron* 10, 201–212. doi: 10.1016/0896-6273(93)90311-e

Mabie, P. C., Mehler, M. F., and Kessler, J. A. (1999). Multiple roles of bone morphogenetic protein signaling in the regulation of cortical cell number and phenotype. *J. Neurosci.* 19, 7077–7088. doi: 10.1523/JNEUROSCI.19-16-07077.1999

McMahon, A. P. (2000). Neural patterning: the role of Nkx genes in the ventral spinal cord. *Genes Dev.* 14, 2261–2264. doi: 10.1101/gad.840800

Mehler, M. F., Mabie, P. C., Zhang, D., and Kessler, J. A. (1997). Bone morphogenetic proteins in the nervous system. *Trends Neurosci.* 20, 309–317.

Meuli, M., and Moehrlen, U. (2014). Fetal surgery for myelomeningocele is effective: a critical look at the whys. *Pediatr. Surg. Int.* 30, 689–697. doi: 10.1007/s00383-014-3524-8

Mitchell, L. E., Scott Adzick, N., Melchionne, J., Pasquariello, P. S., Sutton, L. N., and Whitehead, A. S. (2004). Spina bifida. *Lancet* 364, 1885–1895.

Miyagi, M., Mikawa, S., Sato, T., Hasegawa, T., Kobayashi, S., Matsuyama, Y., et al. (2012). BMP2, BMP4, noggin, BMPRIA, BMPRIB, and BMPRII are differentially expressed in the adult rat spinal cord. *Neuroscience* 203, 12–26. doi: 10.1016/j.neuroscience.2011.12.022

Mizuguchi, R., Sugimori, M., Takebayashi, H., Kosako, H., Nagao, M., Yoshida, S., et al. (2001). Combinatorial roles of olig2 and neurogenin2 in the coordinated induction of pan-neuronal and subtype-specific properties of motoneurons. *Neuron* 31, 757–771. doi: 10.1016/s0896-6273(01)00413-5

Moldenhauer, J. S., and Adzick, N. S. (2017). Fetal surgery for myelomeningocele: after the Management of Myelomeningocele Study (MOMS). *Semin. Fetal Neonatal Med.* 22, 360–366. doi: 10.1016/j.siny.2017.08.004

Molofsky, A. V., Krenick, R., Ullian, E., Tsai, H.-H., Deneen, B., and Richardson, W. D. (2012). Astrocytes and disease: a neurodevelopmental perspective. *Genes Dev.* 26, 891–907. doi: 10.1101/gad.188326.112

Murphy, K. P., Pathak, B., Peiro, J. L., and Oria, M. (2021). Time Course Transcriptome Analysis of Spina Bifida Progression in Fetal Rats. *Brain Sci.* 11:1593. doi: 10.3390/brainsci11121593

Oria, M., Duru, S., Figueira, R. L., Scorletti, F., Turner, L. E., Fernandez-Alonso, I., et al. (2019). Cell necrosis, intrinsic apoptosis and senescence contribute to the progression of exencephaly to anencephaly in a mice model of congenital chranioschisis. *Cell Death Dis.* 10:721. doi: 10.1038/s41419-019-1913-6

Oria, M., Figueira, R. L., Scorletti, F., Sbragia, L., Owens, K., Li, Z., et al. (2018). CD200-CD200R imbalance correlates with microglia and pro-inflammatory activation in rat spinal cords exposed to amniotic fluid in retinoic acid-induced spina bifida. *Sci. Rep.* 8:10638 . doi: 10.1038/s41598-018-28829-5

Pekny, M., and Nilsson, M. (2005). Astrocyte activation and reactive gliosis. *Glia* 50, 427–434. doi: 10.1002/glia.20207

Qi, Y., Cai, J., Wu, Y., Wu, R., Lee, J., Fu, H., et al. (2001). Control of oligodendrocyte differentiation by the Nkx2.2 homeodomain transcription factor. *Development* 128, 2723–2733. doi: 10.1242/dev.128.14.2723

Reemst, K., Noctor, S. C., Lucassen, P. J., and Hol, E. M. (2016). The indispensable roles of microglia and astrocytes during brain development. *Front. Hum. Neurosci.* 10:566. doi: 10.3389/fnhum.2016.00566

Reis, J. L., Correia-Pinto, J., Monteiro, M. P., Costa, M., Ribeiro, A., and Hutchins, G. M. (2008). Immunocytochemical characterization of astrocytosis along the spinal cord of loop-tail/curly-tail mice with myelomeningocele. *Pediatr. Neurosurg.* 44, 288–295. doi: 10.1159/000131677

Reis, J. L., Correia-Pinto, J., Monteiro, M. P., and Hutchins, G. M. (2007). In utero topographic analysis of astrocytes and neuronal cells in the spinal cord of mutant mice with myelomeningocele. *J. Neurosurg.* 106, 472–479. doi: 10.3171/ped.2007.106.6.472

Rowitch, D. H. (2004). Glial specification in the vertebrate neural tube. *Nat. Rev. Neurosci.* 5, 409–419. doi: 10.1038/nrn1389

Rowitch, D. H., and Kriegstein, A. R. (2010). Developmental genetics of vertebrate glial-cell specification. *Nature* 468, 214–222. doi: 10.1038/nature09611

Seo, J. H., Chang, J. H., Song, S. H., Lee, H. N., Jeon, G. S., Kim, D. W., et al. (2008). Spatiotemporal gradient of astrocyte development in the chick optic tectum: evidence for multiple origins and migratory paths of astrocytes. *Neurochem. Res.* 33, 1346–1355. doi: 10.1007/s11064-008-9590-3

Shirasaki, R., and Pfaff, S. L. (2002). Transcriptional Codes and the Control of Neuronal Identity. *Annu. Rev. Neurosci.* 25, 251–281. doi: 10.1146/annurev.neuro.25.112701.142916

Sofroniew, M. V. (2015). Astrogliosis. *Cold Spring Harb. Perspect. Biol.* 7:a020420.

Sugimori, M., Nagao, M., Bertrand, N., Parras, C. M., Guillemot, F., and Nakafuku, M. (2007). Combinatorial actions of patterning and HLH transcription factors in the spatiotemporal control of neurogenesis and gliogenesis in the developing spinal cord. *Development* 134, 1617–1629. doi: 10.1242/dev.001255

Temple, S. (2001). The development of neural stem cells. *Nature* 414, 112–127.

Ulloa, F., and Briscoe, J. (2007). Morphogens and the control of cell proliferation and patterning in the spinal cord. *Cell Cycle* 6, 2640–2649. doi: 10.4161/cc.6.21.4822

Verkhratsky, A., and Parpura, V. (2016). Astrogliopathology in neurological, neurodevelopmental and psychiatric disorders. *Neurobiol. Dis.* 85, 254–261. doi: 10.1016/j.nbd.2015.03.025

Xin, H., Li, Y., Chen, X., and Chopp, M. (2006). Bone marrow stromal cells induce BMP2/4 production in oxygen-glucose- deprived astrocytes, which promotes an astrocytic phenotype in adult subventricular progenitor cells. *J. Neurosci. Res.* 83, 1485–1493. doi: 10.1002/jnr.20834

Yoon, H., Walters, G., Paulsen, A. R., and Scarisbrick, I. A. (2017). Astrocyte heterogeneity across the brain and spinal cord occurs developmentally, in adulthood and in response to demyelination. *PLoS One* 12:e0180697. doi: 10.1371/journal.pone.0180697

Yun, W., Kim, I. Y., Song, G., and You, S. (2020). Rapid induction of gliogenesis in OLIG2 and NKX2.2-expressing progenitors-derived spheroids. *Stem Cells Transl. Med.* 9, 1643–1650. doi: 10.1002/sctm.19-0455

Zhou, Q., and Anderson, D. J. (2002). The bHLH transcription factors OLIG2 and OLIG1 couple neuronal and glial subtype specification. *Cell* 109, 61–73. doi: 10.1016/s0092-8674(02)00677-3

Zhou, Q., Choi, G., and Anderson, D. J. (2001). The bHLH transcription factor Olig2 Promotes oligodendrocyte differentiation in collaboration with Nkx2.2. *Neuron* 31, 791–807. doi: 10.1016/s0896-6273(01)00414-7

Conflict of Interest: The authors declare that the research was conducted in the absence of any commercial or financial relationships that could be construed as a potential conflict of interest.

frontiers | Frontiers in Molecular Neuroscience

ORIGINAL RESEARCH
published: 07 July 2022
doi: 10.3389/fnmol.2022.938930

Regenerative Peripheral Nerve Interfaces Effectively Prevent Neuroma Formation After Sciatic Nerve Transection in Rats

Jiaqing Wu[1†], *Yajun Zhang*[2†], *Xiaoyuan Zhang*[1], *Zhiyu Lin*[3] *and Guangxue Li*[1*]

[1] Department of Plastic Surgery, Peking University People's Hospital, Beijing, China, [2] Trauma Medicine Center, Peking University People's Hospital, Beijing, China, [3] Department of Plastic Surgery, Peking University Third Hospital, Beijing, China

Edited by:
Lingyan Xing,
Nantong University, China

Reviewed by:
Dianwen Qi,
Third Hospital of Hebei Medical University, China
Jinlei Dong,
Shandong Provincial Hospital, China
Abbas Raisi,
Lorestan University, Iran

***Correspondence:**
Guangxue Li
luckylgx1012@163.com

[†] These authors have contributed equally to this work and share first authorship

Specialty section:
This article was submitted to Neuroplasticity and Development, a section of the journal Frontiers in Molecular Neuroscience

Received: 08 May 2022
Accepted: 15 June 2022
Published: 07 July 2022

Citation:
Wu J, Zhang Y, Zhang X, Lin Z and Li G (2022) Regenerative Peripheral Nerve Interfaces Effectively Prevent Neuroma Formation After Sciatic Nerve Transection in Rats. Front. Mol. Neurosci. 15:938930. doi: 10.3389/fnmol.2022.938930

Objective: The disordered growth of nerve stumps after amputation leading to the formation of neuromas is an important cause of postoperative pain in amputees. This severely affects the patients' quality of life. Regenerative peripheral nerve interfaces (RPNIs) are an emerging method for neuroma prevention, but its postoperative nerve growth and pathological changes are yet to be studied.

Methods: The rat sciatic nerve transection model was used to study the effectiveness of RPNI in this experiment. The RPNI (experimental) group ($n = 11$) underwent RPNI implantation after sciatic nerve transection, while the control group ($n = 11$) only underwent sciatic nerve transection. Autotomy behavior, ultrasonography, and histopathology were observed for 2 months postoperatively.

Results: Compared to the control group, the incidence and size of the neuromas formed and the incidence and extent of autotomy were significantly reduced in the RPNI group. The axon density in the stump and degree of stump fibrosis were also significantly reduced in the RPNI group.

Conclusion: RPNI effectively prevented the formation of neuromas.

Keywords: regenerative peripheral nerve interfaces, postoperative pain, neuromas, amputation, autotomy

INTRODUCTION

Pain is a common symptom experienced by amputees, and it is classified as postoperative pain, residual limb pain, phantom limb pain and prosthetic pain (Uustal and Meier, 2014). The incidence of residual limb pain is as high as 74% (Ehde et al., 2000), and 48.7% of these patients have evidence of neuromas (Buchheit et al., 2016). After the nerve of the amputee has been severed, the proximal nerve loses the corresponding distal nerve and innervation target, and it grows haphazardly in all directions. Neuromas are localized masses entangled with the surrounding hyperplastic fibrous connective tissue to form tumor-like structures. Neuromas can cause pain or paraesthesia when stimulated by the tearing, compressing, and stretching of the surrounding tissues (Rajput et al., 2012), and can severely impair the patients' quality of life.

In the past, the prevention and treatment methods for painful neuromas included analgesic drugs (i.e., antidepressants, anticonvulsants, opioids) (Jacobson et al., 1990; Wu et al., 2002; Robinson et al., 2004; Geary et al., 2021; Vu et al., 2022), percutaneous interventional therapies (i.e., injection of steroids, chemical ablation, cryotherapy, radiofrequency ablation, extracorporeal shockwave therapy) (Lloyd et al., 1976; Ramamurthy et al., 1989; Rasmussen et al., 1996; Fanucci et al., 2004; Markovic et al., 2008; Morgan et al., 2014), nerve conduits (Muheremu and Ao, 2015; Kubiak et al., 2018; Kang et al., 2022), surgical treatments (i.e., excision, burial, and implantation of nerve endings) and combination of multiple treatment (Azizi et al., 2012; Raisi and Mohammadi, 2019). However, the abovementioned methods have the shortcomings of unstable long-term benefits, high side effects, and a high risk of recurrence, which make the management and treatment of neuromas burdensome.

In recent years, regenerative peripheral nerve interfaces (RPNIs) (Bhashyam et al., 2021), originally designed for intelligent prosthetic control, have emerged as a treatment option for neuromas (Kung et al., 2013; Urbanchek et al., 2016; Vu et al., 2018). The severed nerve endings are implanted into free muscle grafts that target nerve regenerating axons to survive through the processes of degeneration, regeneration, revascularization, and reinnervation to achieve remodeling of the nerve-muscle junction (Svientek et al., 2020), so as to preserve nerve signals and electromyography signals (Jia et al., 2007; Langhals et al., 2014). Intelligent prosthetic control is achieved by the extraction of biological signals in RPNI (Woo et al., 2014; Irwin et al., 2016; Vu et al., 2020). During the development of this technology, it was discovered that RPNI also prevented the formation of neuromas by avoiding the disordered growth of damaged nerve axons (Woo et al., 2016; Ganesh Kumar and Kung, 2021).

Currently, RPNI has been used as a surgical procedure for the prevention of neuromas in multiple pilot clinical studies (Zimmermann, 2001; Woo et al., 2016; Hooper et al., 2020; Kubiak et al., 2022), and the efficacy of RPNI in preventing neuromas was evaluated by the use of pain scores and postoperative complications as evaluation indicators. Woo SL retrospectively analyzed 46 RPNI implantation procedures in 16 patients, and the majority of the patients reported pain relief from neuromas with great satisfaction (Woo et al., 2016). Hooper RC et al. performed 30 RPNI implantation procedures in 14 patients, and 85% of the patients were pain-free or reported improved outcomes upon long-term follow-up (Hooper et al., 2020). In the clinical study by Kubiak et al., 45 patients who received RPNI did not develop neuromas and only 51% had phantom limb pain, whereas six out of 45 patients in the control group developed neuromas and 91% had phantom limb pain. Several current clinical trials have confirmed the effectiveness of RPNI in the prevention of neuromas and phantom limb pain (Zimmermann, 2001; Pejkova et al., 2022).

However, these clinical trials have their limitations. The results of these trials were only based on the clinical outcome (i.e., the degree of pain) and it is unreasonable and inhumane to use the patients' pathological samples to explore the changes in the nerve stumps after RPNI at the cellular level because the patients' health and safety were a priority. The objective of this experiment was to observe the effect of RPNI on the regeneration process after nerve injury, using animal models and from the perspectives of behavioral studies, imaging, and pathology, so as to better understand the effectiveness and the possible mechanism of RPNI in the prevention of neuromas.

MATERIALS AND METHODS

Ethical Approval

All the animals were purchased from Beijing Vital River Laboratory Animal Technology Co., Ltd. The experimental protocol was approved by the animal ethics committee of the Peking University People's Hospital, approval number 2020PHE050, and the experiments were carried out in the Laboratory Animal Unit of the Peking University People's Hospital. All experiments were designed according to the Animal Research: Reporting of *in vivo* Experiments (ARRIVE) guidelines.

Animals and Surgical Procedures

Twenty-two Sprague Dawley rats (6 weeks-old, 200–300 g in bodyweight) were used in this study. The rats were randomly divided into the RPNI and control groups ($n = 11$/group). All the experimental animals were anesthetized by inhalation of 3% isoflurane (500 mL/min) (RWD Life Science, Shenzhen, China). The process surgical operation of RPNI is shown in **Figure 1**. In a sterile operating room, a longitudinal incision was made in the posterolateral aspect of the rat's thigh and extended to the posterolateral aspect of the calf. The skin and subcutaneous tissue were incised in turn to reveal a musculocutaneous perforator (retrogluteal musculocutaneous perforator). The sciatic nerve was quickly exposed, by entering from the intermuscular septum between the biceps femoris and the semitendinosus muscle close to the anterior side of this perforator. The sciatic nerve was transected and 1 cm was resected at the distal end to avoid reconnection of the nerve. A 7-0 suture was used to mark the branch of the posterior gluteal nerve under the operating microscope as a marker for sampling at the end of the experiment. Subsequently, the tibialis anterior muscle was incised along the anterolateral side of the calf to expose the extensor digitorum longus (EDL) muscle, which was fully dissociated from the popliteal fossa and the foot and then transected from the tendon. The freed EDL was harvested. Then, the EDL was placed at the proximal end of the sciatic nerve, and the epineurium and the muscle membrane were sutured with four stitches of 9-0 suture. The 9-0 suture was longitudinally sutured to the muscle to wrap the nerve ending and complete the establishment of a RPNI. The established RPNI was placed in the lower outer thigh with its position fixed subcutaneously. The control group did not receive any special treatment after sciatic nerve transection. The incision was closed with a 4-0 silk thread and the skin was sutured to close the wound of all the rats.

Behavioral Observation of Self-Mutilation (Autotomy)

Using a double-blind method, the autotomy scores of each group of rats were observed and recorded thrice a week by two researchers. The autotomy scores were quantified according to the modified scale by Wall et al. (1979), i.e., 1 point for the absence of two or more toenails per limb, with a maximum of

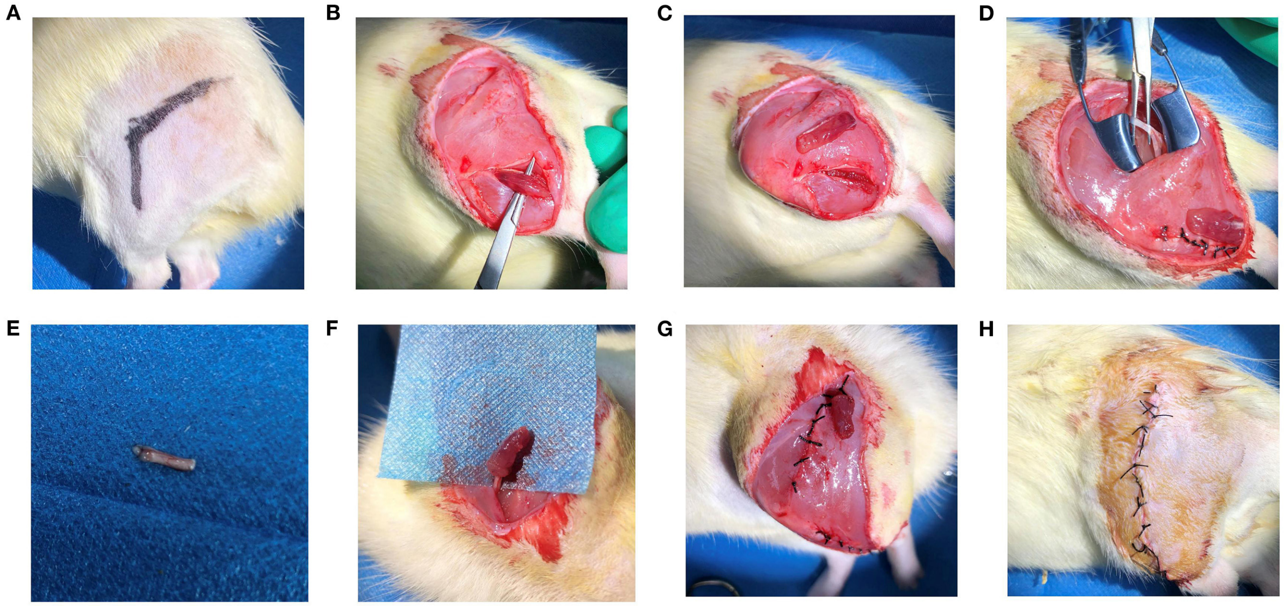

FIGURE 1 | (A) Confirm the surgical approach by exposing the lower limb skin of the rat. **(B)** Expose the extensor digitorum longus of the rat. **(C)** Cut off and acquire the appropriate size extensor digitorum longus. **(D)** Expose the sciatic nerve of the rat. **(E)** Transect the sciatic nerve of the rat. **(F)** Fix the nerve adventitia on the obtained free extensor digitorum longus muscle, and suture the muscle to wrap the nerve. **(G)** Suture the muscle space and fix the RPNI model under the skin. **(H)** Suture the skin and establish the RPNI model.

1 point per limb; and 1 point for missing half of each toe (distal and proximal), up to 10 points per limb.

Ultrasonography

The Toshiba Apolio 500 color ultrasonic diagnostic instrument (Toshiba, Tokyo, Japan) with line array probe and frequency of 5–14.0 MHz was used. Two months postoperation, the rats in each group were fully anesthetized, and the skin of the inspection region was prepared. The projection region of the sciatic nerve on the surgical side of the rat was fully exposed, and two-dimensional ultrasound and color Doppler flow imaging were performed to observe the size, shape, echo, and blood supply of the sciatic nerve tumor. Two researchers measured separately to reduce subjective errors.

Specimen Preparation

All animals were euthanised 2 months postoperation by inhalation of carbon dioxide. The carbon dioxide replacement rate was set to 30% per minute. The skin and muscle were opened layer by layer at the surgical scar, and the 7-0 suture marking was identified for positioning. The proximal nerve stump was collected and fixed in 4% paraformaldehyde at 4°C.

Histological Analysis

After dehydration in ethanol, clearing with xylene, and embedding in paraffin, the distal end of the nerve specimen (i.e., the surgically severed end) was transected into sections of 5 µm thickness. Each specimen was subjected to α-SMA immunohistochemical staining to assess the degree and extent of tissue fibrosis and NF-200 immunofluorescence staining to detect axonal density. The following steps were followed for α-SMA staining: the sections were deparaffinised in water, heat-induced antigen retrieval with EDTA, incubated with 3% hydrogen peroxide for 25 min, and blocked with 5% goat serum for 30 min. Rabbit anti-α-SMA antibody (1:2,000, Cat# 14395-1-AP, RRID:AB_2223009, Proteintech, Beijing, China) was added and incubated at 4°C overnight, followed by incubation with biotinylated anti-rabbit IgG secondary antibody (1:200, Cat# ZB-2010, ZSGB-BIO, Beijing, China) at room temperature for 1 h, diaminobenzidine (DAB) staining was performed under microscopy, and the nuclei were counterstained with haematoxylin, dehydrated and mounted. The following steps were followed for NF-200 immunofluorescence staining: the sections were deparaffinised in water and subjected to antigen retrieval with EDTA. After blocking with 5% goat serum (Solarbio) for 30 min, the sections were incubated with mouse anti-NF-200 antibody (1:200, Cat# N5389, RRID: AB_260781, Sigma, St. Louis, MO, USA) overnight at 4°C, and stored for 2 h at room temperature with Alexa Fluor 594 anti-mouse IgG (1:200, Cat#ZF-0513, ZSGB-BIO). The nuclei were stained with 4′,6-diamidino-2-phenylindole (Sigma).

All images were captured by a Leica DM4 B microscope (Leica, Wetzlar, Germany). Four fields of each pathological were randomly selected and analyzed by Image-Pro Plus 6.0 software (Media Cybernetics, Rockville, MD, USA). The percentage of α-SMA positive staining area was calculated as the α-SMA positive staining area / the total image area × 100. The density of axons was defined as the number of axons within an area of a field.

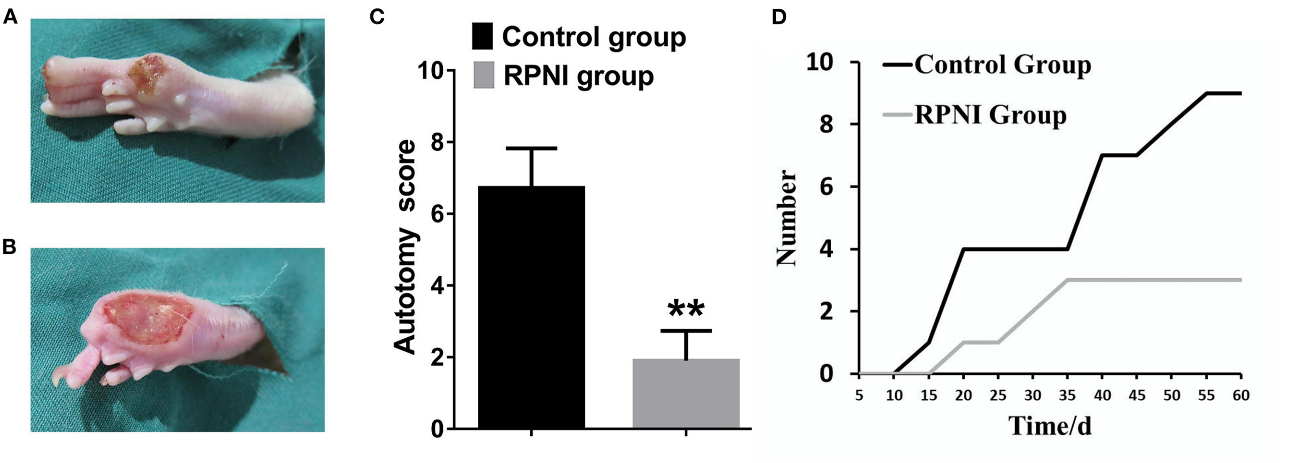

FIGURE 2 | (A) Representative pictures of autotomy behavior of rats in the RPNI group. **(B)** Representative pictures of autotomy behavior of rats in the control group. **(C)** Autotomy score of the control group and autotomy score of the RPNI group. (**$P < 0.01$). **(D)** Autotomy in the control group appeared earlier than that in the RPNI group, and the number of rats with autotomy increased with time.

Statistical Analysis

All numerical data are presented as the mean ± standard deviation (SD). The experimental results were analyzed with SPSS 22.0 software (IBM, Armonk, NY, USA) and the Student's *t*-test was used. Differences were statistically significant at $P < 0.05$.

RESULTS

RPNI Significantly Reduced Autotomy Behavior in Rats

Autotomy was observed in three mice in the RPNI group and in nine mice in the control group at 2 months after the surgery of RPNI. At about 15 days after operation, autotomy began to appear in some rats, and the time in the control group was earlier than that in the PRNI group. The autotomy behavior is shown in **Figure 2**, and the autotomy score of the RPNI group was much lower than that of the control group ($P < 0.01$). RPNI significantly reduced the autotomy behavior in rats.

RPNI Significantly Reduced the Degree of Nerve Stump Hyperplasia

As shown in **Figure 3**, the nerve stumps of the RPNI rats did not increase significantly, while the nerve stumps of the rats in the control group increased significantly and tended to form neuromas. In addition, the ratio of the cross-sectional size of the nerve stump to the normal nerve tissue at the proximal end of the nerve endings in the RPNI group was significantly lower than that in the control group ($P < 0.01$), which indicated that RPNI significantly reduced the degree of regeneration after nerve injury and achieved the goal of preventing neuromas.

RPNI Inhibited the Regenerative of Axons After Sciatic Nerve Transection

Neuromas are formed by the regenerative and disorderly growing axonal after nerve injury. RPNI inhibited the regenerate of axons after sciatic nerve transection. As shown in **Figure 4**, the axonal density revealed by NF-200 immunofluorescence staining of the RPNI group was significantly lower than that of the control group ($P < 0.01$).

RPNI Effectively Reduced the Degree of Neural Fibrosis in the Sciatic Nerve Stump

RPNI inhibited the proliferation of fibroblasts after nerve injury to a certain extent and reduce the entanglement of axons with surrounding fibrous connective tissue which may be beneficial to reduce inflammation around nerve terminals (Zwetsloot et al., 2012; Lieber and Ward, 2013). As shown in **Figure 5**, α-SMA immunohistochemistry revealed that the positive area in the control group was larger ($P < 0.01$).

DISCUSSION

When peripheral nerves are damaged, the nerves that have lost their distal innervated muscles grow in a disordered manner and become entangled with the surrounding tissues to form neuromas, which causes pain. Most of the previous prevention and treatment methods for neuromas were ineffective, but the development of RPNI provided a new direction for the resolution of painful neuromas.

At present, the effectiveness of RPNI in preventing the formation of neuromas is generally recognized (Loewenstein et al., 2022), and its utilization rate is increasing gradually. The research on the postoperative safety of RPNI (Lans et al., 2021) and more innovative surgical methods [c-RPNI (Svientek et al., 2020), TMRpni (Svientek et al., 2022), MC-RPNI (Kurlander et al., 2020), etc.] are also underway. This study attempted to investigate the efficacy of RPNI in preventing neuromas from multiple levels through a sciatic nerve amputation model in rats.

Autotomy behavior in rats is often used to evaluate the degree of nerve pain after peripheral nerve injury (Zimmermann,

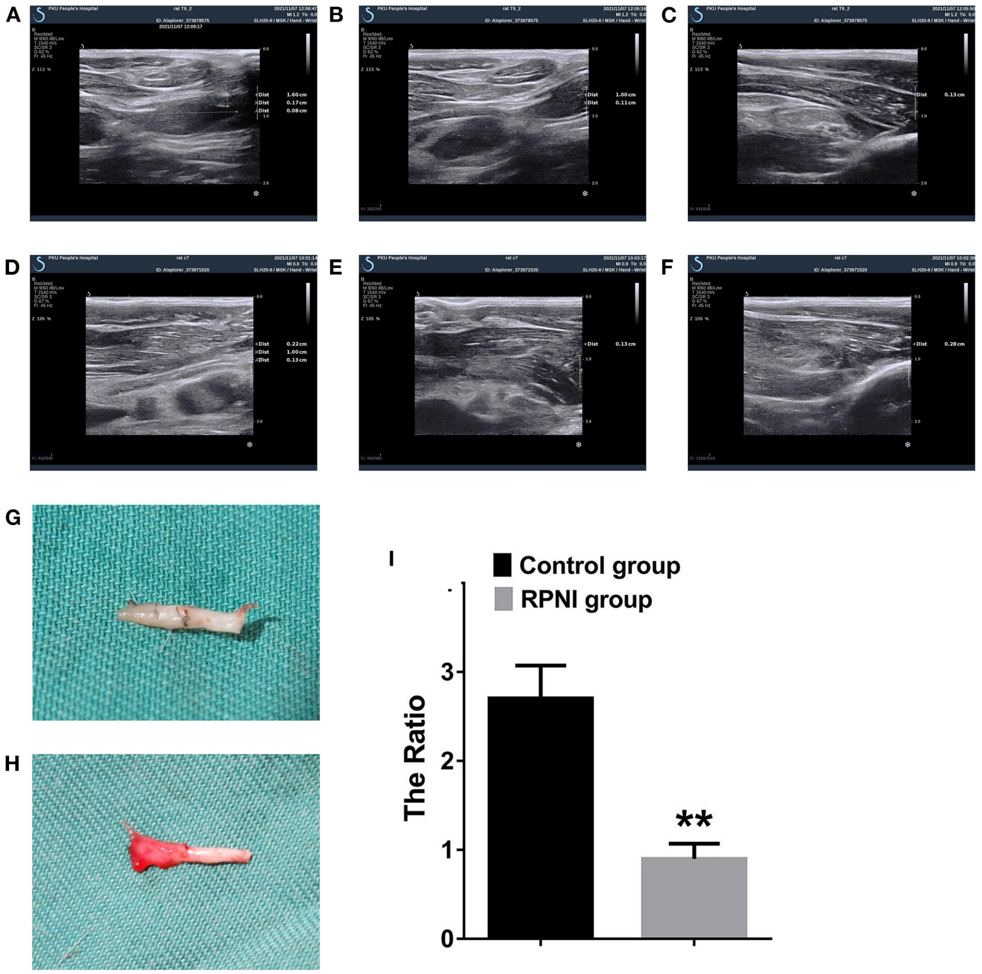

FIGURE 3 | Ultrasound images of rat nerve endings at 8 weeks postoperation. **(A)** Longitudinal section of RPNI rat along the course of the nerve (+ indicates the muscle used to wrap the nerve in the establishment of RPNI, × indicates the distal end of the nerve ending, which is the severed end, ▣ indicates the proximal end of the nerve, i.e., relatively normal nerve tissue). It is observed that the regeneration of nerve stumps in RPNI rats was insignificant, and there was no obvious nerve enlargement. **(B)** Proximal nerve ending in a RPNI rat. **(C)** Distal nerve ending of a RPNI rat. **(D)** The longitudinal section of a control group rat along the course of the nerve, without muscle wrapping, and showed that the nerve was significantly thickened. **(E)** Proximal nerve ending of a rat from the control group. **(F)** Distal nerve ending of a rat from the control group. **(G)** The morphology of the nerve of the RPNI group. There was no obvious expanded neuroma at the end of the nerve. **(H)** The morphology of the nerve of the control group. Expanded neuroma can be observed at the end of the nerve. **(I)** The ratio of the cross-sectional size of the nerve stump to the normal nerve tissue at the proximal end of the nerve endings is estimated by the product of the long diameter and the short diameter of the cross section. There are significant differences between the control group and the RPNI group (**$P < 0.01$).

2001). Marcol et al. (2011) applied microcrystalline chitosan to prevent neuromas, while Pi et al. (2022) used myelin-associated glycoproteins in combination with chitin catheters to prevent the formation of neuromas in their experiments, and used the autotomy behavior of rats as one of the evaluation indicators. Two months following the operation performed on the rats in both the groups, the autotomy behavior of the RPNI group was significantly milder than that of the control group (regardless of the number of rats with autotomy behavior or the degree of autotomy). Since the autotomy behavior of the rats might be affected by environmental, psychological, and other factors, we ensured that the living environment, diet, age, and bodyweight of the two groups of rats were the same, with the only the surgical procedures performed being different. To a large extent, RPNI is considered to be effective in relieving pain after sciatic nerve transection.

Ultrasound imaging is an intuitive way to observe live neuromas. It can accurately measure the thickening of the nerve endings without injuring the rat, so that the experimental data is not damaged during the sampling process. The ratio of the transverse diameter of the nerve stump to the proximal transverse diameter of the rat nerve endings in the RPNI group was smaller in the ultrasound images, which proved that RPNI effectively inhibited the disordered growth and tumourigenesis of nerves.

Svientek et al. found that 3 months after RPNI, muscle revascularization and nerve remodeling were completed (Kubiak et al., 2021), and neuromuscular junctions in the muscle were successfully observed (Svientek et al., 2020). This finding

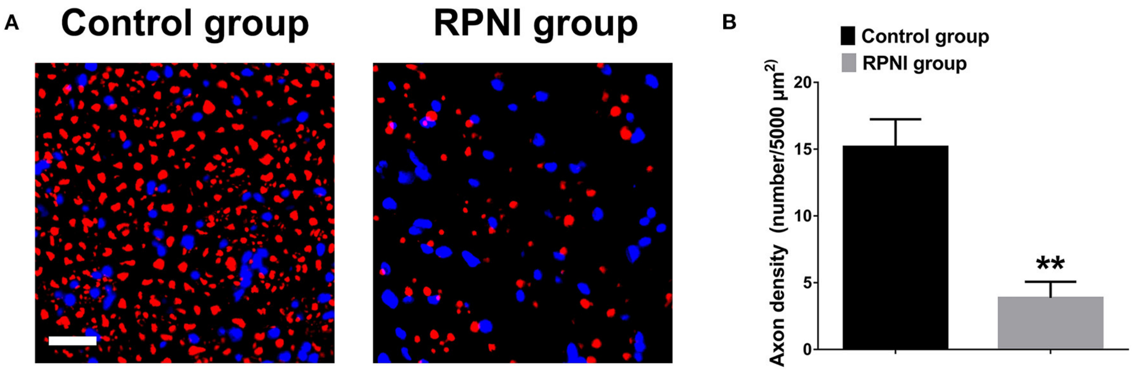

FIGURE 4 | Regenerative peripheral nerve interfaces (RPNI) significantly inhibited axonal regeneration after sciatic nerve transection. **(A)** NF200 immunofluorescence staining of cross sections of the proximal nerve stump. The fluorescence indicator used was Alexa Fluor 594 for NF200 (red). Nuclei are shown in blue. Scale bars: 20 μm. **(B)** Quantitative results of the density of regenerated axons (**$P < 0.01$).

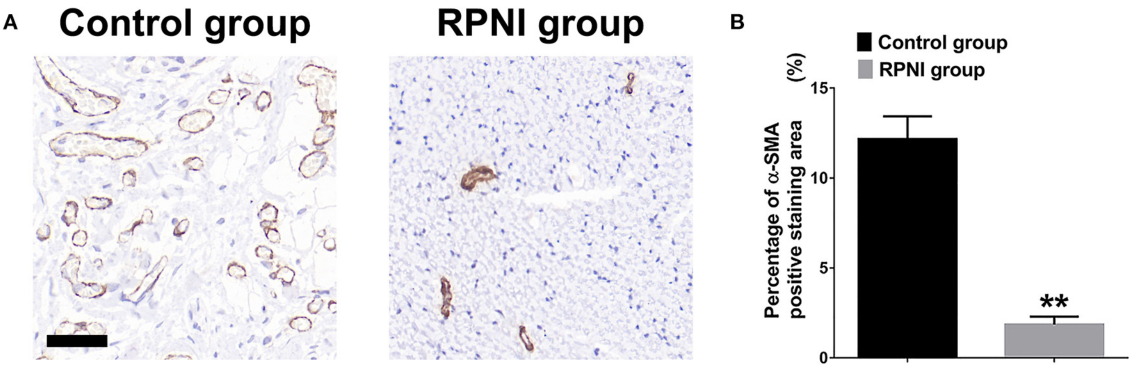

FIGURE 5 | Regenerative peripheral nerve interfaces (RPNI) effectively reduced the degree of neural fibrosis in the sciatic nerve stump. **(A)** α-SMA immunohistochemical staining (brown) of cross sections of the proximal nerve stump. Scale bars: 40 μm. **(B)** Quantitative results of the percentage of α-SMA positive staining area (**$P < 0.01$).

demonstrated that the muscles involved in RPNI wrapping of nerve stumps achieved muscle-nerve junction remodeling during vascular remodeling, and revealed the possibility of RPNI being used as a muscle-nerve interface to extract biological signals. When we dynamically observed the ultrasound images of individual rats, we discovered an interesting phenomenon that confirmed this finding. The growth of the muscle (EDL) used to wrap the nerve in RPNI showed a trend of atrophy followed by surviving growth. At the same time, the proximal sciatic nerve was stimulated with electrodes when the specimen was taken, and the contractile movement of the EDL could be observed. This shows that RPNI forms a complete pathway of brain—spinal cord—peripheral motor nerve—muscle.

NF-200 immunofluorescence staining also confirmed that RPNI effectively reduced irregular axonal growth after nerve injury. NF-200 (neurofilament protein-200) is an important substance that provides structural support to the axons and regulates the diameter of axons. It is arranged in parallel with axons and can reflect the number and growth of axons. In this experiment, NF-200 immunofluorescence staining was used to evaluate the number of axons after nerve injury, and the axonal density of the RPNI group was significantly lower than that of the control group, which proved that RPNI effectively inhibited the regenerative axons which result in the formation of the neuroma after the nerve injury.

In order to further evaluate the degree of neural fibrosis in the two groups, α-smooth muscle actin (α-SMA) immunohistochemical staining was performed. The positive rate of α-SMA was lower in the RPNI group, which indicated that RPNI inhibited fibroblast proliferation and attenuated stump fibrosis after nerve injury to a certain extent. Fibrosis and tangle of regenerated axons and fibrous connective tissue are the pathological basis of neuroma formation. Fibrosis is also related to the activation of a variety of inflammatory pathways and the regulation of gene expression (Zwetsloot et al., 2012; Klingberg et al., 2013; Lieber and Ward, 2013).

Inevitably, this experiment has its limitations. Firstly, the evaluation of pain in rats was relatively limited, and the observation of pain markers such as substance P was lacking. Secondly, there was a lack of more microscopic structural observations. Painful neuromas were thought to be related to various factors such as local inflammation and cytokines, increased Na^+ channel density, and disordered growth of unmyelinated nerve fiber buds after nerve injury (Vu et al., 2020).

This experiment did not involve deeper and broader research into the electrophysiology, inflammatory factors such as TNF-α, and observation under electron microscope. Thirdly, there was no comparison with other neuroma prevention procedures, and the superiority of RPNI in comparison with conventional neuroma prevention procedures and the application of various new materials that has not yet been proven. These require further research.

CONCLUSION

RPNI prevented the formation of neuromas by inducing physiological self-limitation, limiting the regeneration of injured axons, reducing the random and irregular arrangement of regenerated nerve fibers, and preserving the possibility of extracting biological signals through the reconstruction of the neuromuscular junction. It provides more possibilities for the prevention and treatment of postoperative complications of amputees. The potential mechanism and application of RPNI still needs further research and development.

DATA AVAILABILITY STATEMENT

The original contributions presented in the study are included in the article/supplementary material, further inquiries can be directed to the corresponding author/s.

ETHICS STATEMENT

The animal study was reviewed and approved by the Animal Ethics Committee of the Peking University People's Hospital.

AUTHOR CONTRIBUTIONS

GL and YZ contributed to the conception of the study. GL, JW, XZ, and ZL performed the experiment. JW and YZ contributed significantly to analysis and manuscript preparation. All authors contributed to the article and approved the submitted version.

FUNDING

Project (2020YBC12) supported by Peking University Education Big Data Project. Project (RDY2020-04 and RDG2021-04) supported by Peking University People's Hospital Research and Development Funds.

ACKNOWLEDGMENTS

I would like to acknowledge my tutor, Wei Pi, for his valuable assistance and instructive guidance throughout my studies which helped me out of difficulties and brought my work to a higher level. I am extremely grateful to my teammates for their wonderful collaboration and support.

REFERENCES

Azizi, S., Mohammadi, R., Amini, K., and Fallah, R. (2012). Effects of topically administered FK506 on sciatic nerve regeneration and reinnervation after vein graft repair of short nerve gaps. *Neurosurgical Focus* 32, E5. doi: 10.3171/2012.1.FOCUS11320

Bhashyam, A. R., Liu, Y. S., and Kao, D. S. (2021). Targeted peripheral nerve interface: case report with literature review. *Plast. Reconstr. Surg. Global Open* 9, e3532–e3535. doi: 10.1097/GOX.0000000000003532

Buchheit, T., Van de Ven, T., Hsia, H. L. J., McDuffie, M., MacLeod, D. B., White, W., et al. (2016). Pain phenotypes and associated clinical risk factors following traumatic amputation: results from veterans integrated pain evaluation research (VIPER). *Pain Med.* 17, 149–161. doi: 10.1111/pme.12848

Ehde, D. M., Czerniecki, J. M., Smith, D. G., Campbell, K. M., Edwards, W. T., Jensen, M. P., et al. (2000). Chronic phantom sensations, phantom pain, residual limb pain, and other regional pain after lower limb amputation. *Arch. Phys. Med. Rehabil.* 81, 1039–1044. doi: 10.1053/apmr.2000.7583

Fanucci, Z., Masata, S., Fabiano, S., Perugia, D., Squillaci, E., Varrucciu, V., et al. (2004). Treatment of intermetatarsal Morton's neuroma with alcohol injection under US guide: 10-month follow-up. *Eur. Radiol.* 14, 514–518. doi: 10.1007/s00330-003-2057-7

Ganesh Kumar, N., and Kung, T. A. (2021). Regenerative peripheral nerve interfaces for the treatment and prevention of neuromas and neuroma pain. *Hand Clin.* 37, 361–371. doi: 10.1016/j.hcl.2021.05.003

Geary, M., Gaston, R. G., and Loeffler, B. (2021). Surgical and technological advances in the management of upper limb amputees. *Bone Joint J.* 103-b, 430–439. doi: 10.1302/0301-620X.103B3.BJJ-2020-1184.R1

Hooper, R. C., Cederna, P. S., Brown, D. L., Haase, S. C., Waljee, J. F., Egeland, B. M., et al. (2020). Regenerative peripheral nerve interfaces for the management of symptomatic hand and digital neuromas. *Plast. Reconstr. Surg. Global Open* 8, e2792. doi: 10.1097/GOX.0000000000002792

Irwin, Z. T., Schroeder, K. E., Vu, P. P., Tat, D. M., Bullard, A. J., Woo, S. L., et al. (2016). Chronic recording of hand prosthesis control signals via a regenerative peripheral nerve interface in a rhesus macaque. *J. Neural Eng.* 13, 046007. doi: 10.1088/1741-2560/13/4/046007

Jacobson, L., Chabal, C., Brody, M. C., Mariano, A. J., and Chaney, E. F. (1990). A comparison of the effects of intrathecal fentanyl and lidocaine on established postamputation stump pain. *Pain* 40, 137–141. doi: 10.1016/0304-3959(90)90064-K

Jia, X., Koenig, M. A., Zhang, X., Zhang, J., Chen, T., and Chen, Z. (2007). Residual motor signal in long-term human severed peripheral nerves and feasibility of neural signal-controlled artificial limb. *J. Hand Surg. Am.* 32, 657–666. doi: 10.1016/j.jhsa.2007.02.021

Kang, N. U., Lee, S. J., and Gwak, S. J. (2022). Fabrication techniques of nerve guidance conduits for nerve regeneration. *Yonsei Med. J.* 63, 114–123. doi: 10.3349/ymj.2022.63.2.114

Klingberg, F., Hinz, B., and White, E. S. (2013). The myofibroblast matrix: implications for tissue repair and fibrosis. *J. Pathol.* 229, 298–309. doi: 10.1002/path.4104

Kubiak, C. A., Adidharma, W., Kung, T. A., Kemp, S. W. P., Cederna, P. S., and Vemuri, C. (2022). Decreasing postamputation pain with the regenerative peripheral nerve interface (RPNI). *Ann. Vasc. Surg.* 79, 421–426. doi: 10.1016/j.avsg.2021.08.014

Kubiak, C. A., Kung, T. A., Brown, D. L., Cederna, P. S., and Kemp, S. W. P. (2018). State-of-the-art techniques in treating peripheral nerve injury. *Plast. Reconstr. Surg.* 141, 702–710. doi: 10.1097/PRS.0000000000004121

Kubiak, C. A., Svientek, S. R., Dehdashtian, A., Lawera, N. G., Nadarajan, V., Bratley, J. V., et al. (2021). Physiologic signaling and viability of the muscle cuff regenerative peripheral nerve interface (MC-RPNI) for intact peripheral nerves. *J. Neural Eng.* 18, 460–473. doi: 10.1088/1741-2552/ac1b6b

Kung, T. A., Bueno, R. A., Alkhalefah, G. K., Langhals, N. B., Urbanchek, M. G., and Cederna, P. S. (2013). Innovations in prosthetic interfaces for the upper extremity. *Plast. Reconstr. Surg.* 132, 1515–1523. doi: 10.1097/PRS.0b013e3182a97e5f

Kurlander, D. E., Wee, C., Chepla, K. J., Lineberry, K. D., Long, T. C., Gillis, J. A., et al. (2020). TMRpni: combining two peripheral nerve management techniques. *Plast. Reconstr. Surg. Global Open* 8, e3132. doi: 10.1097/GOX.0000000000003132

Langhals, N. B., Woo, S. L., Moon, J. D., Larson, J. V., Leach, M. K., Cederna, P. S., et al. (2014). Electrically stimulated signals from a long-term regenerative peripheral nerve interface. *Annu. Int. Conf. IEEE Eng. Med. Biol. Soc.* 2014, 1989–1992. doi: 10.1109/EMBC.2014.6944004

Lans, J., Hoftiezer, Y., Lozano-Calderón, S. A., Heng, M., Valerio, I. L., and Eberlin, K. R. (2021). Risk factors for neuropathic pain following major upper extremity amputation. *J. Reconstr. Microsurg.* 37, 413–420. doi: 10.1055/s-0040-1718547

Lieber, R. L., and Ward, S. R. (2013). Cellular mechanisms of tissue fibrosis. 4. Structural and functional consequences of skeletal muscle fibrosis. *Am. J. Physiol. Cell Physiol.* 305, C241–252. doi: 10.1152/ajpcell.00173.2013

Lloyd, J. W., Barnard, J. D. W., and Glynn, C. J. (1976). Cryoanalgesia: a new approach to pain relief. *Lancet* 308, 932–934. doi: 10.1016/S0140-6736(76)90893-X

Loewenstein, S. N., Cuevas, C. U., and Adkinson, J. M. (2022). Utilization of techniques for upper extremity amputation neuroma treatment and prevention. *J. Plast. Reconstr. Aesthet. Surg.* 75, 1551–1556. doi: 10.1016/j.bjps.2021.11.077

Marcol, W., Larysz-Brysz, M., Kucharska, M., Niekraszewicz, A., Slusarczyk, W., Kotulska, K., et al. (2011). Reduction of post-traumatic neuroma and epineural scar formation in rat sciatic nerve by application of microcrystallic chitosan. *Microsurgery* 31, 642–649. doi: 10.1002/micr.20945

Markovic, M., Crichton, K., Read, J. W., Lam, P., and Slater, H. K. (2008). Effectiveness of ultrasound-guided corticosteroid injection in the treatment of Morton's neuroma. *Foot Ankle Int.* 29, 483–487. doi: 10.3113/FAI.2008.0483

Morgan, P., Monaghan, W., and Richards, S. (2014). A systematic review of ultrasound-guided and non-ultrasound-guided therapeutic injections to treat morton's neuroma. *J. Am. Podiatr. Med. Assoc.* 104, 337–348. doi: 10.7547/0003-0538-104.4.337

Muheremu, A., and Ao, Q. (2015). Past, present, and future of nerve conduits in the treatment of peripheral nerve injury. *Biomed Res. Int.* 2015, 237507. doi: 10.1155/2015/237507

Pejkova, S., Nikolovska, B., Srbov, B., Tusheva, S., Jovanoski, T., Jovanovska, K., et al. (2022). Prophylactic regenerative peripheral nerve interfaces in elective lower limb amputations. *Pril* 43, 41–48. doi: 10.2478/prilozi-2022-0004

Pi, W., Li, C., Zhang, M., Zhang, W., and Zhang, P. X. (2022). Myelin-associated glycoprotein combined with chitin conduit inhibits painful neuroma formation after sciatic nerve transection. *Neural Regen. Res.* 17, 1343–1347. doi: 10.4103/1673-5374.327351

Raisi, A., and Mohammadi, R. (2019). Effects of local administration of ibuprofen on sciatic nerve regeneration and reinnervation after egg shell membrane conduit repair in rat. *J. Neurosurg. Sci.* 63, 531–540. doi: 10.23736/S0390-5616.16.03217-X

Rajput, K., Reddy, S., and Shankar, H. (2012). Painful neuromas. *Clin. J. Pain* 28, 639–645. doi: 10.1097/AJP.0b013e31823d30a2

Ramamurthy, S., Walsh, N. E., Schoenfeld, L. S., and Hoffman, J. (1989). Evaluation of neurolytic blocks using phenol and cryogenic block in the management of chronic pain. *J. Pain Sympt. Manage.* 4, 72–75. doi: 10.1016/0885-3924(89)90026-2

Rasmussen, M. R., Kitaoka, H. B., and Patzer, G. L. (1996). Nonoperative treatment of plantar interdigital neuroma with a single corticosteroid injection. *Clin. Orthop. Relat. Res.* 44, 188–193. doi: 10.1097/00003086-199605000-00022

Robinson, L. R., Czerniecki, J. M., Ehde, D. M., Edwards, W. T., Judish, D. A., Goldberg, M. L., et al. (2004). Trial of amitriptyline for relief of pain in amputees: results of a ramdomized controlled study. *Arch. Phys. Med. Rehabil.* 85, 1–6. doi: 10.1016/S0003-9993(03)00476-3

Svientek, S. R., Ursu, D. C., Cederna, P. S., and Kemp, S. W. P. (2020). Fabrication of the composite regenerative peripheral nerve interface (C-RPNI) in the adult rat. *J. Vis. Exp*. 15. doi: 10.3791/60841

Svientek, S. R., Wisely, J. P., Dehdashtian, A., Bratley, J. V., Cederna, P. S., and Kemp, S. W. P. (2022). The muscle cuff regenerative peripheral nerve interface for the amplification of intact peripheral nerve signals. *J. Vis. Exp.* 17. doi: 10.3791/63222

Urbanchek, M. G., Kung, T. A., Frost, C. M., Martin, D. C., Larkin, L. M., Wollstein, A., et al. (2016). Development of a regenerative peripheral nerve interface for control of a neuroprosthetic limb. *Biomed Res. Int.* 2016, 5726730. doi: 10.1155/2016/5726730

Uustal, H., and Meier, R. H. (2014). Pain Issues and treatment of the person with an amputation. *Phys. Med. Rehabil. Clin. N. Am.* 25, 45. doi: 10.1016/j.pmr.2013.09.008

Vu, P. P., Irwin, Z. T., Bullard, A. J., Ambani, S. W., Sando, I. C., Urbanchek, M. G., et al. (2018). Closed-loop continuous hand control via chronic recording of regenerative peripheral nerve interfaces. *IEEE Trans. Neural Syst. Rehabil. Eng.* 26, 515–526. doi: 10.1109/TNSRE.2017.2772961

Vu, P. P., Lu, C. W., Vaskov, A. K., Gates, D. H., Gillespie, R. B., Kemp, S. W. P., et al. (2022). Restoration of proprioceptive and cutaneous sensation using regenerative peripheral nerve interfaces in humans with upper limb amputations. *Plast. Reconstr. Surg.* 149, 1149e–1154e. doi: 10.1097/PRS.0000000000009153

Vu, P. P., Vaskov, A. K., Irwin, Z. T., Henning, P. T., Lueders, D. R., Laidlaw, A. T., et al. (2020). A regenerative peripheral nerve interface allows real-time control of an artificial hand in upper limb amputees. *Sci. Transl. Med.* 12, eaay2857. doi: 10.1126/scitranslmed.aay2857

Wall, P. D., Devor, M., Inbal, R., Scadding, J. W., Schonfeld, D., Seltzer, Z., et al. (1979). Autotomy following peripheral nerve lesions: experimental anaesthesia dolorosa. *Pain* 7, 103–113. doi: 10.1016/0304-3959(79)90002-2

Woo, S. L., Kung, T. A., Brown, D. L., Leonard, J. A., Kelly, B. M., and Cederna, P. S. (2016). Regenerative peripheral nerve interfaces for the treatment of postamputation neuroma pain: a pilot study. *Plast. Reconstr. Surg. Global Open* 4, e1038–e1038. doi: 10.1097/GOX.0000000000001038

Woo, S. L., Urbanchek, M. G., Leach, M. K., Moon, J. D., Cederna, P., and Langhals, N. B. (2014). Quantification of muscle-derived signal interference during monopolar needle electromyography of a peripheral nerve interface in the rat hind limb. *Annu. Int. Conf. IEEE Eng. Med. Biol. Soc.* 2014, 4382–4385. doi: 10.1109/EMBC.2014.6944595

Wu, C. L., Tella, P., Staats, P. S., Vaslav, R., Kazim, D. A., Wesselmann, U., et al. (2002). Analgesic effects of intravenous lidocaine and morphine on postamputation pain - A randomized double-blind, active placebo-controlled, crossover trial. *Anesthesiology* 96, 841–848. doi: 10.1097/00000542-200204000-00010

Zimmermann, M. (2001). Pathobiology of neuropathic pain. *Eur. J. Pharmacol.* 429, 23–37. doi: 10.1016/S0014-2999(01)01303-6

Zwetsloot, K. A., Nedergaard, A., Gilpin, L. T., Childs, T. E., and Booth, F. W. (2012). Differences in transcriptional patterns of extracellular matrix, inflammatory, and myogenic regulatory genes in myofibroblasts, fibroblasts, and muscle precursor cells isolated from old male rat skeletal muscle using a novel cell isolation procedure. *Biogerontology* 13, 383–398. doi: 10.1007/s10522-012-9382-7

Conflict of Interest: The authors declare that the research was conducted in the absence of any commercial or financial relationships that could be construed as a potential conflict of interest.

frontiers | Frontiers in Molecular Neuroscience

TYPE Original Research
PUBLISHED 24 August 2022
DOI 10.3389/fnmol.2022.950586

Check for updates

OPEN ACCESS

EDITED BY
Lingyan Xing,
Nantong University, China

REVIEWED BY
Chun Hu,
South China Normal University, China
Yong Cao,
Central South University, China

*CORRESPONDENCE
Guowei Zhang
zgw24@qq.com
Hongsheng Lin
tlinhsh@jnu.edu.cn
Zhisheng Ji
jizhisheng0521@163.com

†These authors have contributed equally to this work

SPECIALTY SECTION
This article was submitted to Neuroplasticity and Development, a section of the journal Frontiers in Molecular Neuroscience

RECEIVED 23 May 2022
ACCEPTED 18 July 2022
PUBLISHED 24 August 2022

CITATION
Luo J, Xie M, Peng C, Ma Y, Wang K, Lin G, Yang H, Chen T, Liu Q, Zhang G, Lin H and Ji Z (2022) Protein disulfide isomerase A6 promotes the repair of injured nerve through interactions with spastin.
Front. Mol. Neurosci. 15:950586.
doi: 10.3389/fnmol.2022.950586

Protein disulfide isomerase A6 promotes the repair of injured nerve through interactions with spastin

Jianxian Luo[1†], Min Xie[1,2,3†], Cheng Peng[1†], Yanming Ma[1], Ke Wang[1], Gengxiong Lin[1], Hua Yang[1], Tianjun Chen[1], Qiuling Liu[1], Guowei Zhang[1*], Hongsheng Lin[1*] and Zhisheng Ji[1*]

[1]Department of Orthopedics, The First Affiliated Hospital, Jinan University, Guangzhou, China, [2]Department of Orthopedics, Zhuhai Hospital Affiliated with Jinan University (Zhuhai People's Hospital), Zhuhai, China, [3]Orthopedics Department I, Zhuhai Hospital of Integrated Traditional Chinese and Western Medicine, Zhuhai, China

The maintenance of appropriate endoplasmic reticulum (ER) homeostasis is critical to effective spinal cord injury (SCI) repair. In previous reports, protein disulfide isomerase A6 (PDIA6) demonstrated to serve as a reversible functional modulator of ER stress responses, while spastin can coordinate ER organization through the modulation of the dynamic microtubule network surrounding this organelle. While both PDIA6 and spastin are thus important regulators of the ER, whether they interact with one another for SCI repair still needs to be determined. Here a proteomics analysis identified PDIA6 as being related to SCI repair, and protein interaction mass spectrometry further confirmed the ability of PDIA6 and spastin to interact with one another. Pull-down and co-immunoprecipitation assays were further performed to validate and characterize the interactions between these two proteins. The RNAi-based knockdown of PDIA6 in COS-7 cells inhibited the activity of spastin-dependent microtubule severing. PDIA6 was also found to promote injured neuron repair, while spastin knockdown reversed this reparative activity. Together, these results thus confirm that PDIA6 and spastin function together as critical mediators of nerve repair, highlighting their potential value as validated targets for efforts to promote SCI repair.

KEYWORDS

PDIA6, spastin, endoplasmic reticulum homeostasis, protein interaction, nerve repair, spinal cord injury

Introduction

Spinal cord injuries (SCIs) result from serious spinal cord damage, adversely impacting the quality of life of affected patients (Venkatesh et al., 2019). SCI repair processes are closely tied to the maintenance of endoplasmic reticulum (ER) homeostasis (Ohri et al., 2013), as the death of many neurons following SCI is not a direct result of the initial injury but is instead secondary to ER stress and other adverse inflammation and damage-related stimuli (Bisicchia et al., 2022). Indeed, prior studies have documented the impact of ER stress on neurons following SCI (Ohri et al., 2013; Liu et al., 2015), with the inhibition of such ER stress being sufficient to protect against SCI-induced neuronal apoptosis, thereby promoting SCI repair (Bi et al., 2020). The mechanisms underlying ER stress-induced neuronal damage following SCI, however, remain to be fully clarified.

Protein disulfide isomerase 6 (PDIA6, likewise called P5) is a key modulator of ER function (Jessop et al., 2009), contributing to ER stress-driven unfolded protein response (UPR) (Matsusaki et al., 2020). The primary proteins that mediate UPR-associated signal transduction are Inositol-requiring enzyme 1 (IRE1), Protein kinase R (PKR)-like endoplasmic reticulum kinase (PERK), and Activating Transcription Factor 6 (ATF6) (Walter and Ron, 2011). PDIA6 cleaves the disulfide bond within oligomeric IRE1, thereby promoting its inactivation, resulting in downstream IRE1 signal pathway activation (Matsusaki et al., 2020). Through this activity, PDIA6 can limit the activation of the UPR pathway under normal physiological conditions (Eletto et al., 2014). Prior work suggests that PDIA6 plays a role in several neurodegenerative disorders such as Alzheimer's disease (AD) and Huntington's disease (HD) (Bai et al., 2015; Montibeller and de Belleroche, 2018).

Spastin is a protein that can sever microtubules, thereby regulating their dynamics and promoting the growth and development of neurons (Ji et al., 2018, 2020). Notably, microtubule dynamics are critical to injured neuron regeneration (Stone et al., 2012), and spastin upregulation has previously been linked to axonal regeneration in damaged neurons (Lai et al., 2020). Spastin gene mutations are also thought to be one of the primary causes of a series of heterogeneous neurodegenerative disorders known as hereditary spastic paraplegia (HSP) (Zhu et al., 2019). These spastin gene mutations can contribute to HSP-related symptoms through both the alteration of ER shape and lipid droplet (LD) dispersion, as both of these phenotypes are microtubule-dependent (Arribat et al., 2020). The ability of spastin to regulate ER morphology through the modulation of microtubule dynamics is also associated with its ability to interact with protrudin (Chang et al., 2013; Vajente et al., 2019).

As these prior studies indicate, both spastin and PDIA6 are important regulators of ER homeostasis, with such homeostasis being essential to functional recovery following SCI (Ji Z. et al., 2021). The specific roles that PDIA6 and spastin play in the context of SCI repair, however, have yet to be clarified. This investigative research was thus developed to study the interactions among these two proteins and their mechanistic functions during the process of repairing injured nerves.

Materials and methods

Animals

Clear of certain microorganisms, female Sprague-Dawley (SD) rats (10-weeks-old, 180–230 g; or 1-day old) were acquired from Experimental Animal Center of Sun Yat-sen University. The Research on Animals: (ARRIVE) guidelines were utilized for reporting of *in vivo* experiments to design all animal studies. Separately kept rats were placed in a 25°C ± 3°C environment, accessing water and food at liberty. The studies involving animals were reviewed and approved by Jinan University of ethics committee.

SCI model establishment

Female rats (10-weeks-old; $n = 36$) were randomized into normal control and SCI model groups, with SCI model rats being further separated into light, moderate, and severe injury subgroups ($n = 9$/group). SCI modeling was achieved *via* injury to the T10 spinal segment as reported previously by Wu et al. (2019). Rats were initially put under anesthesia for a short time *via* intraperitoneal sodium pentobarbital administration (30 mg/kg, Sinopharm Chemical Reagent Co., Ltd., Beijing, China. The T9-11 spinal cord was then exposed through a 2.5 cm longitudinal dorsal incision, with the entirety of the T10 lamina then being removed to expose a ∼2.5 mm × 3 mm spinal region. T10 facets were then fixed using a U-shaped rat stabilizer (University of Louisville) loaded onto the stage of the Louisville Injury System Instrument. Spinal cord height was then adjusted under the impactor using laser guidance, with the depth of impact being adjusted to 0.6, 1.0, or 1.8 mm to simulate light, moderate, or extreme damage. The selected impact level was maintained for 0.5 s, with the impact tip being under the control of a nitrogen tank set to 18 psi (124 kPa). Following injury induction, the stabilizer was separated from the stage, and rats were removed therefrom. The injured spinal segment was then examined, with any bleeding being addressed as appropriate. Then, 3-0 silk sutures were used to close the overlying muscle and skin. Successful SCI model establishment was confirmed based on the observation of peri-wound edema, spinal cord ischemia, delayed paralysis, tail wag reflex, and body and leg swing. Sham-operated control rats underwent total T10 laminectomy but were not subjected to SCI modeling. After surgery, rats were administered gentamicin 2,000 U/d (Chongqing Xianfeng Animal Pharmaceutical Co., Ltd.), and manual pressure was applied to the bladder every 8 h to aid urination until the recovery of spontaneous urination.

Liquid chromatography-mass spectrometry

For glutathione S-transferase (GST)-spastin pull-down assays, a liquid chromatography-mass spectrometry (LC-MS) approach was employed to detect precipitated proteins. Briefly, proteins from samples of T10-centered spinal cord tissue were resolved using NuPAGE 4–12% gels (Life Technologies), visualized with a Colloidal Blue Staining Kit (Life Technologies), and target protein bands were then excised, digested using trypsin, and the resultant peptides were assessed *via* nanoflow reversed-phase liquid chromatography-tandem MS utilizing an HPLC Ultimate 5600 system (AB SCIEX, CA, United States) with a linear ion trap (ThermoElectron, MA, United States) in data-dependent acquisition mode.

Pathological analyses

At 72 h post-SCI, rats were euthanized using sodium pentobarbital (30 mg/kg, i.p.), and samples T10 spinal cord tissue were excised for immunofluorescent, immunohistochemical (IHC), and hematoxylin-eosin staining (Wang et al., 2016; Fan et al., 2020; Bai et al., 2021). After isolation, sections were stained using a streptavidin-biotin complex kit. Briefly, endogenous peroxidase activity was initially quenched *via* incubation for 10 min with 3% H_2O_2 at 37°C, after which sections were washed thrice with phosphate buffer, blocked for 10 min with normal goat serum at 37°C for 10 min, and probed overnight using appropriate primary antibodies (rabbit polyclonal anti-PDIA6, 1:500, Cat# GB11913, Servicebio, Wuhan, China; mouse monoclonal anti-beta III Tubulin, 1:1,000, Cat# GB12139, Servicebio, Wuhan, China; goat polyclonal anti-Mouse IgG, Alexa Fluor 555, 1:1,000, Cat# ab150118, Abcam; Goat polyclonal anti-rabbit, IgG, Alexa Fluor488 1:1,000, Cat# ab150077, Abcam) at 4°C. Samples were then incubated for 1 h with HRP-conjugated anti-rabbit IgG (1:200; Cat# KIT-5004; Fuzhou Maixin, Fuzhou, China) at 37°C. Diaminobiotamine in PBS was then used to stain sections for 30 s, followed by mounting onto glass slides, ethanol gradient-mediated dehydration, xylene treatment, and slides were then imaged *via* microscopy (Olympus, Tokyo, Japan), with Image-Pro Plus 6.0 (Media Cybernetics, GA, United States) being used to quantify staining data.

siRNA and plasmid preparation

The PDIA6 cDNA sequence (NM_001004442.1) was cloned into the pGEX-5x-3 (Amersham Pharmacia Biotech, NJ, United States) and pCMV-Tag2 (Stratagene, CA, United States) vectors. Three siRNA() constructs specific for PDIA6 were prepared and synthesized by Guangzhou IGE Biotechnology (Guangzhou, China). GFP-spastin and GST-spastin constructs were additionally prepared. All constructs were validated *via* DNA sequencing. A validated spastin-specific siRNA and corresponding scrambled control siRNA (siRNA NC) constructs were obtained from Shanghai GenePharma (Shanghai, China).

GST pull-down assays

GST pull-down assays were performed as in prior reports (Ji et al., 2018). Initially, whole samples of spinal cord tissue were disrupted, lysed, and combined with rinsed GST-agarose beads (Invitrogen, CA, United States) at 4°C for 1 h. For 10 min, samples were centrifuged at 1,000 × *g* at 4°C, and supernatants were collected. These steps were repeated one additional time, after which ∼400 μg from each sample was incubated overnight with 200 μL of protein-conjugated beads at 4°C. Samples were then spun for 5 min at 1,000 × *g* at 4°C, with unbound protein then being removed by washing pellets using 1 mL of wash buffer. Samples were then spun again for 1 min at 1,000 × *g* at 4°C, after which precipitate proteins were analyzed *via* Western immunoblotting and MS.

Neuronal culture, transfection, and injury

After 1-day-old SD rats were euthanized with sodium pentobarbital (30 mg/kg, i.p.), brains were harvested, and tissue samples from the hippocampal region were isolated, after which hippocampal neurons were collected following treatment with 0.125% trypsin (Cat# 25200-072; Gibco, MD, United States). These neurons were seeded on poly-D-lysine (Cat# P6407; Gibco)-coated slides (1×10^4 cells/cm^2), after which they were added to Neurobasal-A medium (Cat# 17504044; Gibco) supplemented with 2% B27 (Cat# 17504044; Gibco). Following a 48 h incubation, constructs were inserted into these cells *via* calcium phosphate transfection. Briefly, for neurons in 24-well plates, 100 pmoL of siRNA was combined with 37 μL of 2 M $CaCl_2$ in sterile deionized water (final volume: 300 μL) and combined with 300 μL of 2 × HEPES-buffered saline. Then, 30 μL of this solution was added to each well in a dropwise manner, followed by incubation for 25 min. After 24 h, neurons were fixed for morphological analyses. A model of neuronal damage was established *via* glutamate treatment. Following culture for 48 h, neuronal culture media was replaced with L-glutamate (120 μmol/L), followed by an additional 12 h incubation at 37°C.

Morphological analyses

A Carl Zeiss LSM 700 confocal microscope (Zeiss, Jena, Germany) with a 63 × oil objective and 1,024 × 1,024 pixel resolution was used to analyze neuronal morphology. Image-Pro Plus (Media Controbernetics, MD, United States) was employed to analyze neuron lengths and branches. Those neuronal protrusions with a length less than twice their diameter were not included in these analyses.

Statistical analysis

SPSS v22.0 (IBM Corp., NY, United States) was employed for the entire statistical analyses. Data are given as means ± standard error of the mean (SEM), and were compared *via* One-way ANOVA with *post hoc* LSD, with $P < 0.05$ considered statistically significant.

Results

PDIA6 is associated with SCI

Initially, a rat SCI model was established. At 72 h post-injury, transcriptomic sequencing and LC-MS analyses were performed, revealing the upregulation of PDIA6 in a manner correlated with the severity of SCI (**Figure 1A** and **Supplementary Table 1**). LC-MS analyses additionally confirmed a positive correlation between PDIA6 mRNA and protein expression in spinal cord tissue samples from model rats subjected to varying levels of SCI severity (**Figure 1B** and **Supplementary Table 1**). Immunofluorescent staining of spinal cord sections from these rats similarly revealed higher levels of PDIA6 expression in rats in the moderate and severe SCI groups relative to control animals (**Figures 1C,D**). Consistently, PDIA6 mRNA levels were elevated in rats with different levels of SCI severity relative to control rats, as demonstrated by qPCR (**Figure 1E**). These data thus strongly suggest a potential relationship between PDIA6 and the pathogenesis of SCI.

PDIA6 and spastin interact with one another

Next, the ability of PDIA6 and spastin to interact with one another was assessed. Following the purification of GST-Spastin and GST-PDIA6 (**Figures 2A**, **3A**), GST-Spastin was utilized to pull down proteins from spinal cord lysates, with precipitated proteins then being analyzed *via* LC-MS. In total, 3 PDIA6 peptides (LAAVDATVNQVLASR, NLEPEWAAAASEVK, and TGEAIVDAALSALR) were found to interact with GST-spastin (**Figure 2B**), thus validating the capability of spastin and PDIA6 to interact with one another. Sequence homology for these three peptides was further compared among five species (*Rattus norvegicus, Mus musculus, Homo sapiens, Danio rerio,* and *Xenopus laevis*), revealing a high degree of homology consistent with evolutionary sequence conservation (**Figures 2C–E**). MS analyses further revealed a close relationship between PDIA6 and SCI, suggesting that it may interact with spastin (**Figure 2F**).

To determine whether PDIA6 and spastin can physically interact with one another, GST-Spastin and GST-PDIA6 were next combined with rat brain lysates to perform pull-down assays, which revealed interactions between these two GST-tagged proteins and PDIA6 and spastin, respectively (**Figures 3B,C**). Coimmunoprecipitation (Co-IP) assays using these rat brain lysates similarly confirmed the interaction between spastin and PDIA6 (**Figure 3D**). To further validate this interaction, COS-7 cells were co-transfected using GFP/Flag-PDIA6, GFP-Spastin/Flag-PDIA6, Flag/GFP-Spastin, or Flag-PDIA6/GFP-Spastin, after which GFP- and Flag-specific antibodies were used for pull-down assays. Western immunoblotting revealed an interaction between Flag-PDIA6 and GFP-Spastin (**Figures 3E,F**). Immunofluorescent staining similarly indicated that PDIA6 and spastin co-localize with one another in neurons (**Figure 3G**). Together, these data suggested that spastin and PDIA6 can interact both *in vitro* and *in vivo.*

PDIA6 and spastin interact to control microtubule dynamics

To additionally examine the effects of PDIA6 on spastin functionality, PDIA6-associated changes in microtubule dynamics were next examined. Three different siRNA constructs were tested for their ability to knock down PDIA6 in COS-7 cells *via* Western blotting (**Figures 4A,C**), yielding a ∼54% knockdown efficiency (**Figure 4B**). The effects of PDIA6 on the activity of spastin-dependent microtubule severing were assessed by transfecting COS-7 cells with GFP/NC, GFP-Spastin/NC, or GFP-Spastin/Si-PDIA6 for 24 h (**Figure 4D**). Relative to control cells or cells overexpressing spastin, the fluorescence intensity of the spastin group reduced considerably. Following si-PDIA6 co-transfection, this fluorescence intensity increased significantly relative to that observed in the spastin group (**Figure 4E**). These data suggest that spastin is capable of severing microtubules within COS-7 cells, while PDIA6 knockdown was sufficient to inhibit this spastin-mediated microtubule severing activity.

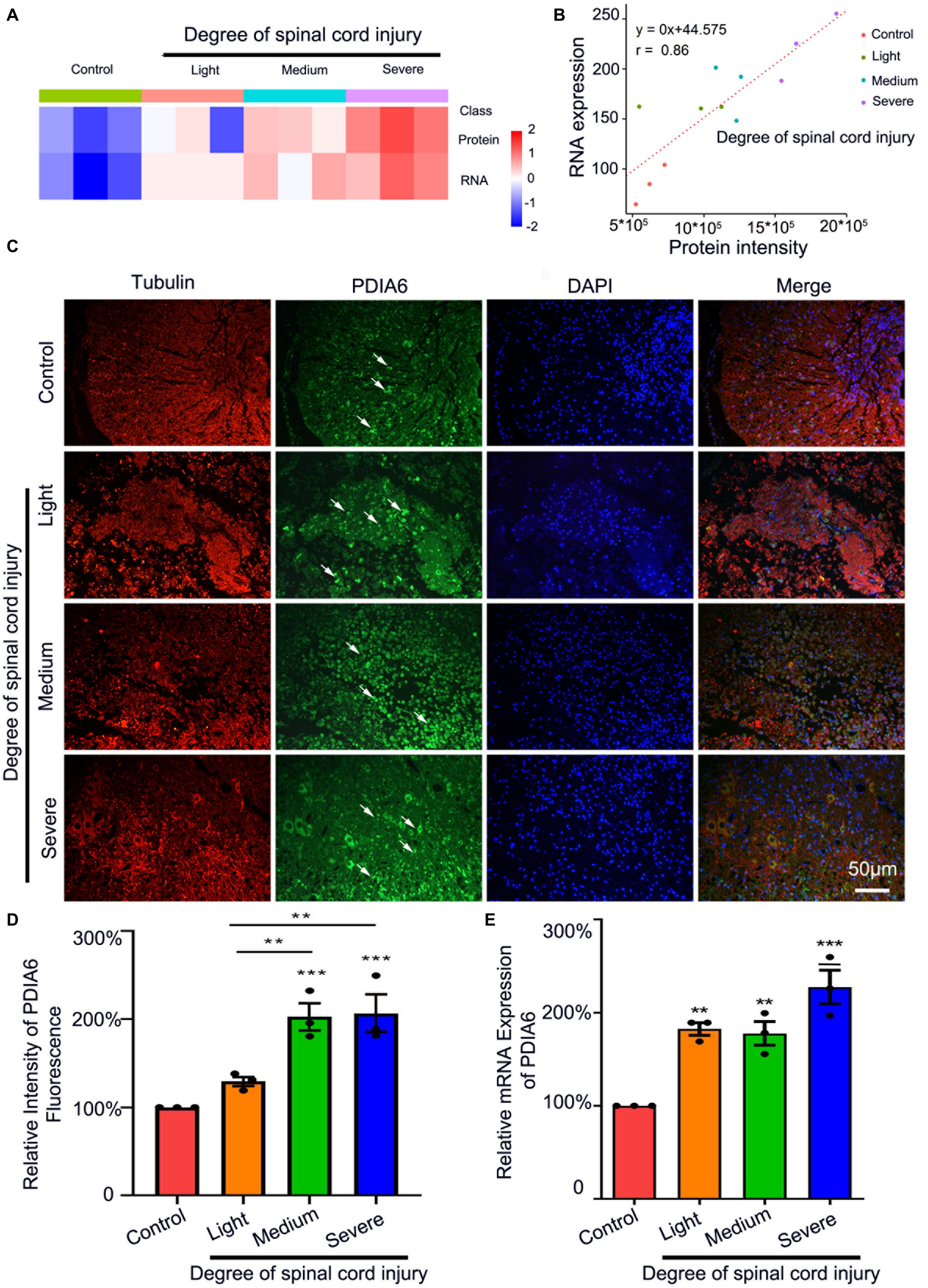

FIGURE 1

PDIA6 is associated with spinal cord injury. **(A)** Transcriptomic sequencing and LC-MS were used to analyze PDIA6 mRNA and protein expression (n = 3/group). **(B)** Correlations between changes in PDIA6 RNA and protein intensity (n = 3/group). **(C)** Immunofluorescent staining was used to detect tubulin (red, Alexa Fluor 555), PDIA6 (green, Alexa Fluor 488), and DAPI (blue, Alexa Fluor 405), revealing an increase in PDIA6 expression with greater SCI severity. Scale bar: 50 μm. **(D)** Immunofluorescent PDIA6 staining intensity was quantified, using β3 Tubulin as a control (n = 3/group). **(E)** Spinal cord samples from rats subjected to varying levels of SCI severity were collected to assess PDIA6 expression *via* qPCR (n = 3 /group). *P < 0.05, **P < 0.01, ***P < 0.01.

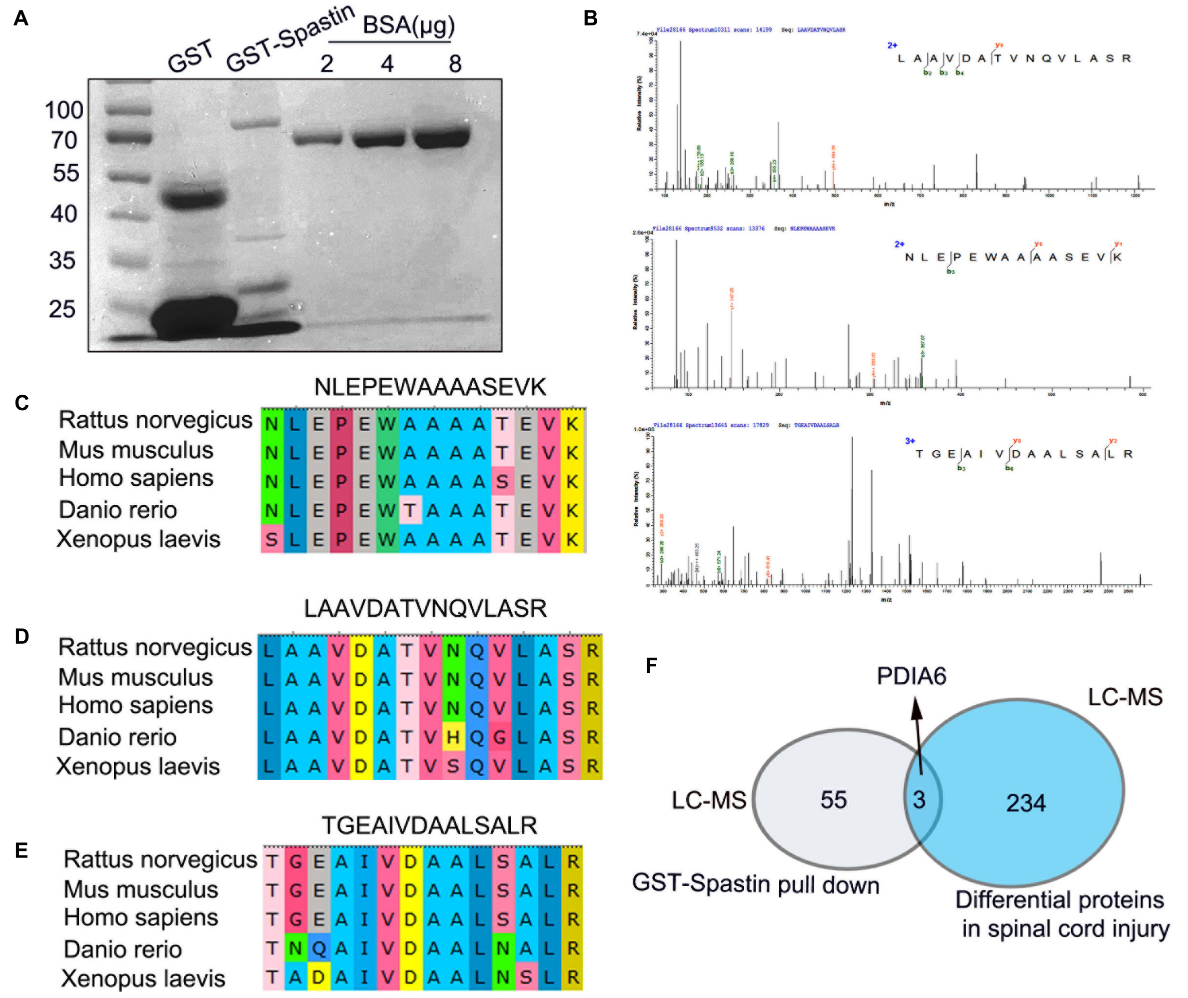

FIGURE 2

Peptides derived from PDIA6 interact with spastin. **(A)** GST and GST-Spastin protein purification, with BSA serving as a loading control. **(B)** Peptides capable of interacting with GST-spastin were analyzed *via* LC-MS, leading to the identification of three PDIA6-derived peptides (LAAVDATVNQVLASR, NLEPEWAAAASEVK, and TGEAIVDAALSALR). **(C–E)** Significant homology was observed among species when assessing the sequences of the three identified PDIA6-derived peptides. **(F)** PDIA6 is both differentially expressed following SCI and has the potential to interact with spastin.

The activity of spastin-dependent microtubule severing is thus PDIA6-dependent.

Interactions between PDIA6 and spastin promote neuronal repair

Lastly, the relationship between PDIA6-spastin interactions and neuronal repair was analyzed. To establish a neuronal injury model system, hippocampal neurons were cultured for 72 h *in vitro,* followed by being damaged by exposure to glutamate (120 μM). These neurons were co-transfected with Flag/NC, PDIA6/NC, or PDIA6/Si-Spastin (Figure 5A), with the selected Si-Spastin construct previously having been demonstrated to achieve ∼92% knockdown efficiency in an analysis of the role of spastin as a regulator of neurite outgrowth (Ji et al., 2018). After 24 h of co-transfection, neurites were harvested, and the total length and number of branching neurites were quantified. Cells transfected with PDIA6/NC exhibited a significant increase in the total length of neuronal branches related to the injury and PDIA6/Si-Spastin groups (Figure 5B). Similar results were also observed with respect to primary and secondary neuronal branch lengths (Figures 5C,D). Total numbers of neuronal branches in the PDIA6/NC group were also significantly elevated relative to the injury and PDIA/Si-Spastin in groups (Figure 5E), with similar results being observed with respect to the numbers of primary and secondary branches (Figures 5F,G).

To further examine the interaction of PDIA6 and spastin in the context of neuronal repair, neurons were co-transfected with the Flag/NC, Si-PDIA6/NC, or Si-PDIA6/Si-Spastin constructs

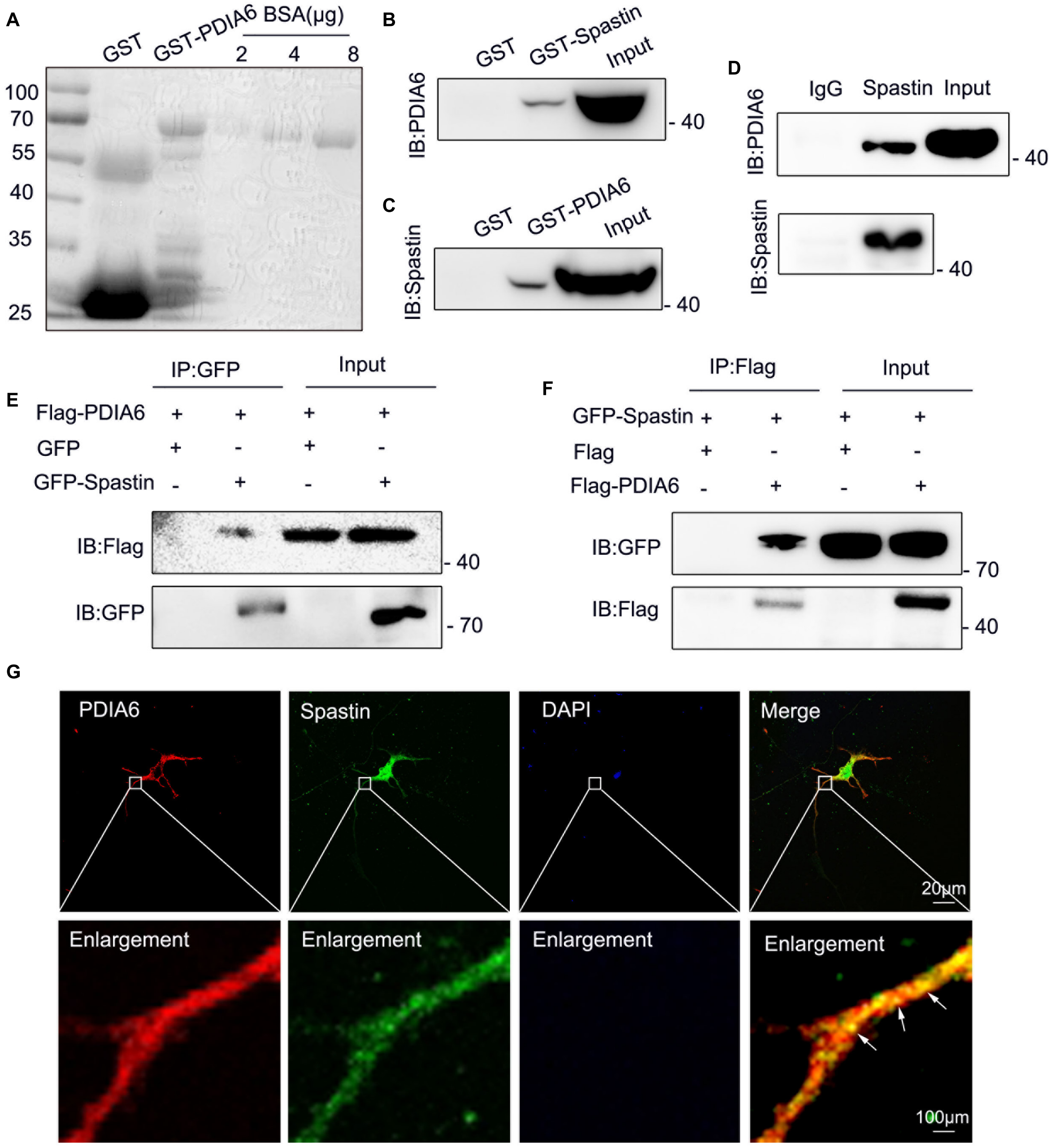

FIGURE 3
PDIA6 and spastin physically interact with one another. **(A)** GST and GST-PDIA6 protein purification, with BSA serving as a loading control. **(B,C)** Following GST, GST-Spastin, and GST-PDIA6 pulldown of enriched rat brain lysates, PDIA6 and spastin were detected *via* Western immunoblotting. **(D)** Immunoprecipitation assays revealed the ability of PDIA6 and spastin to interact with one another, as proteins that co-eluted with anti-spastin could be detected by both anti-spastin and anti-PDIA6 staining. **(E,F)** COS-7 cells were co-transfected with GFP/Flag-PDIA6, GFP-Spastin/Flag-PDIA6, Flag/GFP-Spastin, or Flag-PDIA6/GFP-Spastin, after which GFP- and Flag-specific antibodies were used for immunoprecipitation. **(G)** Endogenous proteins within hippocampal neurons were detected using anti-PDIA6 (red) and anti-spastin (green). Co-localization between spastin and PDIA6 (yellow) is marked with arrows. Scale bars: 20 μm and 100 μm.

(Figure 6A). Total neuronal branch length was significantly shorter for cells transfected with Si-PDIA6/NC and or-PDIA6/Si-Spastin relative to the injury control group, with a great reduction in branch length in the Si-PDIA6/Si-Spastin group relative to the Si-PDIA6/NC (Figure 6B). Primary neuronal branch length values were additionally shorter in Si-PDIA6/NC and Si-PDIA6/Si-Spastin groups relative to the injury control group (Figure 6C), and secondary neuronal branch lengths were similarly shorter in Si-PDIA6/Si-Spastin group relative to the injury group (Figure 6D). Total branch

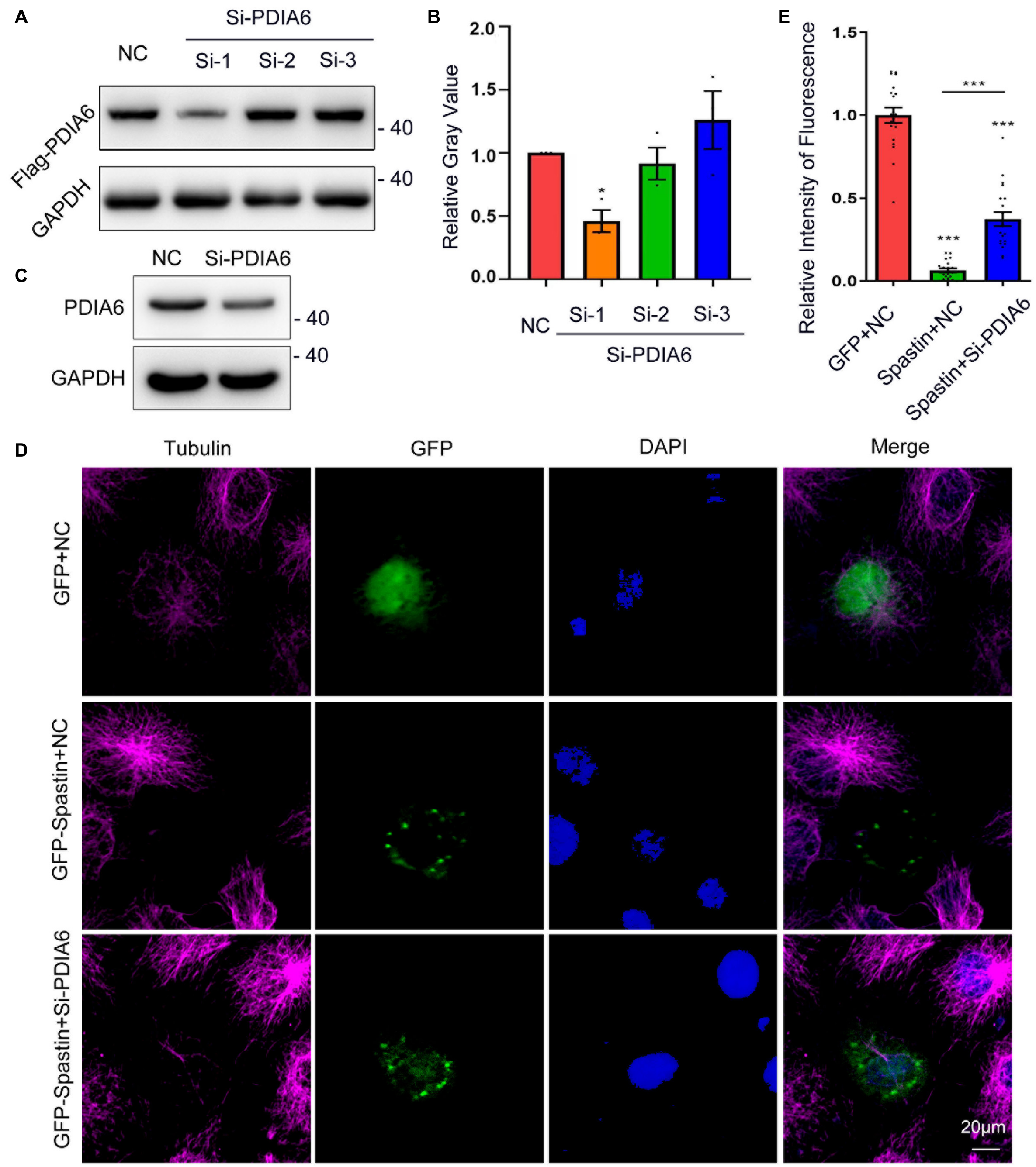

FIGURE 4

PDIA6 and spastin cooperate to control intracellular microtubule dynamics. **(A)** The efficiency of siRNA-mediated PDIA6 knockdown was examined in COS-7 cells that were co-transfected with three different siRNAs (Si-1, Si-2, or Si-3) and the Flag-PDIA6 plasmid. Anti-Flag was then used for Western immunoblotting, with GAPDH serving as a loading control. **(B)** Relative PDIA6 expression. **(C)** COS-7 cells were transfected using PDIA6 siRNA-1, after which endogenous PDIA6 expression was analyzed. **(D)** Microtubules were detected in COS-7 cells following spastin and Si-PDIA6 transfection; GFP (green), tubulin (Pink), DAPI (blue). Spastin severed microtubules within these cells, whereas the knockdown of PDIA6 disrupted this spastin-mediated severing of microtubules. **(E)** Relative to control cells, those in which PDIA6 was knocked down exhibited significantly reduced spastin fluorescent intensity (*n* = 20/group). *$P < 0.05$, **$P < 0.01$, ***$P < 0.01$.

numbers in Si-PDIA6/NC and Si-PDIA6/Si-Spastin groups were significantly reduced relative to the injury group (Figure 6E), with similar results being observed for the number of primary neuronal branches (Figure 6F). The number of secondary neuronal branches in the Si-PDIA6/Si-Spastin group was also less than that in the injury group (Figure 6G). Together, these

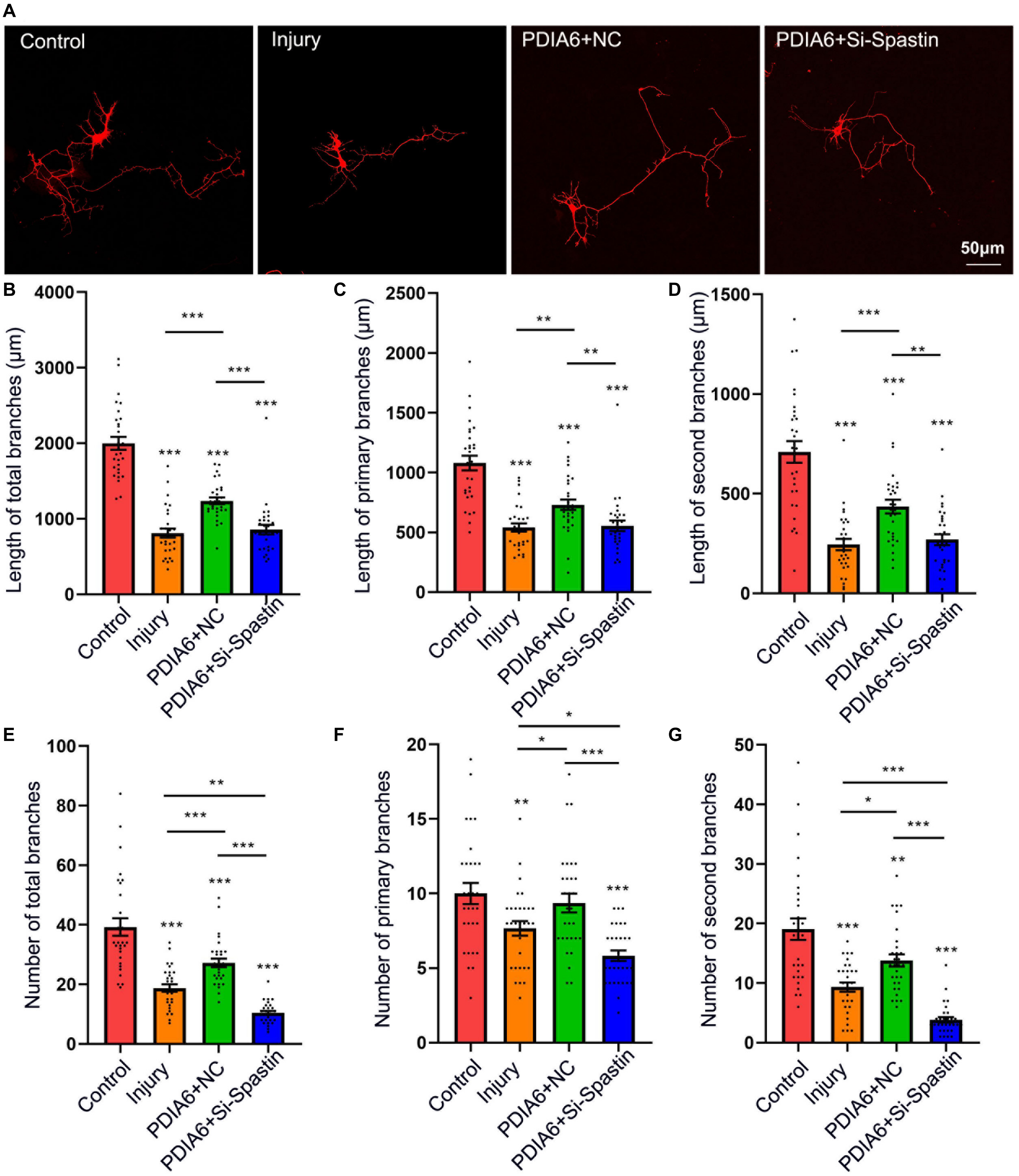

FIGURE 5
PDIA6 interactions with spastin promote injured neuron repair. **(A)** Following culture *in vitro* for 3 days, glutamate (120 μM) was used to injure hippocampal neurons. At 12 h post-injury, neurons were co-transfected for 24 h with Flag/NC, PDIA6/NC, or PDIA6/Si-Spastin. Scale bar: 50 μm. **(B–D)** Total **(B)**, primary **(C)**, and secondary **(D)** branch lengths were measured, indicating that PDIA6 was able to promote the repair of injured neuron branches, while the silencing of spastin suppressed such PDIA6-mediated repair (*n* = 30/group). **(E–G)** Total **(E)**, primary **(F)**, and secondary **(G)** branch numbers were quantified, indicating that PDIA6 promoted branch formation on injured neurons, whereas the knockdown of spastin inhibited this PDIA6-mediated repair (*n* = 30/group). *$P < 0.05$, **$P < 0.01$, ***$P < 0.01$.

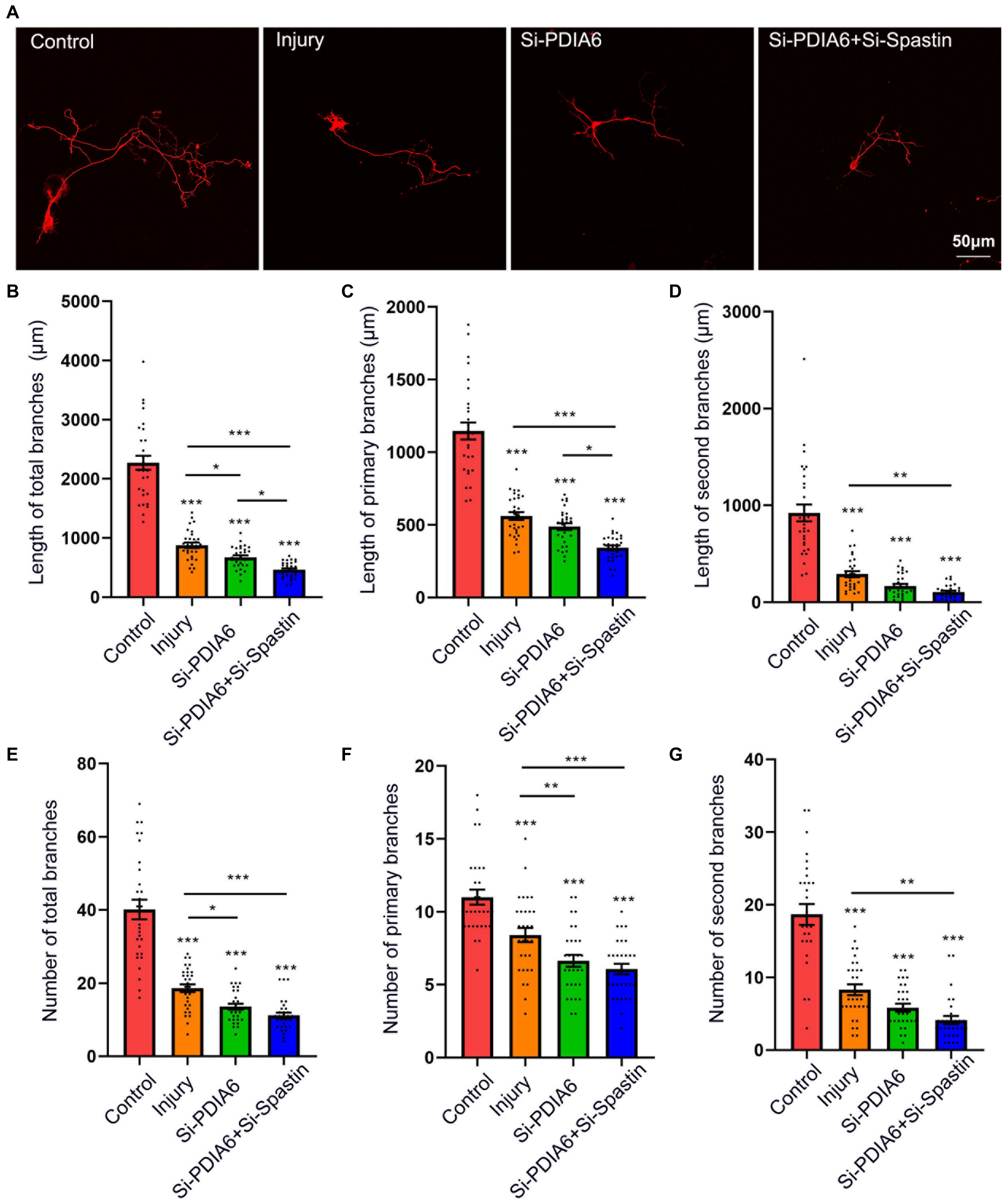

FIGURE 6

The knockdown of PDIA6 and spastin inhibits injured neuron repair. **(A)** Following culture *in vitro* for 3 days, glutamate (120 μM) was used to injure hippocampal neurons. At 12 h post-injury, neurons were co-transfected for 24 h with Flag/NC, Si-PDIA6, or Si-PDIA6/Si-Spastin. Scale bar: 50 μm. **(B–D)** Total **(B)**, primary **(C)**, and secondary **(D)** branch lengths were measured, indicating that PDIA6 knockdown suppressed branch repair in these injured neurons, while the knockdown of both PDIA6 and spastin suppressed injured neuronal repair (*n* = 30/group). **(E–G)** Total **(E)**, primary **(F)**, and secondary **(G)** branch numbers, indicating that PDIA6 knockdown suppressed branch formation by injured neurons, and that PIDA6 and spastin knockdown similarly inhibited branch formation (*n* = 30/group). $^{*}P < 0.05$, $^{**}P < 0.01$, $^{***}P < 0.01$.

data thus confirmed the ability of PDIA6 to promote injured neuron branch repair through interactions with spastin.

Discussion

Here, PDIA6 was found to play a functional role in the context of SCI, interacting with spastin to promote functional recovery following neuronal injury. Specifically, LC-MS and bioinformatics analyses were initially used to explore proteins that were differentially expressed between healthy and damaged spinal cord tissues, revealing a link between SCI and the expression of PDIA6. PDIA6 was subsequently found to directly physically interact with spastin *in vitro* and *in vivo,* promoting recovery following SCI through the enhancement of neurite outgrowth. Together, these data suggest that PDIA6 and spastin coordinate to drive both neurite branch formation and outgrowth.

The damage associated with SCI can be extremely severe, resulting in substantial functional impairment including permanent motor dysfunction in affected patients owing to the limited regenerative responses engaged in humans following such injury (Zhu et al., 2020; Bisicchia et al., 2022). The pathogenesis of SCI is linked to mechanisms that govern both primary and secondary injury (Walsh et al., 2021; Ding and Chen, 2022), with secondary damage in particular contributing to more widespread neuronal death, expanding the affected region of the spinal cord (Lai et al., 2021). These deleterious conditions can contribute to the buildup of unfolded or misfolded proteins, interfering with normal ER function and thereby activating ER-associated cell death (Oakes and Papa, 2015; Han et al., 2021; Mao et al., 2022). According to an increasing number of studies, the inhibition of ER stress-induced cell death can improve functional recovery following SCI (Wu et al., 2020; Saraswat Ohri et al., 2021). The protein disulfide isomerase family protein PDIA6 is an oxidoreductase capable of catalyzing disulfide bond formation and acting as a chaperone to protect against excessive unfolded protein aggregation (Okumura et al., 2015). The function of PDIA6 in SCI, however, is not clarified previously. In this current research, but LC-MS and bioinformatics analyses suggested that PDIA6 was upregulated at the mRNA and protein levels in damaged spinal cord tissues in a rat model of SCI, suggesting a potential role for PDIA6 as a regulator of SCI pathogenesis.

In previous studies, we found that spastin serves as an important regulator of SCI through its ability to regulate microtubule dynamics and to thereby promote the formation and outgrowth of neurites (Ji Z. S. et al., 2021). We therefore hypothesized that PDIA6 may be capable of interacting with spastin to shape the functional recovery of injured neurons. Through a pull-down assay conducted using GST-spastin and rat spinal cord lysates, LC-MS revealed PDIA6 to precipitate with spastin, consistent with our hypothesis. Subsequent co-IP and GST pull-down assays further confirmed these interactions between spastin and PDIA6, and these two proteins were found to co-localize with one another in neurons.

As a protein that severs microtubules, spastin can disassemble long microtubules into shorter fragments that serve as nucleation templates to facilitate further microtubule growth (Roll-Mecak and Vale, 2006; Kapitein and Hoogenraad, 2015; Solowska and Baas, 2015). Several reports have demonstrated that a range of proteins can interact with spastin to modulate its ability to sever microtubules, thereby influencing neurite outgrowth from injured neurons (Ji et al., 2018; Ji Z. S. et al., 2021; Lawrence et al., 2021). As such, the ability of PDIA6 to regulate injured neuronal repair through interactions with spastin and associated regulation of microtubule severing was assessed by overexpressing spastin in COS-7 cells. This resulted in the disruption of the normal microtubular network within these cells consistent with the near-complete severing of longer microtubules. When PDIA6 was simultaneously knocked down, however, this spastin-mediated microtubule severing activity was markedly blunted, confirming the ability of PDIA6 to alter the ability of spastin to sever these microtubules. As such, these data support a model wherein PDIA6 and spastin interact to control intracellular microtubule dynamics.

Promoting axonal regeneration to restore the integrity of neural networks is thought to represent a promising approach to achieving functional recovery following SCI (Li et al., 2017; Sekine et al., 2022). Our previous studies have shown that synergistic interactions between proteins were capable of promoting axonal branching and outgrowth in hippocampal neurons damaged following glutamate exposure (Wu et al., 2021; Ji et al., 2022). Here, the overexpression of PDIA6 in neurons was sufficient to promote axonal outgrowth in damaged neurons, while this beneficial effect was reversed when spastin was silenced in these same cells. Similarly, PDIA6 knockdown impaired neurite outgrowth of damaged neurons. Together, these data thus suggest that PDIA6 promotes neuronal outgrowth through a mechanism dependent on its ability to interact with spastin.

In conclusion, these data suggest that both PDIA6 and spastin are important regulators of neuronal responses to SCI, with the interaction between these two proteins serving to regulate intracellular microtubule dynamics, thereby controlling neurite outgrowth and thus potentially influencing SCI-related repair responses. PDIA6 can additionally promote injured neuron recovery through the regulation of spastin functionality *in vitro,* although this functional activity remains to be confirmed *in vivo.* Future research focused on the molecular mechanisms underlying the observed interactions between PDIA6 and spastin thus has the potential to guide the design of novel therapeutic drugs and other interventions aimed at improving neuronal regeneration following SCI.

Data availability statement

The datasets presented in this study can be found in online repositories. The name of the repository and accession number can be found below: ProteomeXchange, http://www.proteomexchange.org/, PXD035706.

Ethics statement

The studies involving animals were reviewed and approved by the Ethics Committee of Jinan University.

Author contributions

ZJ, HL, and GZ: study conception and design. JL, CP, and MX: experiment implementation. JL, KW, GL, and HY: data acquisition. TC, QL, and JL: data analysis. JL and ZJ: manuscript writing. All authors reviewed and approved the final version of the manuscript.

Funding

This work was supported by the Natural Science Foundation of China (grant nos. 82102314, 31900691, and 32170977) and the Natural Science Foundation of Guangdong Province (grant nos. 2022A1515010438 and 2022A1515012306).

Conflict of interest

The authors declare that the research was conducted in the absence of any commercial or financial relationships that could be construed as a potential conflict of interest.

Publisher's note

Supplementary material

The Supplementary Material for this article can be found online at: https://www.frontiersin.org/articles/10.3389/fnmol.2022.950586/full#supplementary-material

References

Arribat, Y., Grepper, D., Lagarrigue, S., Qi, T., Cohen, S., and Amati, F. (2020). Spastin mutations impair coordination between lipid droplet dispersion and reticulum. *PLoS Genet.* 16:e1008665. doi: 10.1371/journal.pgen.1008665

Bai, G., Cheung, I., Shulha, H. P., Coelho, J. E., Li, P., Dong, X., et al. (2015). Epigenetic dysregulation of hairy and enhancer of split 4 (HES4) is associated with striatal degeneration in postmortem Huntington brains. *Hum. Mol. Genet.* 24, 1441–1456. doi: 10.1093/hmg/ddu561

Bai, W., Li, M., Xu, W., and Zhang, M. (2021). Comparison of effects of high- and low-frequency electromagnetic fields on proliferation and differentiation of neural stem cells. *Neurosci. Lett.* 741:135463. doi: 10.1016/j.neulet.2020.135463

Bi, Y., Chen, X., Cao, Y., Yu, D., Zhao, J., Jing, Y., et al. (2020). Nuclear heme oxidase-1 inhibits endoplasmic reticulum stress-mediated apoptosis after spinal cord injury. *Biomed. Res. Int.* 2020:7576063. doi: 10.1155/2020/7576063

Bisicchia, E., Mastrantonio, R., Nobili, A., Palazzo, C., La Barbera, L., Latini, L., et al. (2022). Restoration of ER proteostasis attenuates remote apoptotic cell death after spinal cord injury by reducing autophagosome overload. *Cell Death Dis.* 13:381. doi: 10.1038/s41419-022-04830-9

Chang, J., Lee, S., and Blackstone, C. (2013). Protrudin binds atlastins and endoplasmic reticulum-shaping proteins and regulates network formation. *Proc. Natl. Acad. Sci. U.S.A.* 110, 14954–14959. doi: 10.1073/pnas.1307391110

Ding, Y., and Chen, Q. (2022). mTOR pathway: A potential therapeutic target for spinal cord injury. *Biomed. Pharmacother.* 145:112430.

Eletto, D., Eletto, D., Dersh, D., Gidalevitz, T., and Argon, Y. (2014). Protein disulfide isomerase A6 controls the decay of IRE1α signaling via disulfide-dependent association. *Mol. Cell* 53, 562–576. doi: 10.1016/j.molcel.2014.01.004

Fan, L., Li, X., and Liu, T. (2020). Asiaticoside inhibits neuronal apoptosis and promotes functional recovery after spinal cord injury in rats. *J. Mol. Neurosci.* 70, 1988–1996. doi: 10.1007/s12031-020-01601-z

Han, Y., Yuan, M., Guo, Y. S., Shen, X. Y., Gao, Z. K., and Bi, X. (2021). Mechanism of endoplasmic reticulum stress in cerebral ischemia. *Front. Cell Neurosci.* 15:704334. doi: 10.3389/fncel.2021.704334

Jessop, C. E., Watkins, R. H., Simmons, J. J., Tasab, M., and Bulleid, N. J. (2009). Protein disulphide isomerase family members show distinct substrate specificity: P5 is targeted to BiP client proteins. *J. Cell Sci.* 122(Pt 23), 4287–4295. doi: 10.1242/jcs.059154

Ji, Z. S., Gao, G. B., Ma, Y. M., Luo, J. X., Zhang, G. W., Yang, H., et al. (2022). Highly bioactive iridium metal-complex alleviates spinal cord injury via ROS scavenging and inflammation reduction. *Biomaterials* 284:121481. doi: 10.1016/j.biomaterials.2022.121481

Ji, Z. S., Li, J. P., Fu, C. H., Luo, J. X., Yang, H., Zhang, G. W., et al. (2021). Spastin interacts with collapsin response mediator protein 3 to regulate neurite growth and branching. *Neural Regen. Res.* 16, 2549–2556. doi: 10.4103/1673-5374.313052

Ji, Z. S., Liu, Q. L., Zhang, J. F., Yang, Y. H., Li, J., Zhang, G. W., et al. (2020). SUMOylation of spastin promotes the internalization of GluA1 and regulates dendritic spine morphology by targeting microtubule dynamics. *Neurobiol. Dis.* 146:105133. doi: 10.1016/j.nbd.2020.105133

Ji, Z., Zhang, G., Chen, L., Li, J., Yang, Y., Cha, C., et al. (2018). Spastin interacts with crmp5 to promote neurite outgrowth by controlling the microtubule dynamics. *Dev. Neurobiol.* 78, 1191–1205. doi: 10.1002/dneu.22640

Ji, Z., Zhou, Z. L., Hao, Q., Zhao, L., Cui, C., Huang, S. B., et al. (2021). Activating transcription factor 6 contributes to functional recovery after spinal cord injury in adult zebrafish. *J. Mol. Neurosci.* 71, 734–745. doi: 10.1007/s12031-020-01691-9

Kapitein, L. C., and Hoogenraad, C. C. (2015). Building the neuronal microtubule cytoskeleton. *Neuron* 87, 492–506.

Lai, B. Q., Zeng, X., Han, W. T., Che, M. T., Ding, Y., Li, G., et al. (2021). Stem cell-derived neuronal relay strategies and functional electrical stimulation for treatment of spinal cord injury. *Biomaterials* 279:121211. doi: 10.1016/j.biomaterials.2021.121211

Lai, M., Pan, M., Ge, L., Liu, J., Deng, J., Wang, X., et al. (2020). NeuroD1 overexpression in spinal neurons accelerates axonal regeneration after sciatic nerve injury. *Exp. Neurol.* 327:113215. doi: 10.1016/j.expneurol.2020.113215

Lawrence, E. J., Arpag, G., Arnaiz, C., and Zanic, M. (2021). SSNA1 stabilizes dynamic microtubules and detects microtubule damage. *Elife* 10:e67282. doi: 10.7554/eLife.67282

Li, Y., Chen, Y., Tan, L., Pan, J. Y., Lin, W. W., Wu, J., et al. (2017). RNAi-mediated ephrin-B2 silencing attenuates astroglial-fibrotic scar formation and improves spinal cord axon growth. *CNS Neurosci. Ther.* 23, 779–789. doi: 10.1111/cns.12723

Liu, S., Sarkar, C., Dinizo, M., Faden, A. I., Koh, E. Y., Lipinski, M. M., et al. (2015). Disrupted autophagy after spinal cord injury is associated with ER stress and neuronal cell death. *Cell Death Dis.* 6:e1582. doi: 10.1038/cddis.2014.527

Mao, H., Chen, W., Chen, L., and Li, L. (2022). Potential role of mitochondria-associated endoplasmic reticulum membrane proteins in diseases. *Biochem. Pharmacol.* 199:115011.

Matsusaki, M., Kanemura, S., Kinoshita, M., Lee, Y. H., Inaba, K., and Okumura, M. (2020). The protein disulfide isomerase family: From proteostasis to pathogenesis. *Biochim. Biophys. Acta Gen. Subj.* 1864:129338.

Montibeller, L., and de Belleroche, J. (2018). Amyotrophic lateral sclerosis (ALS) and Alzheimer's disease (AD) are characterised by differential activation of ER stress pathways: Focus on UPR target genes. *Cell Stress Chaperones* 23, 897–912. doi: 10.1007/s12192-018-0897-y

Oakes, S. A., and Papa, F. R. (2015). The role of endoplasmic reticulum stress in human pathology. *Annu. Rev. Pathol.* 10, 173–194.

Ohri, S. S., Hetman, M., and Whittemore, S. R. (2013). Restoring endoplasmic reticulum homeostasis improves functional recovery after spinal cord injury. *Neurobiol. Dis.* 58, 29–37.

Okumura, M., Kadokura, H., and Inaba, K. (2015). Structures and functions of protein disulfide isomerase family members involved in proteostasis in the endoplasmic reticulum. *Free Radic. Biol. Med.* 83, 314–322.

Roll-Mecak, A., and Vale, R. D. (2006). Making more microtubules by severing: A common theme of noncentrosomal microtubule arrays? *J. Cell Biol.* 175, 849–851. doi: 10.1083/jcb.200611149

Saraswat Ohri, S., Howard, R. M., Liu, Y., Andres, K. R., Shepard, C. T., Hetman, M., et al. (2021). Oligodendrocyte-specific deletion of Xbp1 exacerbates the endoplasmic reticulum stress response and restricts locomotor recovery after thoracic spinal cord injury. *Glia* 69, 424–435. doi: 10.1002/glia.23907

Sekine, Y., Kannan, R., Wang, X., and Strittmatter, S. M. (2022). Rabphilin3A reduces integrin-dependent growth cone signaling to restrict axon regeneration after trauma. *Exp. Neurol.* 353, 114070. doi: 10.1016/j.expneurol.2022.114070

Solowska, J. M., and Baas, P. W. (2015). Hereditary spastic paraplegia SPG4: What is known and not known about the disease. *Brain* 138(Pt 9), 2471–2484.

Stone, M. C., Rao, K., Gheres, K. W., Kim, S., Tao, J., La Rochelle, C., et al. (2012). Normal spastin gene dosage is specifically required for axon regeneration. *Cell Rep.* 2, 1340–1350. doi: 10.1016/j.celrep.2012.09.032

Vajente, N., Norante, R., Redolfi, N., Daga, A., Pizzo, P., and Pendin, D. (2019). Microtubules stabilization by mutant spastin affects er morphology and Ca(2+) handling. *Front. Physiol.* 10:1544. doi: 10.3389/fphys.2019.01544

Venkatesh, K., Ghosh, S. K., Mullick, M., Manivasagam, G., and Sen, D. (2019). Spinal cord injury: Pathophysiology, treatment strategies, associated challenges, and future implications. *Cell Tissue Res.* 377, 125–151. doi: 10.1007/s00441-019-03039-1

Walsh, C. M., Wychowaniec, J. K., Brougham, D. F., and Dooley, D. (2021). Functional hydrogels as therapeutic tools for spinal cord injury: New perspectives on immunopharmacological interventions. *Pharmacol. Ther.* 234:108043. doi: 10.1016/j.pharmthera.2021.108043

Walter, P., and Ron, D. (2011). The unfolded protein response: From stress pathway to homeostatic regulation. *Science* 334, 1081–1086.

Wang, X., Shi, S. H., Yao, H. J., Jing, Q. K., Mo, Y. P., Lv, W., et al. (2016). Electroacupuncture at Dazhui (GV14) and Mingmen (GV4) protects against spinal cord injury: The role of the Wnt/β-catenin signaling pathway. *Neural Regen. Res.* 11, 2004–2011. doi: 10.4103/1673-5374.197145

Wu, C., Xu, H., Li, J., Hu, X., Wang, X., Huang, Y., et al. (2020). Baicalein attenuates pyroptosis and endoplasmic reticulum stress following spinal cord ischemia-reperfusion injury via autophagy enhancement. *Front. Pharmacol.* 11:1076. doi: 10.3389/fphar.2020.01076

Wu, H. T., Yu, Y., Li, X. X., Lang, X. Y., Gu, R. Z., Fan, S. R., et al. (2021). Edaravone attenuates H(2)O(2) or glutamate-induced toxicity in hippocampal neurons and improves AlCl(3)/D-galactose induced cognitive impairment in mice. *Neurotoxicology* 85, 68–78. doi: 10.1016/j.neuro.2021.05.005

Wu, X., Qu, W., Bakare, A. A., Zhang, Y. P., Fry, C. M. E., Shields, L. B. E., et al. (2019). A laser-guided spinal cord displacement injury in adult mice. *J. Neurotrauma* 36, 460–468. doi: 10.1089/neu.2018.5756

Zhu, S., Chen, M., Chen, M., Ye, J., Ying, Y., Wu, Q., et al. (2020). Fibroblast growth factor 22 inhibits er stress-induced apoptosis and improves recovery of spinal cord injury. *Front. Pharmacol.* 11:18. doi: 10.3389/fphar.2020.00018

Zhu, Z., Zhang, C., Zhao, G., Liu, Q., Zhong, P., Zhang, M., et al. (2019). Novel mutations in the SPAST gene cause hereditary spastic paraplegia. *Parkinsonism Relat. Disord.* 69, 125–133.

frontiers | Frontiers in Molecular Neuroscience

TYPE Mini Review
PUBLISHED 07 September 2022
DOI 10.3389/fnmol.2022.983336

OPEN ACCESS

EDITED BY
Feng Rao,
Peking University People's
Hospital, China

REVIEWED BY
Catherina G. Becker,
University of Edinburgh,
United Kingdom

*CORRESPONDENCE
Richard I. Dorsky
richard.dorsky@neuro.utah.edu

SPECIALTY SECTION
This article was submitted to
Neuroplasticity and Development,
a section of the journal
Frontiers in Molecular Neuroscience

RECEIVED 30 June 2022
ACCEPTED 18 August 2022
PUBLISHED 07 September 2022

CITATION
Alper SR and Dorsky RI (2022) Unique advantages of zebrafish larvae as a model for spinal cord regeneration. *Front. Mol. Neurosci.* 15:983336. doi: 10.3389/fnmol.2022.983336

Unique advantages of zebrafish larvae as a model for spinal cord regeneration

Samuel R. Alper and Richard I. Dorsky*

Department of Neurobiology, University of Utah, Salt Lake City, UT, United States

The regenerative capacity of the spinal cord in mammals ends at birth. In contrast, teleost fish and amphibians retain this capacity throughout life, leading to the use of the powerful zebrafish model system to identify novel mechanisms that promote spinal cord regeneration. While adult zebrafish offer an effective comparison with non-regenerating mammals, they lack the complete array of experimental approaches that have made this animal model so successful. In contrast, the optical transparency, simple anatomy and complex behavior of zebrafish larvae, combined with the known conservation of pro-regenerative signals and cell types between larval and adult stages, suggest that they may hold even more promise as a system for investigating spinal cord regeneration. In this review, we highlight characteristics and advantages of the larval model that underlie its potential to provide future therapeutic approaches for treating human spinal cord injury.

KEYWORDS

zebrafish, larva, model, spinal cord, injury, regeneration, transparency, functional recovery

Introduction

Spinal cord injury (SCI) in humans leads to debilitating consequences with little significant functional recovery. As in other regions of the central nervous system (CNS), barriers to spinal cord regeneration identified using mammalian experimental models include the lack of resident progenitor cells capable of replacing lost neurons, intrinsic factors that limit axon regrowth in surviving neurons, and the deposition of extrinsic factors that inhibit axon regrowth across the injury site (Alunni and Bally-Cuif, 2016; Varadarajan et al., 2022). However, the ability to overcome these barriers and to develop therapies for SCI recovery also requires the identification of mechanisms that actively promote regeneration. This has led to the development of SCI models in teleost fish and urodele amphibians, which display a remarkable capacity for spinal cord regeneration throughout their lifespan (Becker et al., 1997; Zukor et al., 2011). This regenerative capacity, combined with the benefits of an extensive set of experimental tools and approaches, has positioned the zebrafish (*Danio rerio*) as an attractive model organism for discovering the mechanisms that promote regeneration after SCI. Recent work using the zebrafish model has shown that regeneration and functional recovery after SCI depends on the lifelong maintenance of multipotent stem and progenitor cells, and on pro-regenerative signals from other cells within and outside the spinal cord (Briona et al., 2015; Goldshmit et al., 2018; Cavone et al., 2021; Becker and Becker, 2022).

While adult zebrafish have been used as a comparison with non-regenerative postnatal mammals, their recovery period of around 6 weeks after SCI (Becker et al., 2004), lack of optical transparency, and complicated surgical procedures (Fang et al., 2012), preclude the use of many tools and approaches that have made the species so successful as an experimental system. Here we summarize evidence that zebrafish larvae, which retain these benefits in addition to their simple anatomy and complex locomotor behavior, represent an effective and reliable animal model with unique advantages for studying spinal cord regeneration. First, we describe how the injury response in zebrafish larvae is distinct from the process of development in the embryo. Next, we highlight regenerative mechanisms that are conserved between zebrafish larvae and adults, and finally we explain the specific experimental advantages of the larval system. In conclusion, we propose that these features endow the larval zebrafish model with a unique potential to expedite discovery of translationally applicable treatments for SCI.

Spinal cord regeneration in zebrafish larvae is distinct from development

Tissue and organ regeneration often involves the recapitulation of developmental processes, and several developmental signaling pathways are indeed reactivated during spinal cord regeneration in adult zebrafish (Cardozo et al., 2017). However, the use of zebrafish larvae as an SCI model has raised the question of whether the injury response at this stage represents true regeneration, as opposed to an extension of embryonic spinal cord development. In fact, experimental evidence shows that due to the particularly rapid pace of zebrafish embryogenesis, most fundamental milestones of spinal cord development have already been reached before the larval stage begins at 3 days post fertilization (dpf), and functional locomotor circuits are present after only one additional day.

The patterning of the zebrafish spinal cord into progenitor domains arranged along the dorsoventral axis (Lewis and Eisen, 2003) occurs through signaling morphogen gradients that are established before 1 dpf (Bonner et al., 2008; Danesin et al., 2021), and shortly thereafter drive expression of the homeodomain transcription factors that define these domains (Gribble et al., 2007; Bonner et al., 2008; Lien et al., 2016). The identity and position of differentiated neuronal subtypes is largely established by 3 dpf (Seredick et al., 2012; Reimer et al., 2013; Lien et al., 2016; Ohnmacht et al., 2016; Andrzejczuk et al., 2018; England et al., 2020), and by 4 dpf these neurons are assembled into functional circuits required for the transition to a mature swimming pattern, increased locomotion, and the emergence of foraging behavior (Buss and Drapeau, 2001; Borla et al., 2002; Kokel et al., 2010; Menelaou and McLean, 2012; Kroll et al., 2021; Pallucchi et al., 2022). Ependymal radial glia (ERG), the resident neural progenitor cells of the zebrafish spinal cord (Briona and Dorsky, 2014a; Hui et al., 2015), begin to establish characteristic marker expression and morphology at 2 dpf (Kim et al., 2008; Briona and Dorsky, 2014a; Matsuoka et al., 2016), and subpopulations of ERG have become fate-restricted by 3 dpf (Ali et al., 2021). Oligodendrocytes, one of the latest born spinal cord cell types, are generated and begin myelinating axon tracts by 2.5 dpf (Park et al., 2002; Kirby et al., 2006; Ali et al., 2021). Together, these studies show that the vast majority of neuronal and glial cell types in the zebrafish spinal cord appear within the first 3 days of life, and terminally differentiated neurons form functional spinal circuitry by the beginning of larval stages.

In addition to its developmental maturity, the larval zebrafish spinal cord also exhibits injury-dependent responses that are specific to regeneration. For example, signals derived from infiltrating innate immune cells do not participate in embryonic spinal cord patterning and differentiation, but have been demonstrated to be necessary and sufficient for both axon regrowth and regenerative neurogenesis in injured larvae (Ohnmacht et al., 2016; Tsarouchas et al., 2018; Nelson et al., 2019; Gollmann-Tepeköylü et al., 2020; Cavone et al., 2021; Vandestadt et al., 2021). Another striking regenerative response that takes place within the larval spinal cord is the formation of a glial bridge across the injury site, over which growing axons can traverse to reinnervate targets (Goldshmit et al., 2012; Klatt Shaw et al., 2021). After SCI, bridge-forming ERG extend processes longitudinally, in contrast to their exclusively radial orientation in the absence of injury (Matsuoka et al., 2016). Interestingly, regeneration-specific responses can even occur in direct opposition to developmental events, such as the production of motor neurons by *olig2*+ progenitors (Ohnmacht et al., 2016) that have already become restricted to producing oligodendrocytes before injury (Reimer et al., 2013). These results parallel data from the regenerating zebrafish retina, in which Müller radial glia dedifferentiate and replace neuronal cell types normally produced by early fate-restricted retinal progenitors (Ng Chi Kei et al., 2017).

Together these data show that larval spinal cord regeneration is not a continuation or even merely a recapitulation of developmental programs, but rather a series of injury-specific responses capable of dynamic changes to local anatomy and circuitry. These studies also demonstrate that larval zebrafish can be used to identify novel molecular and cellular components of the regenerative process.

Conservation of pro-regenerative mechanisms in the larval and adult zebrafish spinal cord

Comparing studies of spinal cord regeneration in larval and adult zebrafish can be difficult due to differences in injury paradigms, experimental perturbations, and assay techniques. However, where direct comparison is possible from the similar use of both models, broad conservation of pro-regenerative signaling pathways and cell types has been observed.

The Wnt signaling pathway promotes regeneration of several zebrafish tissues including the fin, brain, and spinal cord (Wehner et al., 2014, 2017, 2018; Cardozo et al., 2017; Shimizu et al., 2018). After spinal cord injury, Wnt signaling is active at the injury site in both larvae and adults (Briona et al., 2015; Strand et al., 2016), and Wnt pathway inhibition in both larvae and adults results in decreased axon regrowth and locomotor recovery following SCI (Briona et al., 2015; Strand et al., 2016; Wehner et al., 2017, 2018). In larvae, Wnt signaling promotes ERG proliferation and neurogenesis after injury (Briona et al., 2015), and in adults Wnt inhibition leads to increased expression of GFAP at the lesion site; a marker that is normally downregulated as ERG undergo regenerative neurogenesis (Strand et al., 2016). Finally, Wnt signaling has been shown to promote the deposition of pro-regenerative extracellular matrix (ECM) components such as Collagen XII in larvae (Wehner et al., 2017). While the specific Wnt-dependence of ECM deposition has not been tested in adult fish, recent studies demonstrate that vascular pericytes upregulate pro-regenerative ECM components including Collagen XII, and downregulate inhibitory ECM components, after SCI (Mokalled et al., 2016; Tsata et al., 2021).

Other pathways such as Fibroblast growth factor (Fgf) signaling have also been shown to be required for both larval and adult zebrafish spinal cord regeneration. In larvae, motoneuron ablation triggers axon regrowth that is dependent upon Fgf binding protein 3 (FGFbp3), an extracellular chaperone for Fgf ligands (Xu et al., 2022). After SCI in adult zebrafish, Fgf signaling is active in ERG and neurons and drives both axon regrowth and neurogenesis (Goldshmit et al., 2012, 2018). Hedgehog pathway activity, which promotes regenerative neurogenesis throughout life (Kuscha et al., 2012; Reimer et al., 2013; Ribeiro et al., 2017), and drives the switch of *olig2*+ ERG back to neurogenesis after injury in both larval and adult fish (Reimer et al., 2013; Ohnmacht et al., 2016), also amplifies motoneuron regeneration after SCI in both zebrafish larvae and adults through dopamine signaling (Reimer et al., 2013; Ohnmacht et al., 2016). Several other pro-regenerative pathways identified in adult zebrafish including Notch, Retinoic acid, and Bone morphogenetic protein signaling (Reimer et al., 2008, 2009; Hui et al., 2014) will require future studies to assess whether their functions are conserved in larvae.

Similar cellular responses to SCI have also been identified in larval and adult zebrafish. These include the rapid infiltration and gene upregulation by innate immune cells (Hui et al., 2010, 2014), as well as the required role of this immune response in functional recovery (Nelson et al., 2019; Cavone et al., 2021). The detailed process of glial bridging also appears to be conserved between larvae and adults (Goldshmit et al., 2012; Wehner et al., 2017; Klatt Shaw et al., 2021), although the experimental approaches used in these studies raise the possibility that bridge formation may be correlated with, but not absolutely required for, axon regrowth.

Taken together, there is considerable evidence that both the activation of specific molecular and cellular mechanisms and their functions in promoting spinal cord regeneration after SCI are widely conserved between larval and adult stages. This high level of mechanistic continuity throughout the zebrafish lifespan supports the potential applicability of discoveries obtained from the larval model to the regenerative process in all post-embryonic vertebrates, including mammals.

Advantages of the larval zebrafish model

In addition to the well-established genetic and molecular resources that make zebrafish a popular system for studying basic developmental mechanisms and modeling human disease, the larval model allows the use of experimental techniques that are difficult or even impossible to implement in adults, including *in vivo* imaging and high-throughput screening. Both of these powerful approaches rely on the combination of optical transparency, anatomical simplicity, and behavioral complexity of larval zebrafish compared to alternative vertebrate models.

The advantages of working with zebrafish larvae are perhaps most evident when considering the use of *in vivo* microscopic techniques such as live cell tracking, cellular ablations, and optogenetic recording, stimulation, and silencing of neuronal activity. These techniques all provide the ability to monitor and experimentally manipulate the process of spinal cord regeneration in real time at the single-cell level. The transparency of zebrafish larvae has been exploited using fluorescent transgenes to define the movements, morphological changes, lineage, and function of ERG and neurons after SCI (Goldshmit et al., 2018; Anguita-Salinas et al., 2019; Vasudevan et al., 2021). The required role of ERG in regeneration has been demonstrated using live photoablation (Matsuoka et al., 2016), an approach that provides the spatial precision necessary to target single cells while maintaining the overall structural integrity of the spinal cord. Optical accessibility has also allowed the use of chemically modified light-activated substrates to demonstrate the extrasynaptic function of neurotransmitters in spinal cord regeneration (Chang et al., 2021).

The use of large-scale screens to identify genes, proteins, and drugs with novel roles in spinal cord regeneration requires the ability to test hundreds or thousands of animals rapidly and with robust and reproducible anatomical and behavioral assays, and thus aligns almost perfectly with the larval zebrafish model. CRISPR/Cas9-mediated gene knockout in individual F0 larvae has been demonstrated to cause reproducible effects on stereotyped behaviors such as escape response and circadian locomotion (Kroll et al., 2021), and recently developed techniques such as MIC-Drop (Parvez et al., 2021) allow injection and subsequent detection of single-gene targeting reagents. These methods have increased screening efficiency to the point that several hundred genes can be functionally tested by a single researcher in a matter of weeks. The optical accessibility and lack of skeletal tissues in larval zebrafish also allow the use of a range of rapid injury paradigms from simple physical transections to semi-automated laser injuries and cell-specific photoablation (Briona and Dorsky, 2014b; Hecker et al., 2020; El-Daher et al., 2021). Further, a diverse catalog of quantifiable locomotor behaviors including swim kinematics, swim endurance, and escape response, facilitates simple and robust assessment of subsequent functional recovery (Mokalled et al., 2016; Hecker et al., 2020; Vasudevan et al., 2021). Smaller-scale screens using similar approaches have already shown success in identifying pro-regenerative genes and drugs (Chapela et al., 2019; Keatinge et al., 2021), and while the true power of large-scale screening has yet to be fully realized in a zebrafish larval SCI model, its future promise is exciting.

Despite the many experimental advantages of larval zebrafish, several observations support the continued need for an adult SCI model. While the rate of neurogenesis in the uninjured larval spinal cord is much lower than in the embryo (Briona and Dorsky, 2014a) it is still higher than in adults (Park et al., 2007), suggesting that additional barriers to the activation of quiescent neural progenitors may exist after adult injury. In addition, spinal cord-associated meningeal, skeletal, and vascular tissues not present during larval stages may provide additional pro-regenerative signals (Lin et al., 2012), as may adaptive immune cells (Gupta et al., 2021), which do not appear in zebrafish until 4–6 weeks post fertilization (Sullivan et al., 2017). It may be necessary to determine the identity and function of these signals in adult fish, because zebrafish larvae, like *Xenopus* tadpoles (Lin et al., 2012), can recover normal function in their absence.

Discussion

The suitability of the larval zebrafish as an SCI model may be best understood in the context of fish CNS neurogenesis, which unlike in mammals is initially rapid but also never-ending. Thus, while only a few neurogenic niches remain in the adult mammalian CNS, adult zebrafish retain many larval niches and widespread neurogenesis (Goldshmit et al., 2012; Becker and Becker, 2022; Varadarajan et al., 2022). Further illustrating this continuity, the adult zebrafish spinal cord maintains expression of progenitor domain-defining homeodomain transcription factors through adulthood (Reimer et al., 2009). Thus, the ability of the spinal cord to respond to injury, as well as its cellular composition and functional capacity, is much more similar in larval and adult zebrafish than in postnatal and adult mammals.

An additional consideration supporting the use of the larval zebrafish model arises from the recent finding that there is a substantial reorganization of spinal motor circuits between larval and adult stages (Pallucchi et al., 2022). Because our understanding of zebrafish spinal circuitry primarily comes from studies using larvae, and due to the emerging importance of synaptic and modulatory neurotransmitters as pro-regenerative signals (Chang et al., 2021; Huang et al., 2021), our ability to accurately characterize the sources and targets underlying functional recovery after SCI may depend on performing future investigations at a stage before this reorganization occurs.

In conclusion, use of larval zebrafish has the potential to expedite the discovery of new roles for genes, molecules, and cell types involved in spinal cord regeneration. The combination of their numerous practical and technical advantages indicates that the larval SCI model is uniquely positioned to make significant contributions to our understanding of the basic science of spinal cord regeneration and to future clinical efforts to ameliorate the most debilitating consequences of human spinal cord injuries.

Author contributions

SA reviewed the relevant literature, co-wrote, and edited the manuscript. RD co-wrote and edited the manuscript. Both authors contributed to the article and approved the submitted version.

Acknowledgments

We thank Dr. Shannon Odelberg for suggestions and comments on the manuscript.

Conflict of interest

The authors declare that the research was conducted in the absence of any commercial or financial relationships that could be construed as a potential conflict of interest.

Publisher's note

References

Ali, M. F., Latimer, A. J., Wang, Y., Hogenmiller, L., Fontenas, L., Isabella, A. J., et al. (2021). Met is required for oligodendrocyte progenitor cell migration in *Danio rerio*. *G3* 11, jkab265. doi: 10.1093/g3journal/jkab265

Alunni, A., and Bally-Cuif, L. (2016). A comparative view of regenerative neurogenesis in vertebrates. *Development* 143, 741–753. doi: 10.1242/dev.122796

Andrzejczuk, L. A., Banerjee, S., England, S. J., Voufo, C., Kamara, K., and Lewis, K. E. (2018). Tal1, Gata2a, and Gata3 have distinct functions in the development of V2b and cerebrospinal fluid-contacting KA spinal neurons. *Front. Neurosci.* 12, 170. doi: 10.3389/fnins.2018.00170

Anguita-Salinas, C., Sánchez, M., Morales, R. A., Ceci, M. L., Rojas-Benítez, D., and Allende, M. L. (2019). Cellular dynamics during spinal cord regeneration in larval zebrafish. *Dev. Neurosci.* 41, 112–122. doi: 10.1159/000500185

Becker, C. G., Lieberoth, B. C., Morellini, F., Feldner, J., Becker, T., and Schachner, M. (2004). L1.1 is involved in spinal cord regeneration in adult zebrafish. *J. Neurosci.* 24, 7837–7842. doi: 10.1523/JNEUROSCI.2420-04.2004

Becker, T., and Becker, C. G. (2022). Regenerative neurogenesis: the integration of developmental, physiological and immune signals. *Development* 149, dev199907. doi: 10.1242/dev.199907

Becker, T., Wullimann, M. F., Becker, C. G., Bernhardt, R. R., and Schachner, M. (1997). Axonal regrowth after spinal cord transection in adult zebrafish. *J. Comp. Neurol.* 377, 577–595. doi: 10.1002/(SICI)1096-9861(19970127)377:4<577::AID-CNE8>3.0.CO;2-#

Bonner, J., Gribble, S. L., Veien, E. S., Nikolaus, O. B., Weidinger, G., and Dorsky, R. I. (2008). Proliferation and patterning are mediated independently in the dorsal spinal cord downstream of canonical Wnt signaling. *Dev. Biol.* 313, 398–407. doi: 10.1016/j.ydbio.2007.10.041

Borla, M. A., Palecek, B., Budick, S., and O'malley, D. M. (2002). Prey capture by larval zebrafish: evidence for fine axial motor control. *Brain Behav. Evol.* 60, 207–229. doi: 10.1159/000066699

Briona, L. K., and Dorsky, R. I. (2014a). Radial glial progenitors repair the zebrafish spinal cord following transection. *Exp. Neurol.* 256, 81–92. doi: 10.1016/j.expneurol.2014.03.017

Briona, L. K., and Dorsky, R. I. (2014b). Spinal cord transection in the larval zebrafish. *J. Vis. Exp.* e51479. doi: 10.3791/51479

Briona, L. K., Poulain, F. E., Mosimann, C., and Dorsky, R. I. (2015). Wnt/ß-catenin signaling is required for radial glial neurogenesis following spinal cord injury. *Dev. Biol.* 403, 15–21. doi: 10.1016/j.ydbio.2015.03.025

Buss, R. R., and Drapeau, P. (2001). Synaptic drive to motoneurons during fictive swimming in the developing zebrafish. *J. Neurophysiol.* 86, 197–210. doi: 10.1152/jn.2001.86.1.197

Cardozo, M. J., Mysiak, K. S., Becker, T., and Becker, C. G. (2017). Reduce, reuse, recycle - developmental signals in spinal cord regeneration. *Dev. Biol.* 432, 53–62. doi: 10.1016/j.ydbio.2017.05.011

Cavone, L., McCann, T., Drake, L. K., Aguzzi, E. A., Oprişoreanu, A. M., Pedersen, E., et al. (2021). A unique macrophage subpopulation signals directly to progenitor cells to promote regenerative neurogenesis in the zebrafish spinal cord. *Dev. Cell* 56, 1617–1630.e6. doi: 10.1016/j.devcel.2021.04.031

Chang, W., Pedroni, A., Bertuzzi, M., Kizil, C., Simon, A., and Ampatzis, K. (2021). Locomotion dependent neuron-glia interactions control neurogenesis and regeneration in the adult zebrafish spinal cord. *Nat. Commun.* 12, 4857. doi: 10.1038/s41467-021-25052-1

Chapela, D., Sousa, S., Martins, I., Cristóvão, A. M., Pinto, P., Corte-Real, S., et al. (2019). A zebrafish drug screening platform boosts the discovery of novel therapeutics for spinal cord injury in mammals. *Sci. Rep.* 9, 10475. doi: 10.1038/s41598-019-47006-w

Danesin, C., Darche-Gabinaud, R., Escalas, N., Bouguetoch, V., Cochard, P., Al Oustah, A., et al. (2021). Sulf2a controls Shh-dependent neural fate specification in the developing spinal cord. *Sci. Rep.* 11, 118. doi: 10.1038/s41598-020-80455-2

El-Daher, F., Early, J. J., Richmond, C. E., Jamieson, R., Becker, T., and Becker, C. G. (2021). Controlled semi-automated lased-induced injuries for studying spinal cord regeneration in zebrafish larvae. *J. Vis. Exp.* e63259. doi: 10.3791/63259

England, S. J., Cerda, G. A., Kowalchuk, A., Sorice, T., Grieb, G., and Lewis, K. E. (2020). Hmx3a has essential functions in zebrafish spinal cord, ear and lateral line development. *Genetics* 216, 1153–1185. doi: 10.1534/genetics.120.303748

Fang, P., Lin, J. F., Pan, H. C., Shen, Y. Q., and Schachner, M. (2012). A surgery protocol for adult zebrafish spinal cord injury. *J. Genet. Genomics* 39, 481–487. doi: 10.1016/j.jgg.2012.07.010

Goldshmit, Y., Sztal, T. E., Jusuf, P. R., Hall, T. E., Nguyen-Chi, M., and Currie, P. D. (2012). Fgf-dependent glial cell bridges facilitate spinal cord regeneration in zebrafish. *J. Neurosci.* 32, 7477–7492. doi: 10.1523/JNEUROSCI.0758-12.2012

Goldshmit, Y., Tang, J., Siegel, A. L., Nguyen, P. D., Kaslin, J., Currie, P. D., et al. (2018). Different Fgfs have distinct roles in regulating neurogenesis after spinal cord injury in zebrafish. *Neural Dev.* 13, 24. doi: 10.1186/s13064-018-0122-9

Gollmann-Tepeköylü, C., Nägele, F., Graber, M., Pölzl, L., Lobenwein, D., Hirsch, J., et al. (2020). Shock waves promote spinal cord repair via TLR3. *JCI Insight* 5, e134552. doi: 10.1172/jci.insight.134552

Gribble, S. L., Nikolaus, O. B., and Dorsky, R. I. (2007). Regulation and function of Dbx genes in the zebrafish spinal cord. *Dev. Dyn.* 236, 3472–3483. doi: 10.1002/dvdy.21367

Gupta, S., Adhikary, S., and Hui, S. P. (2021). Decoding the proregenerative competence of regulatory T cells through complex tissue regeneration in zebrafish. *Clin. Exp. Immunol.* 206, 346–353. doi: 10.1111/cei.13661

Hecker, A., Anger, P., Braaker, P. N., Schulze, W., and Schuster, S. (2020). High-resolution mapping of injury-site dependent functional recovery in a single axon in zebrafish. *Commun. Biol.* 3, 307. doi: 10.1038/s42003-020-1034-x

Huang, C. X., Zhao, Y., Mao, J., Wang, Z., Xu, L., Cheng, J., et al. (2021). An injury-induced serotonergic neuron subpopulation contributes to axon regrowth and function restoration after spinal cord injury in zebrafish. *Nat. Commun.* 12, 7093. doi: 10.1038/s41467-021-27419-w

Hui, S. P., Dutta, A., and Ghosh, S. (2010). Cellular response after crush injury in adult zebrafish spinal cord. *Dev. Dyn.* 239, 2962–2979. doi: 10.1002/dvdy.22438

Hui, S. P., Nag, T. C., and Ghosh, S. (2015). Characterization of proliferating neural progenitors after spinal cord injury in adult zebrafish. *PLoS ONE* 10, e0143595. doi: 10.1371/journal.pone.0143595

Hui, S. P., Sengupta, D., Lee, S. G., Sen, T., Kundu, S., Mathavan, S., et al. (2014). Genome wide expression profiling during spinal cord regeneration identifies comprehensive cellular responses in zebrafish. *PLoS ONE* 9, e84212. doi: 10.1371/journal.pone.0084212

Keatinge, M., Tsarouchas, T. M., Munir, T., Porter, N. J., Larraz, J., Gianni, D., et al. (2021). CRISPR gRNA phenotypic screening in zebrafish reveals pro-regenerative genes in spinal cord injury. *PLoS Genet.* 17, e1009515. doi: 10.1371/journal.pgen.1009515

Kim, H., Shin, J., Kim, S., Poling, J., Park, H. C., and Appel, B. (2008). Notch-regulated oligodendrocyte specification from radial glia in the spinal cord of zebrafish embryos. *Dev. Dyn.* 237, 2081–2089. doi: 10.1002/dvdy.21620

Kirby, B. B., Takada, N., Latimer, A. J., Shin, J., Carney, T. J., Kelsh, R. N., et al. (2006). In vivo time-lapse imaging shows dynamic oligodendrocyte progenitor behavior during zebrafish development. *Nat. Neurosci.* 9, 1506–1511. doi: 10.1038/nn1803

Klatt Shaw, D., Saraswathy, V. M., Zhou, L., McAdow, A. R., Burris, B., Butka, E., et al. (2021). Localized EMT reprograms glial progenitors to promote spinal cord repair. *Dev. Cell* 56, 613.e7–626.e7. doi: 10.1016/j.devcel.2021.01.017

Kokel, D., Bryan, J., Laggner, C., White, R., Cheung, C. Y., Mateus, R., et al. (2010). Rapid behavior-based identification of neuroactive small molecules in the zebrafish. *Nat. Chem. Biol.* 6, 231–237. doi: 10.1038/nchembio.307

Kroll, F., Powell, G. T., Ghosh, M., Gestri, G., Antinucci, P., Hearn, T. J., et al. (2021). A simple and effective F0 knockout method for rapid screening of behaviour and other complex phenotypes. *eLife* 10, 59683. doi: 10.7554/eLife.59683

Kuscha, V., Barreiro-Iglesias, A., Becker, C. G., and Becker, T. (2012). Plasticity of tyrosine hydroxylase and serotonergic systems in the regenerating spinal cord of adult zebrafish. *J. Comp. Neurol.* 520, 933–951. doi: 10.1002/cne.22739

Lewis, K. E., and Eisen, J. S. (2003). From cells to circuits: development of the zebrafish spinal cord. *Prog. Neurobiol.* 69, 419–449. doi: 10.1016/S0301-0082(03)00052-2

Lien, H. W., Yuan, R. Y., Chou, C. M., Chen, Y. C., Hung, C. C., Hu, C. H., et al. (2016). Zebrafish cyclin Dx is required for development of motor neuron progenitors, and its expression is regulated by hypoxia-inducible factor 2α. *Sci. Rep.* 6, 28297. doi: 10.1038/srep28297

Lin, G., Chen, Y., and Slack, J. M. (2012). Transgenic analysis of signaling pathways required for Xenopus tadpole spinal cord and muscle regeneration. *Anat. Rec.* 295, 1532–1540. doi: 10.1002/ar.22437

Matsuoka, R. L., Marass, M., Avdesh, A., Helker, C. S., Maischein, H. M., Grosse, A. S., et al. (2016). Radial glia regulate vascular patterning around the developing spinal cord. *eLife* 5:e20253. doi: 10.7554/eLife.20253.022

Menelaou, E., and McLean, D. L. (2012). A gradient in endogenous rhythmicity and oscillatory drive matches recruitment order in an axial motor pool. *J. Neurosci.* 32, 10925–10939. doi: 10.1523/JNEUROSCI.1809-12.2012

Mokalled, M. H., Patra, C., Dickson, A. L., Endo, T., Stainier, D. Y., and Poss, K. D. (2016). Injury-induced ctgfa directs glial bridging and spinal cord regeneration in zebrafish. *Science* 354, 630–634. doi: 10.1126/science.aaf2679

Nelson, C. M., Lennon, V. A., Lee, H., Krug, R. G. 2nd, Kamalova, A., Madigan, N. N., Clark, K. J., et al. (2019). Glucocorticoids target ependymal glia and inhibit repair of the injured spinal cord. *Front. Cell Dev. Biol.* 7, 56. doi: 10.3389/fcell.2019.00056

Ng Chi Kei, J., Currie, P. D., and Jusuf, P. R. (2017). Fate bias during neural regeneration adjusts dynamically without recapitulating developmental fate progression. *Neural Dev.* 12, 12. doi: 10.1186/s13064-017-0089-y

Ohnmacht, J., Yang, Y., Maurer, G. W., Barreiro-Iglesias, A., Tsarouchas, T. M., Wehner, D., et al. (2016). Spinal motor neurons are regenerated after mechanical lesion and genetic ablation in larval zebrafish. *Development* 143, 1464–1474. doi: 10.1242/dev.129155

Pallucchi, I., Bertuzzi, M., Michel, J. C., Miller, A. C., and El Manira, A. (2022). Transformation of an early-established motor circuit during maturation in zebrafish. *Cell Rep.* 39, 110654. doi: 10.1016/j.celrep.2022.110654

Park, H. C., Mehta, A., Richardson, J. S., and Appel, B. (2002). olig2 is required for zebrafish primary motor neuron and oligodendrocyte development. *Dev. Biol.* 248, 356–368. doi: 10.1006/dbio.2002.0738

Park, H. C., Shin, J., Roberts, R. K., and Appel, B. (2007). An olig2 reporter gene marks oligodendrocyte precursors in the postembryonic spinal cord of zebrafish. *Dev. Dyn.* 236, 3402–3407. doi: 10.1002/dvdy.21365

Parvez, S., Herdman, C., Beerens, M., Chakraborti, K., Harmer, Z. P., Yeh, J. J., et al. (2021). MIC-Drop: a platform for large-scale *in vivo* CRISPR screens. *Science* 373, 1146–1151. doi: 10.1126/science.abi8870

Reimer, M. M., Kuscha, V., Wyatt, C., Sörensen, I., Frank, R. E., Knüwer, M., et al. (2009). Sonic hedgehog is a polarized signal for motor neuron regeneration in adult zebrafish. *J. Neurosci.* 29, 15073–15082. doi: 10.1523/JNEUROSCI.4748-09.2009

Reimer, M. M., Norris, A., Ohnmacht, J., Patani, R., Zhong, Z., Dias, T. B., et al. (2013). Dopamine from the brain promotes spinal motor neuron generation during development and adult regeneration. *Dev. Cell* 25, 478–491. doi: 10.1016/j.devcel.2013.04.012

Reimer, M. M., Sörensen, I., Kuscha, V., Frank, R. E., Liu, C., Becker, C. G., et al. (2008). Motor neuron regeneration in adult zebrafish. *J. Neurosci.* 28, 8510–8516. doi: 10.1523/JNEUROSCI.1189-08.2008

Ribeiro, A., Monteiro, J. F., Certal, A. C., Cristovão, A. M., and Saúde, L. (2017). Foxj1a is expressed in ependymal precursors, controls central canal position and is activated in new ependymal cells during regeneration in zebrafish. *Open Biol.* 7, 170139. doi: 10.1098/rsob.170139

Seredick, S. D., Van Ryswyk, L., Hutchinson, S. A., and Eisen, J. S. (2012). Zebrafish Mnx proteins specify one motoneuron subtype and suppress acquisition of interneuron characteristics. *Neural Dev.* 7, 35. doi: 10.1186/1749-8104-7-35

Shimizu, Y., Ueda, Y., and Ohshima, T. (2018). Wnt signaling regulates proliferation and differentiation of radial glia in regenerative processes after stab injury in the optic tectum of adult zebrafish. *Glia* 66, 1382–1394. doi: 10.1002/glia.23311

Strand, N. S., Hoi, K. K., Phan, T. M. T., Ray, C. A., Berndt, J. D., and Moon, R. T. (2016). Wnt/β-catenin signaling promotes regeneration after adult zebrafish spinal cord injury. *Biochem. Biophys. Res. Commun.* 477, 952–956. doi: 10.1016/j.bbrc.2016.07.006

Sullivan, C., Matty, M. A., Jurczyszak, D., Gabor, K. A., Millard, P. J., Tobin, D. M., et al. (2017). Infectious disease models in zebrafish. *Methods Cell Biol.* 138, 101–136. doi: 10.1016/bs.mcb.2016.10.005

Tsarouchas, T. M., Wehner, D., Cavone, L., Munir, T., Keatinge, M., Lambertus, M., et al. (2018). Dynamic control of proinflammatory cytokines Il-1β and Tnf-α by macrophages in zebrafish spinal cord regeneration. *Nat. Commun.* 9, 4670. doi: 10.1038/s41467-018-07036-w

Tsata, V., Möllmert, S., Schweitzer, C., Kolb, J., Möckel, C., Böhm, B., et al. (2021). A switch in pdgfrb(+) cell-derived ECM composition prevents inhibitory scarring and promotes axon regeneration in the zebrafish spinal cord. *Dev. Cell* 56, 509.e9–524.e9. doi: 10.1016/j.devcel.2020.12.009

Vandestadt, C., Vanwalleghem, G. C., Khabooshan, M. A., Douek, A. M., Castillo, H. A., Li, M., et al. (2021). RNA-induced inflammation and migration of precursor neurons initiates neuronal circuit regeneration in zebrafish. *Dev. Cell* 56, 2364-2380.e8. doi: 10.1016/j.devcel.2021.07.021

Varadarajan, S. G., Hunyara, J. L., Hamilton, N. R., Kolodkin, A. L., and Huberman, A. D. (2022). Central nervous system regeneration. *Cell* 185, 77–94. doi: 10.1016/j.cell.2021.10.029

Vasudevan, D., Liu, Y. C., Barrios, J. P., Wheeler, M. K., Douglass, A. D., and Dorsky, R. I. (2021). Regenerated interneurons integrate into locomotor circuitry following spinal cord injury. *Exp. Neurol.* 342, 113737. doi: 10.1016/j.expneurol.2021.113737

Wehner, D., Becker, T., and Becker, C. G. (2018). Restoration of anatomical continuity after spinal cord transection depends on Wnt/β-catenin signaling in larval zebrafish. *Data Brief* 16, 65–70. doi: 10.1016/j.dib.2017.10.068

Wehner, D., Cizelsky, W., Vasudevaro, M. D., Ozhan, G., Haase, C., Kagermeier-Schenk, B., et al. (2014). Wnt/β-catenin signaling defines organizing centers that orchestrate growth and differentiation of the regenerating zebrafish caudal fin. *Cell Rep.* 6, 467–481. doi: 10.1016/j.celrep.2013.12.036

Wehner, D., Tsarouchas, T. M., Michael, A., Haase, C., Weidinger, G., Reimer, M. M., et al. (2017). Wnt signaling controls pro-regenerative Collagen XII in functional spinal cord regeneration in zebrafish. *Nat. Commun.* 8, 126. doi: 10.1038/s41467-017-00143-0

Xu, G., Huang, Z., Sheng, J., Gao, X., Wang, X., Garcia, J. Q., et al. (2022). FGF binding protein 3 is required for spinal cord motor neuron development and regeneration in zebrafish. *Exp. Neurol.* 348, 113944. doi: 10.1016/j.expneurol.2021.113944

Zukor, K. A., Kent, D. T., and Odelberg, S. J. (2011). Meningeal cells and glia establish a permissive environment for axon regeneration after spinal cord injury in newts. *Neural Dev.* 6, 1. doi: 10.1186/1749-8104-6-1

Frontiers in
Molecular Neuroscience

Leading research into the brain's molecular structure, design and function

Part of the most cited neuroscience series, this journal explores and identifies key molecules underlying the structure, design and function of the brain across all levels.

Discover the latest Research Topics

See more →

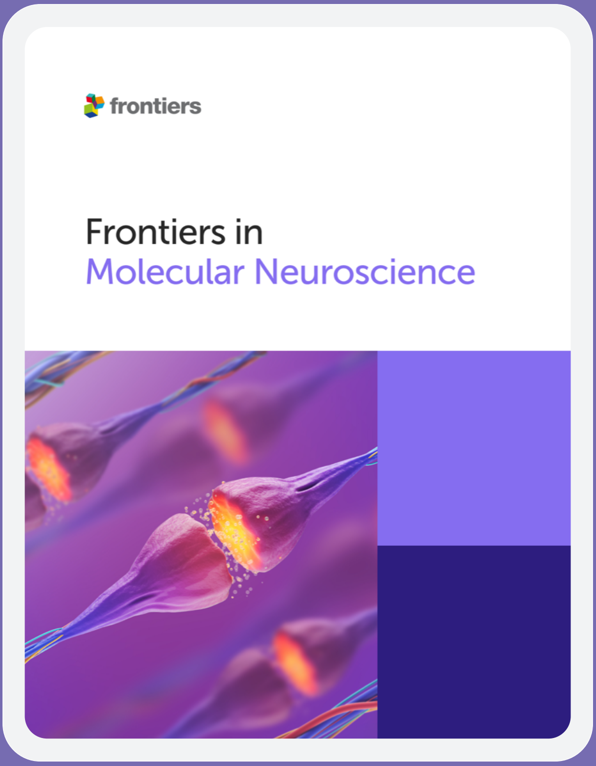

frontiers

Frontiers in
Molecular Neuroscience

Frontiers

Avenue du Tribunal-Fédéral 34
1005 Lausanne, Switzerland
frontiersin.org

Contact us

+41 (0)21 510 17 00
frontiersin.org/about/contact